Incorporating sedimentological observations, hydrogeophysics and conceptual knowledge to constrain 3D numerical heterogeneity models of alluvial systems

Inauguraldissertation

zur

Erlangung der Würde eines Doktors der Philosophie

vorgelegt der

Philosophisch-Naturwissenschaftlichen Fakultät

der Universität Basel

von

Emanuel Huber

aus Wagenhausen (TG)

Bern, 2017

Genehmigt von der Philosophisch-Naturwissenschaftlichen Fakultät

auf Antrag von Prof. Dr. Peter Huggenberger
Angewandte und Umweltgeologie
Universität Basel

Prof. Dr. Philippe Renard
Hydrogéologie stochastique et géostatistique
Université de Neuchâtel

Basel, den 23. Juni 2015

Prof. Dr. Jörg Schibler
Dekan

“ *Blind intelligence destroys sets and totalities, isolates all elements from their environment. It cannot conceive the inseparable link between observer and observed. The key realities are disintegrated, slipping through the cracks between academic disciplines. The human sciences no longer need a concept of the ‘human’, and sightless pedants conclude from this that the human does not exists, except as an illusion. The media are busily engaged in low-grade cretinization while the universities devote themselves to high-grade cretinizations. The result of the dominant methodology is ever greater obscurantism, because there is no longer any association between the scattered elements of learning and no longer any way of encoding them and reflecting upon them.* ”

Edgar Morin (1985) Blind Intelligence. In: *And He Loved Big Brother* (Eds. S.G. Shoham and F. Rosenstiel), Palgrave Macmillan UK, 165–169. doi:10.1007/978-1-349-07831-8_21

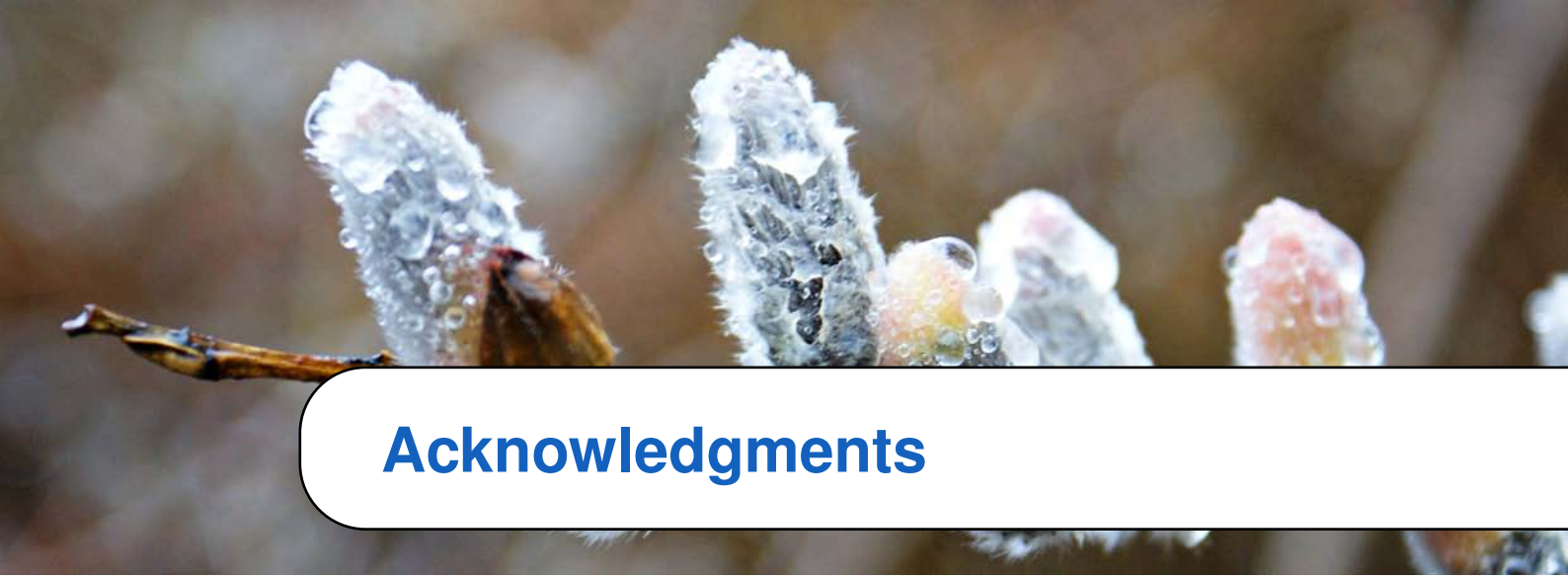

Acknowledgments

Life is like many worlds connected by many different doors. Usually, most of the doors are closed. But a few suddenly open and remain so. When looking back, it is intriguing to observe through which doors we have walked, as if an invisible hand has laid out a path for us. So, how did I end up writing a PhD thesis in geoscience at the University of Basel?

In 2002, I was grateful to receive a golden key — a scholarship — from the Canton of Thurgau (Switzerland), one that opened the door back to Switzerland and allowed me to escape the authoritarian, post-secondary education system of France (i.e., the *classes préparatoires aux grandes écoles*). I studied environmental engineering because I didn't want to end up as just another engineer working all day on how to optimise a screw or design yoghurt pots in a lab without natural light. It was my hope to spend some time on the field, outside.

In 2008, a friend from the Canton of Wallis — merci Léonard! — brought me to Basel's door, to the door of geology. He convinced me to participate in a sedimentology course, one that was held late in the afternoon by Peter Huggenberger of the University of Basel. Since I already had enough credit points, I did not need to attend this course. Learning 'some sedimentology late in the afternoon' was not a particularly appealing activity for a future engineer. This course, however, was not at all boring. Quite the opposite. We particularly enjoyed the field trips. At the same time, I was planning my mandatory internship in the waterworks of the city of Zurich. Unfortunately, the plan was cancelled at the last minute. I do not remember why exactly, but I knocked on Basel's door, i.e., the door of Prof. Huggenberger. 'I will see', was

his answer. A few months later, I was working in his research group for two months on an internship, discovering the field of hydrogeology as well as the nature of scientific thinking. At university, you don't (need to) learn to think, only to repeat like a parrot what you have learnt without having to really understand it. At the end of the internship, I didn't close the door behind me when I left to finish my studies. The door to geology was left slightly ajar.

In 2010, after a hard year spent in Germany, Prof. Huggenberger re-opened this door and offered me a position as a scientific collaborator in his research group in Basel. Six months later, I entered the realm of interdisciplinary scientific research: I pursued a PhD on subsurface heterogeneity of coarse, braided river systems with people from the Swiss universities of Neuchâtel, Lausanne and Bern, and Stanford University in the United States. The significant reduction of my salary that came with the change of position was more than compensated by the wide-open world that stood in front of me.

During one project meeting, we were talking about how the PhD students should arrange their exchange stays, which they were obliged to do as part of the PhD programme. When the discussion came to the exchange stay with the group of Jef Caers at Stanford University, Prof. Caers stated that he would like to work with someone from a completely different background.

'. . . like Emanuel', he said, and turning his head to look at me, 'Would you like to go to Stanford?'

'Oh, yes!' I answered, astonished.

Unexpectedly, a door to the USA — *z'amerika gsy*, the famous Swiss status symbol — stood suddenly open. . .

Now, two years have passed since I defended my thesis. I just came back to Switzerland from a 1.5-year post-doctoral stay at Stanford University and found all the Swiss doors to scientific research closed. But there are many worlds to discover, many doors to knock on and to open. Who knows what the future holds?

Thanks,

First and foremost, to Peter, who introduced me to the world of the coarse, braided river systems, made me discover the fascinating Tagliamento River and the Friuli region (northeast Italy). I particularly appreciate how you sharpened my thoughts as we discussed science, philosophy, politics, human relationships and many other topics. I learned a lot from you — not only knowledge, but also a conceptual way of thinking and how to lead research. You are always ready for a good laugh even if life is not easy, and you are not always politically correct — this is good — and you have a big heart behind your (at times) severe expression.

To Jef, for his interest in our research and for giving a *Swiss geologist* a chance. The stay at Stanford opened the door to uncertainty quantification and stochastic modelling, as well as a post-doctoral position.

To the other members of the *Ensemble project*. To Philippe, who initiated the interdisciplinary Ensemble project, coordinated all the research groups and accepted to be the external referee of the thesis. To Ivan, for your interest in the sedimentological process, your inspiring *physical science* approach to solve or discuss problems and the few beers you shared with me. To David, who invested many hours to train us in statistics and lead us through the door to the complex world of *Markov chain Monte Carlo methods*. To Niklas, for your critical comments and good advice. To Céline, for helping my family and me when we were in Stanford, for having a good sense of humour and trusting me when it comes to garden gnomes. To the other PhD students, Laureline, Guillaume and Tobias[1]. It was nice to share the same global objective and to enjoy together the project meetings and conferences. Thank you, Laureline, for the pleasant tour through the streets of San Francisco. I really enjoyed the San Francisco Museum of Modern Art.

To all the members of the Applied and Environmental Geology group in Basel. I will surely miss that friendly environment where everyone helps each other out. Thank you Jannis, Stefan I and II, Rebecca, Silvia, Horst, Eric, Annette, Eva, Matthias, Birte, and Karin. Special thanks go to Stefan II for your uncomplicated IT-support and to Silvia for efficiently dealing with all the administrative tasks.

To Carla, who always cheerfully welcomed me in Friuli — I will learn Italian, I promise! — and kindly shared some of her knowledge on Friulian geology. To all the guys who voluntary helped me to acquire the ground-penetrating radar data on the field: Lukas (the veteran), Benjamin, Renato, Susan, Laureline, Guillaume, and Ursula. To Claudio, for recharging our empty car battery in the middle of the braidplain of the Tagliamento River.

To my family and friends for their support. Especially to Silvan, who also started a family during his PhD studies, to Pierre *du Jura*, I will never forget our trip in tandem over the Golden Gate Bridge. To Mikael, my older brother,

[1]Tobias tragically died far too early in a mountaineering accident on 19 July 2014 at the Zinalrothorn in Wallis.

for his encouragement and for sharing his experience in the academic world of economic history — there are so many analogies between the (wrong) ways in which economists and the hydrogeologists think.

To Anaëlle and Anastasia, my two *Meiteli*, who make the days and nights colourful and really help to maintain a healthy research–life balance. To Sarah, my charming wife, for your interest in my research and support during my PhD thesis, particularly during the last sprint. Thank you for your unbeatable love and for trustfully following me through adventurous doorways.

This thesis would not have been possible without the financial support of the Swiss National Science Foundation, the Applied and Environmental Geology group (University of Basel, Peter Huggenberger), the Stanford Center for Reservoir Forecasting (Stanford University, Jef Caers), and the 'Freiwillige Akademische Gesellschaft Basel'.

Contents

E. Huber (2017) *Incorporating sedimentological observations, hydrogeophysics and conceptual knowledge to constrain 3D numerical heterogeneity models of alluvial systems.* Ph.D. thesis, Applied and Environmental Geology, University of Basel, Switzerland, 192 pp.

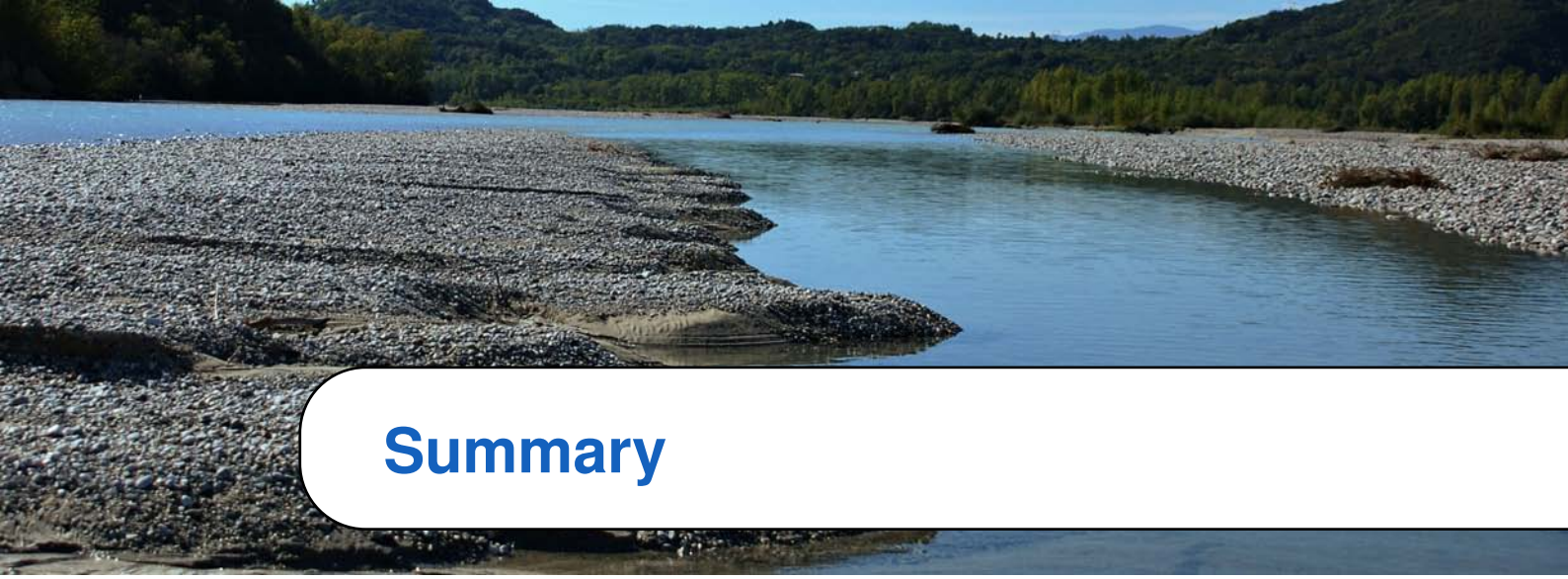

Summary

Coarse, braided river deposits are highly heterogeneous in terms of hydraulic properties and make up many groundwater reservoirs worldwide and more than two-thirds of the exploited aquifers in Switzerland. The management of these resources often requires the understanding of the subsurface flow processes and therefore, of the subsurface heterogeneity.

While coarse, braided river deposits were the focus of many studies, the relationship between the braided river dynamics and the resulting sedimentary structures is still poorly known. A better knowledge of this relationship is the key to geologically more realistic modelling of the subsurface heterogeneity by accounting for the former controls on the fluvial system (slope of the floodplain, terraces, lateral confinement, bedrock steps, etc.).

This thesis aims to (i) investigate the link between braided river morphodynamics and subsurface heterogeneity in a hydrogeological context and (ii) develop a numerical model of subsurface heterogeneity that accounts for this link. The sedimentological knowledge on coarse, braided river deposits was mainly gained from the observation of analogue Pleistocene coarse deposits in Switzerland. The Tagliamento River (northeast Italy) was chosen as a field laboratory to thoroughly study the geomorphology (surface) and near-surface sedimentology of coarse, braided rivers. The Tagliamento River is considered to be one of the last large semi-natural rivers of the Alps that has retained much of its natural sediment and discharge dynamics. The observations focused on a single reach sharing similar characteristics with partly confined valleys such as in the alpine foreland.

The sedimentary structures of coarse, braided river deposits can be comprehensively described by a small limited number of sedimentary structures that have specific hydraulic properties. A handful of depositional elements were identified. Among them, the cross bedded trough fills can significantly influence the flow field because their highly-permeable cross beds act as fast flow conduit. Such trough fills most probably form from confluence scour holes.

The geomorphological analysis of the Cimano-Pinzano reach is based on a LiDAR-derived digital elevation model (LiDAR-derived DEM), aerial and satellite photographs, a water-stage time series and regular field observations. Complex aggradation/degradation dynamics resulted in the formation of higher-lying zones incised by a drainage gully network and surrounded by zones that are often reworked by the river. The main geomorphological elements are

E. Huber (2017) *Incorporating sedimentological observations, hydrogeophysics and conceptual knowledge to constrain 3D numerical heterogeneity models of alluvial systems.* Ph.D. thesis, Applied and Environmental Geology, University of Basel, Switzerland, 192 pp.

identified in terms of their topographic signature and genesis, setting apart the trichotomy *water–vegetation–bar*. Two morphologies mark the active zones: a low-discharge morphology (low-discharge incisions and channels, slip-face lobes, etc.) superimposed on a high-discharge morphology (gravel sheets, scours, etc.). Based on the observations of vertical exposure of Pleistocene coarse, braided river deposits, each morphological element is associated with a depositional element. The preservation potential of the depositional elements is evaluated as a function of the river-bed aggradation dynamics and the resulting subsurface heterogeneity is discussed in terms of its impact on the subsurface flow.

Ground-penetrating radar (GPR) surveys performed on the active zones of the Cimano-Pinzano reach imaged many cross bedded trough fills as observed in ancient deposits. Finding a link between these structures and the evolution of the morphology is challenging. Nevertheless, some hypotheses about the formation of the trough structures are advanced. All the observations suggest the importance of the gravel sheets in the formation of cross bedded trough fills.

An object-based model was developed that mimics the dominant processes of floodplain dynamics. Contrary to existing models, this object-based model possesses the following properties: (i) it is consistent with field observations (outcrops, ground-penetrating radar data, etc.), (ii) it allows different sedimentological dynamics to be modeled that result in different subsurface heterogeneity patterns, and (iii) it is light in memory and computationally fast. To demonstrate its applicability, the object-based model is conditioned to interpreted two-dimensional GPR data and the uncertainty on the three-dimensional subsurface heterogeneity is quantified with Monte Carlo sampling.

The impact of an isolated trough fill complex on subsurface flow mixing is evaluated in terms of advective mixing. The trough fill complex is modelled with the object-based model that is fitted to GPR data. Hydraulic properties are assigned to the model cells and a subsurface flow through the model is simulated. The advective mixing is quantified with particle tracking. The results indicate strong advective mixing as well as a large flow deviation induced by the asymmetry of the trough fills with regard to the main flow direction. These findings depict possible advective mixing found in natural environments and can guide the interpretation of ecological processes such as in the hyporheic zone.

The geomorphological and sedimentological characterisations of the coarse, braided Cimano-Pinzano reach of the Tagliamento River contribute to a better understanding of the morphodynamics of coarse, braided river in relation to the subsurface heterogeneity. The object-based model allows the simulation of various geological settings and the methodology developed for the stereological study can be adapted to other types of data without many changes. Preliminary results of subsurface flow simulations through coarse, braided river deposits show a strong subsurface flow mixing.

1 Introduction

1.1 Rationale

Braided rivers are generally defined as rivers that flow in two or more streams around unstable bars and islands (e.g., Leopold and Wolman, 1957; Howard et al., 1970).

Braided rivers can be sandy (e.g., the Brahmaputra River in India/Bangladesh) as well as gravelly (e.g., the Rakaia River in New Zealand, Figure 1.1). They are generally steeper and wider than single-stream rivers carrying the same flow (Leopold and Wolman, 1957). Frequent variations in water discharge, a high turnover rate of the morphology as well as a wild natural landscape with high ecological value are the marks of braided river systems (Tockner et al., 2009).

Braided rivers were abundant mainly in temperate piedmonts and mountain-valleys, i.e., in areas with young mountains with high sediment supply such as the alpine regions (Tockner et al., 2009). They are still widespread in proglacial outwash plains where the sediment supply is high, the gradients are steep, the alluvial sediments are cohesion-less, and the meltwater discharge shows large fluctuations (Bennett and Glasser, 2009; Benn and Evans, 2010).

Braided rivers are one of the few environments where 'large-scale disturbances' can still occur today. However, these rivers become increasingly threatened by anthropogenic interventions, mainly by engineering works (Tockner et al., 2009). In consequence of river regulations, many coarse, braided rivers lost their natural high dynamics including the braiding character.

Ancient coarse, braided rivers formed heterogeneous deposits that make up many of the groundwater reservoirs worldwide (Huggenberger and Aigner, 1999; Klingbeil et al., 1999; Bayer et al., 2011) and more than two thirds of the exploited aquifers in Switzerland (Huggenberger, 1993). These groundwater reservoirs, when located in densely populated areas, are increasingly exposed to anthropogenic pressures that can lead to conflicting situations. Potential use conflicts are, for example, the extraction of groundwater for drinking water

E. Huber (2017) *Incorporating sedimentological observations, hydrogeophysics and conceptual knowledge to constrain 3D numerical heterogeneity models of alluvial systems.* Ph.D. thesis, Applied and Environmental Geology, University of Basel, Switzerland, 192 pp.

Wikipedia Commons

Figure 1.1 – Mouth of the Rakaia River (Canterbury Plains in New Zealand's South Island). The Rakaia River is one of the largest braided rivers in New Zealand.

supply and industry needs; the exploitation of groundwater as thermal energy; hydrological engineering that can modify the water cycle; and subsurface infrastructure engineering in the saturated zone (Huggenberger and Epting, 2011).

Therefore, the preservation of the groundwater resources in the long term requires understanding the groundwater processes and of the anthropogenic impact on the groundwater (Huggenberger and Epting, 2011). A critical prerequisite is therefore the characterisation of the sedimentary structures (Bayer et al., 2011) that can strongly impact the subsurface flow processes. This is especially true for coarse, braided river deposits that are very heterogeneous in terms of hydraulic properties and show large variations in hydraulic conductivity and porosity at the metre scale (e.g., Jussel et al., 1994; Webb and Anderson, 1996; Anderson et al., 1999; Klingbeil et al., 1999; Heinz et al., 2003).

Vertical outcrop exposures, such as in gravel carries (Figure 1.2), give a direct insight into the sedimentary characteristics of coarse, braided river deposits. Wall excavations in gravel carries allow the inference of the three-dimensional subsurface structures over a width of tens to hundreds of metres and a depth of tens of metres. The hydraulic properties of the sediments can be reliably estimated from disturbed and undisturbed samples in unweathered outcrops (e.g., Jussel et al., 1994; Klingbeil et al., 1999) and ground-penetrating radar (GPR) imaging can be directly compared with vertical exposures (e.g., Huggenberger, 1993).

However, this very rich information content is generally not available for real-case studies on groundwater systems. The hydraulic properties of the aquifer have to be indirectly estimated by combining measurement data with conceptual and numerical models at a specified resolution. Common types of data are, among others, hydraulic heads, natural and synthetic tracer concentrations, drill-core samples, pumping tests, flowmeter measurements and geophysical measurements such as GPR (Figure 1.3). Note that each measurement type has its own support scale that can be larger than the heterogeneity scale. Even

Emanuel Huber

Figure 1.2 – Example of a gravel carry (Marthalen, northeast Switzerland).

at research sites where an extraordinary amount of data is collected over a relatively small area the prediction of the subsurface flow and transport are still challenging (Teutsch et al., 1998).

There is a critical need in hydrogeological modelling for geologically more realistic subsurface models that correctly address the level of connectivity necessary for the model purpose (de Marsily et al., 2005; Kerrou et al., 2008). Indeed, widely-used representations of the subsurface heterogeneity based on smooth basis functions such as co-kriging (Kitanidis and Vomvoris, 1983; Hoeksema and Kitanidis, 1984) or the pilot points approach (RamaRao et al., 1995; Cooley, 2000; Alcolea et al., 2006) fail at reproducing the connectivity of high permeable geological structures that controls subsurface flow and transport (Gómez-Hernández and Wen, 1998; Zinn and Harvey, 2003; Renard and Allard, 2013).

Therefore, the National Research Council (2000) acknowledged the need to better characterise highly heterogeneous deposits and particularly to understand which heterogeneity scale controls the relevant processes. This is a challenge, partly due to (i) the gap in perceiving the subsurface heterogeneity between geologists and modellers, and (ii) different schools of thought that promote their own methods (Refsgaard et al., 2012). The choice of a method should rather be motivated from the perspective of the question that needs to be answered (Michalewicz and Fogel, 2004). Multiple-point statistics (Strebelle and Journel, 2001; Hu and Chugunova, 2008; Mariethoz and Caers, 2014) and object-based models (Lantuejoul, 2002; Allard et al., 2005; Michael et al., 2010; Ruiu et al., 2015) are promising alternatives that can realistically reproduce the small-scale heterogeneities as well as the hydraulic connectivity.

The current conceptual models of coarse, braided river deposits generally focus either on the low-discharge streams and on the surface/near surface (e.g., Webb, 1994; Bridge and Lunt, 2006; Ramanathan et al., 2010; Colombera et al., 2013; Pirot et al., 2014), or concentrate on sedimentological descriptions based on vertical outcrop analysis (e.g., Sun et al., 2008; Comunian et al., 2011). Although lithofacies descriptions become more and more detailed (Bayer et al., 2011), the relationship between the braided river dynamics and the resulting subsurface structures has not been fully explored (Smith et al., 2006). The

Emanuel Huber

Figure 1.3 – Left: observation well installation with the direct-push technology. Top right: flowmeter measurements. Bottom right: pumping test.

interaction between the river bed morphology and the turbulent flow leads to sorting processes that form sediment units with specific permeabilities (Best, 1993). The spatial distribution and the geometry of the preserved sediment units themselves control the connectivity of high/low permeable flow paths and, therefore, can strongly influence the hydraulic heterogeneity patterns (e.g., Anderson et al., 1999; Lunt et al., 2004; Comunian et al., 2011). The challenge in this context is to find a relationship between the present morphology of braided river systems and the hydraulic heterogeneity of ancient deposits (e.g., Siegenthaler and Huggenberger, 1993; Bristow and Jol, 2003; Kelly, 2006).

1.2 Objectives

This thesis focuses on the use of morphological, geological and geophysical observations to develop conceptual knowledge to design and constrain three-dimensional numerical heterogeneity models of coarse, braided river systems for subsurface flow simulations. More specifically, the main objectives are to (i) find a relation between the morphodynamics of coarse, braided rivers and the sedimentary structures of their deposits, (ii) derive a three-dimensional conceptual model to simulate the braided river deposits as a function of the river dynamics, and (iii) assess the potential impact of the subsurface heterogeneity

Box 1.1: ENSEMBLE project

The ENSEMBLE project (Integrated methods for stochastic ensemble aquifer modelling) aimed to integrate the recent developments in quantitative geology, hydrology, numerical, and stochastic modelling to improve the uncertainty quantification in groundwater applications. It involved the Swiss universities of Basel, Bern, Neuchâtel and Lausanne as well as Stanford University. The project focused on the development of new interdisciplinary methods (multiple point statistics, joint hydrogeological and geophysical inversion, fast methods for uncertainty analysis, etc.) to characterise of the heterogeneity of alluvial systems and to efficiently perform stochastic ensemble simulation of groundwater flow and solute transport in such systems. The ENSEMBLE project (2011–2015) was funded by the Swiss National Science Foundation within the Sinergia programme (grant no. CRSI22_132249/1).

on subsurface flow and transport.

1.3 Organisation of the thesis

More than twenty-five years have passed since the seminal work of Huggenberger and co-workers on the sedimentological characterisation of coarse, braided river deposits (Huggenberger et al., 1988; Siegenthaler and Huggenberger, 1993). Chapter 2 briefly reviews some of the current state of knowledge on the sedimentary characteristics of coarse, braided river deposits and introduces the reader to the main sedimentological concepts necessary to fully understand the present work.

The partly coarse, braided Tagliamento River (northeast Italy) is almost morphologically intact and internationally recognised as a model reference for highly dynamic, natural rivers (Ward et al., 1999). Therefore, this river is an ideal field laboratory to investigate the link between morphodynamics and sedimentology. Chapter 3 presents the Tagliamento River in a hydrogeological context and describes the Cimano-Pinzano reach which will be the focus of Chapter 4. Because this reach has been already the subject of several studies, the relevant research findings are succinctly summarised.

The morphodynamics of the Cimano-Pinzano reach is thoroughly studied in Chapter 4. The relationship between the surface processes and the subsurface structure is investigated from a geomorphological perspective in light of sedimentological observations of Pleistocene Rhine deposits from Chapter 2.

Some sedimentary characteristics of the Cimano-Pinzano reach were imaged with GPR as documented in Chapter 5. The GPR data were processed with, among others, an efficient deconvolution algorithm (Appendix, Chapter A

and B) and interpreted in three dimensions when possible. The interpreted subsurface structures are compared with observations made in gravel carries of Pleistocene deposits (Chapter 2) and related to the recent morphological evolution (Chapter 4).

The concepts developed in the previous chapters are crystallized into an object-based model where the main structures are described by simple geometric objects (Chapter 6). This object-based model mimics the floodplain formation in aggrading settings. Because the model is light in memory and fast in execution, it is well suited for Monte Carlo simulations. The model was applied to quantify the uncertainty on the three-dimensional subsurface structure from two-dimensional GPR data (stereological issue) with Monte Carlo sampling.

Chapter 7 evaluates the impact of the main sedimentary structures of coarse, braided river deposits on subsurface flow mixing. The geometrical objects of the object-based model were fitted to interpreted GPR data, and hydraulic properties were assigned to the sedimentary structures. Subsurface flow and advective transport simulations were performed on the synthetic model.

Chapter 8 highlights the main contributions of this thesis and suggests some promising avenues of research on coarse, braided river systems.

The efficient deconvolution approach used to process the GPR data was developed in collaboration with C. Schmelzbach (ETH Zürich) and is presented in Appendix A. The R-package `RGPR` (Appendix B) was developed to process, export, and visualise two- and three-dimensional GPR data, and to delineate reflectors. Appendix C briefly presents the R-package `RConics` that was developed to algebraically compute the intersection of a horizontal ellipsoid with a vertical plan, as required for the stereological problem of Chapter 6. This package is based on the elegant *projective geometry*. A glossary at the end of the thesis explains the main technical terms.

This study was funded by the Swiss National Science Foundation within the ENSEMBLE project (Box 1.1).

Box 1.2: Related publications

Chapter 4 is adapted from **Huber E.** and **Huggenberger P.** (2015) Morphological perspective on the sedimentary characteristics of a coarse, braided reach: Tagliamento River (NE Italy). *Geomorphology*, 248:111–124. doi:10.1016/j.geomorph.2015.07.015

Chapter 7 is adapted from **Huber E.** and **Huggenberger P.** (2016) Subsurface flow mixing in coarse, braided river deposits. *Hydrol. Earth Syst. Sci.*, 20:2035–2046. doi:10.5194/hess-20-2035-2016

Appendix A is adapted from **Schmelzbach C.** and **Huber E.** (2015) Efficient deconvolution of ground-penetrating radar data. *IEEE Transactions on Geoscience and Remote Sensing*, 53(9):5209–5217. doi:10.1109/TGRS.2015.2419235

References

Alcolea A., Carrera J. and **Medina A.** (2006) Pilot points method incorporating prior information for solving the groundwater flow inverse problem. *Advances in Water Resources*, **29**(11): 1678–1689.
doi: 10.1016/j.advwatres.2005.12.009

Allard D., Froidevaux R. and **Biver P.** (2005) Accounting for Non-stationarity and Interactions in Object Simulation for Reservoir Heterogeneity Characterization, In: *Geostatistics Banff 2004* (Eds. O. Leuangthong and C. Deutsch), 14 of Quantitative Geology and Geostatistics, Springer Netherlands, 155–164.
doi: 10.1007/978-1-4020-3610-1_16

Anderson M., Aiken J., Webb E. and **Mickelson D.** (1999) Sedimentology and hydrogeology of two braided stream deposits. *Sedimentary Geology*, **129**(3–4): 187–199.
doi: 10.1016/s0037-0738(99)00015-9

Bayer P., Huggenberger P., Renard P. and **Comunian A.** (2011) Three-dimensional high resolution fluvio-glacial aquifer analog: Part 1: Field study. *Journal of Hydrology*, **405**(1–2): 1–9.
doi: 10.1016/j.jhydrol.2011.03.038

Benn D.I. and **Evans D.J.A.** (2010) *Glaciers and Glaciation*: 2nd Edition. Hodder Education, 802 pp.
ISBN:978-0-340-90579-1

Bennett M.R. and **Glasser N.F.** (2009) *Glacial geology: Ice sheets and landforms*: 2nd Edition. Wiley-Blackwell, Chichester, UK, 385 pp.
ISBN:978-0-470-51691-1

Best J.L. (1993) On the interactions between turbulent flow structure, sediment transport and bedform developments: some considerations from recent experimental research, In: *Turbulence: Perspectives on Flow and Sediment Transport* (Eds. N.J. Clifford, J.R. French and J. Hardisty), John Wiley & Sons, Ltd, Chichester, UK, 61–93.

Bridge J.S. and **Lunt I.A.** (2006) Depositional Models of Braided Rivers, In: *Braided Rivers* (Eds. G.H. Sambrook Smith, J.L. Best, C.S. Bristow and G.E. Petts), Blackwell Publishing Ltd., Ch. 2, 11–50.
doi: 10.1002/9781444304374.ch2

Bristow C.S. and **Jol H.M.** (2003) An introduction to ground penetrating radar (GPR) in sediments. *Geological Society, London, Special Publications*, **211**(1): 1–7.
doi: 10.1144/GSL.SP.2001.211.01.01

Colombera L., Mountney N.P. and **McCaffrey W.D.** (2013) A quantitative approach to fluvial facies models: Methods and example results. *Sedimentology*, **60**(6): 1526–1558. doi: 10.1111/sed.12050

Comunian A., Renard P., Straubhaar J. and **Bayer P.** (2011) Three-dimensional high resolution fluvio-glacial aquifer analog – Part 2: Geostatistical modeling. *Journal of Hydrology*, **405**(1–2): 10–23. doi: 10.1016/j.jhydrol.2011.03.037

Cooley R.L. (2000) An analysis of the pilot point methodology for automated calibration of an ensemble of conditionally simulated transmissivity fields. *Water Resources Research*, **36**(4): 1159–1163. doi: 10.1029/2000wr900008

de Marsily G., Delay F., Gonçalvès J., Renard P., Teles V. and **Violette S.** (2005) Dealing with spatial heterogeneity. *Hydrogeology Journal*, **13**(1): 161–183. doi: 10.1007/s10040-004-0432-3

Gómez-Hernández J. and **Wen X.H.** (1998) To be or not to be multi-Gaussian? A reflection on stochastic hydrogeology. *Advances in Water Resources*, **21**(1): 47–61. doi: 10.1016/s0309-1708(96)00031-0

Heinz J., Kleineidam S., Teutsch G. and **Aigner T.** (2003) Heterogeneity patterns of Quaternary glaciofluvial gravel bodies (SW-Germany): application to hydrogeology. *Sedimentary Geology*, **158**(1–2): 1–23. doi: 10.1016/S0037-0738(02)00239-7

Hoeksema R.J. and **Kitanidis P.K.** (1984) An Application of the Geostatistical Approach to the Inverse Problem in Two-Dimensional Groundwater Modeling. *Water Resources Research*, **20**(7): 1003–1020. doi: 10.1029/wr020i007p01003

Howard A.D., Keetch M.E. and **Vincent C.L.** (1970) Topological and Geometrical Properties of Braided Streams. *Water Resources Research*, **6**(6): 1674–1688. doi: 10.1029/WR006i006p01674

Hu L.Y. and **Chugunova T.** (2008) Multiple-point geostatistics for modeling subsurface heterogeneity: A comprehensive review. *Water Resources Research*, **44**(11). doi: 10.1029/2008wr006993

Huggenberger P. (1993) Radar facies: recognition of facies patterns and heterogeneities within Pleistocene Rhine gravels, NE Switzerland. *Geological Society, London, Special Publications*, **75**(1): 163–176. doi: 10.1144/GSL.SP.1993.075.01.10

Huggenberger P. and **Aigner T.** (1999) Introduction to the special issue on aquifer-sedimentology: problems, perspectives and modern approaches. *Sedimentary Geology*, **129**(3–4): 179–186. doi: 10.1016/S0037-0738(99)00101-3

Huggenberger P. and **Epting J.** (2011) *Urban Geology*: Springer Basel. ISBN:978-3-0348-0184-3

Huggenberger P., Siegenthaler C. and **Stauffer F.** (1988) Grundwasserströmung in Schottern; Einfluss von Ablagerungsformen auf die Verteilung der Grundwasserfliess-geschwindigkeit. *Wasserwirtschaft*, **78**(5): 202–212.

Jussel P., Stauffer F. and **Dracos T.** (1994) Transport modeling in heterogeneous aquifers: 1. Statistical description and numerical generation of gravel deposits. *Water Resources Research*, **30**(6): 1803–1817. doi: 10.1029/94WR00162

Kelly S. (2006) Scaling and Hierarchy in Braided Rivers and their Deposits: Examples and Implications for Reservoir Modelling, In: *Braided Rivers* (Eds. G.H. Sambrook Smith, J.L. Best, C.S. Bristow and G.E. Petts), Blackwell Publishing Ltd., Ch. 4, 75–106. doi: 10.1002/9781444304374.ch4

Kerrou J., Renard P., Hendricks Franssen H.J. and **Lunati I.** (2008) Issues in characterizing heterogeneity and connectivity in non-multiGaussian media. *Advances in Water Resources*, **31**(1): 147–159. doi: 10.1016/j.advwatres.2007.07.002

Kitanidis P.K. and **Vomvoris E.G.** (1983) A geostatistical approach to the inverse problem in groundwater modeling (steady state) and one-dimensional simulations. *Water Resources*

Research, **19**(3): 677–690.
doi: 10.1029/wr019i003p00677

Klingbeil R., Kleineidam S., Asprion U., Aigner T. and **Teutsch G.** (1999) Relating lithofacies to hydrofacies: outcrop-based hydrogeological characterisation of Quaternary gravel deposits. *Sedimentary Geology*, **129**(3–4): 299–310.
doi: 10.1016/S0037-0738(99)00067-6

Lantuejoul C. (2002) *Geostatistical Simulation, Models and Algorithm*: Springer, 256 pp.
ISBN:978-3-540-42202-0

Leopold L.B. and **Wolman M.G.** (1957) River channel patterns: braided, meandering and straight. *US Geological Survey Professional Paper*, **282–B**: 39–85.

Lunt I.A., Bridge J.S. and **Tye R.S.** (2004) A quantitative, three-dimensional depositional model of gravelly braided rivers. *Sedimentology*, **51**(3): 377–414.
doi: 10.1111/j.1365-3091.2004.00627.x

Mariethoz G. and **Caers J.** (2014) *Multiple-Point Geostatistics*: John Wiley & Sons, Ltd.
ISBN:978-1-118-66275-5

Michael H.A., Li H., Boucher A., Sun T., Caers J. and **Gorelick S.M.** (2010) Combining geologic-process models and geostatistics for conditional simulation of 3-D subsurface heterogeneity. *Water Resources Research*, **46**(5): W05527.
doi: 10.1029/2009wr008414

Michalewicz Z. and **Fogel D.B.** (2004) *How to solve it - modern heuristics*: 2nd Edition. Springer, 554 pp.
ISBN:978-3-540-22494-5

National Research Council (2000) *Research Needs in Subsurface Science*: The National Academy Press, Washington (DC), 180 pp.
ISBN:978-0-309-09033-9

Pirot G., Straubhaar J. and **Renard P.** (2014) Simulation of braided river elevation model time series with multiple-point statistics. *Geomorphology*, **214**: 148–156.
doi: 10.1016/j.geomorph.2014.01.022

Ramanathan R., Guin A., Ritzi R.W., Dominic D.F., Freedman V.L., Scheibe T.D. and **Lunt I.A.** (2010) Simulating the heterogeneity in braided channel belt deposits: 1. A geometric-based methodology and code. *Water Resources Research*, **46**(4): W04515.
doi: 10.1029/2009WR008111

RamaRao B.S., LaVenue A.M., de Marsily G. and **Marietta M.G.** (1995) Pilot Point Methodology for Automated Calibration of an Ensemble of conditionally Simulated Transmissivity Fields: 1. Theory and Computational Experiments. *Water Resources Research*, **31**(3): 475–493.
doi: 10.1029/94wr02258

Refsgaard J.C., Christensen S., Sonnenborg T.O., Seifert D., Højberg A.L. and **Troldborg L.** (2012) Review of strategies for handling geological uncertainty in groundwater flow and transport modeling. *Advances in Water Resources*, **36**: 36–50.
doi: 10.1016/j.advwatres.2011.04.006

Renard P. and **Allard D.** (2013) Connectivity metrics for subsurface flow and transport. *Advances in Water Resources*, **51**: 168–196.
doi: 10.1016/j.advwatres.2011.12.001

Ruiu J., Caumon G. and **Viseur S.** (2015) Modeling Channel Forms and Related Sedimentary Objects Using a Boundary Representation Based on Non-uniform Rational B-Splines. *Mathematical Geosciences*, **48**(3): 259–284.
doi: 10.1007/s11004-015-9629-3

Siegenthaler C. and **Huggenberger P.** (1993) Pleistocene Rhine gravel: deposits of a braided river system with dominant pool preservation. *Geological Society, London, Special Publications*, **75**(1): 147–162.
doi: 10.1144/GSL.SP.1993.075.01.09

Smith G.S., Best J., Bristow C. and **Petts G.** (2006) Braided Rivers: Where have we Come in 10 Years? Progress and Future Needs, In: *Braided Rivers* (Eds. G.H. Sambrook Smith, J.L. Best, C.S. Bristow and G.E. Petts), Wiley-Blackwell, 1–10.
doi: 10.1002/9781444304374.ch1

Strebelle S.B. and **Journel A.G.** (2001) Reservoir Modeling Using Multiple-Point Statistics, In: SPE Annual Technical Conference and Exhibition Society of Petroleum Engineers.

Sun A.Y., Ritzi R.W. and **Sims D.W.** (2008) Characterization and modeling of spatial variability in a complex alluvial aquifer: Implications on solute transport. *Water Resources Research*, **44**(4).
doi: 10.1029/2007WR006119

Teutsch G., Klingbeil R. and **Kleineidam S.** (1998) Numerical modelling of reactive transport using aquifer analogue data, In: *Groundwater Quality: Remediation and Protection* (Eds. M. Herbert and K. Kova), *IAHS Series of Proceedings and Reports*, **250**, International Association of Hydrological Sciences, IAHS Press, 381–390.

Tockner K., Paetzold A., Karaus U., Claret C. and **Zettel J.** (2009) Ecology of Braided Rivers, In: *Braided Rivers* (Eds. G.H. Sambrook Smith, J.L. Best, C.S. Bristow and G.E. Petts), Blackwell Publishing Ltd., 339–359.
doi: 10.1002/9781444304374.ch17

Ward J., Tockner K., Edwards P., Kollmann J., Bretschko G., Gurnell A., Petts G. and **Rossaro B.** (1999) A reference river system for the Alps: the 'Fiume Tagliamento'. *Regulated Rivers: Research & Management*, **15**(1–3): 63–75.
doi: 10.1002/(SICI)1099-1646(199901/06)15:1/3<63::AID-RRR538>3.0.CO;2-F

Webb E. (1994) Simulating the three-Dimensional Distribution of Sediment Units in Braided-Stream Deposits. *Journal of Sedimentary Research*, **64B**(2): 219–231.

Webb E.K. and **Anderson M.P.** (1996) Simulation of Preferential Flow in Three-Dimensional, Heterogeneous Conductivity Fields with Realistic Internal Architecture. *Water Resources Research*, **32**(3): 533–545.
doi: 10.1029/95WR03399

Zinn B. and **Harvey C.F.** (2003) When good statistical models of aquifer heterogeneity go bad: A comparison of flow, dispersion, and mass transfer in connected and multivariate Gaussian hydraulic conductivity fields. *Water Resources Research*, **39**(3).
doi: 10.1029/2001wr001146

2 Characterisation of coarse, braided river deposits

Abstract The sedimentology contributes to aquifer characterization by inferring the former depositional environments from outcrops or subsurface imaging and developing conceptual models. These conceptual models can then be translated into numerical models to quantitatively address hydrogeological issues. There is a critical need in hydrogeological modelling for geologically more realistic models of subsurface heterogeneity. Indeed, widely-used models based on smooth basis functions, such as cokriging or the pilot-point approach, fail at reproducing the connectivity of high permeable geological structures that controls subsurface flow and transport. Therefore, a correct characterisation of the subsurface heterogeneity and an appropriate conceptual model are the critical keys to successful modelling. This chapter introduces the reader into the sedimentology of coarse, braided river deposits. Some representative vertical outcrops of Pleistocene coarse, braided river deposits in northeast Switzerland are presented to illustrate the main concepts.

2.1 Rationale

In order to better understand groundwater circulation within Quaternary valley fill deposits, Huggenberger and co-workers focused on the subsurface characterisation of Pleistocene coarse deposits in gravel carries in northeast Switzerland (e.g., Huggenberger et al., 1988; Siegenthaler and Huggenberger, 1993; Huggenberger, 1993; Huggenberger et al., 1994; Beres et al., 1995, 1999; Huggenberger and Regli, 2006). These sediments were deposited in a glacio-fluvial environment (e.g., Preusser et al., 2011) most probably by a braided river system as indicated by the landscape morphology (0.4°-slope of the alluvial plain, maximum extension of the ice cover, large volume of large-sized clasts

E. Huber (2017) *Incorporating sedimentological observations, hydrogeophysics and conceptual knowledge to constrain 3D numerical heterogeneity models of alluvial systems.* Ph.D. thesis, Applied and Environmental Geology, University of Basel, Switzerland, 192 pp.

deposited in a relatively short time, etc., see Siegenthaler and Huggenberger, 1993).

To develop a conceptual model of subsurface heterogeneity, it is necessary to (i) describe the subsurface into coherent sedimentological units (and subunits), (ii) investigate systematic relationships between the sedimentological units, (iii) develop a structuring schemes, and (iv) interpret the observations in terms of sedimentological processes. The following sections present the sedimentological model developed by Huggenberger and co-workers.

2.2 Sedimentary description of coarse, braided river deposits

Miall (1985) proposed an elaborated lithofacies code to describe and classify fluvial deposits. This lithofacies code was further developed and extended by Keller (1996) and Heinz and Aigner (2003a) (Box 2.2). This code is often too detailed to describe in a straightforward manner complex, laterally-varying sediment heterogeneity. Furthermore, the numerous lithofacies generally translate into a handful of hydrofacies as demonstrated by hydraulic measurements of samples or empirical laws linking grain-size distribution to hydraulic conductivity (see Section 2.2.3).

For these reasons, Huggenberger and Regli (2006) proposed a novel classification scheme (Table 2.1) to describe the main characteristic heterogeneities of coarse, braided river deposits for hydrogeological applications. This classification consists in a hierarchical arrangement of heterogeneity including, in order of increasing size, sedimentary textures, sedimentary structures, and depositional elements.

2.2.1 Sedimentary textures

A sedimentary texture reflects a particular grain-size distribution and sediment sorting. Sedimentary textures are commonly used to describe drill-core samples (see also the Unified Soil Classification System). Depending on the river catchment, some textures can be easily identified by their colour in the field (e.g., Siegenthaler and Huggenberger, 1993). The definitions of seven sedimentary textures from Huggenberger and Regli (2006) are listed below and some of them are illustrated on Figure 2.1 (some terminologies are explained in Box 2.1).

- ▷ open-framework gravel (OW): 'A well-sorted gravel, in which pore space is free of sand and silt, although clay and silt particles occasionally drape the pebbles'.
- ▷ bimodal gravel (BM): A gravel consisting 'of a matrix of well-sorted medium sand that fills interstices of a framework of well-sorted pebbles and occasional cobbles'.

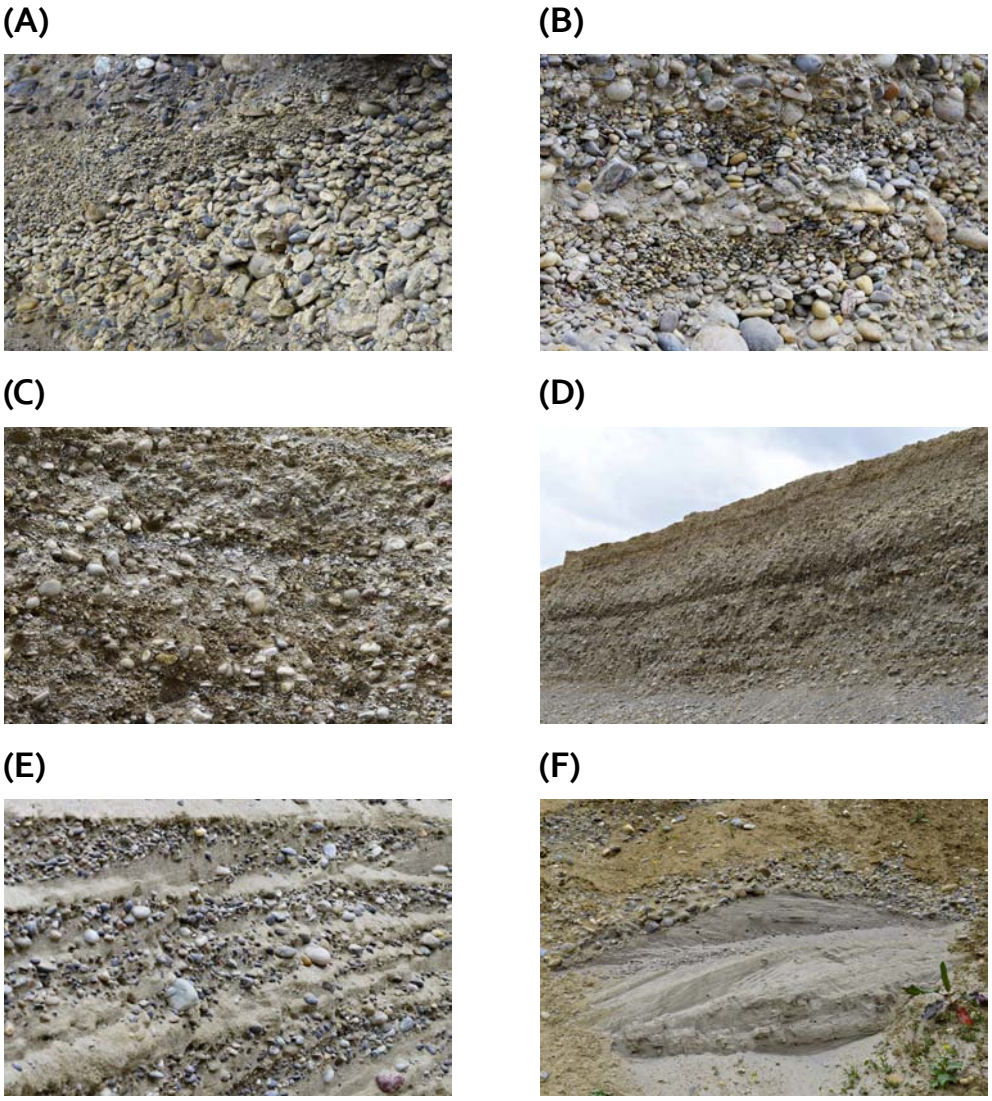

Figure 2.1 – Photographs of vertical outcrop exposures in a gravel carry near Muenchwilen AG (northwest Switzerland). **(A)** A fining-upward open-framework gravel, **(B)** open-framework–bimodal gravel couplets, **(C)** poorly-sorted gravel, **(D)** horizontal to sub-horizontal layering of 3-m-thick poorly-sorted gravel, **(E)** silty gravel, **(F)** sand.

- ▷ poorly-sorted gravel (GP): A 'poorly-sorted gravel, containing coarse sand, granules, pebbles and, rarely, cobbles. The gravel particles are well-rounded. Clay and silt particles never make up more than 5 %'.
- ▷ poorly-sorted, sandy gravel (GM): A 'poorly-sorted gravel with sand and silt'.
- ▷ silty gravel (SG): A 'poorly-sorted gravel, often containing up to 30 % sand and nearly 20 % silt and clay'.
- ▷ sand (SA): Poorly sorted to well-sorted sand without significant silt or clay fractions.
- ▷ silt (SI): Poorly graded silt.

2.2.2 Sedimentary structures

A sedimentary structure describes the spatial arrangement of one or two alternating sedimentary textures. Among all the sedimentary structures identified by Huggenberger and Regli (2006) and listed in Table 2.1, the open-framework–bimodal gravel (OW–BM) structure is the most singular (Figures 2.1B and 2.3 as well as chapter heading photograph on page 13). It consists of fining-upwards, normal graded sequences of bimodal gravel (BM) at the base and OW at the top with a sharp boundary between the sand in the BM and the open pores of the OW.

The hydraulic properties of the sedimentary structures were measured on disturbed and undisturbed samples by Jussel (1992); Jussel et al. (1994) in gravel carries in northeast Switzerland (see Table 2.2). the OW and OW–BM couplets can significantly influence subsurface flow processes, because of their high permeability relative to the other sedimentary structures. Furthermore, the OW–BM couplets show a strong anisotropy of the three-dimensional hydraulic conductivity tensor.

2.2.3 Other sedimentary descriptions

Anderson et al. (1999) identified in an outcrop in Wisconsin (U.S.A.) 11 lithofacies that were condensed into 7 hydrofacies. About 85 % of the coarse, braided river deposits consisted of only 4 lithofacies. They noticed the significant impact of the OW on the flow system even if the OW proportion was very small (about 4 % of the deposits).

Klingbeil et al. (1999) identified in the Singen basin (south Germany) 23 (!) lithofacies that were merged into 5 hydrofacies after hydraulic measurements: (i) BM, (ii) OW, (iii) planar/trough/horizontal gravels, (iv) massive gravels, and (v) SA.

Heinz et al. (2003) distinguished 5 main lithofacies in the 'former fluvial drainage zones of the Rhine glacier' (south Germany): (i) SA, (ii) well sorted gravel (GS-x), (iii) GP (the most frequently observed lithofacies), (iv) OW–BM couplets, and (v) GM. But they sophisticated their hydrofacies description by

Table 2.1 – Sedimentary textures, sedimentary structures, and depositional elements proposed by Huggenberger and Regli (2006). See the text for more details.

sedimentary textures	sedimentary structures	depositional elements
open-framework gravel (OW)	OW — fining upward beds	scour or trough fill
bimodal gravel (BM)	OW–BM — fining upwards sequences	gravel sheet or gravel dune
poorly-sorted gravel (GP)	GP — thick sheets	bedload sheet or traction carpet
poorly-sorted, sandy gravel (GM)	GM — massive bedding	overbank deposit
silty gravel (SG)	GP and GM — alternating layers	
sand (SA)	SG — massive beds related to GM	
silt (SI)	SA — different settings	
	SI — thin beds	

distinguishing 12 hydrofacies.

Bayer et al. (2011) identified 4 lithofacies: (i) GP (the most frequently observed lithofacies), (ii) OW–BM couplets, (iii) well sorted gravel and sand (GS-x), and (iv) SA. Following Heinz et al. (2003) they derived 10 hydrofacies but noticed that their classification could be simplified by grouping hydrofacies with similar hydraulic properties.

2.3 Depositional elements

Depositional elements are the results of either depositional (or accretionary) processes or erosional and depositional (or cut-and-fill) processes that leave a specific structure in the subsurface. In vertical outcrop exposures, depositional elements can be identified by (i) erosional lower-bounding surfaces, (ii) sedimentary structures, and (iii) clast orientation (Siegenthaler and Huggenberger, 1993). Four main depositional elements are generally observed in coarse, braided river deposits: (i) trough fill deposits, (ii) horizontally bedded gravel sheets (iii) massive, coarse-grained gravel sheets, and (iv) overbank deposits (Huggenberger and Regli, 2006).

2.3.1 Overbank deposits

The overbank deposits are composed of SA and SI and were mainly deposited by low velocity flows (e.g., on higher-lying areas or during flow recession).

Table 2.2 – Hydraulic properties of the sedimentary structures, after Jussel (1992) and Jussel et al. (1994).

	OW lense	OW–BM	GP	GM	SA	SI
Mean hydraulic conductivity K (mm/s)[a]	100	10	0.15	0.02	0.26	0.005
Standard deviation $\sigma_{\ln K_1}$[b]	0	0	0.5	0.6	0.4	0
Standard deviation $\sigma_{\ln K_2}$[c]	–	–	0.15	0.2	0	0
Anisotropy factor K_{hor}/K_{vert}	1	0.0025	1	1	1	1
Horizontal direction of K **tensor** κ (°)		−135–135	0	0	0	0
Inclination of K **tensor** ψ (°)	0	−19(9)[d]	0	0	0	0
Porosity n (%)	34.9	30.0	20.1	14.1	42.6	40.0
Standard deviation porosity σ_n (%)	1.4	3.9	1.4	1.0–3.1	0.8–4.4	–

[a] geometric mean hydraulic conductivity, at 10 °C
[b] between elements
[c] within elements
[d] reads 'average value (standard deviation value)'

2.3.2 horizontally bedded gravel sheets

Horizontally bedded gravel sheets mainly consist of GP with a bedded appearance that extends up to tens of metres. Occasionally, some single GM beds alternate with the GP (Huggenberger and Regli, 2006). The thickness of these gravel sheets typically varies between 0.1 m and 0.3 m but can reach 1 m. The horizontally bedded gravel sheets most likely originate from remnant of gravel sheets (also called 'unit bars', see Chapters 3 and 4) because the gravel sheet is the only geomorphological element that has a depositional character and is very extensive (Siegenthaler and Huggenberger, 1993, Chapter 4).

2.3.3 Massive coarse-grained gravel sheets

Laterally extensive, massive and coarse-grained gravel sheets are composed of GM. Their thickness ranges between few decimetres up to several metres (Huggenberger and Regli, 2006). The massive, coarse-grained layers of GM were surely deposited by large magnitude discharges with solid-solid momentum transfer (e.g., debris flow, glacial outburst, see Siegenthaler and Huggenberger, 1993).

2.3.4 Trough fills

Description

Trough fills with clear-cut erosional lower-bounding surface and tangential cross-beds are commonly observed in vertical exposures in gravel carries (e.g., Siegenthaler and Huggenberger, 1993; Jussel et al., 1994; Beres et al., 1995, 1999; Rauber et al., 1998; Stauffer and Rauber, 1998; Teutsch et al., 1998; Anderson et al., 1999; Klingbeil et al., 1999; Whittaker and Teutsch, 1999; Heinz and Aigner, 2003b; Heinz et al., 2003; Huggenberger and Regli, 2006; Bayer et al., 2011). On sections perpendicular to the former main flow direction, the trough fills show circular-arc-like erosional lower-bounding surfaces with strongly curved tangential cross-beds while on parallel sections the erosional lower-bounding surfaces are spoon-shaped with straighter but still tangential cross-beds (Siegenthaler and Huggenberger, 1993; Huggenberger and Regli, 2006).

Table 2.3 – Trough sizes estimated from interpreted three-dimensional ground-penetrating radar datasets. '41(13)' reads 'average value (standard deviation value)'.

	Beres et al. (1999)		Heinz and Aigner (2003b)	
	Site 1	**Site 2**	**Type A**	**Type B and C**
Length (m)	41(13)	35(6)	20–55	5–15
Width (m)	23(5)	20(3)	17–37	4–10
Thickness (m)	2.0(5)	1.9(3)	0.8–3.3	0.1–1.4
Orientation (°)	257(23)	239(6)	–	–

The sedimentary structure of the trough fills generally consists of alternating OW–BM couplet cross-beds (Figure 2.3), although fills consisting of GP cross-beds, SA cross-beds or interfingering cross-beds of GP and SA are not uncommon (e.g., Siegenthaler and Huggenberger, 1993). The BM grain size is positively correlated with the OW–BM cross-bed thickness that varies between 0.1 m and 0.5 m (Siegenthaler and Huggenberger, 1993; Heinz et al., 2003; Huggenberger and Regli, 2006).

Jussel et al. (1994) systematically quantified the size of trough fills in gravel carries (northeast Switzerland) and noticed that the trough length is log-normally distributed. Beres et al. (1999) performed three-dimensional ground-penetrating radar (GPR) imaging at two sites near Huentwangen (northeast Switzerland) and compared the GPR data with excavated vertical exposures. They inferred the dimensions of completely imaged trough fills from horizontal slices of three-dimensional GPR data (Table 2.3). They noticed that the interpreted trough fills were rather asymmetric and curved. Heinz and Aigner (2003b) carried out the same exercise in 4 gravel carries corresponding to 3 different types of 'sedimentary architecture of gravel bodies' in southwest Germany (Table 2.3).

The variations in size and proportion of trough fills correlate with the distance from the gravel carries to the former ice front (Siegenthaler and Huggenberger, 1993). About 1 km downstream from the former ice front, the trough fill sections are relatively small (1 m–10 m); 5 km downstream, the trough fill sections are several tens of metres wide and represent about one half of the deposits; 9 km downstream the trough fill sections are the largest (up to 100 m wide) and make one third of the deposits. The three-dimensional GPR surveys of Beres et al. (1999) confirmed this correlation. Similarly, Heinz et al. (2003) observed in 11 gravel pits in northwest Germany that the trough fill size and proportion positively correlate with the estimated former stream power per unit width.

Sedimentological interpretations

Siegenthaler and Huggenberger (1993) convincingly argued that trough fills form from filled confluence scour holes. This interpretation has been embraced by a significant number of studies on Quaternary coarse deposits (e.g., Jussel et al., 1994; Beres et al., 1995; Rauber et al., 1998; Stauffer and Rauber, 1998; Teutsch et al., 1998; Anderson et al., 1999; Beres et al., 1999; Klingbeil et al., 1999; Whittaker and Teutsch, 1999; Heinz and Aigner, 2003b; Heinz et al., 2003; Bayer et al., 2011). Confluence scours (Figure 2.4) are generally characterised by a scour hole and two avalanches faces at the upstream end of the scour hole where each streams enter into the scour (see the reviews of Ashmore and Gardner, 2008; Best and Rhoads, 2008). Many points of the comprehensive argumentation of Siegenthaler and Huggenberger (1993) are listed below.

- ▷ The morphology and size of the troughs (i.e., the erosional lower-bounding surfaces) are in most cases a similar to that of confluence scour holes (e.g., spoon-shaped).
- ▷ Unequal discharge as well as discharge fluctuations of the joining streams can result in:

Figure 2.3 – Vertical gravel pit exposure (Huentwangen, northeast Switzerland) perpendicular to the former main flow direction. The diameter of the red circle is about 90 cm.

Figure 2.4 – Confluence scour observed on the braidplain of the Tagliamento River. The white arrows indicate the flow direction (Orthophoto 2011, from the Autonomous Region of Friuli Venezia Giulia).

- Asymmetric scour holes (e.g., the asymmetric, curved trough fills observed by Beres et al. (1999)).
- Migration of the scour holes (e.g., Ashmore and Gardner, 2008), explaining the extremely large size of some trough fills.
- Shallowing/deepening of the scour holes.

▷ Two processes can fill the scour holes and explain the observed sedimentary structures:

- Foresets deposition at the avalanche face (upstream end of the scour holes). The observed interfingering of GP and SA could be explained by the load of different sediment types from the joining streams (Siegenthaler and Huggenberger, 1993).
- Lateral accretion of the scour hole during migration, possibly with migrating gravel dunes on the scour hole flanks as shown on Figure 2.4A (Huggenberger and Regli, 2006).

▷ Because the scour holes are located at the lowest positions they have the largest preservation potential (i.e., the largest chance of being preserved in the sedimentary records; Siegenthaler and Huggenberger, 1993).

▷ The differences in trough fill proportion and size between gravel carries can be explained by differences in the former fluvial system dynamics (e.g., discharge magnitude, the sediment input, the slope and the lateral confinement). The proportion of trough fills is expected to decrease with increasing aggradation rate. The trough fill size may be related to the stream power per unit width (Heinz et al., 2003) as suggested by the

positive correlation between the BM grain size and the thickness of the OW–BM couplets (Siegenthaler and Huggenberger, 1993).

Without indications, the phrase 'scour fill' is used interchangeably with 'trough fill' in the following chapters.

2.4 Examples

Figure 2.5 shows a typical gravel pit exposure from the Huentwangen site (north-east Switzerland) that is *perpendicular* to the former general flow direction. The lower section of the exposure is characterized by the superposition of several trough fills identified by erosional lower-bounding surfaces and cross-bedding. The former indicate the spatial extent of the erosional processes that shaped the trough fills while the latter can indicate the direction of migration. The top section of the exposure is dominated by poorly-sorted gravel (GP) lacking in the fine sediment fraction. The layered structure results from variation of the sand fraction and alternation of sand-free gravel. A few lags with dominant pebbles and cobbles indicate a reworking of the deposited gravel that left the coarse fraction.

Figures 2.6 and 2.7 show two vertical exposures from the Marthalen gravel carry (northeast Switzerland). Figures 2.6 is *perpendicular* to the the former general flow direction whereas Figure 2.7 is *parallel*. Note how the troughs are more elongated on the vertical exposure parallel to the general flow direction. Similarly to Figure 2.5, the upper section of the exposure consists of GP that is delimited from the lower section by a lag of dominant pebbles and cobbles. Some trough structures marked by clear-cut erosional lower-bounding surfaces and tangential cross-beds were identified.

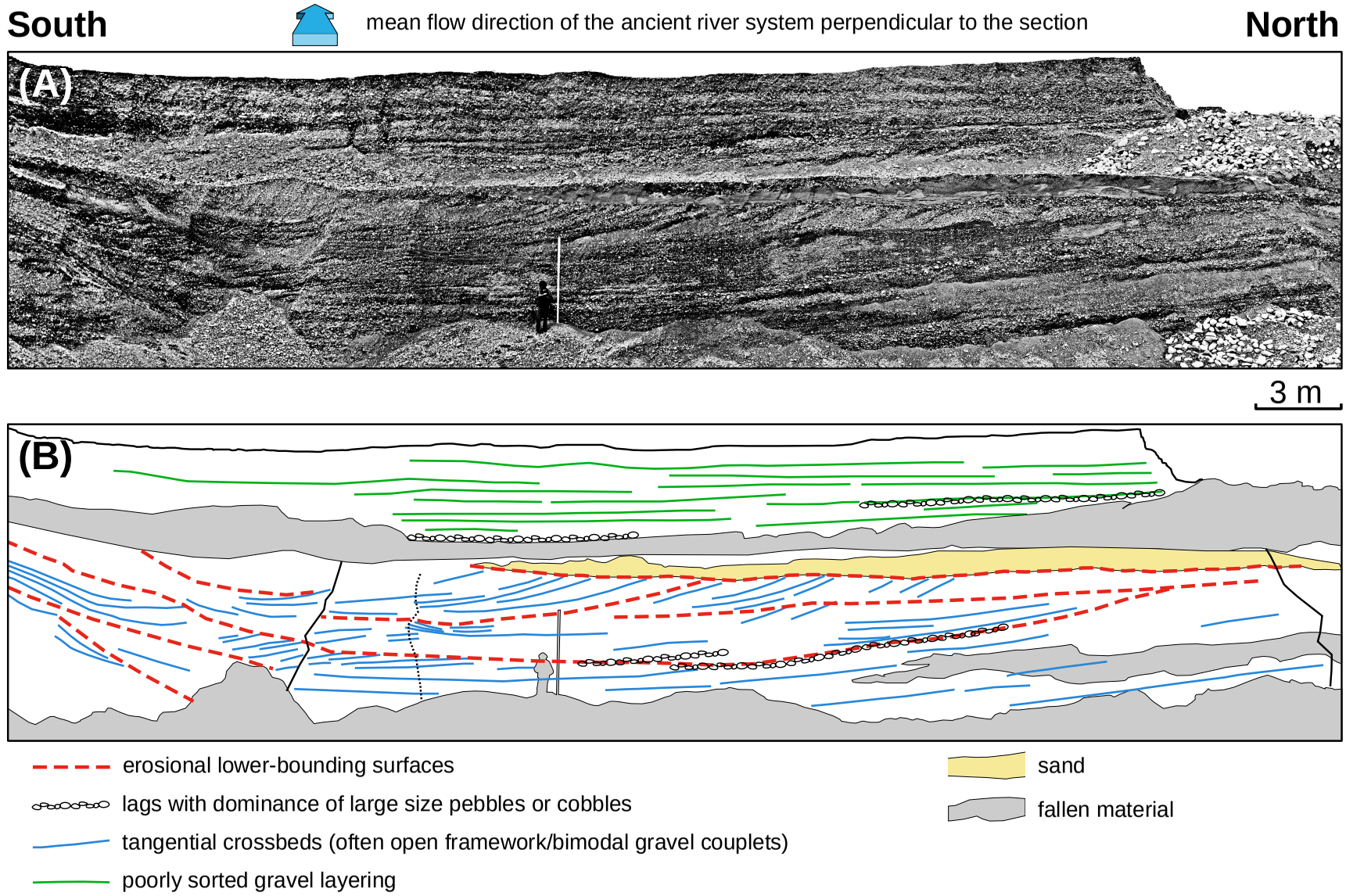

Figure 2.5 – **(A)** Gravel pit exposure (Huentwangen, northeast Switzerland) perpendicular to the former main flow direction (photograph from Peter Huggenberger). **(B)** Interpretation of **(A)**. See the text for more details.

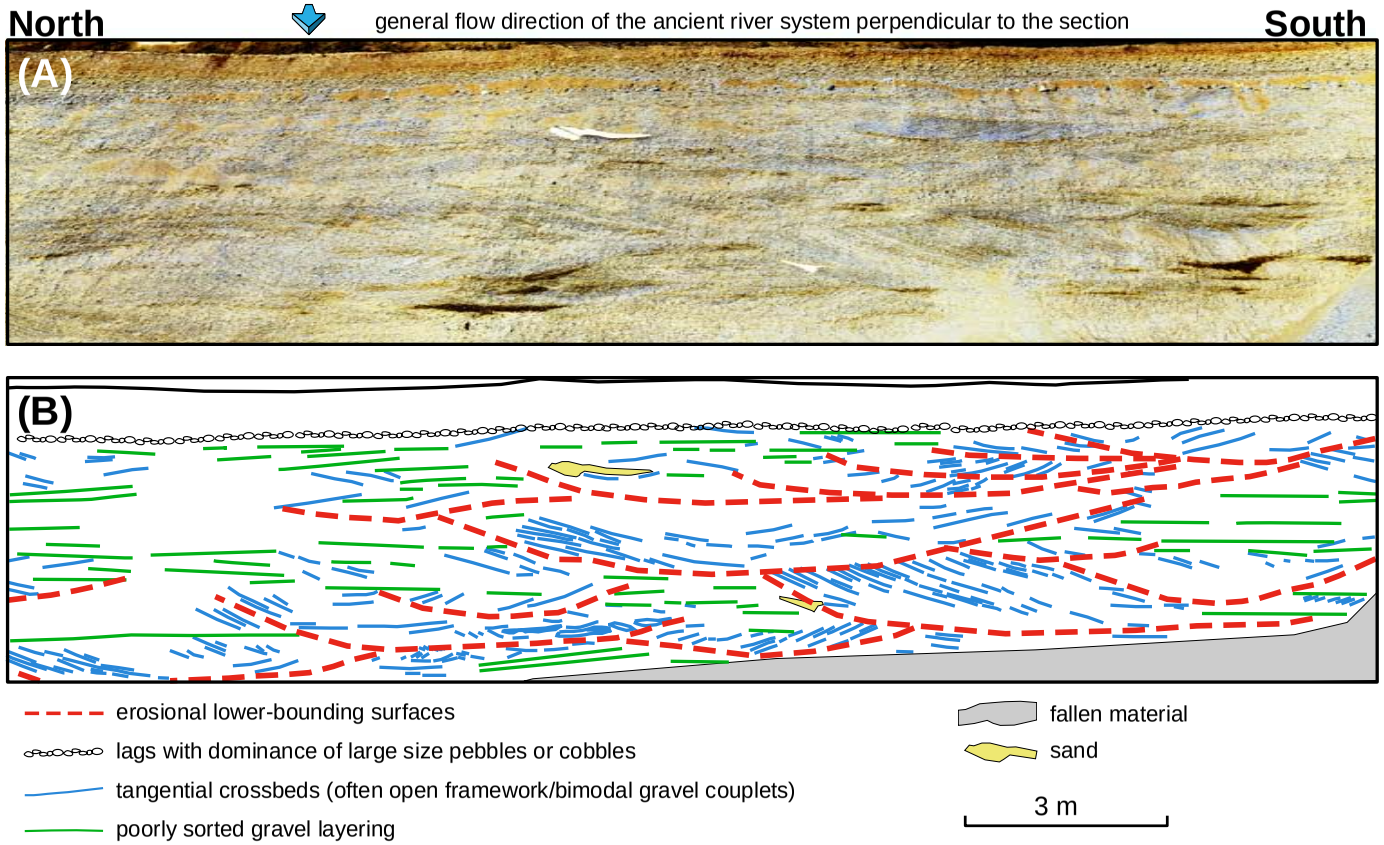

Figure 2.6 – **(A)** Gravel pit exposure (Marthalen, northeast Switzerland) perpendicular to the former main flow direction (photograph from Emanuel Huber). **(B)** Interpretation of **(A)**. See the text for more details.

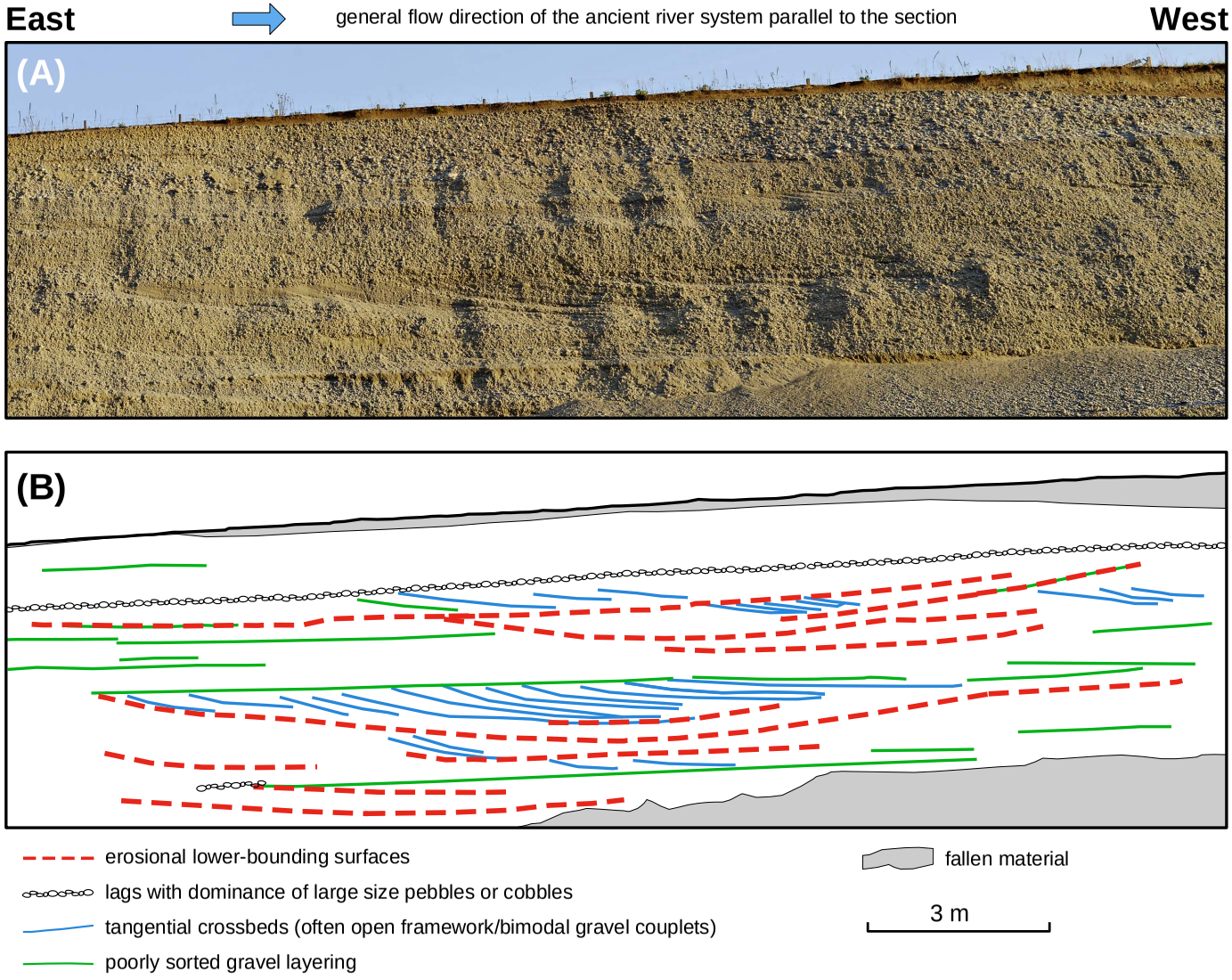

Figure 2.7 – **(A)** Gravel pit exposure (Marthalen, northeast Switzerland) parallel to the former main flow direction (photograph from Emanuel Huber). **(B)** Interpretation of **(A)**. See the text for more details.

Box 2.1: Sediment characterisation

Sorting 'A *well-sorted* sediment is characterized by a narrow range of grain sizes, whereas a *poorly sorted* sediment contains a wide range of grain sizes' (Allaby, 2013).

Support 'In a *clast-supported* sediment, there the larger fragments or clasts are separated from each other within the finer-grained matrix. In a *matrix-supported* sediment, the particles are in contact with one another and form the mechanical framework of the rock or sediment' (Allaby, 2013).

Grading 'A *normally-graded* sediment is sorted with the coarsest grain size at the base and the finest at the top. An *inverse-graded* sediment is sorted with the finest at the base and coarsest at the top' (Allaby, 2013).

Particle size British standard classification based on the particle diameter: >200 mm, boulder; 60 mm–200 mm, cobble; 2 mm–60 mm, gravel; 0.06 mm–2 mm, sand; 0.002 mm–0.006 mm, silt; <0.002 mm, clay (Allaby, 2013).

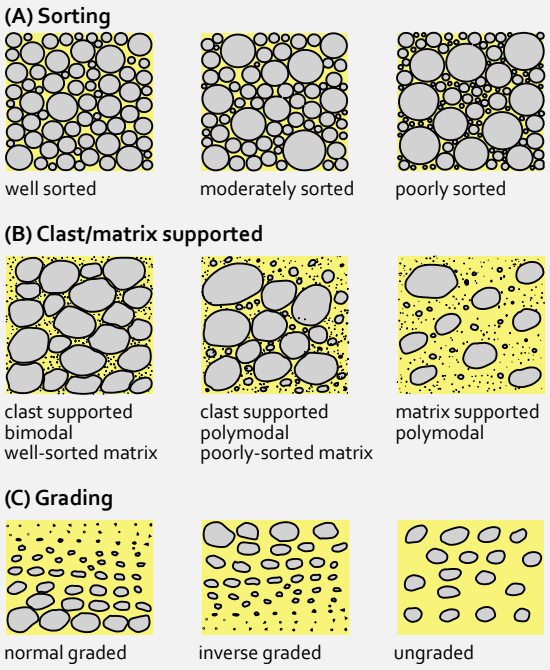

Figure 2.2 – **(A)** Sediment sorting (adapted from Pettijohn et al., 1987), **(B)** Clast/matrix-supported sediment (adapted from Harms et al., 1975), **(C)** Sediment grading (adapted from Harms et al., 1975).

Box 2.2: Lithofacies code–scheme

The lithofacies code (after Keller, 1996; Heinz and Aigner, 2003a) is defined by a series of indices $[i_0]I_1 i_2 i_3 [i_4]$ where the indices within brackets are optional.

Indices	Meaning	Abbreviations
i_0	grain size matrix	b: boulder c: cobbles g: gravel s: sand f: fines (silt/clay)
I_1	grain size	G: gravel S: sand GS: sand-gravel mixture F: fines (silt/clay)
i_2	texture	c: clast-supported m: matrix-supported '–': well sorted
i_3	stratification	x: stratified m: massive (no bedding) g: graded (normal, inverse)
i_4	additional information	i: imbrication a: alternation: e.g., o open framework, b bimodal h: horizontally stratified p: planar stratified t: trough cross stratified r: ripple cross-bedding

Examples:
Gcm: poorly sorted gravel
S–x: pure sand
GS–x: well sorted gravel
Gcg,a: alternation of BM and OW sequences
(c,b)Gm,i: cobble- and boulder-rich, poorly sorted gravel

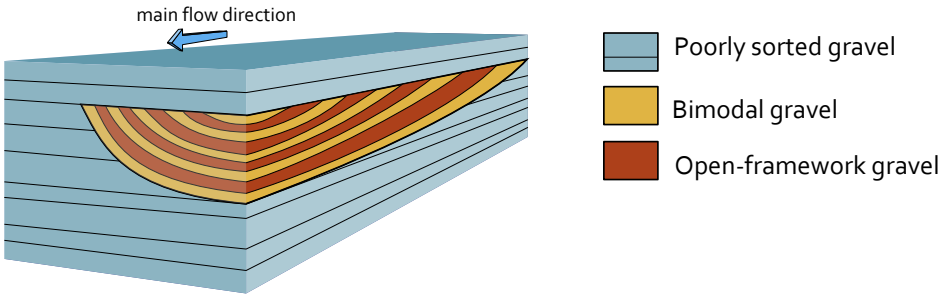

Figure 2.8 – Simplified conceptual model of a single trough fill (with alternating open-framework–bimodal gravel (OW–BM) couplets) embedded into layers of poorly-sorted gravel (GP).

2.5 Conclusion

Ancient deposits are valuable as they reveal (i) the depositional elements that have been preserved over the geological time, (ii) the relative proportion of the preserved depositional elements (spatial distribution), (iii) their geometries, and (iv) hydraulic properties (Miall, 2014). Furthermore, natural analogue outcrops provide clues on the erosional and depositional processes that formed the depositional elements.

The description of sedimentary deposits at a highly detailed level can be useful to better understand the sedimentological processes. However, within a hydrogeologic modelling framework, the focus lies rather on understanding the hydrogeologic system. 'Only some of [the] details are important to modeled system behavior and to the questions to be answered by the analysis. [One] need to understand that effective groundwater modeling involves discovery of which these factors might be' (Voss, 2011).

The sedimentary structures of coarse, braided river deposits can be comprehensively described by a small limited number of sedimentary structures (Table 2.1) that have specific hydraulic properties. A handful of depositional elements were identified. As schematically represented in Figure 2.8, coarse, braided river deposits are composed of two main depositional elements, remnants of gravel sheets and trough fills with clear-cut erosional lower-bounding surfaces.

The trough fills consisting of alternating layers of OW–BM couplets can significantly influence the flow field because the highly-permeable OW texture acts as fast flow conduit (Huggenberger and Regli, 2006). Several studies showed the impact of the OW–BM cross-beds on the flow field, transport concentration and sorption processes with two-dimensional and three-dimensional subsurface flow models (e.g., Jussel et al., 1994; Rauber et al., 1998; Stauffer and Rauber, 1998; Teutsch et al., 1998; Anderson et al., 1999; Whittaker and Teutsch, 1999; Heinz et al., 2003; Stauffer, 2007; Huber and Huggenberger, 2016). Trough fills most probably form from confluence scour holes (Siegenthaler and Huggenberger, 1993) and a systematic in the size distribution of the trough fills was observed at the km scale. The spatial distribution of remnant erosional lower-bounding surfaces in the subsurface is therefore an indicator for the dynamics of the former braided river system. The GP was often the most frequently observed texture and originate from the deposition of laterally extensive gravel sheets.

Observation of ancient deposits and of the surface/near subsurface are two key puzzle pieces to understanding the sedimentary processes and the subsurface heterogeneity. The challenge is to link these two puzzle pieces together (Smith et al., 2006).

References

Allaby M. (Ed.) (2013) *A Dictionary of Geology and Earth Sciences*: 4th Edition. Oxford University Press.
ISBN:978-0-199-65306-5

Anderson M., Aiken J., Webb E. and **Mickelson D.** (1999) Sedimentology and hydrogeology of two braided stream deposits. *Sedimentary Geology*, **129**(3–4): 187–199.
doi: 10.1016/s0037-0738(99)00015-9

Ashmore P. and **Gardner J.T.** (2008) Unconfined Confluences in Braided Rivers, In: *River Confluences, Tributaries and the Fluvial Network* (Eds. S.P. Rice, A.G. Roy and B.L. Rhoads), John Wiley & Sons, Ltd, 119–147.
doi: 10.1002/9780470760383.ch7

Bayer P., Huggenberger P., Renard P. and **Comunian A.** (2011) Three-dimensional high resolution fluvio-glacial aquifer analog: Part 1: Field study. *Journal of Hydrology*, **405**(1–2): 1–9.
doi: 10.1016/j.jhydrol.2011.03.038

Beres M., Green A., Huggenberger P. and **Horstmeyer H.** (1995) Mapping the architecture of glaciofluvial sediments with three-dimensional georadar. *Geology*, **23**(12): 1087–1090.
doi: 10.1130/0091-7613(1995)023<1087:MTAOGS>2.3.CO;2

Beres M., Huggenberger P., Green A.G. and **Horstmeyer H.** (1999) Using two- and three-dimensional georadar methods to characterize glaciofluvial architecture. *Sedimentary Geology*, **129**(1–2): 1–24.
doi: 10.1016/S0037-0738(99)00053-6

Best J.L. and **Rhoads B.L.** (2008) Sediment Transport, Bed Morphology and the Sedimentology of River Channel Confluences, In: *River Confluences, Tributaries and the Fluvial Network* (Eds. S.P. Rice, A.G. Roy and B.L. Rhoads), John Wiley & Sons, Ltd, 45–72.
doi: 10.1002/9780470760383.ch4

Harms J., Southard J., Spearing D. and **Walker R.** (1975) *Depositional environments as interpreted from primary sedimentary structures and stratification sequences*: S.E.P.M. Short Course, 161 pp.

Heinz J. and **Aigner T.** (2003a) Hierarchical dynamic stratigraphy in various Quaternary gravel deposits, Rhine glacier area (SW Germany): implications for hydrostratigraphy. *International Journal of Earth Sciences*, **92**(6): 923–938.
doi: 10.1007/s00531-003-0359-2

Heinz J. and **Aigner T.** (2003b) Three-dimensional GPR analysis of various Quaternary gravel-bed braided river deposits (southwestern Germany). *Geological Society, London, Special Publications*, **211**(1): 99–110.
doi: 10.1144/gsl.sp.2001.211.01.09

Heinz J., Kleineidam S., Teutsch G. and **Aigner T.** (2003) Heterogeneity patterns of Quaternary glaciofluvial gravel bodies (SW-Germany): application to hydrogeology. *Sedimentary Geology*, **158**(1–2): 1–23.
doi: 10.1016/S0037-0738(02)00239-7

Huber E. and **Huggenberger P.** (2016) Subsurface flow mixing in coarse, braided river deposits. *Hydrology and Earth System Sciences*, **20**(5): 2035–2046.
doi: 10.5194/hess-20-2035-2016

Huggenberger P. (1993) Radar facies: recognition of facies patterns and heterogeneities within Pleistocene Rhine gravels, NE Switzerland. *Geological Society, London, Special*

Publications, **75**(1): 163–176.
doi: 10.1144/GSL.SP.1993.075.01.10

Huggenberger P., Meier E. and **Pugin A.** (1994) Ground-probing radar as a tool for heterogeneity estimation in gravel deposits: advances in data-processing and facies analysis. *Journal of Applied Geophysics*, **31**(1–4): 171–184.
doi: 10.1016/0926-9851(94)90056-6

Huggenberger P. and **Regli C.** (2006) A Sedimentological Model to Characterize Braided River Deposits for Hydrogeological Applications, In: *Braided Rivers* (Eds. G.H. Sambrook Smith, J.L. Best, C.S. Bristow and G.E. Petts), Blackwell Publishing Ltd., Ch. 3, 51–74.
doi: 10.1002/9781444304374.ch3

Huggenberger P., Siegenthaler C. and **Stauffer F.** (1988) Grundwasserströmung in Schottern; Einfluss von Ablagerungsformen auf die Verteilung der Grundwasserfliessgeschwindigkeit. *Wasserwirtschaft*, **78**(5): 202–212.

Jussel P. (1992) Modellierung des Transports gelöster Stoffe in inhomogenen Grundwasserleitern. Ph.D. thesis, ETH Zürich, nr. 9663.

Jussel P., Stauffer F. and **Dracos T.** (1994) Transport modeling in heterogeneous aquifers: 1. Statistical description and numerical generation of gravel deposits. *Water Resources Research*, **30**(6): 1803–1817.
doi: 10.1029/94WR00162

Keller B. (1996) Lithofazies-Codes für die Klassifikation von Lockergesteinen. *Mitteilung der Schweizerischen Gesellschaft für Boden- und Felsmechanik*, **132**: 5–12.

Klingbeil R., Kleineidam S., Asprion U., Aigner T. and **Teutsch G.** (1999) Relating lithofacies to hydrofacies: outcrop-based hydrogeological characterisation of Quaternary gravel deposits. *Sedimentary Geology*, **129**(3–4): 299–310.
doi: 10.1016/S0037-0738(99)00067-6

Miall A. (2014) *Fluvial Depositional Systems*: Springer International Publishing.
ISBN:978-3-319-00665-9

Miall A.D. (1985) Architectural-element analysis: A new method of facies analysis applied to fluvial deposits. *Earth-Science Reviews*, **22**(4): 261–308.
doi: 10.1016/0012-8252(85)90001-7

Pettijohn F., Potter P. and **Siever R.** (1987) *Sand and Sandstone*: *Springer Study Edition Series*. Springer New York.
ISBN:9780387963501

Preusser F., Graf H.R., Keller O., Krayss E. and **Schlüchter C.** (2011) Quaternary glaciation history of northern Switzerland. *Quaternary Science Journal*, **60**(2-3): 282–305.
doi: 10.3285/eg.60.2-3.06

Rauber M., Stauffer F., Huggenberger P. and **Dracos T.** (1998) A numerical three-dimensional conditioned/unconditioned stochastic facies type model applied to a remediation well system. *Water Resources Research*, **34**(9): 2225–2234.
doi: 10.1029/98WR01378

Siegenthaler C. and **Huggenberger P.** (1993) Pleistocene Rhine gravel: deposits of a braided river system with dominant pool preservation. *Geological Society, London, Special Publications*, **75**(1): 147–162.
doi: 10.1144/GSL.SP.1993.075.01.09

Smith G.S., Best J., Bristow C. and **Petts G.** (2006) Braided Rivers: Where have we Come in 10 Years? Progress and Future Needs, In: *Braided Rivers* (Eds. G.H. Sambrook Smith, J.L. Best, C.S. Bristow and G.E. Petts), Wiley-Blackwell, 1–10.
doi: 10.1002/9781444304374.ch1

Stauffer F. (2007) Impact of highly permeable sediment units with inclined bedding on solute transport in aquifers. *Advances in Water Resources*, **30**(11): 2194–2201.
doi: 10.1016/j.advwatres.2007.04.008

Stauffer F. and **Rauber M.** (1998) Stochastic macrodispersion models for gravel aquifers. *Journal of Hydraulic Research*, **36**(6): 885–896.
doi: 10.1080/00221689809498591

Teutsch G., Klingbeil R. and **Kleineidam S.** (1998) Numerical modelling of reactive transport using aquifer analogue data, In: *Groundwater Quality: Remediation and Pro-*

tection (Eds. M. Herbert and K. Kova), *IAHS Series of Proceedings and Reports*, **250**, International Association of Hydrological Sciences, IAHS Press, 381–390.

Voss C.I. (2011) Editor's message: Groundwater modeling fantasies —part 1, adrift in the details. *Hydrogeology Journal*, **19**(7): 1281–1284.
doi: 10.1007/s10040-011-0789-z

Whittaker J. and **Teutsch G.** (1999) Numerical simulation of subsurface characterization methods: application to a natural aquifer analogue. *Advances in Water Resources*, **22**(8): 819–829.
doi: 10.1016/S0309-1708(98)00056-6

3 The Cimano-Pinzano reach of the Tagliamento River (northeast Italy)

Abstract The Tagliamento River (northeast Italy) is considered as one of the last large seminatural rivers of the Alps that has retained much of its natural sediment and discharge dynamics. A reach sharing similar characteristics with partly confined valleys such as in the alpine foreland was selected to investigate the relationship between the river dynamics and the subsurface heterogeneity. The geomorphological settings of this reach are described and the main findings of previous studies are summarised. As the morphological terminology can be misleading some morphological terms are defined at the end of this chapter.

3.1 The Tagliamento River, a reference ecosystem

The Tagliamento River (Figure 3.3) is in the Friuli Venezia Giulia region in northeast Italy and is considered as one of the last large semi-natural rivers of the Alps (Ward et al., 1999). According to Bertoldi et al. (2009), the Tagliamento River 'retains the most extensive and connected length of dynamic braided rivers within the Alps'.

The source of the Tagliamento River lies in the Carnian Alps at the Mauria Pass (1195 m a.s.l.). The Tagliamento River flows for 170 km through a 2500-km^2-funnel-shaped catchment (Figure 3.4). About 85 % of the catchment lies in mountainous area (Prealps and Alps) where heavy rainfalls frequently occur. There, the mean annual precipitation reaches locally about 3000 mm (Norbiato et al., 2007). The discharge regime of the Tagliamento River shows therefore large fluctuations (Bertoldi et al., 2009, Table 3.1).

From its source to the Pinzano gorge, the Tagliamento River is mostly gravelly braided and corresponds to a 'partly confined valley with bedrock-controlled

E. Huber (2017) *Incorporating sedimentological observations, hydrogeophysics and conceptual knowledge to constrain 3D numerical heterogeneity models of alluvial systems.* Ph.D. thesis, Applied and Environmental Geology, University of Basel, Switzerland, 192 pp.

Emanuel Huber

Figure 3.1 – Direct sediment coupling between the foothills and the (almost dry) Tagliamento River, near Madonna del Ponte (Villa Santina).

discontinuous floodplain' as defined by Brierley et al. (2002). That means that the up to 5-km-wide floodplain is confined by the foothills and locally narrowed by bedrock gorges and the geology (Figure 3.2). These narrow locations often originate from thrust tectonics and some of them are associated with a marked change of the river slope (e.g., the Pinzano gorge, see Figure 3.4). The active zones of the floodplain are up to 2 km wide. Downstream the Pinzano gorge, the Tagliamento River flows through the Venetian-Friulian plain (unconfined settings) and stays gravelly braided until Varmo. The gravel-sand transition as well as the braided-meandering transition are located near Varmo. There, the Tagliamento River narrows to 180 m. Spaliviero (2003) noted that the 'riverbed [between Pinzano and Varmo] is aggrading and the transition from braiding to meandering is shifting downstream'. From Latisana to the Golf of Trieste (Adriatic Sea) the meandering Tagliamento River is strongly dammed.

The Tagliamento catchment is a tectonically active landscape system locally characterised by highly fractured rocks (e.g., cataclasite; Cucchi et al., 2010) that deliver large amounts of sediments. The drainage system of the Tagliamento River in the mountainous part of the catchment is often directly coupled with the adjacent hills: the mobilised sediments from the hills can reach the streams (Figure 3.1; Church, 2002). Therefore, periods of intensive rainfall combined with steep hill slopes and extensive sediment sources lead to heavy sediment loads into the Tagliamento River and its tributaries. Large convective storm precipitations result in flash floods which can carry important quantities of sediments. These large flood events have significant erosional or aggrading (i.e., depositional) capacities and regularly reshape completely the river bed including the braided pattern.

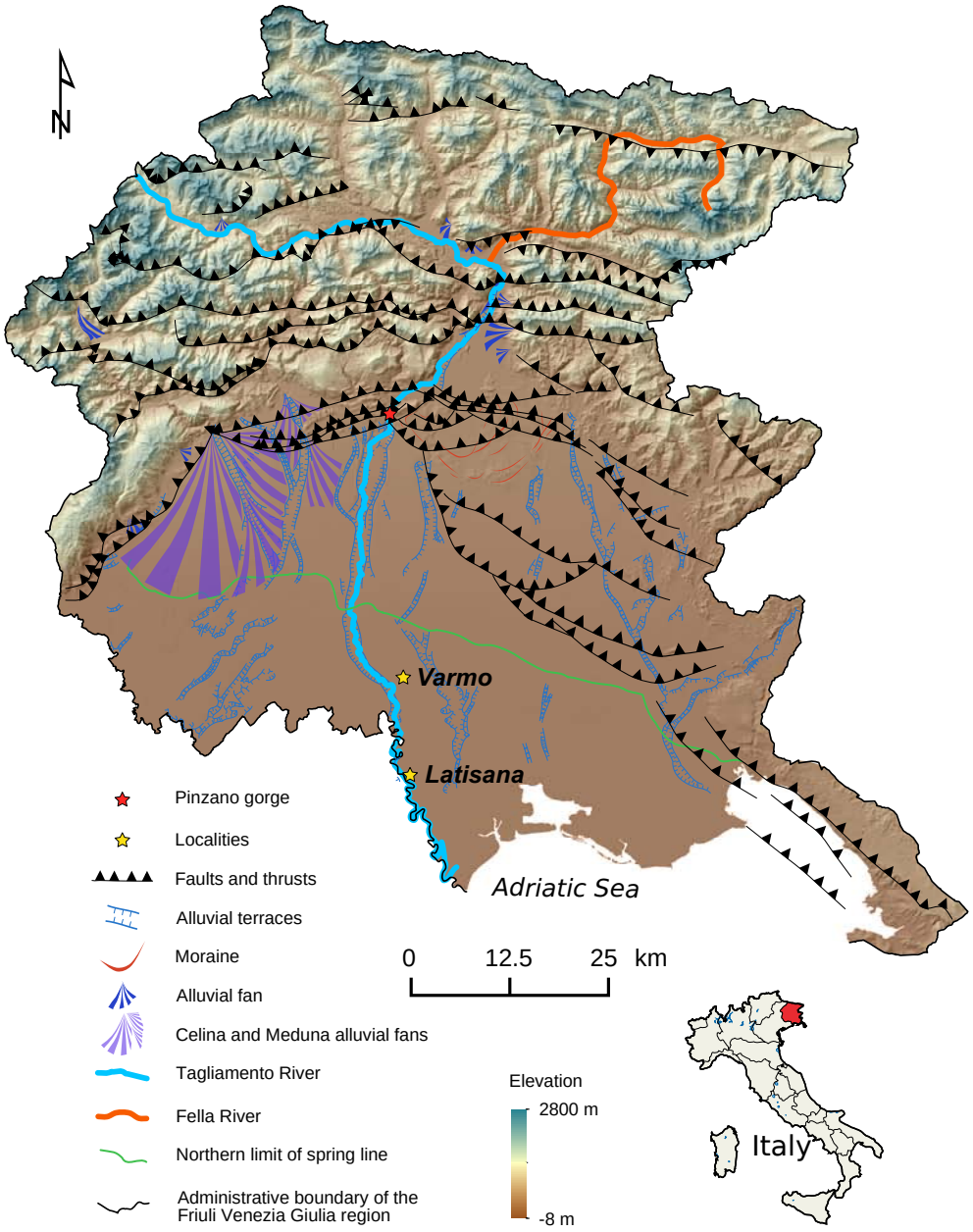

Figure 3.2 – Hillshaded digital elevation model of the Friuli Venezia Giulia region (40-m resolution). The location of the Friuli Venezia Giulia region is highlighted in red on the small map of Italy (adapted from the 'Carta geologica del Friuli Venezia Giulia').

The Tagliamento alluvial system offers the opportunity to study the relation between the surface morphology, the geometry and size of the principal depositional elements that constitute the sediments in many of the river valleys in the Alps and its foreland. Furthermore, slope differences between river reaches (Figure 3.4) can lead to either aggradations or degradation. Therefore, marked differences in preservation potential of the main depositional elements are to be expected over relatively short distances.

United States Geological Survey/NASA Landsat 5

Figure 3.3 – The Tagliamento River from space. Landsat 5 Thematic Mapper image recorded the 20 September 2010. At the west of the Tagliamento River the dryland braided Cellina and Meduna Rivers form a giant 'V' shape.

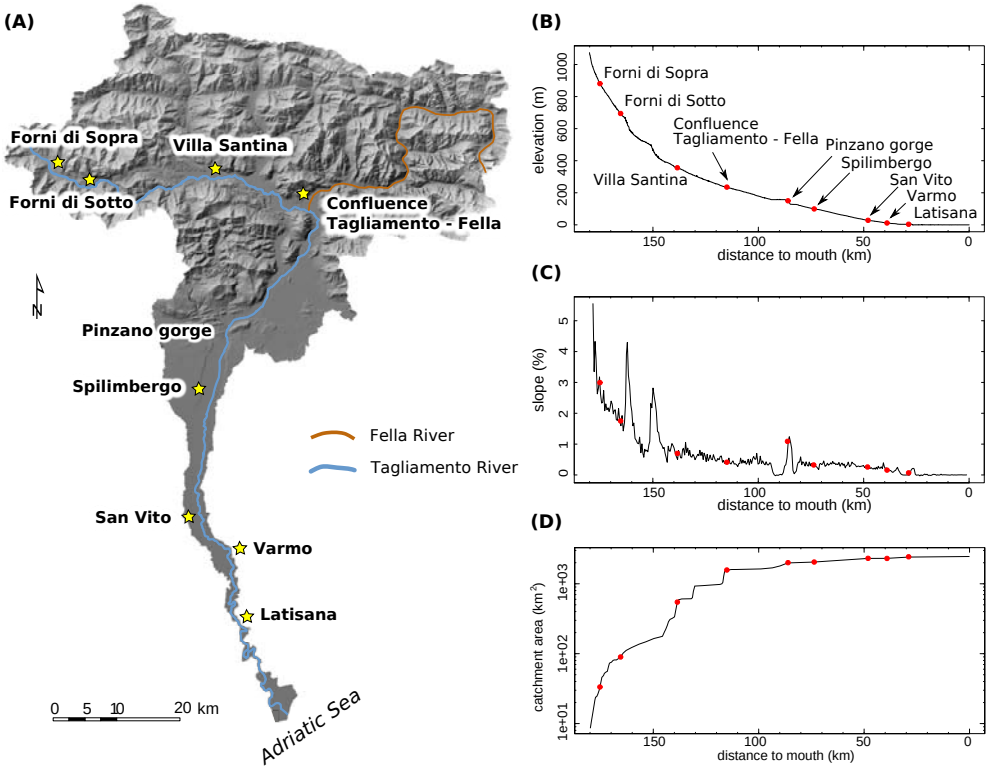

Figure 3.4 – (A) The Tagliamento catchment. (B)–(D) The elevation, slope and cumulative catchment area of the Tagliamento River as a function of its course length (estimated from a 40-m-resolution digital elevation model).

3.2 The Cimano-Pinzano reach

For our study, we are primarily interested in the partly-confined valleys in the external part of mountain ranges and foothills, as the dynamics are comparable to important large valleys in similar structural settings: they are akin in terms of gravel and sand proportions, and lateral sediment migration dominates over longitudinal transport.

The present work focuses on the 6.5-km-long Cimano-Pinzano reach delimited at the upstream end by the Cimano bridge (Figure 3.7) and downstream by the Pinzano gorge (Figure 3.5). The Cimano bridge is built on a large, stable wooded island with a centre formed by a 100-m-narrow and 600-m-long Tertiary conglomerate (Cucchi et al., 2010). The Tagliamento River flows

Table 3.1 – Discharge of the Tagliamento River at Venzone (20 km upstream the Pinzano gorge) where the catchment area is 1866 km^2 (from Bertoldi et al., 2009). Q_{50} means the 50-year return interval peak discharge.

	Discharge m^3/s
$Q_{\text{annual mean}}$	90
Q_{50}	3500
Q_{100}	4300
Q_{500}	6000

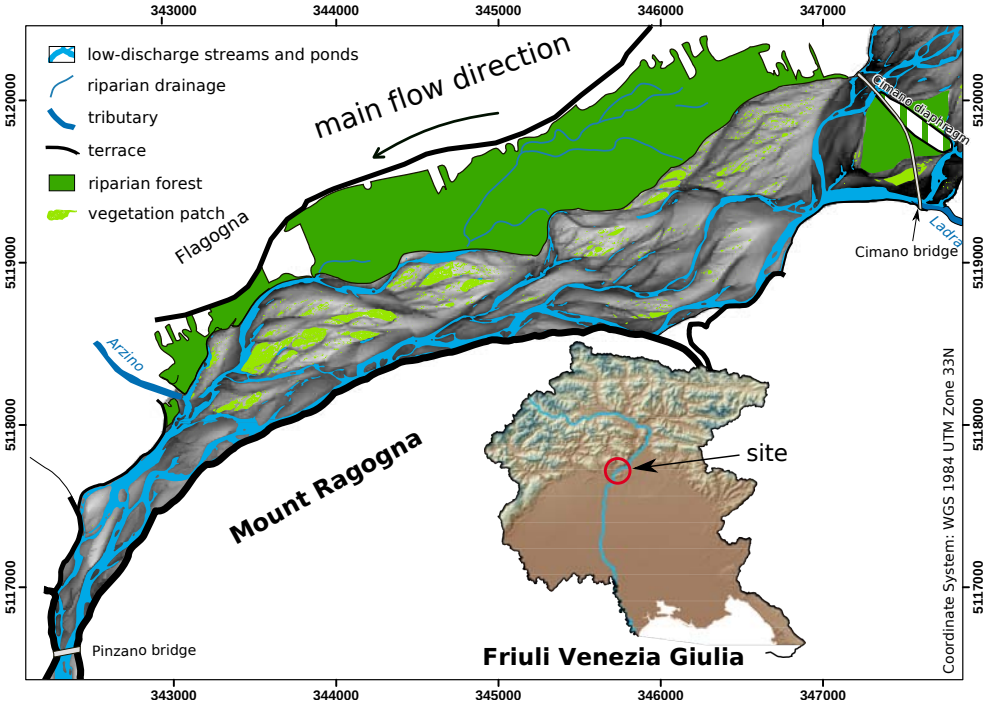

Figure 3.5 – The Cimano-Pinzano reach in May 2005. The background of the braidplain is the relative LiDAR-derived digital elevation model (LiDAR-derived DEM).

around both sides of the bedrock island. The 125-m-wide Pinzano gorge is located at the southernmost foreland thrust in the subalpine molasses and confines the Tagliamento River into a more or less single-thread stream before it flows into the Venetian-Friulian plain (Figure 3.2). At the Pinzano gorge, the catchment area of the Tagliamento River reaches 85 % of the whole catchment area (Figure 3.4). The southeastern side of the braidplain is confined by Tertiary conglomerates of the foothills of Mount Ragogna. The western flank bounds an inactive fluvial terrace (100 m to 900 m wide) lying 20 m above the present active alluvial plain. The Tagliamento River has a braided pattern at low discharge between the Cimano bridge and the Pinzano gorge. The braidplain (3.8 km^2) is up to 1 km wide and is characterized by the presence of a few large wooded islands (Figure 3.7). Thus, this reach was classified as island-braided by Ward et al. (1999). The Arzino tributary (catchment size of 120 km^2) enters the Tagliamento River at Flagogna. Figure 3.6A shows the lower part of the reach at medium discharge shortly before a large flood event with a 6.4-year recurrence interval. Figure 3.6B was taken a few days later.

As a result of the active thrusting of southern subalpine molasse onto the Venetian-Friulian plain (active foreland thrust system; Figure 3.2; Bechtold et al., 2009), the elevation of the bedrock surface at the Pinzano gorge acts as a base level, influencing the aggradation/degradation history of the Cimano-Pinzano reach. Recent neotectonic structures near the Pinzano gorge, would favour an aggradation of the Cimano-Pinzano reach in the timescale of hundreds to several thousands of years (timescale of landscape-shaping tectonic events in the area; Burrato et al., 2008; Bechtold et al., 2009). However, the analy-

(A)

(B)

Figure 3.6 – Mosaic photographs (courtesy of Michael Doering) of the lower part of the Cimano-Pinzano reach where the Arzino River enters the Tagliamento River. **(A)** Photographs taken the 30 October 2004 (water stage at the Villuzza gauging station: 210 cm) shortly before a large flood event with a 6.4-year recurrence interval (Figure 3.8). **(B)** Photographs taken the 4 November 2004 (water stage at the Villuzza gauging station: 105 cm), after the large flood event.

Emanuel Huber

Figure 3.7 – Tagliamento River (Photograph taken from Monte Ragnogna looking toward the North, the Cimano Bridge).

sis of aerial photographs indicates a more complex aggradation-degradation dynamic within the river reach at the decadal timescale caused by variable flood frequency, sediment supply including anthropogenic influences of gravel exploitation, and vegetation changes in the surrounding areas and upstream.

Previous studies based on historical aerial photographs and field observations showed that the morphological evolution of the Cimano-Pinzano reach is highly dynamic.

Zanoni et al. (2008) analysed historical aerial photographs of the Cimano-Pinzano reach (among others) over a period of 60 years. They concluded that established islands are 'remarkably transient features' as they did not survive for more than 23 years.

Van Der Nat et al. (2003) mapped the different types of habitat over 2.5 years and concluded that 'more than 59 % of the aquatic area and 29 % of vegetated islands were restructured'.

Bertoldi et al. (2009) related the river stage frequency to inundation and morphological shaping. Their wavelet analysis of the water stage series recorded at the Villuzza gauging station (just downstream from the Pinzano gorge, see Figure 3.8) between 1981 and 2006 showed that the water stage fluctuations were very irregular and not significantly influenced by anthropogenic interventions. Furthermore, they deduced that flow stages above 300 cm (at the Villuzza gauging station) were 'required to significantly erode floodplain and island margins or to cut avulsion channels that dissect new islands from the floodplain' (Bertoldi et al., 2009).

Welber et al. (2012) analysed the response of morphological features of the lower part of the reach to flood events. Using automated high-frequency photographic

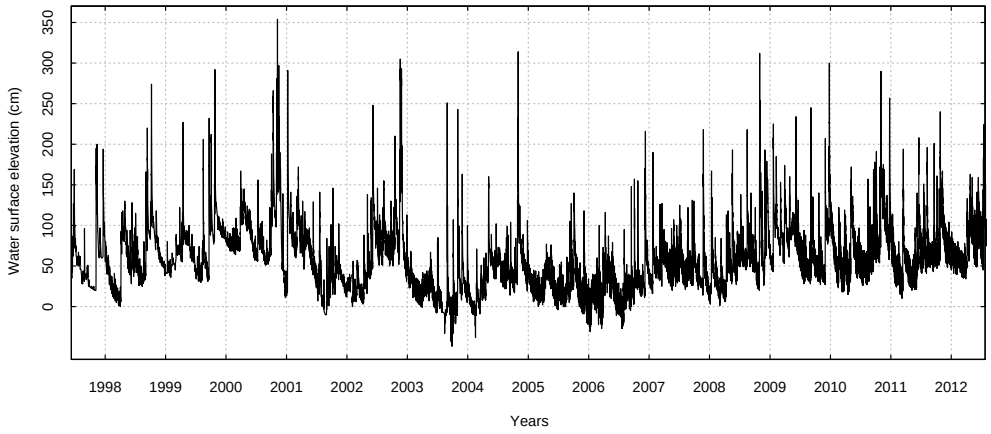

Figure 3.8 – Water elevation (cm) recorded at the Villuzza station, downstream from the Pinzano Gorge (note that the river bed is highly mobile and can change after each flood event).

records over two years (2008–2009), they observed that the low-discharge patterns were confined to 46 % of the studied subreach and that short-lived water bodies represented 30 % of the wetted area. Small changes in the vegetation distribution were documented as well as 'a strong link between vegetation distribution and [stream] persistence' (Welber et al., 2012).

Recently, Surian et al. (2015) concluded that the turnover between 1954 and 2011 was 'remarkably rapid with 50 % of in-channel vegetation persisting for less than 5–6 years and only 10 % of vegetation persisting for more than 18–19 years'. They also noticed that low-magnitude and relatively frequent flood events (recurrence interval of 2.5 years) significantly eroded the vegetation.

Thirteen kilometres downstream from the studied reach Mao and Surian (2010) observed that the lower morphological units and the 'low bars' experienced full gravel removal for high-frequency, low-magnitude floods (i.e., recurrence interval < 1 year and 1.1 year, respectively). On the 'higher bars', only partial gravel removal and fine sediment deposition was observed for a flood event with a recurrence interval of 3.5 years.

While most studies on the Cimano-Pinzano reach have focused on morphological and biological processes, the relationship between the morphology and the sedimentary deposits has not drawn much attention.

3.3 Coarse, braided river morphology

Braided rivers are generally defined as rivers that flow in two or more streams around unstable bars and islands (e.g., Leopold and Wolman, 1957; Howard et al., 1970). This definition stems from river observations carried out at low discharge and reflects the general perception of braided rivers in terms of a pattern that arises from the planform trichotomy 'water–sediment–vegetation'. This perception ignores the complex topography of the river bed as well as the

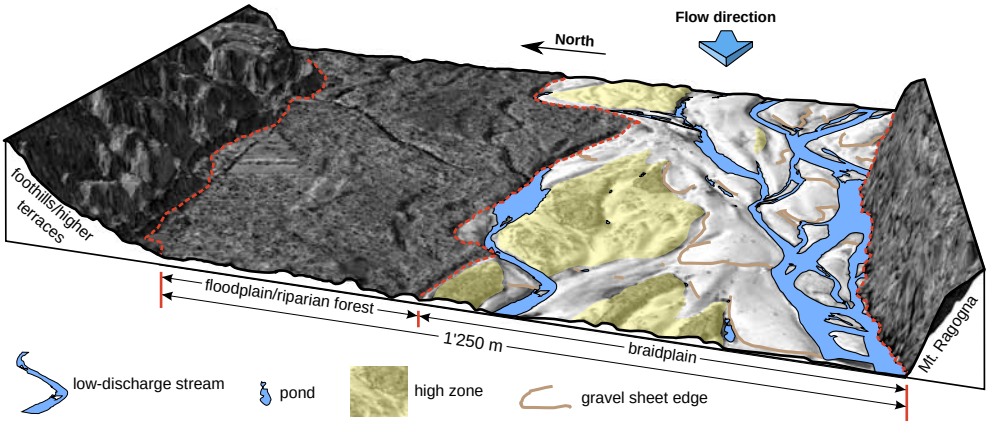

Figure 3.9 – Portion of the Quickbird photograph projected on the LiDAR-derived DEM. The main morphological elements described in the Terminology Section are here represented.

river dynamics at high discharge. The braided river morphology can only be comprehensively understood if (i) water as morphological element is discarded and the focus lies on the river bed topography, and (ii) the role of the river dynamics in the formation of the river bed morphology is accounted for.

The braided river plain, or *braidplain*, is defined as the area that has been subjected to recent morphological changes by the river (see Figure 2). Bank-full stage refers to the water elevation necessary to completely inundate the braidplain (up to some emergent vegetation patches). The braidplain consists of higher-lying zones (presumably called 'bar assemblages' in Lunt et al. (2004) or 'high bars' in Mao and Surian (2010) and abbreviated to *high zones hereafter*) with a dendritic drainage network surrounded by lower-lying zones called 'lower-lying actively-braiding belt' by Hicks et al. (2002) and abbreviated to *active zone* hereafter, following Gurnell et al. (2000) and Petts et al. (2000).

The connected inundated areas form the *low-discharge stream network*, whereas the isolated water bodies are called *ponds*. Note that throughout this paper the term *stream*, without any specification, is used specifically for the connected inundated areas *at the observation time* (i.e., a planform definition that is water-stage dependent). The term *channel* is exclusively reserved to describe rather elongated depressions that have been shaped by flowing water (physical/geometrical definition that is water-stage independent).

The term 'bar' is avoided for the following reasons. (1) 'Bar' is a very general term that describes any type of gravel accumulations that form topographic highs (e.g., A.S.C.E., 1966; Smith, 1974). The classification of bars according to their planview shape is not directly related to their sedimentary properties. (2) In the literature 'bar' refers alternatively to morphologies identified by their topography and/or their planform shape defined by the water shoreline (i.e., shape of exposed gravel areas). Therefore, we use the phrase *gravel sheet* (Todd, 1989; Hicks et al., 2002, 2007; Benn and Evans, 2010) to describe relatively unaltered depositional units of gravel that form sheet-like layers that are elongated in the direction of their formative discharge, rather lobate in planform, and deposited on a former topography. The gravel sheets commonly

have an avalanche face at the front and lateral edges, they are a few centimetre to 2 m thick and up to 200 m wide (Hicks et al., 2002). This definition is water-stage independent and refers to a specific depositional process that forms clearly-bounded landforms.

Scours are defined as 'distinct depressions in the river bed caused by erosion processes that are intrinsic to the fluvial channel and result from changes in hydraulic conditions' (Eilertsen and Hansen, 2008). Scours can be classified into bend, confluence, obstacle, and confinement scours.

3.4 Conclusion

The Tagliamento River shows a high dynamics behaviour in terms of discharge fluctuations and sediment loads. A braided reach of the Tagliamento River was chosen to study the relationship between the morphodynamics and the near-surbsurface structures. This reach is representative for many partly confined valleys such as in the Alpine foreland. While most studies have only focused on the vegetation and inundation dynamics, the fluvial morphodynamics and its impact on subsurface heterogeneity have been overlooked.

References

A.S.C.E. (1966) Nomenclature for Bed Forms in Alluvial Channel, Report of the Task Force on Bed Forms in Alluvial Channels of the Committee on Sedimentation. *Journal of the Hydraulics Division*, **92**(3): 51–64.

Bechtold M., Battaglia M., Tanner D.C. and **Zuliani D.** (2009) Constraints on the active tectonics of the Friuli/NW Slovenia area from CGPS measurements and three-dimensional kinematic modeling. *Journal of Geophysical Research*, **114**(B3): B03408. doi: 10.1029/2008jb005638

Benn D.I. and **Evans D.J.A.** (2010) *Glaciers and Glaciation*: 2nd Edition. Hodder Education, 802 pp. ISBN:978-0-340-90579-1

Bertoldi W., Gurnell A., Surian N., Tockner K., Zanoni L., Ziliani L. and **Zolezzi G.** (2009) Understanding reference processes: linkages between river flows, sediment dynamics and vegetated landforms along the Tagliamento River, Italy. *River Research and Applications*, **25**(5): 501–516. doi: 10.1002/rra.1233

Brierley G., Fryirs K., Outhet D. and **Massey C.** (2002) Application of the River Styles framework as a basis for river management in New South Wales, Australia. *Applied Geography*, **22**(1): 91–122. doi: 10.1016/S0143-6228(01)00016-9

Burrato P., Poli M.E., Vannoli P., Zanferrari A., Basili R. and **Galadini F.** (2008) Sources of Mw 5+ earthquakes in northeastern Italy and western Slovenia: An updated view based on geological and seismological evidence. *Tectonophysics*, **453**(1–4): 157–176. doi: 10.1016/j.tecto.2007.07.009

Church M. (2002) Geomorphic thresholds in riverine landscapes. *Freshwater Biology*, **47**(4): 541–557.
doi: 10.1046/j.1365-2427.2002.00919.x

Cucchi F., Finocchiaro F. and **Muscio G.** (2010) Geositi del Friuli Venezia Giulia: Regione Autonoma Friuli Venezia Giulia.

Eilertsen R.S. and **Hansen L.** (2008) Morphology of river bed scours on a delta plain revealed by interferometric sonar. *Geomorphology*, **94**(1–2): 58–68.
doi: 10.1016/j.geomorph.2007.04.005

Gurnell A., Petts G., Hannah D., Smith B., Edwards P., Kollmann J., Ward J. and **Tockner K.** (2000) Wood storage within the active zone of a large European gravel-bed river. *Geomorphology*, **34**(1–2): 55–72.
doi: 10.1016/s0169-555x(99)00131-2

Hicks D.M., Duncan M., Walsh J., Westaway R. and **Lane S.** (2002) New views of the morphodynamics of large braided rivers from high-resolution topographic surveys and time-lapse video, In: *The structure, function and management of fluvial sedimentary systems* (Eds. F.J. Dyer, M.C. Thoms and J.M. Olley), 276, International Association of Hydrological Sciences, Wallingford, United Kingdom, 373–380.

Hicks D.M., Duncan M.J., Lane S.N., Tal M. and **Westaway R.** (2007) Contemporary morphological change in braided gravel-bed rivers: new developments from field and laboratory studies, with particular reference to the influence of riparian vegetation, In: *Developments in Earth Surface Processes* (Eds. H. Habersack, H. Piégay and M. Rinaldi), Elsevier BV, 557–584.
doi: 10.1016/s0928-2025(07)11143-3

Howard A.D., Keetch M.E. and **Vincent C.L.** (1970) Topological and Geometrical Properties of Braided Streams. *Water Resources Research*, **6**(6): 1674–1688.
doi: 10.1029/WR006i006p01674

Leopold L.B. and **Wolman M.G.** (1957) River channel patterns: braided, meandering and straight. *US Geological Survey Professional Paper*, **282–B**: 39–85.

Lunt I.A., Bridge J.S. and **Tye R.S.** (2004) A quantitative, three-dimensional depositional model of gravelly braided rivers. *Sedimentology*, **51**(3): 377–414.
doi: 10.1111/j.1365-3091.2004.00627.x

Mao L. and **Surian N.** (2010) Observations on sediment mobility in a large gravel-bed river. *Geomorphology*, **114**(3): 326 – 337.
doi: 10.1016/j.geomorph.2009.07.015

Norbiato D., Borga M., Sangati M. and **Zanon F.** (2007) Regional frequency analysis of extreme precipitation in the eastern Italian Alps and the August 29, 2003 flash flood. *Journal of Hydrology*, **345**(3–4): 149–166.
doi: 10.1016/j.jhydrol.2007.07.009

Petts G., Gurnell A., Gerrard A., Hannah D., Hansford B., Morrissey I., Edwards P., Kollmann J., Ward J., Tockner K. and **Smith B.** (2000) Longitudinal variations in exposed riverine sediments: a context for the ecology of the Fiume Tagliamento, Italy. *Aquatic Conservation: Marine and Freshwater Ecosystems*, **10**(4): 249–266.
doi: 10.1002/1099-0755(200007/08)10:4<249::aid-aqc410>3.0.co;2-r

Smith N.D. (1974) Sedimentology and Bar Formation in the Upper Kicking Horse River, a Braided Outwash Stream. *The Journal of Geology*, **82**(2): 205–223.

Spaliviero M. (2003) Historic fluvial development of the Alpine-foreland Tagliamento River, Italy, and consequences for floodplain management. *Geomorphology*, **52**(3–4): 317–333.
doi: 10.1016/S0169-555X(02)00264-7

Surian N., Barban M., Ziliani L., Monegato G., Bertoldi W. and **Comiti F.** (2015) Vegetation turnover in a braided river: frequency and effectiveness of floods of different magnitude. *Earth Surface Processes and Landforms*, **40**(4): 542–558.
doi: 10.1002/esp.3660

Todd S.P. (1989) Stream-driven, high-density gravelly traction carpets: possible deposits in the Trabeg Conglomerate Formation, SW Ireland and some theoretical considerations of their origin. *Sedimentology*, **36**(4): 513–530.
doi: 10.1111/j.1365-3091.1989.tb02083.x

Van Der Nat D., Tockner K., Edwards P.J., Ward J. and **Gurnell A.M.** (2003) Habitat change in braided flood plains (Tagliamento, NE-Italy). *Freshwater Biology*,

48(10): 1799–1812.
doi: 10.1046/j.1365-2427.2003.01126.x

Ward J., Tockner K., Edwards P., Kollmann J., Bretschko G., Gurnell A., Petts G. and **Rossaro B.** (1999) A reference river system for the Alps: the 'Fiume Tagliamento'. *Regulated Rivers: Research & Management*, **15**(1–3): 63–75.
doi: 10.1002/(SICI)1099-1646(199901/06)15:1/3<63::AID-RRR538>3.0.CO;2-F

Welber M., Bertoldi W. and **Tubino M.** (2012) The response of braided planform configuration to flow variations, bed reworking and vegetation: the case of the Tagliamento River, Italy. *Earth Surface Processes and Landforms*, **37**(5): 572–582.
doi: 10.1002/esp.3196

Zanoni L., Gurnell A., Drake N. and **Surian N.** (2008) Island dynamics in a braided river from analysis of historical maps and air photographs. *River Research and Applications*, **24**(8): 1141–1159.
doi: 10.1002/rra.1086

4 A morphological perspective on the subsurface heterogeneity

> *Field relations are the final court of appeal.*
>
> **J.H. Bretz** (1962) Dynamic equilibrium and the Ozark land forms. American Journal of Science, 260:427–38. doi:10.2475/ajs.260.6.427

Abstract In order to understand heterogeneity distribution of hydraulic properties, many studies have proposed models of coarse, braided river deposits. However, they often focus either on the surface/near surface or on ancient deposit analysis. Furthermore, the link between morphological (surface) and sedimentological (outcrops) information has not been fully explored yet. This publication aims to characterize the morphodynamics of a braided, gravel-bed reach of the Tagliamento River (NE Italy) and to assess its relationship with the subsurface heterogeneity. The morphological analysis is based on a LiDAR-derived digital elevation model, aerial and satellite photographs from 1998 to 2011, as well as field observations. A water-stage time series allows the morphological changes to be related to the discharge dynamics. The sedimentological knowledge on coarse, braided river deposits was mainly gained from the observation of analogue Pleistocene coarse deposits in Switzerland. The main geomorphological elements are identified in terms of their topographic signature and genesis, setting apart the trichotomy *water–vegetation–bar*. The braidplain is characterized by higher-lying zones with dentritic gully drainage networks and active zones where most of the morphology reworking occurs. Furthermore, two morphologies mark the active zones: a low-discharge morphology (low-discharge incisions and channels, slip-face lobes, etc.) superimposed on a high-discharge morphology (gravel

E. Huber (2017) *Incorporating sedimentological observations, hydrogeophysics and conceptual knowledge to constrain 3D numerical heterogeneity models of alluvial systems.* Ph.D. thesis, Applied and Environmental Geology, University of Basel, Switzerland, 192 pp.

sheets, scours, etc.). Each morphological element is related to a depositional (i.e., sedimentological) element whose preservation potential in the subsurface is assessed as a function of the river-bed aggradation dynamic. The settings that impact the subsurface flow in terms of fast pathway and connectivity are addressed.

Adapted from **Huber E.** and **Huggenberger P.** (2015) Morphological perspective on the sedimentary characteristics of a coarse, braided reach: Tagliamento River (NE Italy). *Geomorphology*, 248:111–124. doi:10.1016/j.geomorph.2015.07.015

4.1 Introduction

Despite the efforts to understand braided river systems and the resulting subsurface heterogeneity patterns, some fundamental aspects of the dynamics of these systems are not fully explored yet, in particular the link between morphological (surface) and sedimentological (outcrop) information (Smith et al., 2006). The dynamics of braided rivers is a key to understanding the preservation potential of characteristic depositional elements and the resulting subsurface sedimentary textures and structures (Huggenberger and Regli, 2006). The relationship between the river-bed morphology and the turbulent flow leads to sorting processes that form sediment units with a characteristic permeability (Best, 1993). The spatial distribution and the geometry of the preserved depositional elements themselves control the connectivity of high/low permeable units and, therefore, can strongly influence the hydraulic heterogeneity patterns (e.g., Anderson et al., 1999; Lunt et al., 2004; Comunian et al., 2011). The challenge in this context is to find a relationship between the present morphology of braided river systems and the geometry of architectural elements of ancient deposits (e.g., Siegenthaler and Huggenberger, 1993; Bristow and Jol, 2003; Kelly, 2006).

The present work aims to characterize the morphodynamics of a gravel-bed braided reach of the Tagliamento River (northeast Italy) and to assess its relationship with sedimentary records. We seek to better understand the subsurface hydraulic heterogeneity as a function of the morphodynamics for subsurface flow and transport simulations.

Specifically, we attempt (i) to identify the main geomorphological elements in terms of their topographic signature and genesis (we set aside the planform trichotomy *water–vegetation–bar*); (ii) to quantify the geomorphological effectiveness of the flood events and therefore the rate of turnover of the main geomorphological elements; (iii) to relate the morphological elements with depositional elements, i.e., to assess how the morphological elements are reworked/filled and buried in the sedimentary records; and (iv) to assess the

preservation potential of the main depositional elements in the subsurface as a function of the river-bed aggradation dynamic.

The analysis is based on a LiDAR-derived digital elevation model (LiDAR-derived DEM), aerial and satellite photographs as well as on-field observations of the Tagliamento River (see Chapter 3) and of gravel pit exposures of Pleistocene coarse deposits in Switzerland (see Chapter 2).

4.2 Method

The Cimano-Pinzano reach (see Chapter 3) was selected to investigate the relationship between river dynamics and subsurface heterogeneity because this reach share similar characteristics with partly confined valleys such as in the Alpine foreland.

4.2.1 Data

A water stage time-series for the period 1997–2012 (Villuzza station, downstream from the Pinzano gorge, Figure 3.8) allowed morphological changes to be related with the discharge history. The planimetry as well as the morphological analysis of the reach are mainly based on a Quickbird panchromatic photograph[1] from May 2005, a LiDAR-derived DEM[2] from 23 May 2005, and regular field observations since 2009. Orthophotos available online[3] from 1998, 2003, 2007 and 2011 completed our observations. All the orthophotos, the Quickbird photograph and the LiDAR-derived DEM are displayed at the end of the chapter in Figures 4.10 to 4.15. Note that in the LiDAR-derived DEM, the elevation of the wetted parts of the river bed is the water surface elevation and not the elevation of the submerged river bed. The photograph and the digital elevation model (DEM) look different because the sharp color contrasts on the photograph (e.g., between the water and the sediments) are not necessarily related to sharp elevation changes on the DEM (and vice versa).

4.2.2 Geomorphology

The LiDAR-derived DEM was detrended to better visualize the braidplain topography and to compare the relative elevations of the morphological features. The longitudinal gradient was estimated by the mean elevation of the braidplain over a disk of a radius larger than the maximal braidplain width and removed from the LiDAR-derived DEM. We used both the relative DEM and the

[1] 0.5-m resolution, water stage at recording time = 50(13) cm

[2] 2.2-m resolution, water stage at recording time = 44 cm, surveyed by the U.K. Natural Environment Research Council (NERC) and processed by Bertoldi et al. (2011)

[3] WebGIS-application of the Autonomous Region of Friuli Venezia Giulia, URL: http://irdat.regione.fvg.it/WebGIS (last accessed on 10th of May 2017), coordinates 344 156 and 5 118 590 (ETRS89-TM33)

Quickbird photograph combined with our field experiences on the Tagliamento braidplain to map the morphological features observed at low discharge: high and active zones, low-discharge streams, ponds, gravel sheet edges, depositional lobes, etc. We also delineated gravel sheet edges on the orthophoto from 2003 on which the braidplain morphology could be reliably identified. The inundated areas were automatically delineated using the color information of the Quickbird photograph and the elevation information of the DEM. The delineated polygons were then hand-edited to correct any misclassifications. We computed smoothed centrelines of the stream network polygon and we inserted segments perpendicular to the centrelines every 2 m. These segments were then clipped by the stream network polygon and used to assess the distribution of the width of the low-discharge stream. Furthermore, the water surface elevation of the stream network centrelines was extracted from the LiDAR-derived DEM and projected on the centreline of the braidplain. This procedure allows for a comparison of the elevation of the low-discharge streams and for examining their (vertical) positions within the braidplain. The longitudinal mean elevation and elevation range of the braidplain were estimated on the polygons formed by the area between two consecutive cross sections.

The lateral dynamics of braided river systems are known to be related to the transverse gradients of the braidplain that result from unequal sediment deposition (Ashmore, 1982; Bryant et al., 1995; Jones and Schumm, 1999; Ashworth et al., 2007). The transverse gradients were estimated by the slope of cross sections and by the slope of the local elevation minima of the same cross sections. Local elevation minima may act as local attractors that drain the water and sediment flows. Both types of transverse slopes were compared. To calculate the cross sections, a smoothed centreline of the braidplain corresponding to the longitudinal orientation of the braidplain was computed. Cross sections were traced at right angles to the centreline every 2 m. They were then clipped to the braidplain polygon, and the elevation information of the LiDAR-derived DEM was extracted for the cross sections.

The orthophotos were mainly used in association to the water-stage time-series to evaluate the morphological changes within the braidplain between 1998 and 2011. We focused on the high/active zone dynamics and on the reworking of the active zones.

4.2.3 Sedimentology

The sedimentological observations within the braidplain were limited to exposures (i.e., cut banks) above the water level. The sedimentary characteristics at the surface (e.g., coarse armour layer) can impact the transport initiation at low discharge but have likely little influence on the morphological shaping at high discharge (Bertoldi et al., 2010). Therefore, we do not focus on the sediment composition at the surface.

Exhaustive sedimentological observations over several years were made in different gravel pits of Pleistocene coarse deposits located in Switzerland (e.g., Siegenthaler and Huggenberger, 1993; Huggenberger et al., 1998; Beres et al., 1999; Regli et al., 2002; Huggenberger and Regli, 2006; Kock et al., 2009; Bayer

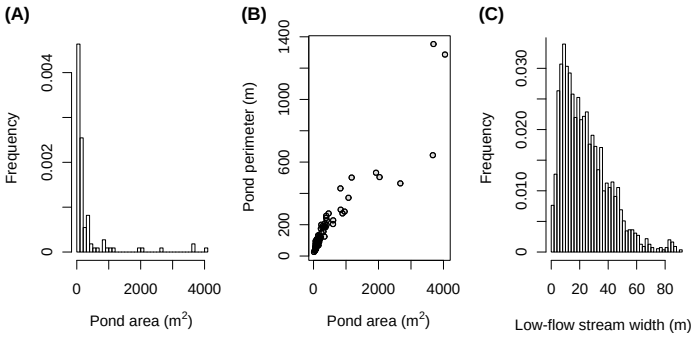

Figure 4.1 – **(A)** Frequency distribution of the pond area; **(B)** pond perimeter as function of pond area; **(C)** frequency distribution of the low-discharge stream width.

et al., 2011, see also Chapter 2). The observations were made on vertical sections at different stages of the wall excavations allowing the three-dimensional shape of the main sedimentological elements to be assessed with regard to the main former flow direction.

4.3 Results

4.3.1 Reach characterization

About 6 % of the surface of the braidplain is vegetated, and 17 % is inundated at the time of the Quickbird record (May 2005). We identified 11 large vegetation patch complexes. The topology of the low-discharge stream network corresponds to a partially connected network (see Figure 3.5). Most of the low-discharge streams are connected in a reticulate/braided way (anabranch), but about 24 low-discharge streams are only connected to the network at the downstream end (i.e., pseudo anabranch or 'one-way connected stream with flowing water'; Arscott et al., 2002). The width of the low-discharge streams ranges from a few decimeters up to 100 m, the mean width being 24 m (Figure 4.1). We observed 100 ponds with elongated planform (average length-to-width ratio ≈5) often found in local depressions (Figure 4.1). We counted about 60 ponds, each with an area $> 100\,\mathrm{m}^2$.

The mean longitudinal slope is almost constant (0.32 %). After the removal of the longitudinal elevation trend, the low-relief topography shows height variations of up to 3.6 m over the whole reach. The average elevation difference over a radius of 10 m reaches 3 m, indicating locally large topographic gradients. The LiDAR-derived DEM (2005) consists of high zones surrounded by active zones. The high and active zones differ markedly not only in their relative elevation differences but also in their topographic signatures (see Figure 3.5). The high zones lie about 1 m to 2 m above the adjacent active zones and are on average 700 m long and 350 m wide. A drainage system incises 0.4 m to 1.5 m below the top surfaces of the high zones and forms 1-m- to 35-

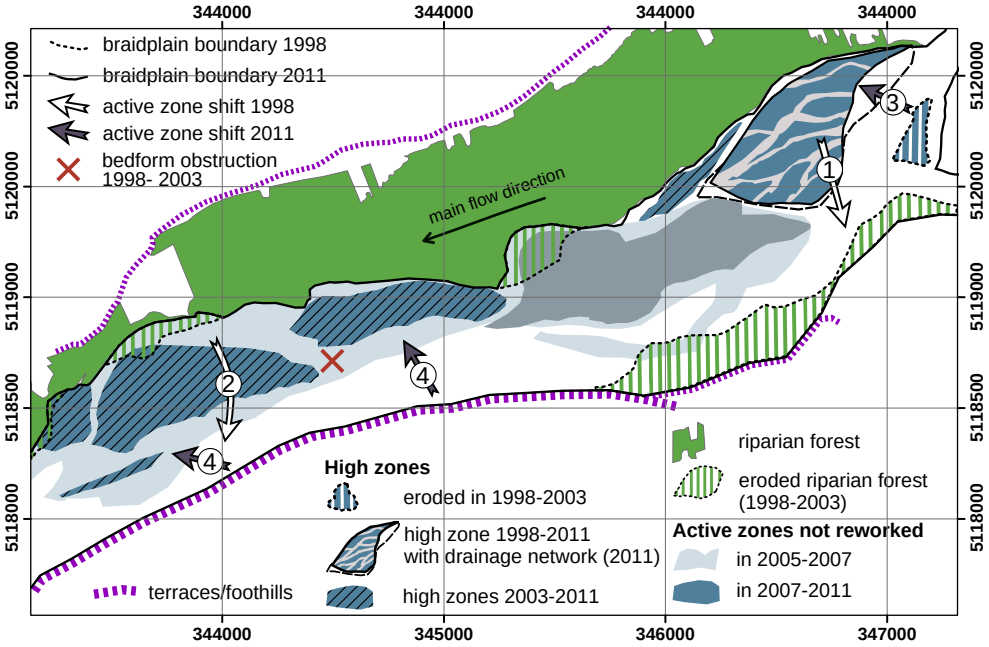

Figure 4.2 – Morphological development of the Tagliamento floodplain between 1998 and 2011. The numbers on the arrows identify the active zone shifts that are discussed in the main text.

m-wide gullies. Contrarily to the active zones, the high zones generally are vegetated. The active zones are characterized by the presence of gravel sheets and low-discharge streams. characterized by the presence of gravel sheets and low-discharge streams.

4.3.2 High zone/active zone dynamics (1998-2011)

Braidplain evolution

The analysis of the aerial and satellite data shows that between 1998 and 2005 an active zone shift (active zone shifts (1) and (2) in Figure 4.2) occurred toward the southwest boundary. This shift consisted in (i) the erosion of large area of riparian forest that can be presumably attributed to a flood event with a 32-year recurrence interval (the braidplain area increased by 9 %; Figure 4.3), (ii) the transformation of a large area of the active zone into a high zone (just downstream from the Cimano bridge), (iii) the formation of two high zones from relicts of former high zones (large vegetation patches) in the middle of the reach, and (iv) the obstruction of a large bedform (marked by a '**X**' in Figure 4.2) between these two newly formed high zones. Between 2005 and 2007, more than 50 % of the braidplain was not reworked by the flows but still 15 % of the high zone downstream from the Cimano bridge was eroded (active zone shift (3) in Figure 4.2). Between 2007 and 2011, 35 % of the braidplain was not reworked; and an active zone shift toward the northern boundary occurred in the middle of the reach (active zone shift (4) in Figure 4.2). Figure 4.3 shows, for the periods considered, the recurrence interval of the flood events as well as the areal proportions of the active/high zone combined with their

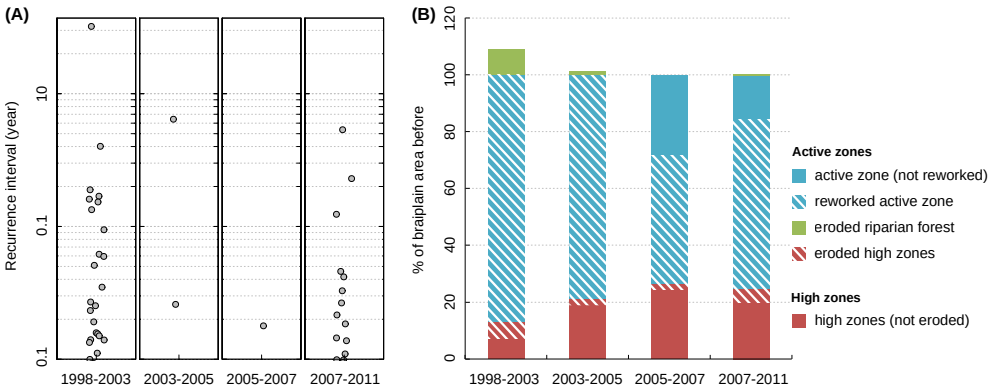

Figure 4.3 – For each time interval defined by the record time of the aerial/satellite photographs: **(A)** recurrence interval of the flood events larger than 0.1 year; **(B)** areal proportion of the high/active zone relative to the area of the braidplain at the beginning of the time interval.

reworked proportions.

High zone formation

The braidplain evolution from 1998 to 2011 shows how the high zone downstream from the Cimano bridge formed. Between 1998 and 2003, an area ($0.5\,\text{km} \times 1\,\text{km}$) within the active zone was more or less *abandoned* by the river. That means that this area still experienced some erosion but was out of the discharges that would have completely reshaped it. Then vegetation developed, particularly at the edge of the highest locations. The hydraulic resistance of the vegetation to the flow further reshaped the abandoned area by inducing local scouring and sediment deposition (fine as well as coarse sediments) transforming the rather flat and smooth surfaces of the gravel sheets into a complex topography (see Gurnell et al., 2005, for more details on this process). Over time a dendritic drainage network that was not related to the abandoned morphology incised through the high zone and widened whereas the top surfaces of the high zone grew vertically by the deposition of trapped fine sediments. From 2003 onward, the high zone was further eroded at its edge by lateral scouring of the flow. The lateral scouring, often expressed in the form of cutbanks, can be seen as an instantaneous indicator for the current trend of lateral shift of the active zones. On the field between 2011 and 2014 we observed that the gravel substrate of the high zones lay higher than the surface of the surrounding active zones/gullies and that the height of the deposited fine sediments reached locally more than 1 m. The presence of mature vegetation is an indicator for high zones, although vegetation can colonize some parts of the active zones that are not reworked by the river over a given time period (as between 2007 and 2011).

Planimetry

The transverse slope computed on the whole cross sections shows a similar pattern as the transverse slope computed only on the local minima (Figure 4.4).

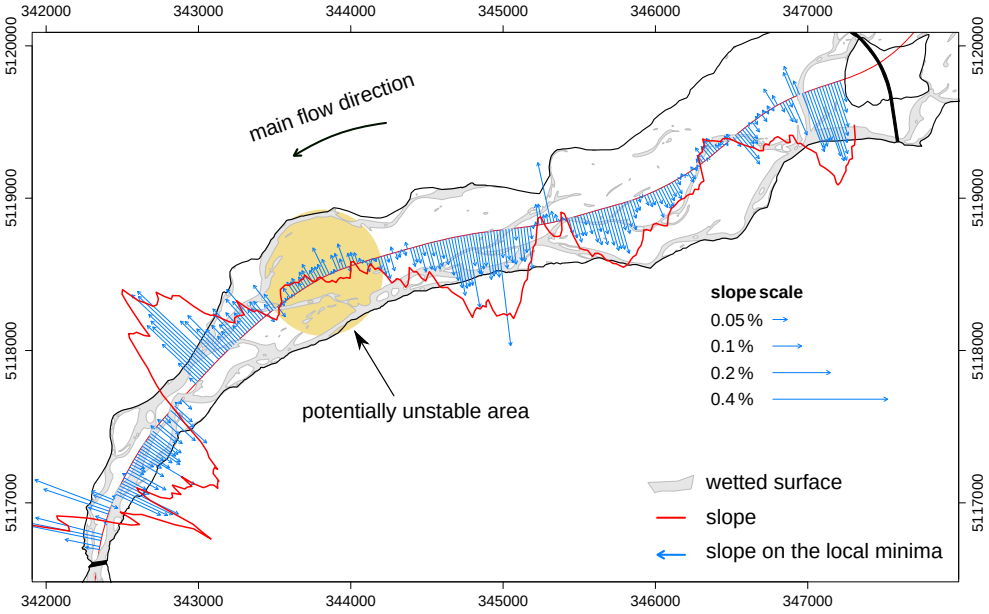

Figure 4.4 – Direction and magnitude of the transverse slope of the braidplain represented by arrows/lines. Two methods are compared: (i) the slope of the lateral cross sections and (ii) the slope of the local minima of the lateral cross sections.

The upstream part of the reach is characterized by a dominant transverse slope toward the left side (southeast) of the braidplain with some locations where the transverse slope goes to zero. This slope direction corresponds to the location of the main active zones in the left side of the reach, indicating a relative stability; and it can result from the active zone shift observed between 1998 and 2005. Larger slope variations with changes of slope direction are observed in the downstream part of the reach. The observed relationship between the transverse slope and the braidplain width indicates the following trend: (i) the transverse slope is roughly inversely proportional to the width of the braidplain; and (ii) the transverse slope tends toward zero at the locations where the braidplain width is a local minimum (i.e., slight bottleneck locations).

The location of an area that is likely to experience a planimetric change in the near future under aggrading conditions is highlighted in Figure 4.4. In this area, the location of the main active zone (southeast) does not correspond to the lowest positions as shown by the slope direction. Furthermore, we observed between 2007 and 2011 an active zone shift toward the northwest boundary in this area (active zone shift (4) in Figure 4.2).

4.3.3 Morphology of the active zones

Gravel sheets

The principal bedform observed within the active zones is the gravel sheet. Only a few gravel sheets are very well preserved; the extent of about 30 gravel sheets is more or less recognizable over 100 relicts of gravel sheets on the LiDAR-derived DEM as well as on the orthophoto from 2003. The length of

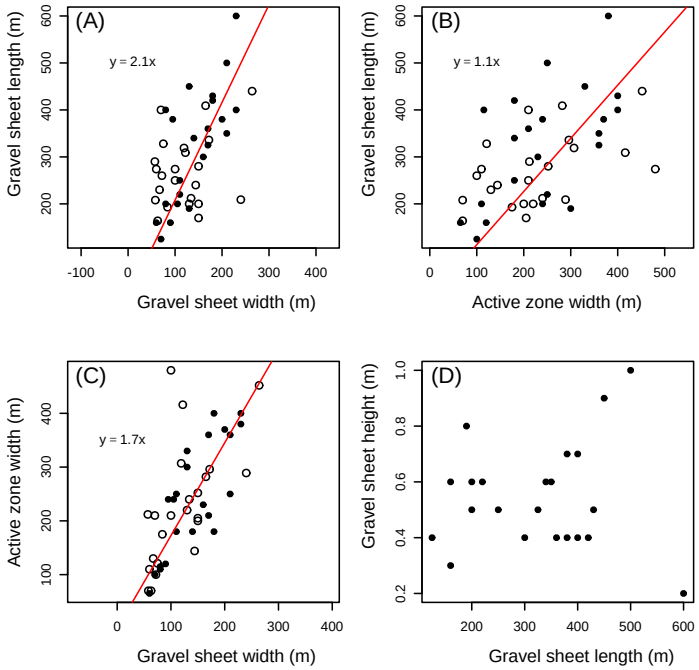

Figure 4.5 – Dimensions of well-preserved gravel sheets inferred from the 2003 orthophoto (circles) and from the 2005 Quickbird photograph and LiDAR-derived DEM (black dots). The gravel sheet heights correspond to the height of the front avalanche face of the gravel sheets.

these well-preserved gravel sheets ranges from 160 m up to 600 m and positively correlates with their width (median length-to-width ratio ≈1.92; Figure 4.5). The width of the gravel sheets is proportional to the width of the active zone. The avalanche face height ranges from centimeters up to 2 m (estimated average height from field observations and LiDAR-derived DEM analysis: 0.6 m). The gravel sheets delineated in 2003 and 2005 present no significant differences in size (Figure 4.5).

Figures 4.6B and 4.6D shows a complex overlapping of remnants of gravel sheets with an orientation varying from north–south to east–west. Some of the gravel sheet remnants present low-discharge incisions with a depositional lobe at their front end. Furthermore, a low-discharge stream with a high curvature has strongly eroded this complex topography. The history of such highly superposed and reworked patterns is hardly reconstructable. In Figures 4.6C and 4.6E a 1-m-thick, well-preserved gravel sheet (about 150 m × 250 m) is dissected in its middle by a low-discharge incision (20 m wide and up to 1 m deep). This low-discharge incision deposited a lobe of sediment (60 m × 25 m) at the edge of the gravel sheet into a large low-discharge stream. Another trace of dissection is also visible on the west side of the gravel sheet. The southeast edge of the gravel sheet is reworked by a sequence of edge collapses with depositional lobes. These lobes are called slip-face lobes (Rice et al., 2009) and are frequently found in sequences at the lateral edges of the gravel sheets where the transverse gradient is larger than the longitudinal gradient. Compare also the northeast to southwest orientation of the gravel sheet with the east to west orientation of the large low-discharge stream (Figures 4.6C and 4.6E). These two different

orientations mark the difference between the character of the river at high- and low-discharge conditions. Note also how much morphological information is gained from the LiDAR-derived DEM (compare Figure 4.6 panels B and C with Figure 4.6 panels D and E).

Furthermore, the gravel sheets can also be partially washed out by the flow, resulting in an armouring of their surface and/or smooth erosion that thins the gravel sheets and fuzzes their edges (e.g., the gravel sheet in Figures 4.8C and D). Lateral accretion of the gravel sheets as well as the superimposition of thin gravel dunes on gravel sheets were not observed in the field or in the data.

Low-discharge streams and channels

Figure 4.7A shows the projection of the water surface elevation of the low-discharge stream network and of the largest ponds on the centreline of the braidplain superimposed over the mean, minimum, and maximum elevation of the braidplain for each lateral polygon. The planform of the low-discharge stream network is represented in Figure 4.7B. While the mean braidplain elevation shows a slightly upward-concave profile along the centreline, the minimum braidplain elevation presents a step-like pattern. The steps coincide with the location of bend erosion of the northern bank of the braidplain (compare Figure 4.7A and B) highlighting the link between lateral erosion and scouring. Most of the branches of the projected low-discharge stream network also show a step-like pattern (step length: 200(110) m, step height:0.53(23) m). The relative elevation between two low-discharge streams can strongly vary along the stream length (e.g., a higher-lying stream can end up as a lower-lying stream) indicating local variations of the potential energy between the low-discharge streams (i.e., topographic gradients). Differences in potential energy can drive morphological changes (e.g., avulsion). The elevation of the low-discharge streams is generally lower than the mean braidplain elevation, and in most cases a stream lies at the lowest location of the braidplain. The maximum elevation fluctuations reveal the presence of large higher-lying zones (large maximum elevation).

The morphology of the low-discharge channels is assessed by studying the topography of abandoned low-discharge streams on the LiDAR-derived DEM outside the reach. Based on the analysis of the topography (different cross-sectional geometry), we can distinguish two different types of low-discharge stream bed morphology: low-discharge incision and low-discharge channel.

The braidplain is locally overprinted by incisions often at the edges of gravel sheets but also through the gravel sheets (see Figure 4.6). A closer look reveals a succession of steep and low gradient segments in the longitudinal direction: an incision into a morphological feature (strong topographic gradient) is followed by a plateau with sometimes small negative slopes where the low-discharge channel widens. The step-like longitudinal pattern of the low-discharge streams supports this observation (Figure 4.7). Therefore, the length of the low-discharge incisions can be roughly inferred from the projected low-discharge stream network (e.g., 200(110) m).

One to two main low-discharge channels with a light meander planform shape

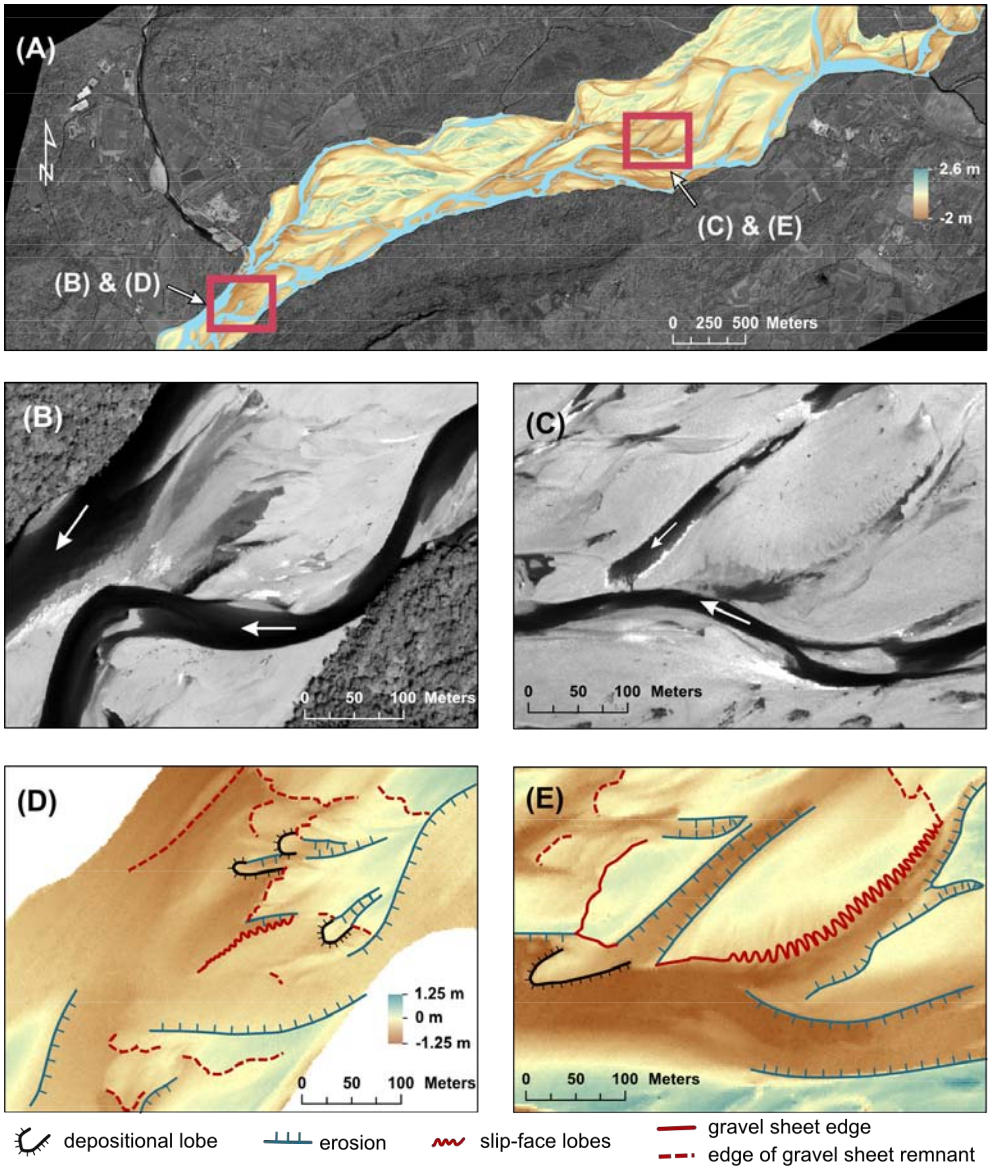

Figure 4.6 – Two examples of gravel sheet reworking and overlapping. **(A)** Position of the two locations in the braidplain (Quickbird photograph as background, LiDAR-derived DEM of the braidplain, delineated streams in blue). **(B)** and **(C)** Quickbird photograph. **(D)** and **(E)** LiDAR-derived DEM with superposed interpretations. Note that the Quickbird photograph and the light detection and ranging (LiDAR) data were recorded in the same time and that they represent the same morphology.

are identified on the LiDAR-derived DEM. They have a well-defined erosional surface with sharp boundary that is identifiable segment-wise in about 80 % of the cases. These well-defined channel beds are only up to 0.5 m deep with regard to the lowest adjacent bank and between 10 m and 50 m wide. They are wider than the low-discharge incisions. The elevation profile of the main channel shows an almost constant elevation profile (e.g., the stream in red in Figure 4.4).

Traces of lateral accretion by low-discharge incision/channel migration are not

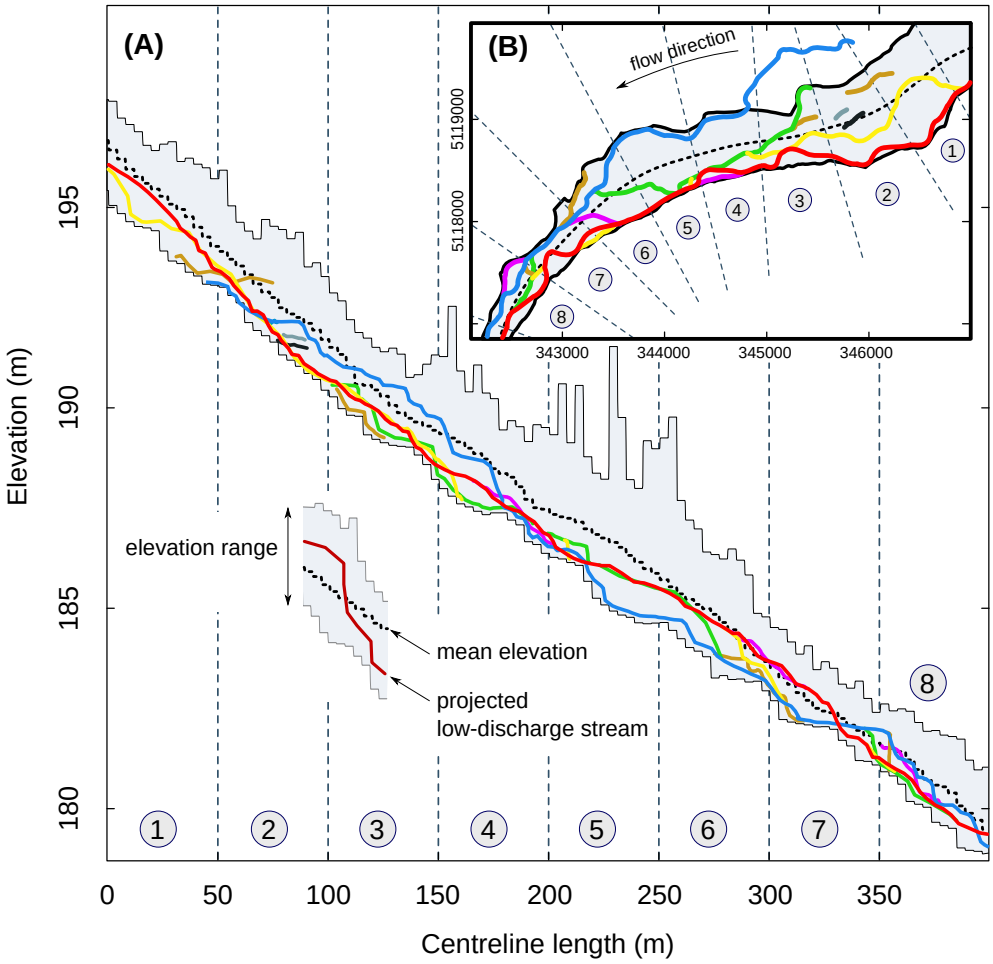

Figure 4.7 – **(A)** Elevation of the stream network projected on the centreline as function of the centreline length; **(B)** stream network planform with the floodplain boundaries. The centreline corresponds to the thick black dashed line.

visible in the field or in the data.

Scours

Interestingly, while scour fill structures can represent a large part of coarse, braided deposits (Siegenthaler and Huggenberger, 1993; Best and Ashworth, 1997), preserved scour holes were rarely observed in the studied reach.

The low-discharge stream confluences are rather low angle and not all of them form scours. Moreover, at some low-discharge stream confluences a slip-face lobe has been deposited from one tributary (e.g., Figure 4.6C and E). On the orthophotos from 2003 to 2011, only one low-discharge stream confluence scour just downstream from the Cimano bridge is clearly visible through the clear water. This 50-m-long and 15-m-wide scour shows two avalanche faces at its upstream edges where the low-discharge streams enter into the confluence.

Between the edges of the gravel sheets and the confining structures, shallow ponds fed by groundwater exfiltration and large amounts of sand in association

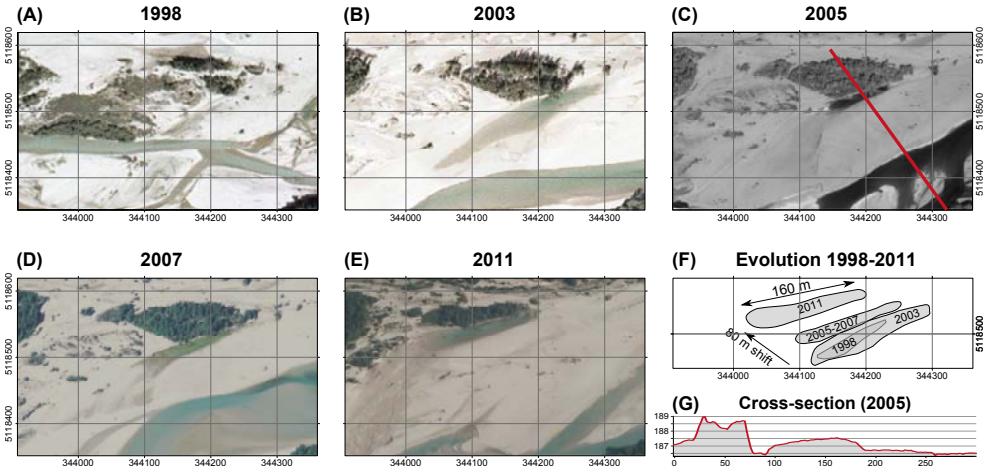

Figure 4.8 – **(A)–(E)** Migration of an obstacle scour between 1998 and 2011. The partially filled scours are identified by the local depression filled with water (except in 1998); **(F)** schematic migration of the local depression; **(G)** cross section of the LiDAR-derived DEM (2005) indicated by the red line on **(C)**. Note that on **(C)** a well-preserved gravel sheet with an avalanche at its front edge lies between the obstacle scour and the low-discharge stream. The main flow direction is from upper right to lower left.

with sequences of slip-face lobes were often observed. Similar observations were also made between the edges of two gravel sheets. This can be attributed to the presence of filled scours that were formed at high discharge by flow turbulences induced by the braidplain topography. In the (dry) LiDAR-derived DEM, about 20 partially filled scours can be identified in the studied reach, which are up to 20 m wide, 180 m long, and 1 m deep (on average only 0.5 m deep) and have a trough rather than a spoon shape. They are located at the lowest parts of the floodplain.

Figure 4.8 illustrates the lateral migration of a partially filled obstacle scour formed between the edges of a high zone and a gravel sheet. Between 1998 and 2011 the scour migrated over 80 m. On the DEM 2005, the water surface within the scour is almost at the same elevation as the water surface of the lowest low-discharge stream (Figure 4.8G). We estimate the filled scour being up to 100 m long.

4.3.4 Geomorphological effectiveness of floods

High zones and riparian forest

In 13 years, 54 % of the high zones from 1998 were eroded, mainly 1998–2003 (45 %). Large parts of riparian forest (9 % of the 1998 braidplain area) were eroded in 1998–2003, most likely by the flood event with a 32-year recurrence interval (compare Figure 4.3A and 4.3B). Even small events (e.g., events with recurrence intervals less than half a year) were able to rework the high zones, as between 2005 and 2007 where 7 % of the high zones were eroded. Furthermore, other studies quantified a turnover rate of established islands (i.e., the vegetated part of the high zones) that was < 25 years (e.g., Zanoni et al., 2008; Surian et al., 2015). Under the present conditions the life span of the high zones (and

their vegetation) is limited up to 25 years by the lateral erosion of the river. The enhanced resistance of the vegetation to the flow seems only to postpone the (partial) erosion of the high zones until the next large flood event.

Active zones

Large flood events with a recurrence interval larger than 6.4 years completely reworked the active zones. Even small events (recurrence intervals < 2 months) were able to partially rework the active zone (i.e., 45 % of the active zone, see Figure 4.3)). Furthermore, the flood event from 31 October 2004 with a 6.4-year recurrence interval (314 cm water stage) was identified as having formed the gravel sheets in Figures 4.6B-E and Figure 4.8. The main gravel sheet observed in 2005 in Figure 4.8 was presumably completely reworked by the flood event on 30 October 2008 with a 5.4-year recurrence interval (312 cm water stage). Between its formation and its complete destruction, we observe in 2007 the lateral erosion (up to 45 m) and diffusion (over max. 20 m) of the gravel sheet (Figure 4.8D). The formation of slip-face lobes can be observed during the flow recession of the 20 January 2009 flood event (225 cm water stage; see the Supporting information in Bertoldi, 2012). On 22 January 2009 (159 cm water stage), a slight sequence of slip-face lobes is visible, and three days later (80 cm water stage) they were almost fully developed. Under the present conditions we expect that the active zones are completely reworked (e.g., formation of new gravel sheets and low-discharge incisions/channels) within < 10 years (some of their parts being reworked more than once).

4.3.5 Sedimentological observations

Field observations (Tagliamento River)

Numerous exposures (i.e., cut banks) of partially/strongly reworked gravel sheets and of the high zones revealed a poorly sorted gravel texture with sometimes very low-angle horizontal bedding/coarse lags. The sediments on the avalanche faces of the gravel sheets are often rounded and grain supported. An small excavation of a cut bank revealed thin, inclined layers of open-framework gravel (OW) (Figure 4.9).

Observations of gravel pit exposures (Switzerland)

In vertical outcrop exposures of ancient braided deposits, the depositional elements can be identified by (i) erosional bounding surfaces, (ii) sedimentary structures (i.e., one or two sedimentary textures that can alternate), and (iii) clast orientation (Siegenthaler and Huggenberger, 1993). Field observations of gravel pit exposures of Pleistocene coarse deposits in Switzerland (see Chapter 2) showed that the main types of depositional elements are horizontal layers and 'cross-bedded sets [...] with trough-shaped, erosional concave upward lower-bounding surfaces' (Huggenberger and Regli, 2006).

The horizontal layers correspond to poorly sorted gravels sometimes with horizontal beddings. The erosional bounding surface of the trough fills is

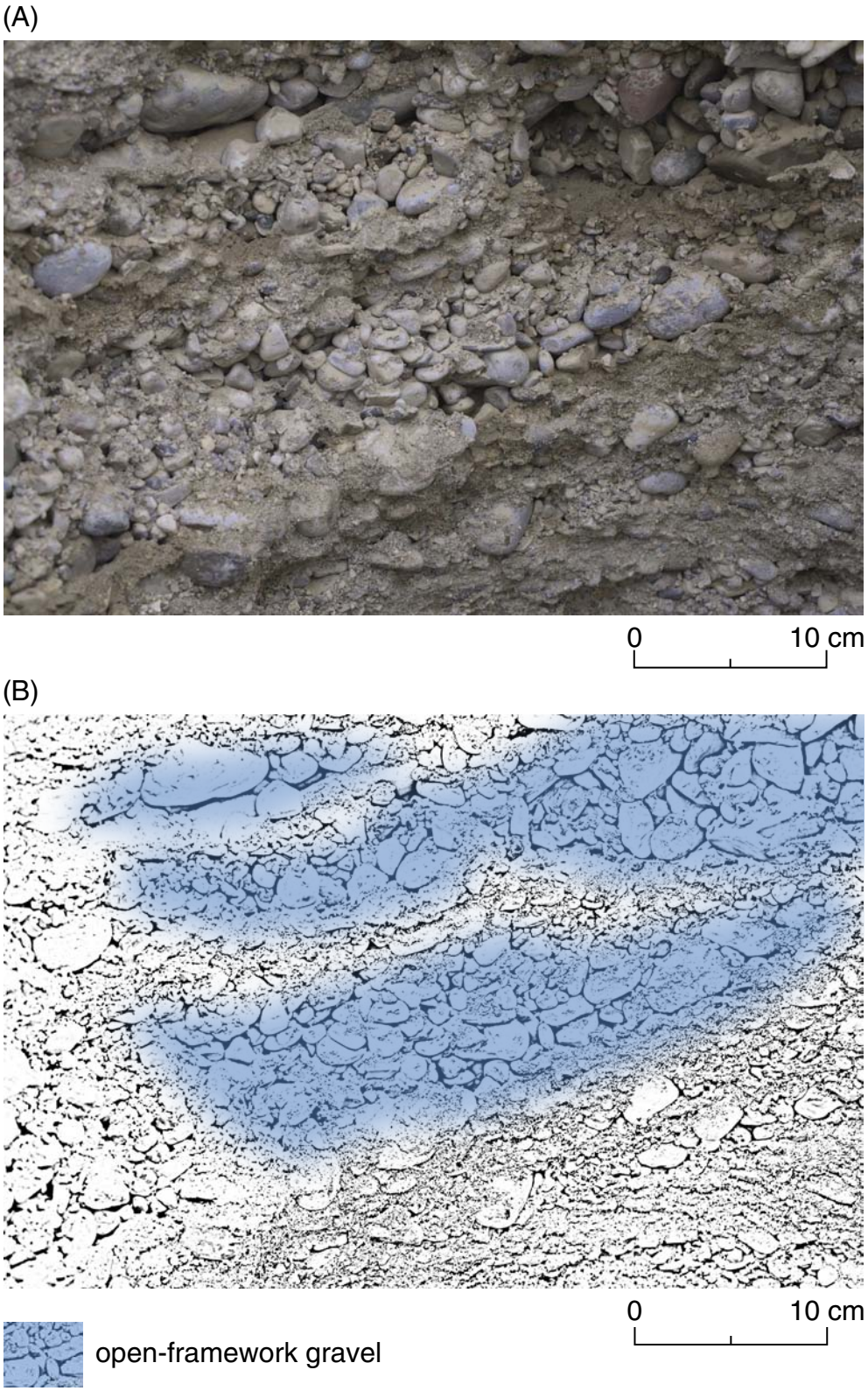

Figure 4.9 – **(A)** Photograph of a vertical exposure. **(B)** Sketch indicating where are the thin layers of open-framework gravel.

generally spoon-shaped and oriented in the main flow direction. The trough fills mostly consist of open-framework–bimodal gravel (OW–BM) couplet cross-beds (see also Siegenthaler and Huggenberger, 1993; Huggenberger and Regli, 2006). No trough fills are observed at the top of the gravel pit exposures. A horizontal layer lies in most cases on top of the trough fills when the latter are not eroded by other trough fills. Surprisingly, small-scale incisions are almost absent from the deposits (Heinz et al., 2003).

4.4 Discussion

4.4.1 High zones and active zones

A shift of the active zones toward the southwest associated with high zone formations (Figure 4.2) was observed between 1998 and 2005. The period of generally low discharges (mainly between 2003 and 2007) and the fact that the gravel substrate of the high zone is higher than the surface of the surrounding active zones suggest a local entrenchment of the river. Because no sediment flux measurements are available, we do not know if the entrenchment resulted (i) from a large deposition of sediments before 2003 followed by a local incision of the active zone or (ii) from a local/unequal aggradation that increased the transverse gradient toward the southwest (Figure 4.4) and occasioned the active zone shift. A regular monitoring of the topography would allow a better understanding of the active zone shifts and high zone formations in relation with the aggrading/degrading character of the reach and the transverse slope.

The topography of the active zones (e.g., the transverse slope, the confinement by the high zones) plays an important role by (i) controlling the stream power per unit width that impacts the sediment transport competence and capacity by the flows (Church, 2002) and (ii) conveying the flow toward obstacles (e.g., high zones) where the erosion process can operate by the abrasion of the obstacle with moving bedload particles (Sklar and Dietrich, 2004; Cook et al., 2014) and by scouring at the edge of the obstacle (Eilertsen and Hansen, 2008). In consequence, the active zone topography influences the geomorphological effectiveness of flood events. That can explain why small flood events (recurrence interval < 2 months) were able to significantly erode the high zones between 2005 and 2007 (Figure 4.3).

4.4.2 High-discharge/low-discharge morphologies

As highlighted in Section 4.3.3 (Figure 4.6), the braided river morphology in the active zones — always observed during low-discharge — is the overprinting of a high-discharge morphology by a low-discharge morphology, both being the two extremes of a continuum (Church, 2002; Huggenberger and Regli, 2006).

The high-discharge morphology is built during flood events that partially reshape the braidplain: large gravel sheets form, are mobilized and transported,

higher-lying zones are eroded, trees are uprooted, and the deepest scours are formed (Salter, 1993). Scours are produced by flow turbulences induced by topography especially near obstacles (e.g., along the side of the high zones; Gurnell et al., 2005), between gravel sheets, and between the gravel sheets and the confining banks (Ashmore, 1982; Ashmore and Parker, 1983; Best and Roy, 1991). As the gravel sheets migrate during the flood event, the scours induced by the topography of the gravel sheets can also migrate longitudinally and transversely (Ashmore and Gardner, 2008). The braidplain reshaping is largely determined by the discharge magnitude and duration and by the sediment pulses. The active zones are completely reshaped by high-energy events (recurrence interval > 6 years; Figure 4.3) and still partially reshaped by low-energy events (recurrence interval < 1 year). Periods of low discharges favor the vegetation development in the active zones that, in turn, favor the formation of a complex topography during flood events (e.g., Gurnell et al., 2005).

Field observations suggest that the low-discharge morphology is built during the hydrograph recession. The falling stage overprints a part of the high-discharge morphology with low-discharge incisions, lateral edge collapses of gravel sheets forming sequences of slip-face lobes, and sediment deposition (Figure 4.6, see also Best and Roy, 1991; Bridge, 1993; Hicks et al., 2002, 2007; Bristow et al., 2009; Rice et al., 2009). A rapid decrease of the discharge increases the transverse hydraulic gradients compared to the longitudinal ones and thus favor low-discharge incisions. In a laboratory experiment after the simulation of a flood event, Marti and Bezzola (2006) observed the formation of a large slightly meandering channel under low sediment supply conditions. This observation can explain the formation of the main low-discharge channels with their three-dimensional geometry that differs from the low-discharge incisions. The scours formed at high discharge are most probably covered by migrating gravel sheets (Ashmore and Gardner, 2008) and/or filled during the flow recession (Bridge, 1993). Storz-Peretz and Laronne (2013) assessed with buried chains scour-and-fill processes at confluences in a dryland braided river. They noticed that the scour holes formed during flood events were filled during the flow recession, and no evidence of their formation was detectable post-flood. This explains why scour holes are infrequently observed at low discharge and why the few observed (filled) scours are rather shallow. Interestingly, only a few low-discharge stream confluences form scours (see also Ashmore and Gardner, 2008).

In consequence, a correct decryption of the morphology must consider that (i) the braidplain observed at low discharge is always a combination of high- and low-discharge morphologies; (ii) the low-discharge morphology depends on the high-discharge morphology; and (iii) some high-discharge morphological elements (e.g., scours) can be indiscernible at low discharge.

4.4.3 Sedimentology

From morphological elements to depositional elements

The braidplain morphology observed at low discharge is a snapshot of a complex history that yields some clues to the erosional and depositional processes portrayed in vertical sections by erosional bounding surfaces. The formation of depositional elements is the result of either depositional (accretionary) processes or erosional and depositional (cut-and-fill) processes (Huggenberger and Regli, 2006) that create a morphology at a certain time.

The gravel sheets have a depositional character and a very low topography except at their edges. Because of the high river dynamics, we do not expect that complete gravel sheets will be entirely preserved in the sedimentary records (e.g., Smith, 1974). Rather, while the gravel sheets experience thinning and lateral erosion by the river, only remnants of gravel sheets are expected to be preserved in the subsurface. Parker et al. (2013) made a similar observation for sandy unit bar deposits and concluded that the identification of their remnants could be difficult. Smith (1974) observed on intact gravel sheets a general trend of upward grain-size fining, whereas he could not find evidence of a vertical grain-size trend on strongly reworked gravel sheets. In outcrops the poorly-sorted gravel (GP) texture was identified with remnants of gravel sheets (Siegenthaler and Huggenberger, 1993; Beres et al., 1999; Heinz et al., 2003; Huggenberger and Regli, 2006; Benn and Evans, 2010).

The slip-face lobes and depositional lobes are erosional and depositional features with a small extent. The slip-face lobes lie at the lowest location of the braidplain where the river will flow during the next flood event. Therefore, the probability that the slip-face lobes will be preserved in the sedimentary records is nearly zero.

The formation, migration, and subsequent filling of the scours are erosional and depositional processes that create depositional elements, i.e., scour fills, characterized by sharp erosional lower-bounding surfaces and specific sedimentary textures resulting from the flow separation downstream of the avalanche faces of the scours (e.g., Ashmore and Gardner, 2008). The few identified scours at the surface are not representative of the abundance of scour fills in the near subsurface for the following reasons. (i) Most surely, some scours are completely covered by sediments (e.g., gravel sheets) and therefore are not identifiable at the surface (e.g., Bridge, 1993; Ashmore and Gardner, 2008; Storz-Peretz and Laronne, 2013). (ii) The migration of the scours creates erosional lower-bounding surfaces in the deposits that can be five times larger than the scour-hole surfaces observed at low discharge (Figure 4.8; see also Heinz et al., 2003; Ashmore and Gardner, 2008). Scour fills were identified in outcrops by OW–BM couplet cross-beds and erosional lower-bounding surfaces (Siegenthaler and Huggenberger, 1993; Beres et al., 1999; Heinz et al., 2003; Huggenberger and Regli, 2006).

The low-discharge incisions and channels are shaped by erosional processes that can leave erosional lower-bounding surfaces in the near subsurface. The low-discharge incisions located on the gravel sheets are likely to be removed by the reworking of the gravel sheets. The low- discharge incisions/channels at

the edges of the gravel sheets can be filled with sediments. Because the low-discharge incisions and channels are preferential flow paths, no flow separations and therefore no specific sediment sorting are expected to occur there. Rather, the low-discharge incision and channel fills likely consist of poorly sorted sediments from the gravel sheets and may be hardly distinguishable from the remnants of gravel sheets (Lunt et al., 2004). Ashworth et al. (2011) came to a similar conclusion for channel fill and *compound bar* deposits of the sandy braided South Saskatchewan River.

However, how the active zones are reworked by a large flood event with recurrence interval larger than 5 years is still unclear (i.e., how the gravel sheets form and migrate, and how aggradation occurs in relation with active zone shifts). We formulate two alternative working hypotheses: the pre-flood topography is either (1) covered by newly formed gravel sheets that migrate or (2) completely reworked up to a certain depth during the flood event followed by the formation and migration of gravel sheets. Compared to hypothesis (2), hypothesis (1) favors the preservation of the low-discharge morphology in the near subsurface.

Because the high zones develop from abandoned active zones, the sedimentary structure of the high zones corresponds to that of the active zone reworked by local erosion and gravel deposition, by the incision of drainage networks, and by the deposition of fine sediments. In consequence, the main depositional elements are gravel sheet deposits (GP with possibly horizontal bedding), low-discharge incision/channel-fills (poorly sorted deposits similar to the remnant of gravel sheets), and scour fills (distinctive erosional lower-bounding surfaces in the deposits and cross-bed filling).

Preservation potential of the depositional elements

The preservation potential of a sedimentological unit in the sedimentary records is generally defined as the probability that the sedimentological unit will escape reworking (e.g., Meijer et al., 2008). The preservation potential of the depositional elements is a function of (i) their topographic positions (Siegenthaler and Huggenberger, 1993), (ii) their three-dimensional proportion (spatial

Table 4.1 – Characteristics of the main depositional elements of a coarse, braided river.

Depositional element	Character	Areal proportion	Topographic level	Preservation potential	Hydraulic properties
gravel sheet deposits	depositional	large	high	low to large	medium porosity & hydraulic conductivity
scour fills	erosional & depositional	low to medium	low	largest	large porosity & hydraulic conductivity
incision/channel fills	erosional & depositional	low to medium	medium	low to large	medium porosity & hydraulic conductivity

density and shape), (iii) the aggrading/degrading character of the river, and (iv) the three-dimensional proportion of the other cut-and-fill depositional elements. During each formative event, the areal/volumetric proportion of the erosional elements at the lowest topographic positions (e.g., scours) combined with the rate of aggradation determine the preservation potential of the previously deposited elements (scour fills, gravel sheet deposits, low-discharge incision/channel fills, etc.). Note that the near-surface is not representative for the preservation potential of depositional elements as the near-surface is likely to still experience scouring by the river. The preservation potential can be confidently assessed at a depth below the deepest possible river erosion.

Section 4.3.4 shows that the high zones generally persist < 25 years before they are eroded by the river. In aggradating settings, the high zones, particularly those that are stabilized by the vegetation, will be mainly scoured by the lateral migration of the active zones, resulting in pronounced erosional signatures in the subsurface. In case of high aggradation, the high zones could be buried and therefore partially preserved in the subsurface records. The preservation potential of the floodplain is similar to that of the vegetated high zones. Parts of the floodplain can be preserved if the rate of aggradation is large.

Table 4.1 gives an overview of the characteristics of the main depositional elements of a coarse, braided river. The scour fills, by their low topographic level, have the largest preservation potential. If the low-discharge incisions/channels are preserved in the sedimentary records, they have a smaller preservation potential than the scour fills and a larger preservation potential than the gravel sheet deposits. However, small-scale depositional elements rarely appear on outcrop observations (see also Heinz et al., 2003). Either the low-discharge incision/channel fills can barely be distinguished from the adjacent poorly sorted deposits or the low-discharge incisions/channels are completely reworked when the active zones are reshaped by medium and large flood events. The preservation potential of the slip-face lobe deposits can be considered as null.

4.4.4 Hydrogeology

In a hydrogeological perspective, the scour fill deposits consisting of OW–BM couplet cross-beds contrast strongly with the other deposits in terms of hydraulic properties. Indeed, the OW texture is characterized by a very high hydraulic conductivity and porosity compared to the other sedimentary textures (e.g., Huggenberger et al., 1988; Jussel et al., 1994; Klingbeil et al., 1999; Heinz et al., 2003). Therefore, the three-dimensional spatial distribution of OWs in the subsurface is likely to act as a fast pathway for the subsurface flow. As a consequence, the high-discharge morphology, through its large preservation potential, hydraulically impacts much more the subsurface than the low-discharge morphology. The low-discharge morphology mainly produces discontinuities in the deposits that can be considered as noise that is immersed into the low to medium permeable deposits.

The length of the fast flow pathways is controlled by the size of the scour fills and their preservation. Long pathways are formed under high aggradation rates and high discharge dynamic conditions (i.e., frequent large flood events).

Settings that favor a large proportion of highly permeable scour fill deposits and therefore a high density of erosion surfaces in the deposits are (i) a low aggradation rate and (ii) a large discharge dynamic (Table 4.2). However, under such settings, the connectivity of the OW may be often interrupted by erosional lower-bounding surfaces, but still the largest quantity of subsurface water may flow through a small fraction of the deposits, the OW. On the contrary, a high aggradation rate combined with a low-discharge dynamic increases the preservation potential of the gravel sheets as less scours are formed. Under low aggradation and low discharge dynamic, the low-discharge incisions might completely rework the high-discharge morphology (i.e., gravel sheets). An alternation of aggradation-degradation with an aggrading trend increases the subsurface heterogeneity compared to solely aggradation with the same trend.

4.5 Conclusion

This work aimed at characterizing the morphodynamics of a gravel-bed, braided reach (Tagliamento River) and at assessing its impact on the sedimentary deposits.

The surface morphology of the braidplain is not representative of the subsurface heterogeneity because (i) cut-and-fill processes such as scour formation, migration, and filling can leave no clues of their existence when the braidplain is observed at low discharge; (ii) the morphology at the highest position has the smallest preservation potential (e.g., the high zones are unlikely preserved in the subsurface even if they are stabilized by wooded vegetation, rather their erosion leaves erosional surfaces in the sedimentary records); (iii) the high-discharge morphology impacts more the hydraulic subsurface heterogeneity, but it is overprinted by the low-discharge morphology; and (iv) the near-subsurface that is more related to the morphology is likely to experience cut-and-fill processes in the future.

Therefore, the characterization of the subsurface structure through a pure mor-

Table 4.2 – Relationship between surface dynamics and the abundance of depositional elements in the deposits: (++, +, +/−, −) stand for very large, large, medium and low proportions.

		Aggradation rate	
		low	high
Discharge dynamics	high	+ scour fills - remnant of gravel sheets +/- low-discharge incisions/channels	+/- scour fills + remnant of gravel sheets - low-discharge incisions/channels
	low	+/- scour fills +/- remnant of gravel sheets + low-discharge incisions/channels	- scour fills ++ remnant of gravel sheets +/- low-discharge incisions/channels

phological approach (e.g., topography stacking) underestimates the proportion of cut-and-fill depositional elements that are likely to control the fast pathways of the subsurface flow.

The qualitative preservation potential rules presented here could be implemented into a sedimentological stochastic model based on fuzzy logic. Different working hypotheses and settings regarding river dynamics could be considered, and the simulation outputs could be tested against vertical outcrop exposures. Further research should focus on the reworking of the active zones, more particularly on the processes behind the formation and migration of gravel sheets and scours over time, particularly at high discharge and during the hydrograph recession. These processes control the morphodynamic and the sedimentary processes.

Acknowledgements

We thank A. Gurnel and W. Bertoldi who kindly provided us the LiDAR-derived DEM, M. Doering for the Quickbird photographs and the Servizio Idraulica of the Autonomous Region of Friuli Venezia Giulia for the water stage time-series. Special thanks go to L. Josset for constructive comments on a previous version of the manuscript. The critical comments from R. A. Marston and three anonymous reviewers helped to improve the quality of the manuscript.

Figure 4.10 – Orthophoto 1998 (from the Autonomous Region of Friuli Venezia Giulia).

Figure 4.11 – Orthophoto 2003 (from the Autonomous Region of Friuli Venezia Giulia).

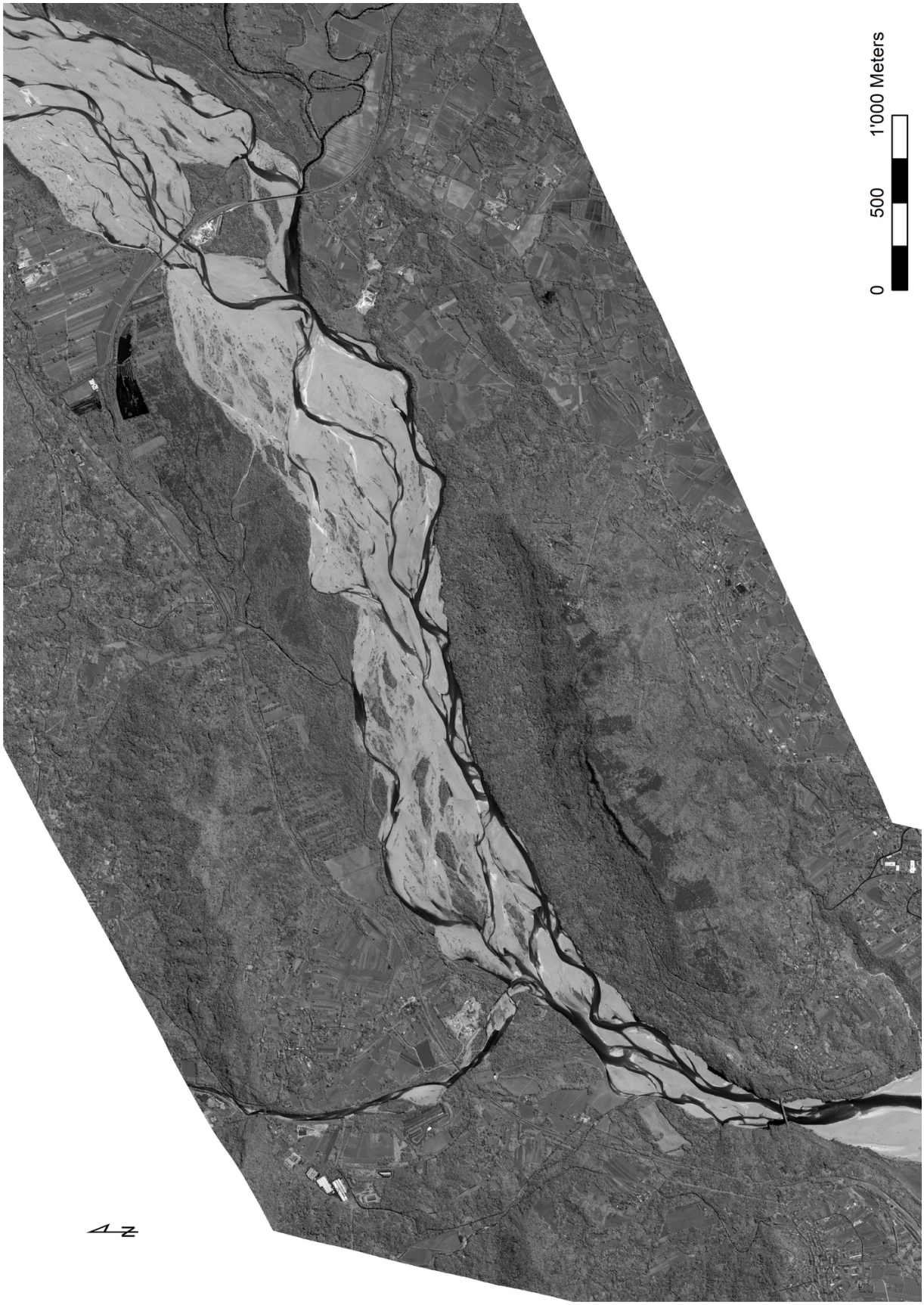

Figure 4.12 – Quickbird panchromatic photograph, May 2005 (courtesy of Michael Doering).

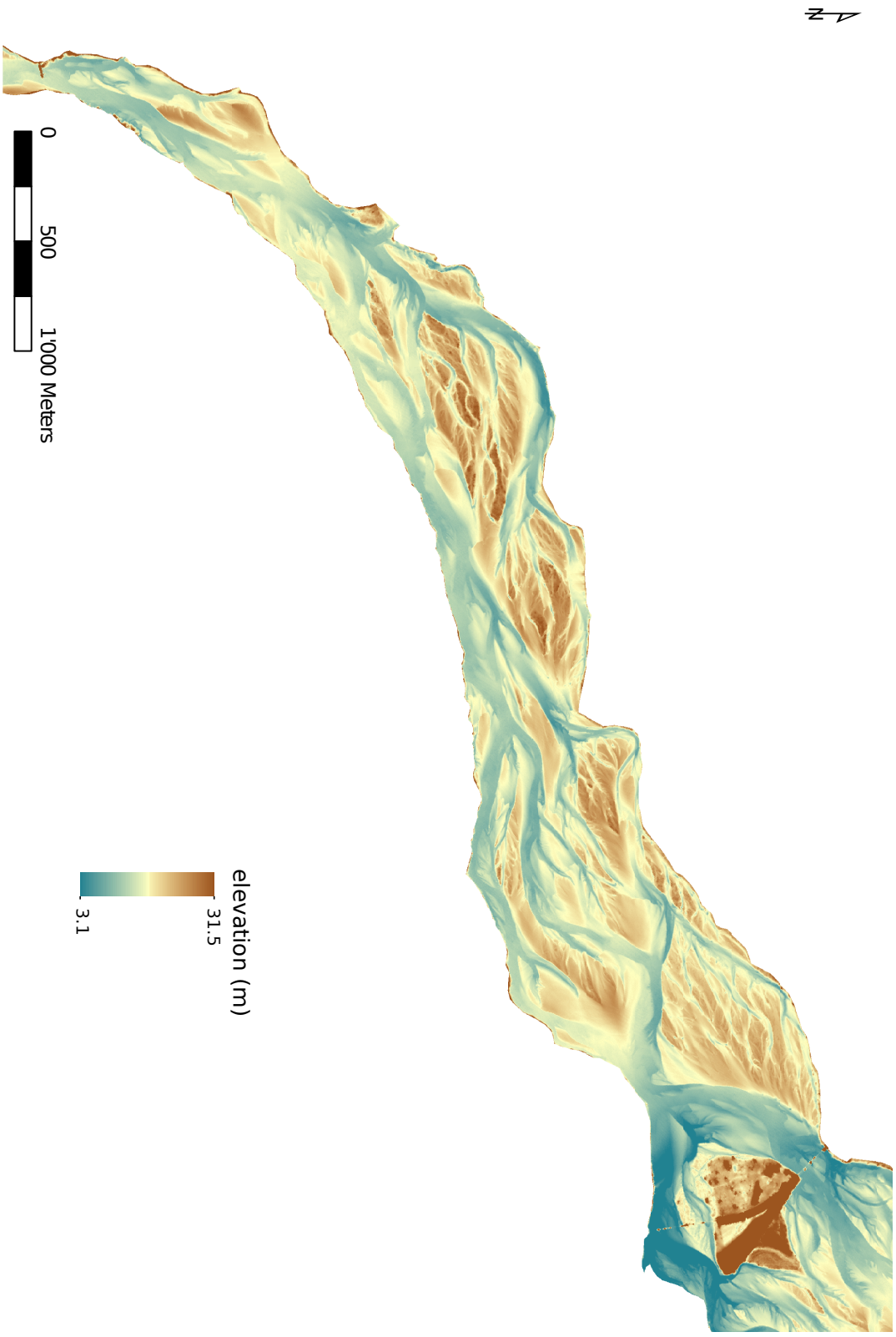

Figure 4.13 – LiDAR-derived DEM, 23 May 2005 (from the U.K. Natural Environment Research Council).

Figure 4.14 – Orthophoto 2007 (from the Autonomous Region of Friuli Venezia Giulia).

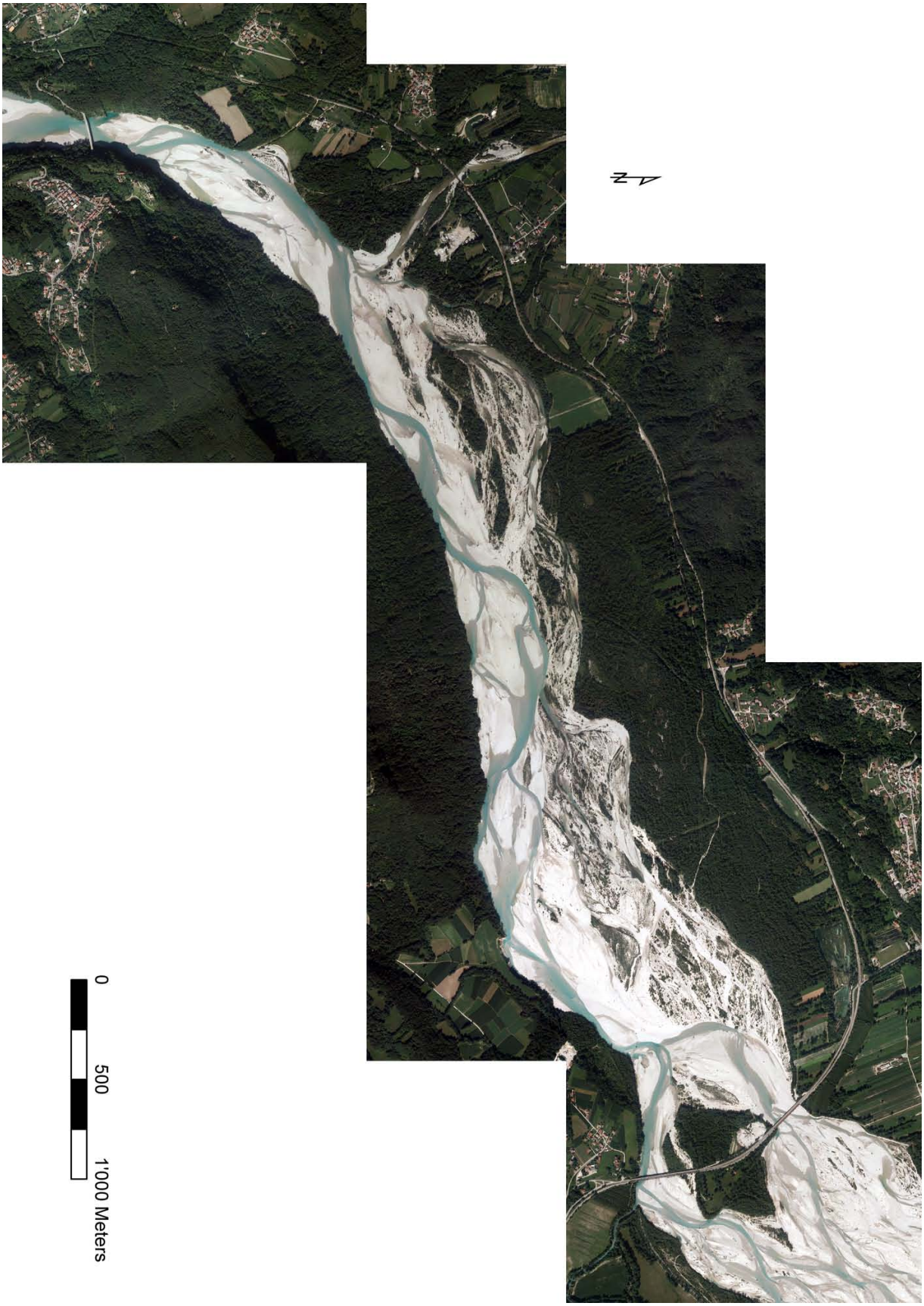

Figure 4.15 – Orthophoto 2011 (from the Autonomous Region of Friuli Venezia Giulia).

References

Anderson M., Aiken J., Webb E. and **Mickelson D.** (1999) Sedimentology and hydrogeology of two braided stream deposits. *Sedimentary Geology*, **129**(3–4): 187–199.
doi: 10.1016/s0037-0738(99)00015-9

Arscott D.B., Tockner K., van der Nat D. and **Ward J.V.** (2002) Aquatic Habitat Dynamics along a Braided Alpine River Ecosystem (Tagliamento River, Northeast Italy). *Ecosystems*, **5**(8): 0802–0814.
doi: 10.1007/s10021-002-0192-7

Ashmore P. and **Gardner J.T.** (2008) Unconfined Confluences in Braided Rivers, In: *River Confluences, Tributaries and the Fluvial Network* (Eds. S.P. Rice, A.G. Roy and B.L. Rhoads), John Wiley & Sons, Ltd, 119–147.
doi: 10.1002/9780470760383.ch7

Ashmore P. and **Parker G.** (1983) Confluence scour in coarse braided streams. *Water Resources Research*, **19**(2): 392–402.
doi: 10.1029/WR019i002p00392

Ashmore P.E. (1982) Laboratory modelling of gravel braided stream morphology. *Earth Surface Processes and Landforms*, **7**(3): 201–225.
doi: 10.1002/esp.3290070301

Ashworth P.J., Best J.L. and **Jones M.A.** (2007) The relationship between channel avulsion, flow occupancy and aggradation in braided rivers: insights from an experimental model. *Sedimentology*, **54**(3): 497–513.
doi: 10.1111/j.1365-3091.2006.00845.x

Ashworth P.J., Smith G.H.S., Best J.L., Bridge J.S., Lane S.N., Lunt I.A., Reesink A.J.H., Simpson C.J. and **Thomas R.E.** (2011) Evolution and sedimentology of a channel fill in the sandy braided South Saskatchewan River and its comparison to the deposits of an adjacent compound bar. *Sedimentology*, **58**(7): 1860–1883.
doi: 10.1111/j.1365-3091.2011.01242.x

Bayer P., Huggenberger P., Renard P. and **Comunian A.** (2011) Three-dimensional high resolution fluvio-glacial aquifer analog: Part 1: Field study. *Journal of Hydrology*, **405**(1–2): 1–9.
doi: 10.1016/j.jhydrol.2011.03.038

Benn D.I. and **Evans D.J.A.** (2010) *Glaciers and Glaciation*: 2nd Edition. Hodder Education, 802 pp.
ISBN:978-0-340-90579-1

Beres M., Huggenberger P., Green A.G. and **Horstmeyer H.** (1999) Using two- and three-dimensional georadar methods to characterize glaciofluvial architecture. *Sedimentary Geology*, **129**(1–2): 1–24.
doi: 10.1016/S0037-0738(99)00053-6

Bertoldi W. (2012) Life of a bifurcation in a gravel-bed braided river. *Earth Surface Processes and Landforms*, **37**(12): 1327–1336.
doi: 10.1002/esp.3279

Bertoldi W., Gurnell A.M. and **Drake N.A.** (2011) The topographic signature of vegetation development along a braided river: Results of a combined analysis of airborne lidar, color air photographs, and ground measurements. *Water Resources Research*, **47**(6): na–na.
doi: 10.1029/2010wr010319

Bertoldi W., Zanoni L. and **Tubino M.** (2010) Assessment of morphological changes induced by flow and flood pulses in a gravel bed braided river: The Tagliamento River (Italy). *Geomorphology*, **114**(3): 348 – 360.
doi: 10.1016/j.geomorph.2009.07.017

Best J.L. (1993) On the interactions between turbulent flow structure, sediment transport and bedform developments: some considerations from recent experimental research, In: *Turbulence: Perspectives on Flow and Sediment Transport* (Eds. N.J. Clifford, J.R. French and J. Hardisty), John Wiley & Sons, Ltd, Chichester, UK, 61–93.

Best J.L. and **Ashworth P.J.** (1997) Scour in large braided rivers and the recognition of sequence stratigraphic boundaries. *Nature*, **387**(6630): 275–277.
doi: 10.1038/387275a0

Best J.L. and **Roy A.G.** (1991) Mixing-layer distortion at the confluence of channels of different depth. *Nature*, **350**(6317): 411–413.
doi: 10.1038/350411a0

Bridge J.S. (1993) The interaction between channel geometry, water flow, sediment transport and deposition in braided rivers, In: *Braided Rivers* (Eds. J.L. Best and C.S. Bristow), 75, Geological Society, London, Special Publications, Ch. The interaction between channel geometry, water flow, sediment transport and deposition in braided rivers, 13–71.
doi: 10.1144/GSL.SP.1993.075.01.02

Bristow C.S., Best J.L. and **Roy A.G.** (2009) Morphology and Facies Models of Channel Confluences, In: Alluvial Sedimentation Blackwell Publishing Ltd., 89–100.
doi: 10.1002/9781444303995.ch8

Bristow C.S. and **Jol H.M.** (2003) An introduction to ground penetrating radar (GPR) in sediments. *Geological Society, London, Special Publications*, **211**(1): 1–7.
doi: 10.1144/GSL.SP.2001.211.01.01

Bryant M., Falk P. and **Paola C.** (1995) Experimental study of avulsion frequency and rate of deposition. *Geology*, **23**(4): 365.
doi: 10.1130/0091-7613(1995)023<0365:esoafa>2.3.co;2

Church M. (2002) Geomorphic thresholds in riverine landscapes. *Freshwater Biology*, **47**(4): 541–557.
doi: 10.1046/j.1365-2427.2002.00919.x

Comunian A., Renard P., Straubhaar J. and **Bayer P.** (2011) Three-dimensional high resolution fluvio-glacial aquifer analog – Part 2: Geostatistical modeling. *Journal of Hydrology*, **405**(1–2): 10–23.
doi: 10.1016/j.jhydrol.2011.03.037

Cook K.L., Turowski J.M. and **Hovius N.** (2014) River gorge eradication by downstream sweep erosion. *Nature Geoscience*, **7**(9): 682–686.
doi: 10.1038/ngeo2224

Eilertsen R.S. and **Hansen L.** (2008) Morphology of river bed scours on a delta plain revealed by interferometric sonar. *Geomorphology*, **94**(1–2): 58–68.
doi: 10.1016/j.geomorph.2007.04.005

Gurnell A., Tockner K., Edwards P. and **Petts G.** (2005) Effects of deposited wood on biocomplexity of river corridors. *Frontiers in Ecology and the Environment*, **3**(7): 377–382.
doi: 10.1890/1540-9295(2005)003[0377:eodwob]2.0.co;2

Heinz J., Kleineidam S., Teutsch G. and **Aigner T.** (2003) Heterogeneity patterns of Quaternary glaciofluvial gravel bodies (SW-Germany): application to hydrogeology. *Sedimentary Geology*, **158**(1–2): 1–23.
doi: 10.1016/S0037-0738(02)00239-7

Hicks D.M., Duncan M., Walsh J., Westaway R. and **Lane S.** (2002) New views of the morphodynamics of large braided rivers from high-resolution topographic surveys and time-lapse video, In: *The structure, function and management of fluvial sedimentary systems* (Eds. F.J. Dyer, M.C. Thoms and J.M. Olley), 276, International Association of Hydrological Sciences, Wallingford, United Kingdom, 373–380.

Hicks D.M., Duncan M.J., Lane S.N., Tal M. and **Westaway R.** (2007) Contemporary morphological change in braided gravel-bed rivers: new developments from field and laboratory studies, with particular reference to the influence of riparian vegetation, In: *Developments in Earth Surface Processes* (Eds. H. Habersack, H. Piégay and M. Rinaldi), Elsevier BV, 557–584.
doi: 10.1016/s0928-2025(07)11143-3

Huggenberger P., Hoehn E., Beschta R. and **Woessner W.** (1998) Abiotic aspects of channels and floodplains in riparian ecology. *Freshwater Biology*, **40**(3): 407–425.
doi: 10.1046/j.1365-2427.1998.00371.x

Huggenberger P. and **Regli C.** (2006) A Sedimentological Model to Characterize Braided River Deposits for Hydrogeological Applications, In: *Braided Rivers* (Eds. G.H. Sambrook Smith, J.L. Best, C.S. Bristow and G.E. Petts), Blackwell Publishing Ltd., Ch. 3,

51–74.
doi: 10.1002/9781444304374.ch3

Huggenberger P., Siegenthaler C. and **Stauffer F.** (1988) Grundwasserströmung in Schottern; Einfluss von Ablagerungsformen auf die Verteilung der Grundwasserfliessgeschwindigkeit. *Wasserwirtschaft*, **78**(5): 202–212.

Jones L.S. and **Schumm S.A.** (1999) Causes of Avulsion: An Overview, In: *Fluvial Sedimentology VI* (Eds. N.D. Smith, J. Rogers, L.S. Jones and S.A. Schumm), Blackwell Publishing Ltd., 169–178.
doi: 10.1002/9781444304213.ch13

Jussel P., Stauffer F. and **Dracos T.** (1994) Transport modeling in heterogeneous aquifers: 1. Statistical description and numerical generation of gravel deposits. *Water Resources Research*, **30**(6): 1803–1817.
doi: 10.1029/94WR00162

Kelly S. (2006) Scaling and Hierarchy in Braided Rivers and their Deposits: Examples and Implications for Reservoir Modelling, In: *Braided Rivers* (Eds. G.H. Sambrook Smith, J.L. Best, C.S. Bristow and G.E. Petts), Blackwell Publishing Ltd., Ch. 4, 75–106.
doi: 10.1002/9781444304374.ch4

Klingbeil R., Kleineidam S., Asprion U., Aigner T. and **Teutsch G.** (1999) Relating lithofacies to hydrofacies: outcrop-based hydrogeological characterisation of Quaternary gravel deposits. *Sedimentary Geology*, **129**(3–4): 299–310.
doi: 10.1016/S0037-0738(99)00067-6

Kock S., Huggenberger P., Preusser F., Rentzel P. and **Wetzel A.** (2009) Formation and evolution of the Lower Terrace of the Rhine River in the area of Basel. *Swiss Journal of Geosciences*, **102**(2): 307–321.
doi: 10.1007/s00015-009-1325-1

Lunt I.A., Bridge J.S. and **Tye R.S.** (2004) A quantitative, three-dimensional depositional model of gravelly braided rivers. *Sedimentology*, **51**(3): 377–414.
doi: 10.1111/j.1365-3091.2004.00627.x

Marti C. and **Bezzola G.R.** (2006) Bed Load Transport in Braided Gravel-Bed Rivers, In: *Braided Rivers* (Eds. G.H. Sambrook Smith, J.L. Best, C.S. Bristow and G.E. Petts), Blackwell Publishing Ltd., 199–215.
doi: 10.1002/9781444304374.ch9

Meijer X.D., Postma G., Burrough P.A. and **de Boer P.L.** (2008) Modelling the Preservation of Sedimentary Deposits on Passive Continental Margins during Glacial-Interglacial Cycles, In: *Analogue and Numerical Modelling of Sedimentary Systems: From Understanding to Prediction* (Eds. P. de Boer, G. Postma, K. van der Zwan, P. Burgess and P. Kukla), Wiley-Blackwell, 223–238.
doi: 10.1002/9781444303131.ch10

Parker N.O., Smith G.H.S., Ashworth P.J., Best J.L., Lane S.N., Lunt I.A., Simpson C.J. and **Thomas R.** (2013) Quantification of the relation between surface morphodynamics and subsurface sedimentological product in sandy braided rivers. *Sedimentology*, **60**(3): 820–839.
doi: 10.1111/j.1365-3091.2012.01364.x

Regli C., Huggenberger P. and **Rauber M.** (2002) Interpretation of drill core and georadar data of coarse gravel deposits. *Journal of Hydrology*, **255**(1-4): 234 – 252.
doi: 10.1016/S0022-1694(01)00531-5

Rice S.P., Church M., Wooldridge C.L. and **Hickin E.J.** (2009) Morphology and evolution of bars in a wandering gravel-bed river; lower Fraser river, British Columbia, Canada. *Sedimentology*, **56**(3): 709–736.
doi: 10.1111/j.1365-3091.2008.00994.x

Salter T. (1993) Fluvial scour and incision: models for their influence on the development of realistic reservoir geometries. *Geological Society, London, Special Publications*, **73**(1): 33–51.
doi: 10.1144/gsl.sp.1993.073.01.04

Siegenthaler C. and **Huggenberger P.** (1993) Pleistocene Rhine gravel: deposits of a braided river system with dominant pool preservation. *Geological Society, London, Special Publications*, **75**(1): 147–162.
doi: 10.1144/GSL.SP.1993.075.01.09

Sklar L.S. and **Dietrich W.E.** (2004) A mechanistic model for river incision into bedrock by saltating bed load. *Water Resources Research*, **40**(6): n/a–n/a. doi: 10.1029/2003wr002496

Smith G.S., Best J., Bristow C. and **Petts G.** (2006) Braided Rivers: Where have we Come in 10 Years? Progress and Future Needs, In: *Braided Rivers* (Eds. G.H. Sambrook Smith, J.L. Best, C.S. Bristow and G.E. Petts), Wiley-Blackwell, 1–10. doi: 10.1002/9781444304374.ch1

Smith N.D. (1974) Sedimentology and Bar Formation in the Upper Kicking Horse River, a Braided Outwash Stream. *The Journal of Geology*, **82**(2): 205–223.

Storz-Peretz Y. and **Laronne J.B.** (2013) Morphotextural characterization of dryland braided channels. *Geological Society of America Bulletin*, **125**(9-10): 1599–1617. doi: 10.1130/b30773.1

Surian N., Barban M., Ziliani L., Monegato G., Bertoldi W. and **Comiti F.** (2015) Vegetation turnover in a braided river: frequency and effectiveness of floods of different magnitude. *Earth Surface Processes and Landforms*, **40**(4): 542–558. doi: 10.1002/esp.3660

Zanoni L., Gurnell A., Drake N. and **Surian N.** (2008) Island dynamics in a braided river from analysis of historical maps and air photographs. *River Research and Applications*, **24**(8): 1141–1159. doi: 10.1002/rra.1086

5 Subsurface characterisation of a coarse, braided river with GPR

> *Thus advancing the science of hydrology will require not only developing theories that get the right answers but also testing whether they get the right answers for the right reasons.*

J.W. Kirchner (2006) Getting the right answers for the right reasons: Linking measurements, analyses, and models to advance the science of hydrology. Water Resources research, 42:W03S04.
doi:10.1029/2005WR004362

Abstract Ground-penetrating radar (GPR) is a useful, high-resolution tool to image the near subsurface and, therefore, to study the depositional processes. While many previous studies focused on ancient, coarse, braided river deposits, few studies investigated the near sub-surface of coarse, braided river systems. Furthermore, the relationship between the surface morphology and the subsurface structure has not been fully explored. This study investigates this relationship by characterising the near subsurface of a coarse, braided reach of the Tagliamento River with GPR. The interpreted data are analysed in light of the recent geomorphological evolution of the reach and previous observations of ancient, coarse braided deposits.

E. Huber (2017) *Incorporating sedimentological observations, hydrogeophysics and conceptual knowledge to constrain 3D numerical heterogeneity models of alluvial systems.* Ph.D. thesis, Applied and Environmental Geology, University of Basel, Switzerland, 192 pp.

5.1 Introduction

Deposits of former coarse, braided river systems make up many of the exploited groundwater water reservoirs worldwide (Huggenberger and Aigner, 1999; Klingbeil et al., 1999; Huggenberger and Regli, 2006; Slomka and Eyles, 2013). These deposits are highly heterogeneous in terms of hydraulic properties (e.g., Jussel, 1992; Jussel et al., 1994; Klingbeil et al., 1999; Heinz et al., 2003). Characterising the heterogeneity of these deposits is a critical prerequisite for reliable subsurface flow and transport simulations, as well as uncertainty assessments.

The sedimentology contributes to the aquifer characterisation by inferring the former depositional environments and developing conceptual models from observed deposits (Lunt et al., 2004). The spatial distribution and the geometry of the preserved depositional elements control the connectivity of high/low permeable sedimentary structures, and can therefore strongly influence subsurface flow and transport. Ancient deposits are sources of valuable information on subsurface heterogeneity because they reveal (i) the geometries of depositional elements, (ii) which depositional elements have been preserved over the geological time, (iii) the relationship between the depositional elements (inclusive their spatial distribution), and (iv) the hydraulic properties of the sedimentary structures (see Chapter 2). Therefore, ancient deposits shed some light on the erosional and depositional processes as well as on the scale of the morphological elements.

Whereas many studies focusing on the sedimentary structures of coarse, braided river deposits were carried out on *ancient* deposits (e.g., Huggenberger, 1993; Beres et al., 1995, 1999; Huggenberger et al., 1994; Asprion and Aigner, 1997, 1999; Heinz and Aigner, 2003; Kostic and Aigner, 2007; Bayer et al., 2011), very few studies investigated the near-subsurface structure of *modern* coarse, braided river environments (e.g., Lunt et al., 2004, Sagavanirktok River, Alaska). For this reason, the link between the morphodynamics of coarse, braided rivers and the resulting subsurface structure has not been fully explored (Smith et al., 2006) although this link is a critical key to developing geologically realistic models of the subsurface heterogeneity (Huggenberger and Regli, 2006).

The study of the morphodynamics of coarse, braided rivers is challenging. In coarse, braided rivers, the most formative processes occur during high-discharge events, as attested by the comparison of pre-flood with post-flood morphology (Huber and Huggenberger, 2015). However, these high-discharge processes cannot be directly observed and are hardly measurable because of the high turbidity of the river water, the violence of the river flow, and the high riverbed mobility. Furthermore, parts of the morphology formed at high-discharge (e.g., gravel sheets, scours) are reworked during the discharge recession. For example, scours formed during high-discharge events are generally filled during the discharge recession leaving no clues of their presence at low discharge (Storz-Peretz and Laronne, 2013).

Therefore, integrative approaches combining observations of coarse, braided river morphodynamics with geophysical near-subsurface imaging and observations of ancient deposits are necessary. Previous studies on quaternary

glacio-fluvial, coarse deposits showed the suitability of ground-penetrating radar (GPR) to accurately characterise the main sedimentary structures by comparing GPR surveys with excavated outcrops (Huggenberger, 1993; Beres et al., 1995, 1999; Huggenberger et al., 1994, 1998; Asprion and Aigner, 1997, 1999; Heinz and Aigner, 2003; Kostic and Aigner, 2007; Bayer et al., 2011). In fact, the dielectric properties of the deposits are mainly related to the porosity in the saturated zone and to the water saturation in the unsaturated zone, which in turn depend on the lithology (Huggenberger, 1993). GPR is therefore a useful high resolution tool to identify the sedimentary structures within shallow fluvial deposits and, thus, to study the depositional processes (Jol, 1995; Dam and Schlager, 2000; Lunt et al., 2004; Bridge and Lunt, 2006; Schmelzbach et al., 2011).

The present study aims to investigate the relationship between the morphodynamics of a coarse, braided river reach and its near-subsurface structure imaged by GPR. More specifically, GPR data were collected within distinct morphological areas of the Cimano-Pinzano reach of the Tagliamento River (see Chapter 3) and compared to observations made in ancient deposits (e.g., vertical exposure in gravel carries, Chapter 2). Then, the GPR data are interpreted in light of present-day morphology and aerial/satellite photographs from 1998 to 2013 (see also Chapter 4).

Many large European rivers are strongly regulated and the geomorphological and sedimentological processes that built up their floodplains are no more observable. In contrast, the Tagliamento River is almost morphologically intact and, therefore, represents an ideal field laboratory to study the relationship between surface morphology and subsurface heterogeneity (see Chapter 3). The Cimano-Pinzano reach was selected for its structural and sedimentological similarity with many partly confined valleys such as in the Alpine foreland.

Huber and Huggenberger (2015) described the recent morphodynamics of the Cimano-Pinzano reach and discussed the impact of high-discharge events on the morphology and near-subsurface. The morphology of the braidplain consists of higher-lying zones (often vegetated) that are surrounded by actives zones (gravel free surfaces) that are regularly reworked by the river. The higher-lying zones grow vertically by fine sediment deposition during high-discharge events, are incised by drainage networks and are laterally eroded by the river. The actives zones consist in a low-discharge morphology (low-flow incisions and channels, slip-face lobes) superimposed on a high-discharge morphology (gravel sheets, scours). At low-discharge, the stream network shows a braided pattern. More details can be found in Huber and Huggenberger (2015) as well as in Chapter 4.

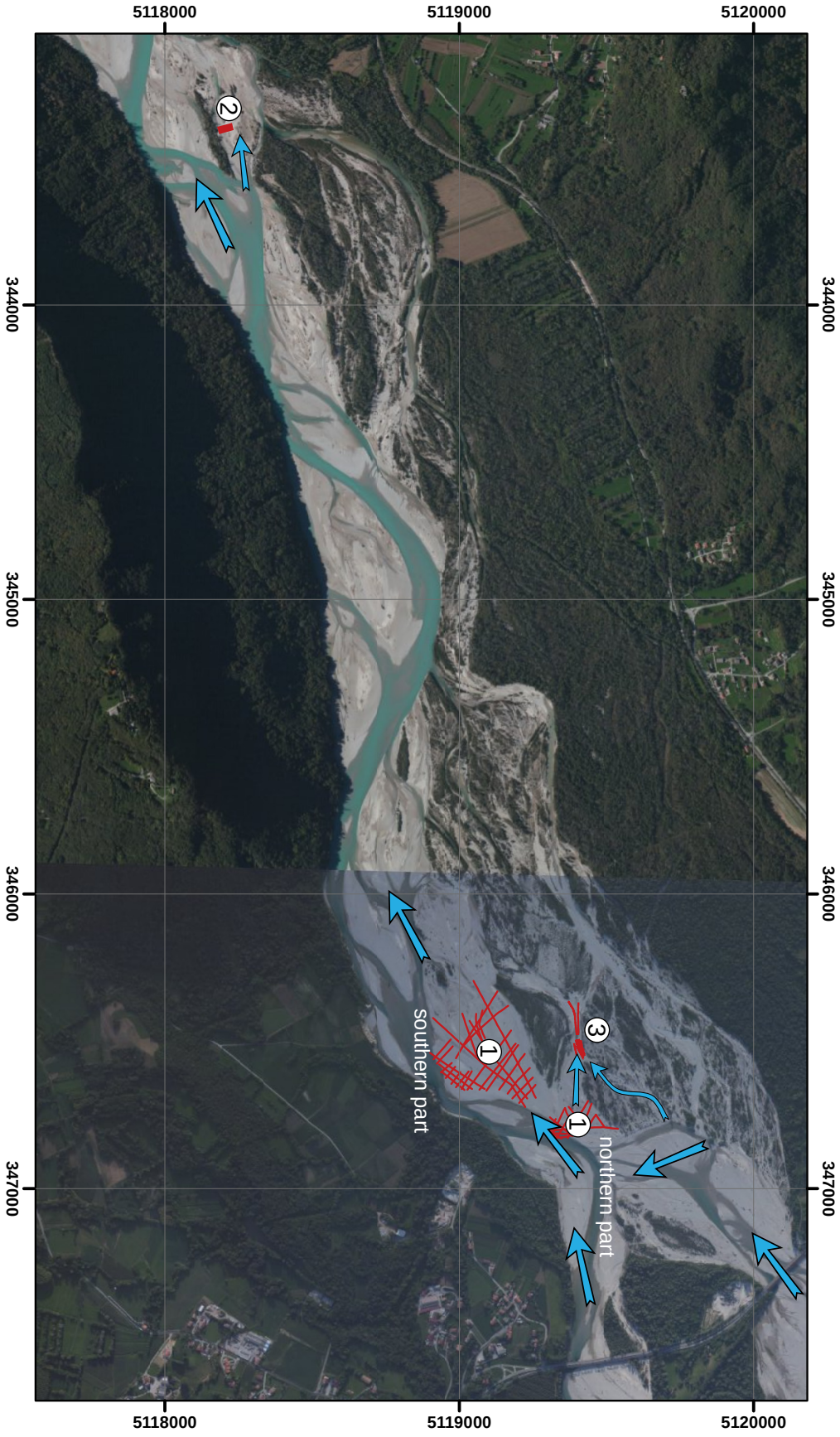

Figure 5.1 – The Cimano-Pinzano reach. The ground-penetrating radar profiles are represented by the red lines and the circled number indicate to which survey the GPR profiles belong. The blue arrows indicate the main flow direction at high discharge (background photograph: ESRI World Imagery).

5.2 Method

5.2.1 GPR data acquisition

The GPR data were acquired with a PulseEkko Pro GPR system (manufactured by Sensors and Software, Inc., Mississagua, Ontario) with a pair of unshielded 100-MHz antennae separated by 1 m. The recording of the GPR waves (e.g., the GPR traces) at regular intervals along the survey lines was triggered by an odometer. The position of the survey lines, the topography of the survey area and the edge of the water surfaces were surveyed with a total station (South, NTS 355L). The elevations of the free-water surface edges (ponds or stream) were interpolated to estimate the groundwater level below the survey areas.

Three GPR surveys were conducted at distinct places within the braidplain of the Cimano-Pinzano reach (Figure 5.1 and Table 5.1). GPR data acquisition on the braidplain of the Tagliamento River are laborious and challenging because the terrain can be very rough, the survey areas are sometimes hardly accessible and the position of the streams can suddenly change after a high-discharge event making the planing of GPR surveys a gamble.

The GPR profiles parallel to the general flow direction within the survey area are called *along-flow profiles* and the GPR profiles perpendicular to the general flow direction are called *across-flow profiles*. The along-flow profiles are displayed such that the general flow direction is from the left to the right and the across-flow profiles are displayed such that the general flow direction is from the reader position into the Figure. Note also that the GPR data are displayed without vertical exaggeration to facilitate the comparison with vertical exposures of ancient deposits (e.g., Chapter 2).

5.2.2 GPR data processing

The GPR data processing aims to increase the signal-to-noise ratio without introducing artefacts in the data. The processing workflow was performed with the R-package RGPR (Appendix, Chapter B) and was adapted to each survey but was identical for all the GPR data belonging to the same survey. All the different processing steps that where applied in this study are listed below.

- ▷ First-breaks picking (Sabbione and Velis, 2010) and time-zero adjustment.
- ▷ DC-shift removal.
- ▷ Constant offset correction to compensate for the 1-m-offset between transmitter and receiver antennae (the acquisition time of the traces is converted into the corresponding acquisition time for a mono-static antennae GPR).

Table 5.1 – Characteristics of the three ground-penetrating radar survey.

	Date	**Extent**
Survey 1	October 2010	325 m × 700 m
Survey 2	October 2011	25 m × 50 m
Survey 3	January 2014	55 m × 20 m

- ▷ Removal of the low-frequency trend estimated with either a Hampel filter (e.g., Pearson, 2002) or a Gaussian kernel.
- ▷ Spherical and exponential amplitude corrections were applied to compensate for geometric spreading and attenuation (e.g., Kruse and Jol, 2003; Grimm et al., 2006).
- ▷ Automatic Gain Control (Yilmaz, 2001).
- ▷ Band-pass frequency filtering to remove the low and high noisy frequencies.
- ▷ A 3×3-median filter to remove non-linear high-frequency noise.
- ▷ Mixed-phase deconvolution (Schmelzbach and Huber, 2015) to compress the GPR signal into spikes (resolution enhancement) and shift the signal at the true reflectivity structure.
- ▷ Adaptive smoothing based on the propagation–separation approach by Polzehl and Spokoiny (2006) implemented in the `adimpro` package for R (Polzehl and Tabelow, 2007).
- ▷ Topographic Kirchhoff migration (Lehmann and Green, 2000; Dujardin and Bano, 2013) with constant GPR wave velocity that leads to results that are accurate enough for the purpose of the study. The velocities of the GPR waves are derived from a common mid-point (CMP) GPR survey (Dix, 1955; Tillard, 1995; Booth et al., 2010).

The high spatial sampling of survey 2 ($0.25\,\text{m} \times 0.25\,\text{m}$) allows horizontal slices of the data cube to be extracted. The horizontal slices (also called time- or depth-slices) were generated at different depths without vertical averaging as we observed that the fine-scale structures get lost by vertical averaging. The fine-scale structures are important to characterise the internal structure between two main reflectors and can inform on the sedimentologcial processes. Horizontal slices enhance the three dimensional continuity of the reflectors as they attenuate the impact of small misalignments between the profiles. The algorithm proposed by Oimoen (2000) was applied to remove striping noise (see also Ernenwein and Kvamme, 2008).

5.2.3 GPR data interpretation

The interpretation of the GPR profiles is based on (i) continuity of the dominant reflectors within and between the profiles, (ii) differences of reflection patterns, and (iii) angular unconformity between the reflectors that can indicate an erosion surface or the superposition of two sedimentary structures with different sedimentary textures (Beres et al., 1995, 1999). No interpretation is made where the reflector patterns are not unequivocal (e.g., chaotic pattern). If the spatial sampling of the data permits it, surfaces were interpolated from connected reflectors in GoCAD (Paradigm).

5.2.4 Sedimentological interpretation

The morphodynamics of the coarse, braided Cimano-Pinzano reach was characterized (Chapter 4) based on a LiDAR-derived DEM from 2005, aerial and

satellite photographs from 1998 to 2011 as well as field observations (Table 5.2). A water-stage time series allowed the morphological changes to be related to the discharge dynamics of the Tagliamento River. More details are given in Chapter 4.

We compared the orientation of the subsurface structures, their sizes and internal structures with the past and present morphology including the formative flow directions. The sedimentological interpretation of the GPR data is particularly challenging for the foolowing reasons:

- ▷ paucity of aerial and satellite data (elevation data are especially crucial to better characterise the morphology and understand the relationship between the different morphological units);
- ▷ the morphology is not necessarily representative of the subsurface structure as illustrated by cut-and-fill processes (the morphology observed at low-discharge is not identical to the high-discharge morphology, see Chapter 4);
- ▷ indications of the age of the imaged subsurface are not available, and therefore it cannot be excluded that the morphology and the subsurface are locally unrelated.

5.3 GPR survey and sedimentological interpretation

The interpolated groundwater levels lie between 0 m–1.4 m below the surface of all the survey areas. The wave velocities vary between 0.09 m/ns and 0.11 m/ns and are comparable in size and variation to earlier findings in similar sediments (e.g., Beres et al., 1999). In the upper 4 m to 5 m they are slightly above 0.10 m/ns. Since the groundwater table is located between 0 m and 1.4 m below the terrain surface, a possible signal from the groundwater surface is practically covered by the strong reflection of the air and ground waves.

Only a selection of the many recorded GPR profiles is presented for illustration purpose.

Table 5.2 – Available data for the morphological analysis. FVG stands for the Autonomous Region of Friuli Venezia Giulia and NERC for U.K. Natural Environment Research Council.

Data	Date	Source
Orthophoto	1998	FVG
Orthophoto	2003	FVG
LiDAR-derived DEM	23 May 2005	NERC
Satellite photograph	May 2005	Quickbird panchromatic
Orthophoto	2007	FVG
Orthophoto	2011	FVG
Aerial satellite photographs	2012/2013 (?)	ESRI World Imagery

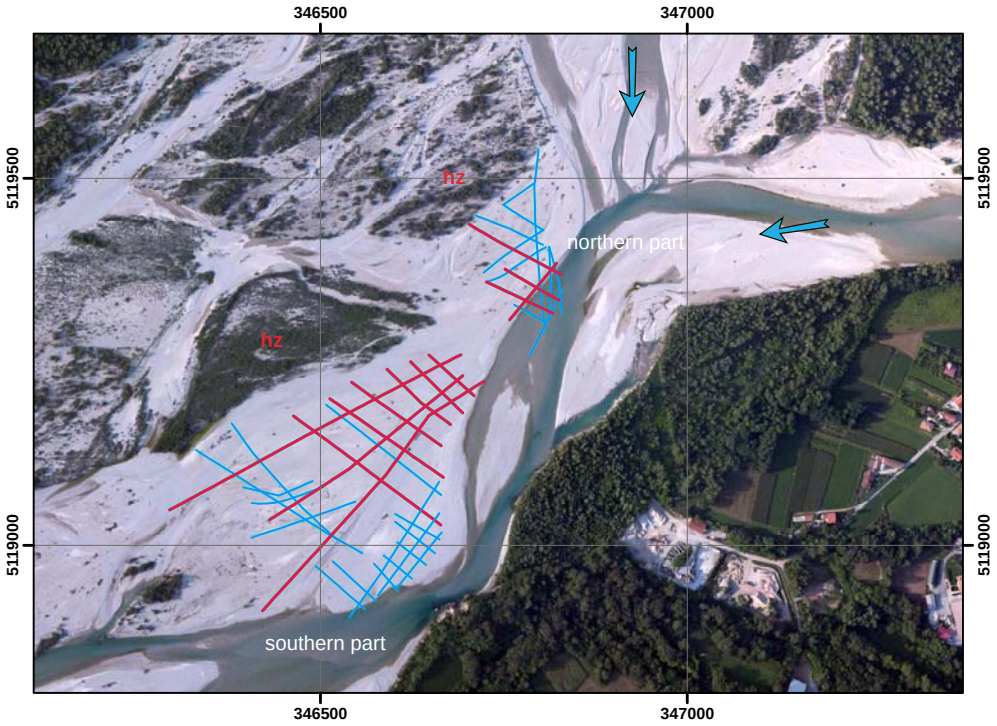

Figure 5.2 – Survey 1: Location of the ground-penetrating radar survey grid superimposed on the aerial photograph from 2013. The red lines indicate the ground-penetrating radar profiles that are displayed in the fence diagrams (Figures 5.3 and 5.4). The blue arrows indicate the general flow direction. The letters *hz* (in red) stand for *high zone*.

5.3.1 Survey 1

Survey 1 consists of a series of large-spaced, perpendicular profiles (trace spacing is 0.25 m, in total 5431 m of GPR data over an area of 325 m × 700 m) on an large flat gravel surface downstream from the Cimano bridge (Figure 5.1 and 5.2). At the survey location, the floodplain is about 925 m wide.

In general, the reflectors on the across-flow profiles are much less continuous than the reflectors on the along-flow profiles (Figure 5.3). Similarly to Beres et al. (1995, 1999), we generally observe more or less continuous dominant low-angle reflectors on the along-flow profiles. Inclined to tangential reflectors dominate on the across-flow profiles. Oblique parallel reflectors with steep dipping on across-flow profiles occasionally present a sub-horizontal dip the main flow direction. This marked difference in the sedimentary structure between across- and along-flow profiles illustrates the difficulty to correctly interpreted tow-dimensional GPR data. Therefore, we focused our analysis on the intersections of GPR profiles and on the structures that could be identified with certainty.

Figure 5.3A displays a fence diagram of some of the GPR profiles from the southern part of survey 1. We identified just below the surface a large storey (400 m × 200 m) that is about 2 m thick and coincide with the extent of the large gravel surface where the survey was performed (Figure 5.3B). The storey is characterised by dominant horizontal to sub-horizontal reflectors on the

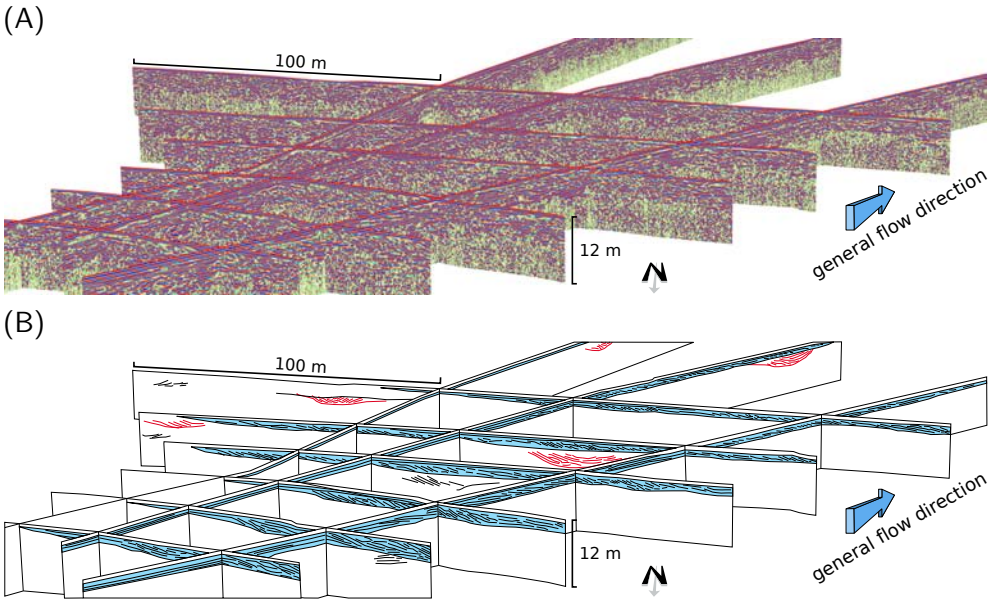

Figure 5.3 – Survey 1, southern part: **(A)** fence diagram of some selected GPR profile from survey 1. **(B)** Interpretation of **(A)**. Trough cross stratified structure are displayed in red, a large storey is displayed in blue ($2 \times$ vertical exaggeration).

along-flow profiles but some reflectors on the western along-flow profile are moderately dipping downstream. The reflectors on the across-flow profiles generally dip strongly toward the west (i.e., toward the high zone). Below the storey most of the reflectors are horizontal to sub-horizontal irrespectively of their orientation within the braidplain. Five large trough cross stratified structures with tangential reflector were identified. Three of them lie immediately below the storey. Interestingly, the troughs are located in the downstream half of the local grid. A few other cross stratified structures were observed but could not be identified as being trough cross stratified.

Figure 5.4A displays a fence diagram of some selected processed GPR profiles of the northern part of the survey 1 located downstream from the Cimano bridge. The top reflectors are mainly horizontal to sub-horizontal in the longitudinal as well as in the perpendicular direction. Below the top reflectors, we interpreted up to four main trough-shaped structures that are nested over an area of 100 m $\times$ 50 m and a depth of 5 m as represented by different colours on Figure 5.4b. The long axis of this trough complex is orientated in the general flow direction. The main reflectors are sub-horizontal and trough-shaped on the profiles parallel to the general flow direction. Some short downstream-dipping reflectors are occasionally visible. On the profiles perpendicular to the general flow direction, inclined and tangential reflectors dominate and generally clearly contrast in their orientations. We found about 5 other such trough in the northern part of survey 1.

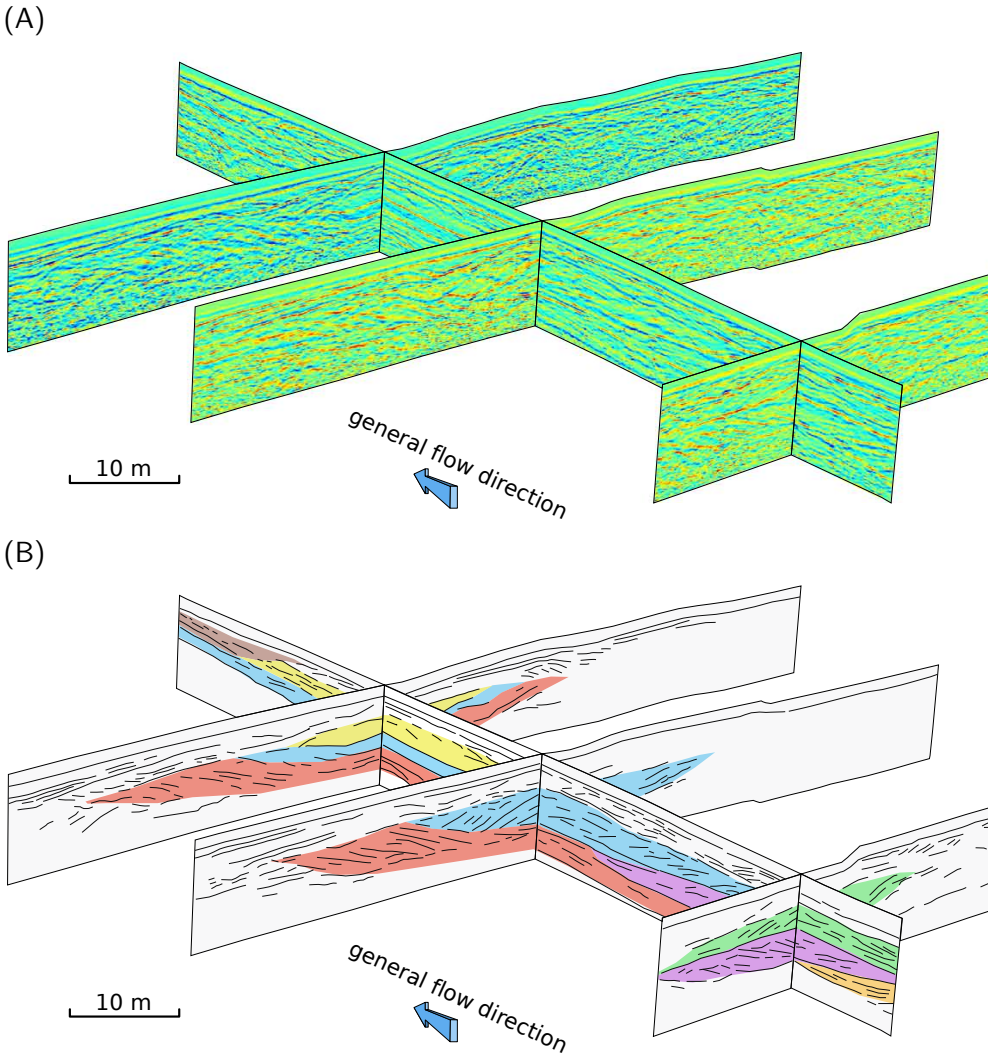

Figure 5.4 – Survey 1, northern part: **(A)** fence diagram of some selected GPR profile from survey 1. **(B)** Interpretation of **(A)** with coloured trough-fills ($2 \times$ vertical exaggeration).

Sedimentological interpretation

The large storey on the southern part of survey 1 is likely to originate from the deposition of a huge large gravel sheet. The south–west orientation of the dipping reflectors within the storey would indicate the propagation direction of the gravel sheet. This direction is in accordance with the present morphology. Furthermore, as the active zone increasingly widens at the southern part of survey 1, we can expect enhanced sediment deposition that could explain the relative high thickness of the storey. Four of the five trough fill deposits are covered by the storey. Their location at the downstream half of the GPR grid could be related to the width of the active zone. A part from the identified trough fills and some obscure cross-bedded reflectors, the rest of the imaged subsurface structure shows horizontal to sub-horizontal pattern.

The fence diagram (Figure 5.4) illustrates how trough fill deposits can stack in three-dimension and form complex structures characterized by different

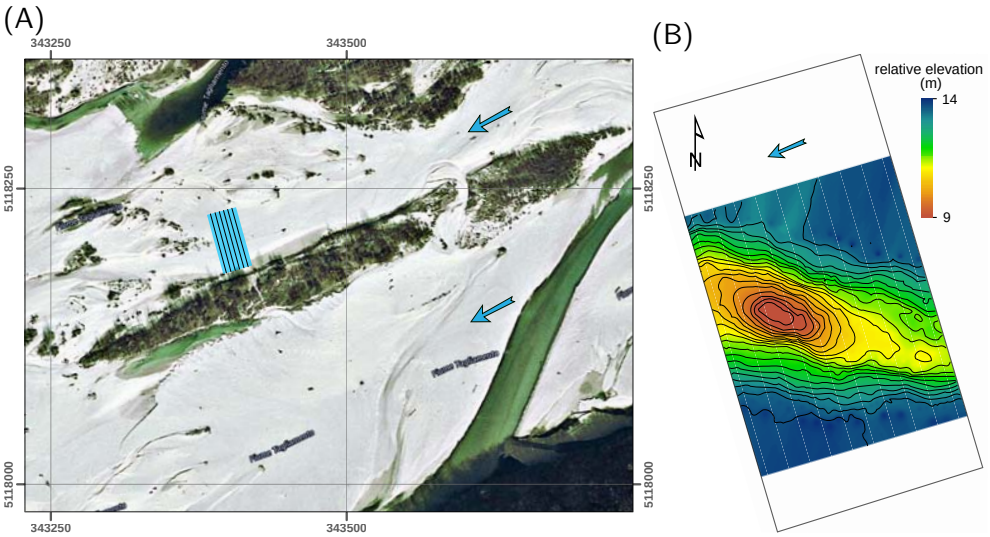

Figure 5.5 – Survey 2: **(A)** Location of the ground-penetrating radar survey grid superimposed on a aerial photograph (Google map). **(B)** Elevation map of the lower reflector R1 (see Figure 5.6B). The contour are traced every 0.25 m. The blue arrows indicate the general flow direction.

angularity of the cross-beds. Such a deposit can be the result of several events.

The northern part of survey 1 lies close to the low-discharge channel confluence downstream the Cimano diaphragm. Therefore, it can be assumed that the trough complex in Figure 5.4 was formed by low-discharge confluence scours. However, the aerial photographs do not support this hypothesis as we always observe on the data that the low-discharge confluence is located at least 60 m upstream the GPR survey area.

At high-discharge, the survey area lies at the confluence of the two branches of the Tagliamento River that flow on both side of the Cimano diaphragm. Therefore, we expect that the trough fills have more chances to be formed by the high-discharge flow than the low-discharge channels and incisions.

5.3.2 Survey 2

Survey 2 (Figures 5.1 and 5.5) is located on top of a flat gravel surface in an active zone at the lower part of the river reach where the floodplain narrows (the survey width corresponds to 8 % of the 650 m width of the floodplain). There, we recorded a grid of parallel across-flow profiles over a 25 m × 50 m area with 0.25-m trace spacing in x- and y-direction. Two perpendicular CMP surveys were performed 4 months later.

On the across-flow profiles of survey 2 (Figure 5.6) a more than 30-m-large trough is identified by its lower reflector (R1 in Figure 5.6B) and its internal structure consisting of inclined reflectors (represented in blue in Figure 5.6B). These reflectors dip in opposite direction away from the thin, vegetated high-zone south to the GPR grid . Some of the inclined reflectors are curved and merge tangentially with the lower reflector. The top of the trough is dominated by long, continuous, horizontal reflectors (represented in violet in Figure 5.6B). The other reflectors are rather sub-horizontal and occasionally discontinuous.

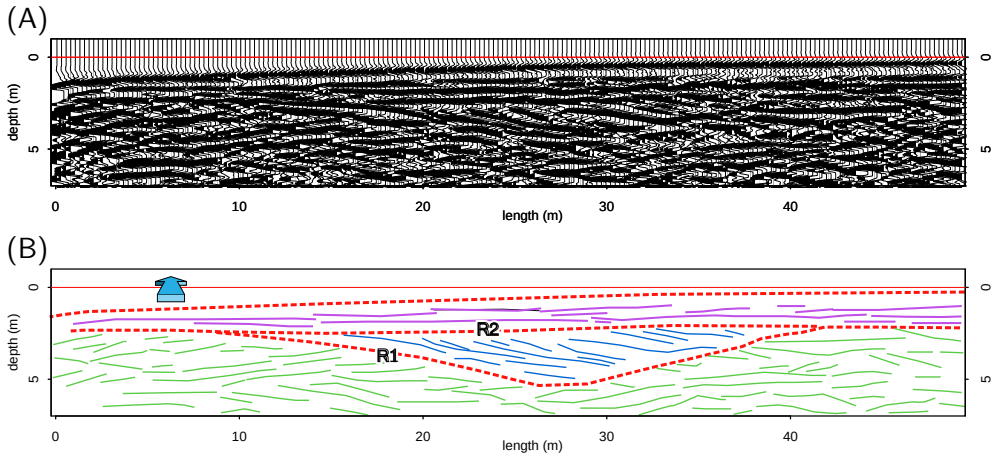

Figure 5.6 – Survey 2: **(A)** Across-flow ground-penetrating radar profile situated 2.5 m to the downstream end of the GPR grid (Figure 5.5A) Water flows in the inward direction. **(B)** interpretation of **(A)**. The red dashed lines indicate the boundaries of three different units.

Figure 5.7A illustrates the relationship between the vertical and horizontal GPR information. The inclined reflectors on across-flow profiles are visible on the horizontal slice as a stripe pattern that contrasts with the surrounding less distinct pattern. The lower reflector of the trough as well as the internal structure were delineated on the horizontal slices and interpolated as surfaces (Figure 5.7B). The surface of the lower reflector is spoon-shaped, 2.5 m deep, 20 m wide and more than 30 m long. This trough has an angle of 50° with the general flow direction. Within the trough, six inclined almost planar surfaces could be delineated. They are parallel to the horizontal length axis of the trough and spaced between 2 m and 5 m. The inclined surfaces decrease in steepness from approximately 50° to 30° from south–east to north–west. Note that during the delineation and interpolation process much of the tangential aspect of the reflector within the trough got lost (compare Figure 5.6 with Figure 5.11). Taking a cross section of the interpolated surfaces along the main axis of the trough, we observed that the internal reflectors are a sub-horizontal to slightly trough-shaped. On top of the trough lies a flat, 2-m-thick unit with sub-horizontal structure. At a depth of about 4 m there is a change in the orientation of the low-angle dipping reflectors around the trough.

Sedimentological interpretation

Finding a relation between the morphology within the survey area and the trough cross stratified structure in the subsurface is difficult. In 1998, the survey area was within a high zone being formed (sparse vegetation, hummocky terrain, absence of low-discharge channel or incision). Between 1998 and today, the survey area always lay within a active zone. Interestingly, the morphology indicates that the shaping flow direction had the same orientation as the trough. As the reflector within the trough are not inclined toward the thin high zone, we can exclude that the trough was formed by the lateral erosion of the high zone from 1998. Because of the configuration of the high zones around the

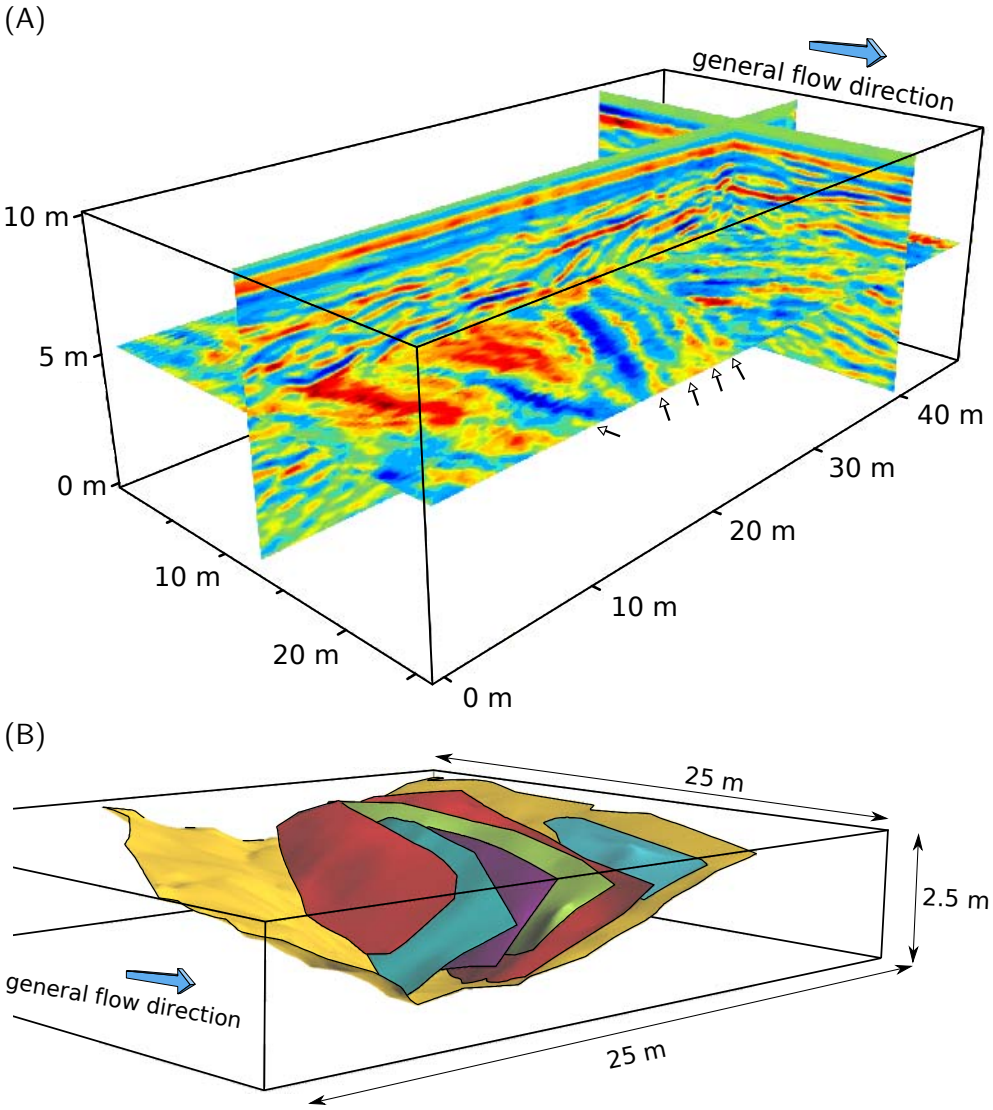

Figure 5.7 – Survey 2: **(A)** Two vertical GPR profiles and one horizontal-slice of survey 2. The arrows indicates indicate the position of the inclined, curved reflectors within the trough structure. **(B)** Surfaces resulting from the delineation and interpolation of the time slices.

survey area, the occurrence of a low-discharge confluence is unlikely. In 2005, we observe that a low-flow incision goes through the location of the trough and that a more than 40-m wide gravel sheet lies partly on the northern corner of the GPR grid. From these puzzling geomorphological observations we can conclude that either the trough was formed before 1998 or the formation of the trough cross stratified structure resulted from an other mechanism than low-discharge confluence.

At least, survey 2 (Figure 5.6) illustrates very well the relationship frequently observed in ancient, coarse, braided deposits between layers of poorly-sorted gravel (GP) and trough fill deposits consisting of alternating open-framework gravel (OW)-bimodal gravel (BM) couplets: a layer of GP is generally found on top of a trough fill. From a sedimentological point of view, we would interpret

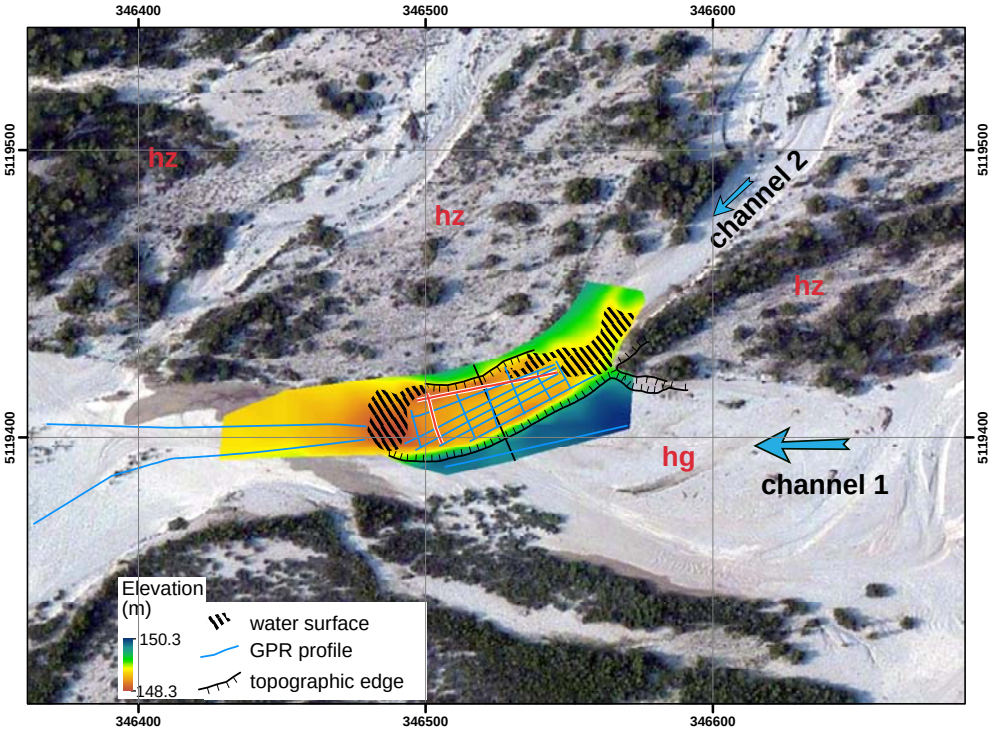

Figure 5.8 – Survey 3: Position of ground-penetrating radar profiles is superimposed on the surveyed topography (background: ESRI World Imagery). The two red lines indicate the across-flow and along-flow profiles displayed in Figures 5.9 and 5.10. The blue arrows indicate the main flow directions at high-discharge. The letters *hz* (in red) stand for *high zone* and show the location of the high zone that is dessicated by a drainage gully network. The letters *hg* (in red) stand for *higher-lying gravel surface*.

the trough cross stratified structure as being a scour fill covered by a remnant of gravel sheet and embedded in a matrix of gravel sheet relics.

5.3.3 Survey 3

A GPR grid was surveyed within a local depression[1] at the confluence of two channels close to a high zone complex (Figures 5.1 and 5.8). The extent of the GPR grid (55 m × 20 m) was limited by two ponds located at the upstream and downstream ends of the depression. The spacing between along-flow profiles is about 4 m and between across-flow profiles 10 m. Three additional along-flow GPR profiles were surveyed outside the depression to allow the comparison of the subsurface structure below the depression and around.

Three dominant reflectors were identified on the GPR profiles, delineated (Figures 5.9 and 5.10), and then interpolated as surfaces (Figures 5.11 and 5.12). The first reflector (R1) lies up to 1.5 m below the floor of the depression and its extent seems to coincide with the extent of the depression (Figure 5.12A). Furthermore, R1 is spoon shaped and is oriented is parallel to the depression. Short, north–west downward dipping reflectors are barely visible on some profiles between the ground-wave and R1 (Figure 5.10)

[1] A long hollow of limited extent

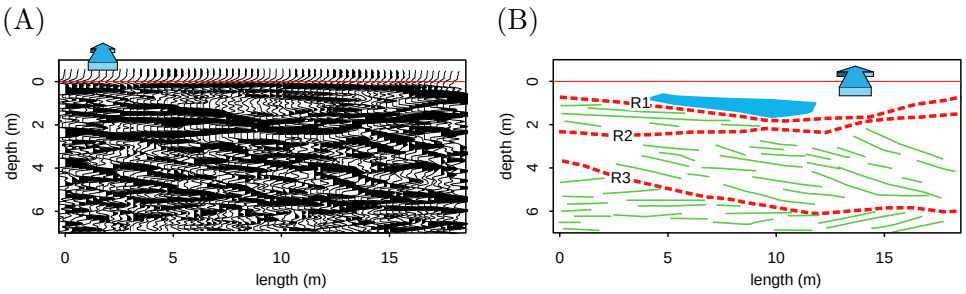

Figure 5.9 – Survey 3: **(A)** Across-flow ground-penetrating radar profile and **(B)** the interpreted reflectors (the blue area indicate a zone of poor reflection).

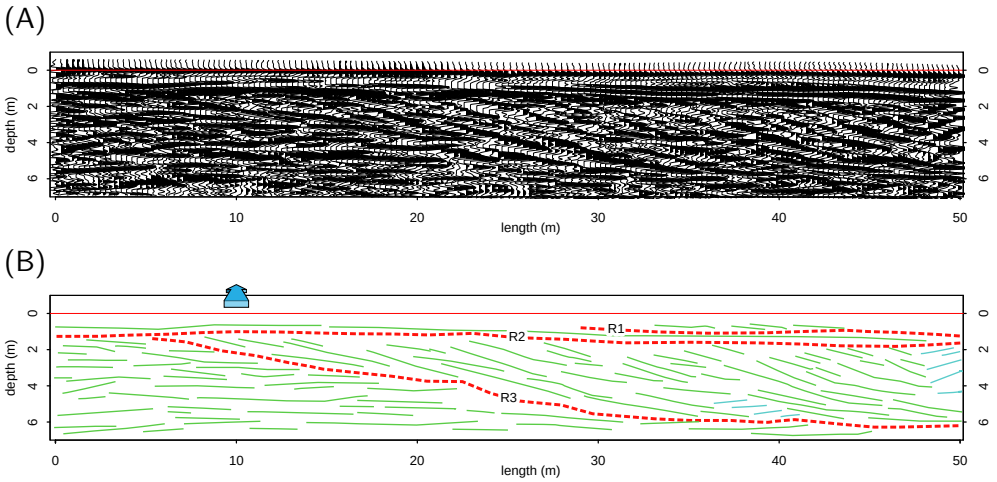

Figure 5.10 – Survey 3: **(A)** Along-flow ground-penetrating radar profile and **(B)** the interpreted reflectors.

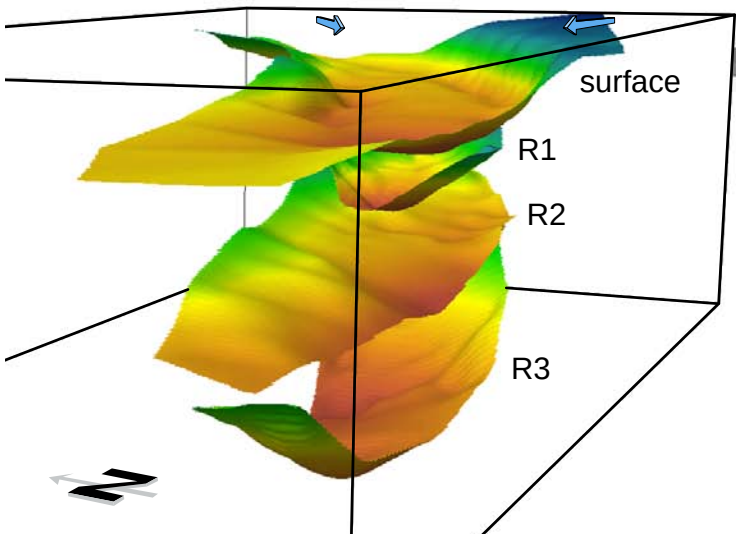

Figure 5.11 – Survey 3: Perspective view of the surveyed topography and of the three interpolated reflectors R1, R2 and R3. The blue arrows indicate the flow directions ($5 \times$ vertical exageration).

The northern part of reflector R2 is very close to R1. R2 is rather sub-horizontal

and gently dips toward the south. The internal structure between R1 and R2 consists of gentle sub-horizontal reflectors (absence of cross-bedding). The reflector R2 is clearly much larger than the depression and extends beyond the southern boundary of the depression (Figure 5.12B).

The 5-m-deep, spoon-shaped reflector R3 is the most striking reflector. It strongly dips downward toward the north–west (i.e., toward the high zone) and dips upstream shortly downstream from the depression. The internal structure between R2 and R3 corresponds to strongly downward inclined reflectors oriented toward north–west. The southern boundary of R3 seems to extend beyond the depression but it is unclear if the northern boundary of R3 coincides with the edge of the high zone (Figure 5.12C).

Sedimentological interpretation

Confluence As the depression floor is relatively flat and the depression is located at the confluences of two channels[2], we expected the presence of a filled (confluence) scour below the depression floor. The depression is delimited on the north by a sparsely vegetated high zone (indicated by the letters *hz* on Figures 5.8,5.12 and 5.13) and on the south by a higher-lying gravel surface (indicated by the letters *hg* on Figures 5.8,5.12 and 5.13) that is higher than the opposite high-zone. The floor of the depression at the survey location is slightly higher in the middle (Figures 5.8 and 5.11). The largest channel of the confluence (called thereafter *channel 1*) is about 80 m wide and is directly connected to the active zone downstream from the Cimano bridge. Depending on the discharge ratio between the left and the right branches of the Tagliamento River at the Cimano diaphragm, channel 1 can be directly feed by the left branch of the Tagliamento river (see Figure 5.1). The small channel (called thereafter *channel 2*) is about 16 m wide and incises into the high zone. Channel 2 is fed by water and sediment from the right branch of the Tagliamento River at the Cimano diaphragm. The confluence angle is about 50°.

Evolution of the morphology Figure 5.13 shows the evolution of the site from 2003 to 2013. The high zone formed between 1998 and 2003, presumably from the incision of the active zones of the braidplain (Chapter 4). In 2003, a large gravel sheet (*gs* in Figure 5.13) lies partly at the edge of the high zone. Between 2003 and 2005, the high zone experienced lateral erosion of its southern edge. In 2005, a (new) gravel sheet lies about 40 m away from the high zone edge forming a channel, i.e., channel 1, that is 1.6 m deeper than the high zone (according to the LiDAR-derived DEM). A drainage gully network develop and incises the high zone. In 2007, channel 2 is already formed and it deposited a sediment lobe into a 10-m-wide incision. The large gravel is slightly eroded and smaller gravel sheets (*gs* in Figure 5.13) migrate through channel 1. In 2011, the higher-lying gravel surface (*hg* in Figure 5.13) and the depression are already developed. Small gravel sheets originating from channel 1 and 2

[2] As stated in Chapter 4, *channel* describes here rather elongated depressions that have been shaped by flowing water (physical/geometrical definition that is water-stage independent)

migrate through the confluence. In 2013 only a gravel sheet originating from channel 2 is identifiable. Furthermore, a pond is located just at the intersection between channel 2 and an incised small channel within channel 1. At the survey time (2014), the higher-lying gravel surface is about 0.2 m higher than the high zone indicating a net sediment deposition within channel 1 between 2005 and 2014.

Comparing the surfaces of the three main reflectors and their associated internal structures with the evolution of the morphology (erosion and deposition), we formulate the following hypotheses that are *conditional to the available data*.

- ▷ The reflector R3 is the erosional lower-bounding surface resulting from the scouring of the high zone between 1998 and 2005 at the interface between the large gravel and the edge of the high zone The extent of R3 that coincides with the high zone edge, the orientation of the internal reflector toward the north–west, and the high depth of R3 requiring an important erosion process support this hypothesis.
- ▷ The reflector R2 corresponds to the erosional surface formed between 2003 and 2005 during the incision of channel 1. This would explain why R2 have its maximum depth located at the centre of channel 1 (Figure 5.12). After 2005, aggradation of the bed of channel 1 occurred, possibly trough by the migration of gravel sheets. Remnants of gravel sheets could correspond to the sub-horizontal reflectors between R1 and R2.
- ▷ The reflector R1 was formed during a flood event by the scouring of the floor of the depression by the flow originating from channel 2. When the discharge decreased, sediment transport stalled, filling slightly the scoured channel. A fast sediment deposition may explain why the floor of the depression is higher in the middle.

We rejected the hypothesis that one of the reflector surface was formed by a flow confluence for the following reasons. (i) The depression is not the result of a partly-filled confluence scour but the erosion of the higher-lying gravel surface by channel 2. The more than 1-m-high edge between the floor of the depression and the top of the higher-lying gravel surface is very steep. The steepness rather results from the lateral erosion of the higher-lying gravel surface by the channel 2 than from the advancement of the higher-lying zone into the depression that would result in an avalanche face. (ii) Between 2005 and 2007 the bed discordance between channel 1 and 2 would prevent the formation of a confluence scour (e.g., Best and Rhoads, 2008). (iii) Between 2007 and today we observe that the morphological activity of channel 2 dominates that of channel 1.

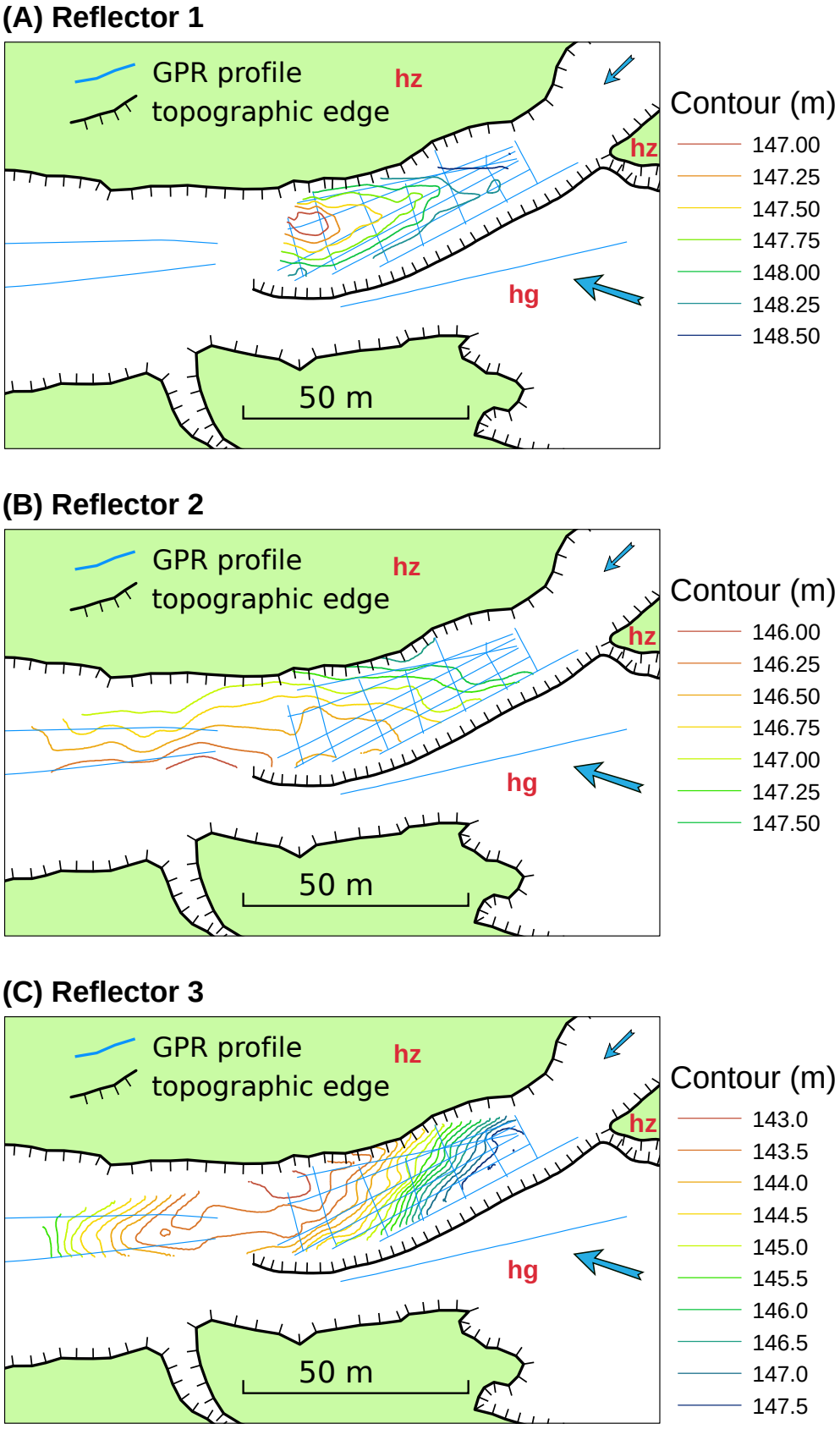

Figure 5.12 – Survey 3: **(A)**–**(C)** contour lines of the interpolated surfaces from the ground-penetrating radar reflectors superimposed on a simplified representation of the morphology. The blue arrows indicate the main flow directions at high-discharge. The letters *hz* (in red) stand for *high zone*, *hg* (in red) for *higher-lying gravel surface* and *gs* (in red) for *gravel sheet*.

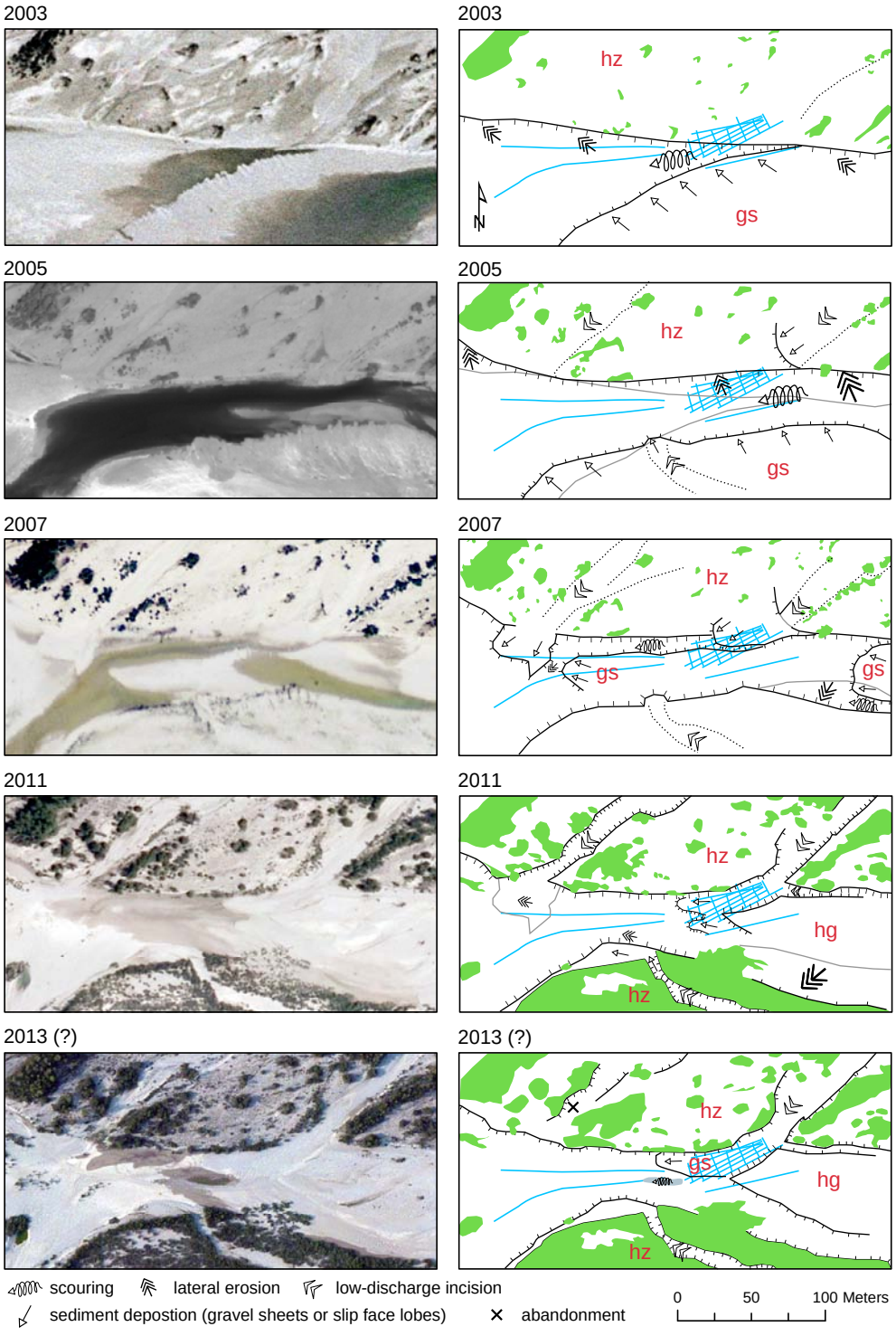

Figure 5.13 – Survey 3: Evolution of the morphology from 2003 to 2013. The blue liens correspond to the ground-penetrating radar profiles. The letters *hz* (in red) stand for *high zone*, *hg* (in red) for *higher-lying gravel surface* and *gs* (in red) for *gravel sheet*.

5.4 Conclusion

The GPR surveys revealed the presence of several cross-bedded troughs within the braidplain of the Tagliamento River. They are about 30 m wide and more than 50 m long. The cross bedding is slightly curved and partly tangential to the trough-shaped lower-bounding surface. In along-flow section the bedding is less inclined than in across-flow section. Above the trough structure lies always a horizontal to sub-horizontal unit. These findings agree very well with observations made in vertical outcrops of Pleistocene coarse, braided river deposits in northeast Switzerland (Chapter 2, Siegenthaler and Huggenberger, 1993; Huggenberger and Regli, 2006).

In the southern part of survey 1, the deposits from a huge gravel sheet were identified by their large extent and planar cross-bedded reflectors. All the trough fills within this area lie below the lower boundary of the gravel sheet deposits. Note, however, that the gravel sheet deposit has a low preservation potential as it will be likely reworked by the river in a near future.

Relating the subsurface structure with the morphology is very challenging. We assumed that the cross-bedded troughs were formed by flow turbulence either in relation to the topography of gravel sheets or in relation to high-discharge flow confluence. At one survey location the evolution of the morphology compared with the interpreted GPR data suggested that scour fills can also form at the interface between a gravel sheet and a high zone. If this hypothesis is correct, an alternation of aggrading–degrading phases would enhance the formation of high zones and therefore of scour fills. The hypotheses stated in this study must be further investigated. Furthermore, imaging the subsurface of different reaches carefully selected according to their morphodynamics could throw light on the impact of the aggradation rate and lateral mobility of the high zone on the subsurface.

Large scale surveys with a large spacing between the profiles are difficult to interpret because of, among others, the anisotropy of the subsurface structure resulting in different along-flow and across-flow sections. However, the interpretation could be assisted by conditioning a numerical subsurface model to the GPR data.

Acknowledgements

Special thanks go to H. Dresman for constructive comments.

References

Asprion U. and **Aigner T.** (1997) Aquifer architecture analysis using ground-penetrating radar: Triassic and Quaternary examples (S. Germany). *Environmental Geology*, **31**(1–2): 66–75.
doi: 10.1007/s002540050165

Asprion U. and **Aigner T.** (1999) Towards realistic aquifer models: three-dimensional georadar surveys of Quaternary gravel deltas (Singen Basin, SW Germany). *Sedimentary Geology*, **129**(3–4): 281–297.
doi: 10.1016/s0037-0738(99)00068-8

Bayer P., Huggenberger P., Renard P. and **Comunian A.** (2011) Three-dimensional high resolution fluvio-glacial aquifer analog: Part 1: Field study. *Journal of Hydrology*, **405**(1–2): 1–9.
doi: 10.1016/j.jhydrol.2011.03.038

Beres M., Green A., Huggenberger P. and **Horstmeyer H.** (1995) Mapping the architecture of glaciofluvial sediments with three-dimensional georadar. *Geology*, **23**(12): 1087–1090.
doi: 10.1130/0091-7613(1995)023<1087:MTAOGS>2.3.CO;2

Beres M., Huggenberger P., Green A.G. and **Horstmeyer H.** (1999) Using two- and three-dimensional georadar methods to characterize glaciofluvial architecture. *Sedimentary Geology*, **129**(1–2): 1–24.
doi: 10.1016/S0037-0738(99)00053-6

Best J.L. and **Rhoads B.L.** (2008) Sediment Transport, Bed Morphology and the Sedimentology of River Channel Confluences, In: *River Confluences, Tributaries and the Fluvial Network* (Eds. S.P. Rice, A.G. Roy and B.L. Rhoads), John Wiley & Sons, Ltd, 45–72.
doi: 10.1002/9780470760383.ch4

Booth A., Clark R. and **Murray T.** (2010) Semblance response to a ground–penetrating radar wavelet and resulting errors in velocity analysis. *Near Surface Geophysics*, **8**(3): 235–246.
doi: 10.3997/1873-0604.2010008

Bridge J.S. and **Lunt I.A.** (2006) Depositional Models of Braided Rivers, In: *Braided Rivers* (Eds. G.H. Sambrook Smith, J.L. Best, C.S. Bristow and G.E. Petts), Blackwell Publishing Ltd., Ch. 2, 11–50.
doi: 10.1002/9781444304374.ch2

Dam R.L.V. and **Schlager W.** (2000) Identifying causes of ground-penetrating radar reflections using time-domain reflectometry and sedimentological analyses. *Sedimentology*, **47**(2): 435–449.
doi: 10.1046/j.1365-3091.2000.00304.x

Dix C.H. (1955) Seismic velocities from surface measurements. *Geophysics*, **20**(1): 68–86.
doi: 10.1190/1.1438126

Dujardin J.R. and **Bano M.** (2013) Topographic migration of GPR data: Examples from Chad and Mongolia. *Comptes Rendus Geoscience*, **345**(2): 73–80.
doi: 10.1016/j.crte.2013.01.003

Ernenwein E.G. and **Kvamme K.L.** (2008) Data processing issues in large-area GPR surveys: correcting trace misalignments, edge discontinuities and striping. *Archaeological Prospection*, **15**(2): 133–149.
doi: 10.1002/arp.331

Grimm R.E., Heggy E., Clifford S., Dinwiddie C., McGinnis R. and **Farrell D.** (2006) Absorption and scattering in ground-penetrating radar: Analysis of the Bishop Tuff. *Journal of Geophysical Research: Planets*, **111**(E6).
doi: 10.1029/2005je002619

Heinz J. and **Aigner T.** (2003) Three-dimensional GPR analysis of various Quaternary gravel-bed braided river deposits (southwestern Germany). *Geological Society, London, Special Publications*, **211**(1): 99–110.
doi: 10.1144/gsl.sp.2001.211.01.09

Heinz J., Kleineidam S., Teutsch G. and **Aigner T.** (2003) Heterogeneity patterns of Quaternary glaciofluvial gravel bodies (SW-Germany): application to hydrogeology.

Sedimentary Geology, **158**(1–2): 1–23.
doi: 10.1016/S0037-0738(02)00239-7

Huber E. and **Huggenberger P.** (2015) Morphological perspective on the sedimentary characteristics of a coarse, braided reach: Tagliamento River (NE Italy). *Geomorphology*, **248**: 111–124.
doi: doi:10.1016/j.geomorph.2015.07.015

Huggenberger P. (1993) Radar facies: recognition of facies patterns and heterogeneities within Pleistocene Rhine gravels, NE Switzerland. *Geological Society, London, Special Publications*, **75**(1): 163–176.
doi: 10.1144/GSL.SP.1993.075.01.10

Huggenberger P. and **Aigner T.** (1999) Introduction to the special issue on aquifer-sedimentology: problems, perspectives and modern approaches. *Sedimentary Geology*, **129**(3–4): 179–186.
doi: 10.1016/S0037-0738(99)00101-3

Huggenberger P., Hoehn E., Beschta R. and **Woessner W.** (1998) Abiotic aspects of channels and floodplains in riparian ecology. *Freshwater Biology*, **40**(3): 407–425.
doi: 10.1046/j.1365-2427.1998.00371.x

Huggenberger P., Meier E. and **Pugin A.** (1994) Ground-probing radar as a tool for heterogeneity estimation in gravel deposits: advances in data-processing and facies analysis. *Journal of Applied Geophysics*, **31**(1–4): 171–184.
doi: 10.1016/0926-9851(94)90056-6

Huggenberger P. and **Regli C.** (2006) A Sedimentological Model to Characterize Braided River Deposits for Hydrogeological Applications, In: *Braided Rivers* (Eds. G.H. Sambrook Smith, J.L. Best, C.S. Bristow and G.E. Petts), Blackwell Publishing Ltd., Ch. 3, 51–74.
doi: 10.1002/9781444304374.ch3

Jol H.M. (1995) Ground penetrating radar antennae frequencies and transmitter powers compared for penetration depth, resolution and reflection continuity. *Geophysical Prospecting*, **43**(5): 693–709.
doi: 10.1111/j.1365-2478.1995.tb00275.x

Jussel P. (1992) Modellierung des Transports gelöster Stoffe in inhomogenen Grundwasserleitern. Ph.D. thesis, ETH Zürich, nr. 9663.

Jussel P., Stauffer F. and **Dracos T.** (1994) Transport modeling in heterogeneous aquifers: 1. Statistical description and numerical generation of gravel deposits. *Water Resources Research*, **30**(6): 1803–1817.
doi: 10.1029/94WR00162

Klingbeil R., Kleineidam S., Asprion U., Aigner T. and **Teutsch G.** (1999) Relating lithofacies to hydrofacies: outcrop-based hydrogeological characterisation of Quaternary gravel deposits. *Sedimentary Geology*, **129**(3–4): 299–310.
doi: 10.1016/S0037-0738(99)00067-6

Kostic B. and **Aigner T.** (2007) Sedimentary architecture and 3D ground-penetrating radar analysis of gravelly meandering river deposits (Neckar Valley, SW Germany). *Sedimentology*, **54**(4): 789–808.
doi: 10.1111/j.1365-3091.2007.00860.x

Kruse S.E. and **Jol H.M.** (2003) Amplitude analysis of repetitive GPR reflections on a Lake Bonneville delta, Utah, In: *Ground Penetrating Radar in Sediments* (Eds. C. Bristow and H. Jol), 211, Geological Society of London, 287–298.
doi: 10.1144/gsl.sp.2001.211.01.23

Lehmann F. and **Green A.G.** (2000) Topographic migration of georadar data: Implications for acquisition and processing. *Geophysics*, **65**(3): 836–848.
doi: 10.1190/1.1444781

Lunt I.A., Bridge J.S. and **Tye R.S.** (2004) A quantitative, three-dimensional depositional model of gravelly braided rivers. *Sedimentology*, **51**(3): 377–414.
doi: 10.1111/j.1365-3091.2004.00627.x

Oimoen M. (2000) An effective filter for removal of production artifacts in U.S. Geological Survey 7.5-minute digital elevation models, In: Proceedings of the Fourteenth International Conference on Applied Geologic Remote Sensing, 06–08 November, Las Vegas, Nevada (Veridian ERIM International, Ann Arbor, Michigan) 311–319.

Pearson R. (2002) Outliers in process modeling and identification. *IEEE Transactions on Control Systems Technology*, **10**(1): 55–63.
doi: 10.1109/87.974338

Polzehl J. and **Spokoiny V.** (2006) Local Likelihood Modeling by Adaptive Weights Smoothing. *Probability Theory and Related Fields*, **135**: 335–362.

Polzehl J. and **Tabelow K.** (2007) Adaptive Smoothing of Digital Images: The R Package adimpro. *Journal of Statistical Software*, **19**(1): 1–17.

Sabbione J.I. and **Velis D.** (2010) Automatic first-breaks picking: New strategies and algorithms. *Geophysics*, **75**(4): 67–76.

Schmelzbach C. and **Huber E.** (2015) Efficient Deconvolution of Ground-Penetrating Radar Data. *Geoscience and Remote Sensing, IEEE Transactions on*, **PP**(99): 1–9.
doi: 10.1109/TGRS.2015.2419235

Schmelzbach C., Scherbaum F., Tronicke J. and **Dietrich P.** (2011) Bayesian frequency-domain blind deconvolution of ground-penetrating radar data. *Journal of Applied Geophysics*, **75**(4): 615–630.
doi: 10.1016/j.jappgeo.2011.08.010

Siegenthaler C. and **Huggenberger P.** (1993) Pleistocene Rhine gravel: deposits of a braided river system with dominant pool preservation. *Geological Society, London, Special Publications*, **75**(1): 147–162.
doi: 10.1144/GSL.SP.1993.075.01.09

Slomka J. and **Eyles C.** (2013) Characterizing heterogeneity in a glaciofluvial deposit using architectural elements, Limehouse, Ontario, Canada. *Canadian Journal of Earth Sciences*, **50**(9): 911–929.
doi: 10.1139/cjes-2013-0020

Smith G.S., Best J., Bristow C. and **Petts G.** (2006) Braided Rivers: Where have we Come in 10 Years? Progress and Future Needs, In: *Braided Rivers* (Eds. G.H. Sambrook Smith, J.L. Best, C.S. Bristow and G.E. Petts), Wiley-Blackwell, 1–10.
doi: 10.1002/9781444304374.ch1

Storz-Peretz Y. and **Laronne J.B.** (2013) Morphotextural characterization of dryland braided channels. *Geological Society of America Bulletin*, **125**(9-10): 1599–1617.
doi: 10.1130/b30773.1

Tillard S. (1995) Analysis of GPR data: wave-propagation velocity determination. *Journal of Applied Geophysics*, **33**(1–3): 77–91.
doi: 10.1016/0926-9851(94)00023-h

Yilmaz O. (2001) *Seismic Data Analysis*: 2nd Edition. 10 of Investigations in Geophysics. Society Of Exploration Geophysicists, Tulsa, USA.
ISBN:1560800941

6 Geophysical stereology: from 2D GPR data to 3D subsurface structure

> *The relationship between a problem and a method should be discussed from the perspective of a problem, and not the method. Doing otherwise actually causes more harm than good in the long run, because like all 'hand outs', it leaves the students incapable of fending (i.e., thinking) for themselves.*
>
> **Z. Michalewicz & D.B. Fogel** (2004) How to Solve It: Modern Heuristics. Springer, 2004, 554 pp. ISBN: 978-3-540-22494-5

Abstract Two-dimensional geophysical data raise a stereological issue because they yield only apparent dimensions of three-dimensional subsurface structures. In this contribution, the stereological problem is modelled with a Bayesian approach aiming to quantify the posterior uncertainty on the three-dimensional subsurface structure based on a two-dimensional geophysical data. In geostatistical terms, the prior is formulated with a three-dimensional marked point process (MPP), also called object-based model, that mimics the depositional and erosional history of the sediment deposits. Because the complexity of the MPP prevents from calculating analytically the posterior, iterative sampling of the posterior is required. Furthermore, an analytically intractable normalisation constant hinders the joint sampling of realisations and parameters of the MPP. The parameters of the MPP are therefore estimated by their maximum a posteriori (MAP) using a novel approximate Bayesian computation (ABC) approach based on Bayesian linear regression in the canonical correlation analysis (CCA) space. The posterior given the MAP

E. Huber (2017) *Incorporating sedimentological observations, hydrogeophysics and conceptual knowledge to constrain 3D numerical heterogeneity models of alluvial systems.* Ph.D. thesis, Applied and Environmental Geology, University of Basel, Switzerland, 192 pp.

estimate of the MPP parameters is then sampled with Markov chain Monte Carlo (MCMC). However, the likelihood cannot be easily calculated and there ABC MCMC based on the extended Metropolis update is used. The method is applied to a ground-penetrating radar (GPR) data acquired on a coarse, braided reach of the Tagliamento River (northeast Italy).

6.1 Introduction

Geophysical surveys are used across disciplines to gain a better understanding of the subsurface structure. In oil and gas exploration and production, costly three-dimensional and even time-lapse (four-dimensional) seismic surveys are used to characterise reservoir structure as well as constrain variation in petrophysical properties (Dubrule, 2003; Caers, 2005; Avseth et al., 2010).

In many other applications such as in characterisation of subsurface heterogeneity (Huber and Huggenberger, 2015b), groundwater (Mahmoudzadeh et al., 2012) or geothermal systems (Hermans et al., 2012), for cost reasons, geophysical measurements are often limited to a set of survey lines, i.e., a set of two-dimensional geophysical data. In essence, this raises a *stereological* issue because the three-dimensional subsurface properties can only be inferred from two-dimensional data (Howard and Reed, 2010; Baddeley and Vedel Jensen, 2004). The structural characteristics (e.g., shape, size, texture) of two-dimensional geophysical surveys are only apparent properties of the three-dimensional subsurface. These apparent properties can drastically change depending on the position and orientation of the survey lines (Beres et al., 1995).

Three-dimensional subsurface structure modelling based on two-dimensional geophysical data (e.g., Bristow and Jol, 2003; Jol, 2009) generally ignores the stereological bias. This bias consists in an over-representation of large structures in two-dimensional data because large structures are more frequently imaged than small structures (Lantuejoul, 2002). Furthermore, conditioning a three-dimensional model to two-dimensional data is not trivial (Lantuejoul, 2002; Hauge et al., 2007). For example, an incorrect approach is to first place structures/objects that fit the two-dimensional observations and then populate the remaining structures/objects in the domain as in Rauber et al. (1998). This results in placing disproportionally larger structures/objects near the observations and leads to inconsistent probabilistic models (Caers, 2012).

This study aims to quantify the three-dimensional subsurface structure from a two-dimensional ground-penetrating radar (GPR) data using a latent variable model and accounting for the stereological issue in a Bayesian framework. The objective is not to reproduce the data but to condition the subsurface structure to the data for further investigation (e.g., subsurface flow and transport simulation). The data consist of a set of curves on the vertical plane that corresponds

to subsurface structures interpreted from GPR data. The Bayesian approach is needed because for real-field application requiring complex objects, data and model assumptions, the analytical solutions typical for stereology (e.g., Hedin, 2011) no longer apply.

Turning geological prior knowledge into a quantitative Bayesian prior is challenging. In this work, a new stochastic model of the subsurface is presented that consists in a three-dimensional marked point process (MPP) with separable xy- and z-dimensions, and independent marks. This MPP simulates the depositional and erosional history of coarse, braided river deposits and reflects our conceptual understanding of braided river systems. The data are simulated by vertical sections of the MPP realisations that are filtered to account for (i) erosion of older structures by younger, (ii) smooth imaging of the subsurface structures by GPR, and (iii) ability of the geophysicist to interpret the structures.

The quantification of the posterior in a Bayesian framework faces three main challenges. (i) The complexity of the MPP prevents the analytical calculation of the posterior. (ii) The likelihood function cannot be easily computed because it involves a set of l^o observed curves and a set of l simulated curves with l not necessarily equal to l^o. (iii) The normalisation constant of the prior is analytically intractable and depends on the MPP parameters prohibiting parameter inference with classical Markov chain Monte Carlo (MCMC).

Stereological problems are usually solved by means of analytical equations (Glaser and Glaser, 2000; Russ and Dehoff, 2000; Baddeley and Vedel Jensen, 2004). Such equations make a large amount of assumptions that are untenable for the MPP that has not a simple analytical expression, hence Monte Carlo (MC) sampling is required. A MCMC approach is therefore used to sample the posterior. However, classical MCMC approaches require the computation of the likelihood function that cannot be here easily computed (second challenge). Combining MCMC with approximate Bayesian computation (ABC) allows the computation of the likelihood function to be circumvented. But, this approach does not allow the simultaneous estimation of the model parameters (third challenge). To overcome this issue, the model parameters are first estimated with a novel regression-based ABC approach, and then the posterior is sampled with MCMC. While the focus and application of this study are on coarse, braided river systems, the presented method can be used as a template for conditioning stochastic latent models with analytical intractable prior and likelihood functions that are difficult to compute.

First, the particular case study is presented, namely, the GPR data, the associated stereological issue and the MPP. Next, the stereological problem is formulated in a generic Bayesian framework. Original approaches that tackle the challenges associated with the posterior sampling are presented. Finally, a real field application with the GPR data is presented. The algorithms used in the MCMC sampling are provided along with the text.

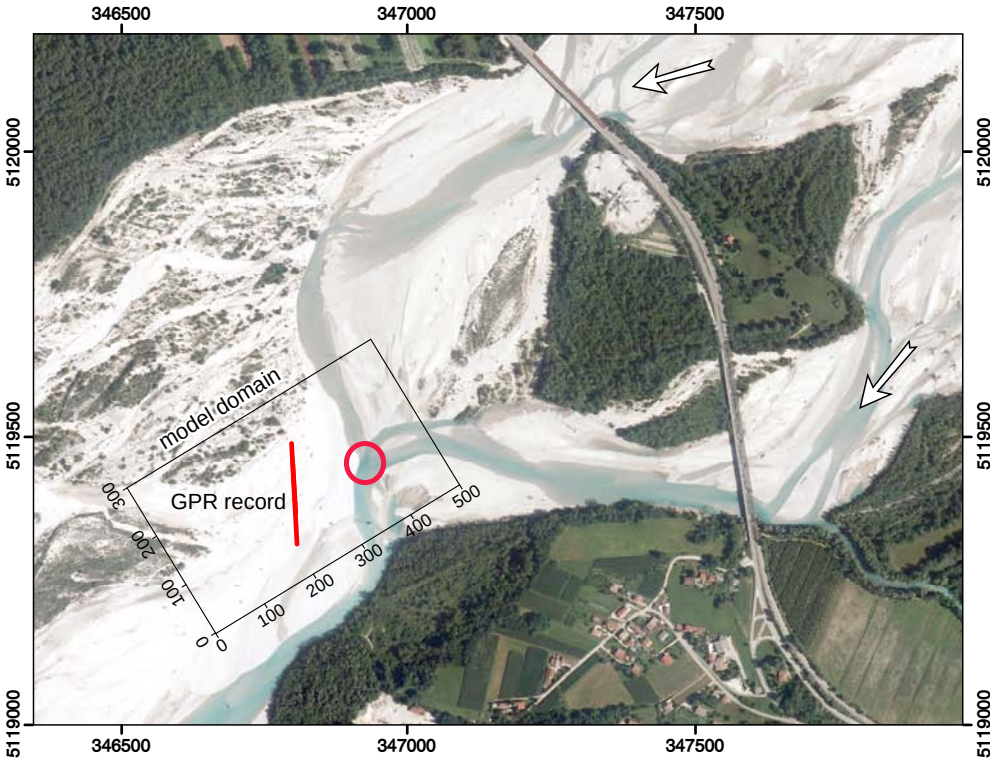

Figure 6.1 – Coarse, braided reach of the Tagliamento River near Cimano at low discharge. The segment indicates the position of the GPR data, the circle the position of a low-discharge confluence scour, and the two arrows the river flow direction. The rectangle represents the model boundary of the marked point process

6.2 Case study

6.2.1 Observations

Ground-Penetrating Radar data

A two-dimensional GPR data was acquired within a coarse, braided reach of the Tagliamento River (northeast Italy) with a PulseEkko Pro GPR system with two unshielded 100-MHz antennas (Fig. 6.1). The topography of the GPR data was surveyed with a total station (South, NTS 355L). The penetration depth of the GPR signal was of the order of 7 m with a resolution of 0.2 m.

The GPR data (Fig. 6.2) was processed to compensate for signal amplitude attenuation with depth and to increase the signal-to-noise ratio. Then, a time-to-depth conversion with constant wave velocity (0.10 m/ns) was applied to the processed GPR data.

Sedimentological Interpretation

The sedimentological interpretation of the GPR data (Fig. 6.2) relies on the delineation of distinct radar facies (Beres and Haeni, 1991). Their delineation is based on a sedimentological understanding of the depositional environment. The radar facies are defined by (i) continuity of the dominant reflectors,

(ii) differences of reflection patterns, and (iii) angular unconformity between the reflectors that indicates an erosion surface or the superposition of two structures with different textures (Neal, 2004). Our sedimentological conceptual understanding is derived from the observation of ancient/analogue deposits of coarse, braided river (Huggenberger and Regli, 2006). Field observations of gravel-pit exposures of Pleistocene coarse, braided deposits in Switzerland show that the main types of sedimentological elements for coarse, braided river systems are (i) horizontal to sub-horizontal layers of poorly-sorted gravel (GP) deposited by gravel sheets (also called unit bars, Hicks et al., 2002; Huber and Huggenberger, 2015a) and (ii) scour fills mainly consisting of highly-permeable open-framework–bimodal gravel (OW–BM) cross-beds (Siegenthaler and Huggenberger, 1993; Jussel et al., 1994; Beres et al., 1995, 1999; Klingbeil et al., 1999; Heinz et al., 2003; Huggenberger and Regli, 2006). On the GPR data trough-shaped reflectors are identified to be the erosional lower-bounding surfaces of scour fills and delineated (Fig. 6.2). The age hierarchy of the scour fills is inferred following the rule 'newer structures erode older structures'. Additionally, a few sub-horizontal reflectors are interpreted as the interface between layers of GP (Fig. 6.2).

Stereological Issue

The interpretation of the GPR data is biased against small-scale structures because small-scale structures are possibly (i) not resolved by the GPR (resolution issue) or (ii) not identified by the geologist (interpretation issue), or (iii) relict of larger structures (identification issue). In consequence, the small-scale structures are potentially underestimated by the intrepretation of the GPR data. The apparent sizes of the scour fills can be easily inferred from the GPR data (Fig. 6.2) but these properties are biased because larger objects have more chances to be imaged by GPR. Therefore, indicators of the system dynamics, such as the scour-fill ratio and the preservation potential of scour fills (Siegenthaler and Huggenberger, 1993), are prone to be biased when evaluated from two-dimensional GPR data.

6.2.2 Conceptual Model

The formulation of conceptual, sedimentological knowledge into geologically realistic mathematical models is of crucial importance for (stochastic) subsurface modeling, because inadequate representations of the geology can result in biased model predictions and underestimated prediction uncertainties (Linde et al., 2015).

Because of the permeability constrast between GP and open-framework gravel (OW), the layers of GP are regarded as a background matrix in which the high-permeable scour fills are embedded (Stauffer, 2007; Huber and Huggenberger, 2015b). The scour fills are generally spoon-shaped and most probably originate from filled confluence scours (Siegenthaler and Huggenberger, 1993; Jussel et al., 1994; Beres et al., 1995, 1999; Klingbeil et al., 1999; Heinz et al., 2003; Huggenberger and Regli, 2006). A confluence scour is indicated in Fig. 6.1

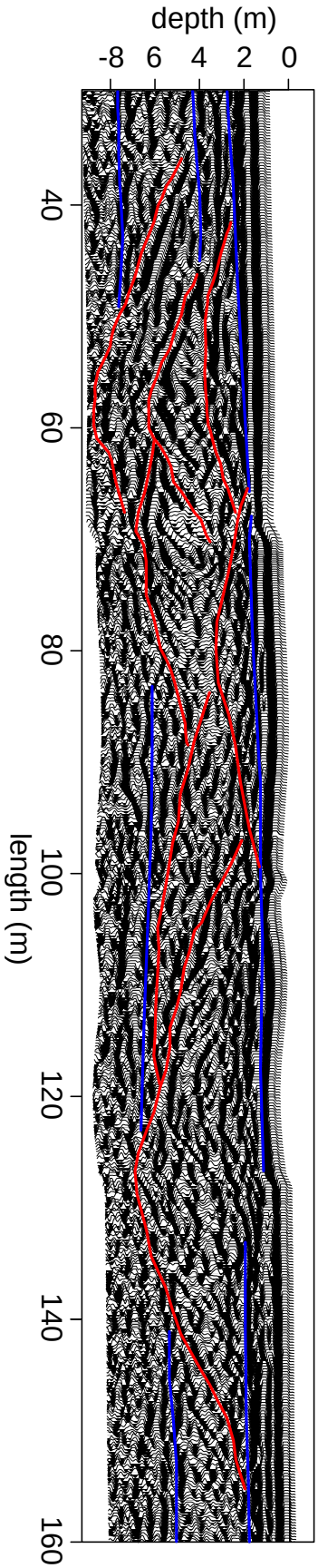

Figure 6.2 – Sedimentological interpretation superimposed on the GPR data. The red lines correspond to the erosional lower-bounding surfaces of scour fills and the blue lines to horizontal layers of poorly-sorted gravel (GP) (2× vertical exaggeration factor)

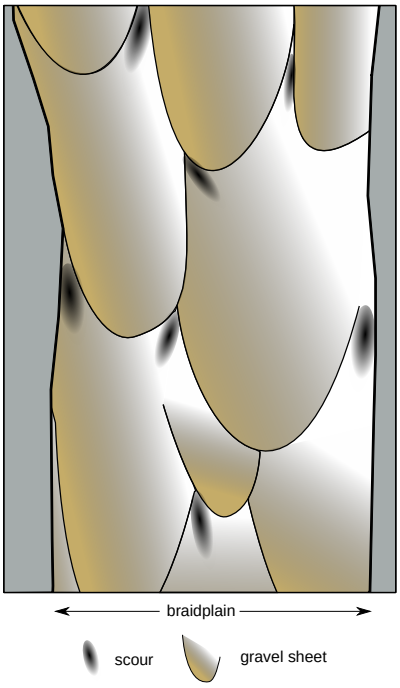

Figure 6.3 – Sketch illustrating the interaction between the gravel sheets (also called unit bars) and the scours on the braidplain (top view). The river flow direction is from top to bottom.

but many scours formed at high discharge are filled during the flow recession, leaving at the surface no evidence of their existence (Storz-Peretz and Laronne, 2013; Huber and Huggenberger, 2015a).

Observations indicate that the position of the scour fills depends on the position of the gravel sheets (Figure 6.3) and therefore it is expected that the scour fills do not overlap. There is very little knowledge how the braidplain elevation levels raise while coarse, braided rivers accumulate unconsolidated sediments on the braidplain. It is generally assumed that sediment deposition discontinuously occurs in the form of sediment layers (e.g., gravel sheets) deposited during flood events.

6.2.3 Marked Point Process

The conceptual model is now expressed in a mathematical form.

The spoon-shaped scour fills can be approximated by truncated ellipsoids (Figure 6.4, Siegenthaler and Huggenberger, 1993; Beres et al., 1999; Huber and Huggenberger, 2015b) and, therefore, the three-dimensional spatial distribution of scour fills is simulated with a MPP with separable horizontal and vertical dimensions and independent marks. The MPP is a compound Strauss process. It consists of k horizontal layers whose elevations $\mathbf{z}$ follow a Poisson process with intensity λ_z. On each layer, the points are simulated with an independent Strauss process with independent marks consisting of truncated ellipsoids with random dimensions and horizontal orientations. The Strauss process account for spatial interaction between the points. In the following the term objects is used for points and marks.

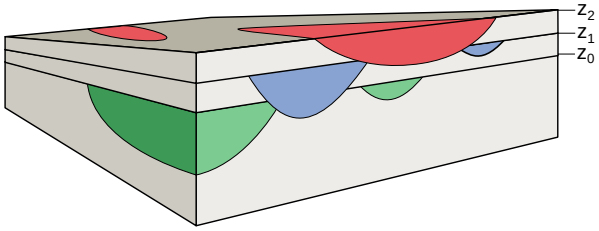

Figure 6.4 – Conceptual model of coarse braided river deposits: scour fills (in green, blue and red) are deposited on each layer (grey).

Vertical Poisson process

The layer elevations $\mathbf{z} = \{z_1, \ldots, z_k\}$ are modelled by a one-dimensional homogeneous Poisson process of intensity λ_z that expresses the mean layer height. The probability distribution of this one-dimensional homogeneous point process on the vertical model domain Ω_z with respect to the unit intensity Poisson process is (van Lieshout, 2010)

$$f_{\text{Pois}}(\mathbf{z}) = \lambda_z^k \exp\left((1 - \lambda_z) \cdot \Delta_z\right), \tag{6.1}$$

with Δ_z the vertical model height. The number of layers follows a Poisson distribution with intensity $\lambda_z \cdot \Delta_z$ and the layer elevations are independently identically distributed over Ω_z (complete spatial randomness).

Horizontal Strauss process

On the horizontal layer t $(t = 1, \ldots, k)$, the object positions $\mathbf{s} = \{s_1, \ldots, s_n\}$, with $s_i = (x_i, y_i)$ are modelled with an independent Strauss process defined by an interaction distance d, and parameters β and γ. The vertical position of the objects $\mathbf{s}$ is equal to the layer elevation z_t. The probability density of the Strauss process on the horizontal model domain Ω_{xy} with respect to the unit intensity Poisson process is given by (Illian et al., 2008)

$$f_{\text{Strauss}}(\mathbf{s}) = \frac{\beta^n \gamma^{v(\mathbf{s},d)}}{Z(\beta, \gamma, d)}, \tag{6.2}$$

with $v(\mathbf{s}, d) = \sum_{i=1}^{n-1} \sum_{j=i+1}^{n} \mathbb{1}\left(\|s_i - s_j\|_\kappa \leq d\right)$. The indicator function $\mathbb{1}(\cdot)$ is equal to 1 if the distance $\|\cdot\|_\kappa$ between s_i and s_j is less than d. To reflect the anisotropic distance between the scour fills, the pairwise distance between points is defined by

$$\|s_i - s_j\|_\kappa = \sqrt{\left(\frac{x_i - x_j}{\kappa}\right)^2 + \left(\frac{y_i - y_j}{1}\right)^2}, \tag{6.3}$$

with κ the anisotropy factor.

When $\beta = +\infty$, the Strauss process is equivalent to a hard core point process (i.e., the pairwise distance between the objects is not smaller than d). When

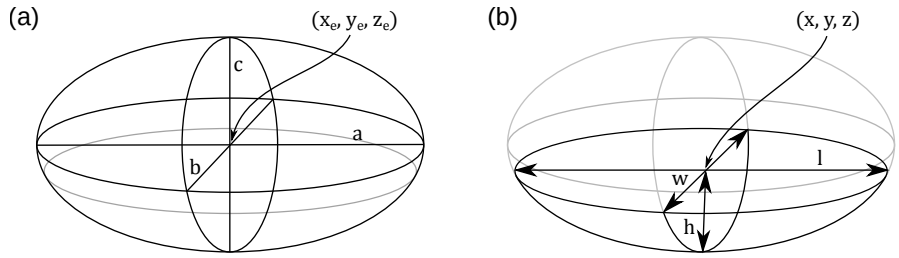

Figure 6.5 – (a) Ellispoid. (b) Truncated ellipsoid.

$\beta = 0$ the Strauss process is equivalent to the Poisson process (i.e., there is no interaction between the objects).

In Equation 6.2, the normalisation constant, $Z(\beta, \gamma, d)$, depends on the Strauss process parameters and is analytically intractable.

Object properties (marks)

The marks (i.e., the objects) are independent from the Poisson and Strauss process and correspond to truncated ellipsoids aligned with the horizontal plane and oriented with respect to the vertical plane. The object parameters are ϕ (horizontal orientation), l (length), w (width), h (height), and r (truncation ratio of the ellipsoid).

Because the scour fills have specific proportions ($l > w > h$) it is more appropriate to describe the object dimensions by length l, length-width ratio $r_{\mathrm{w}} = l/w$ and length-height ratio $r_{\mathrm{h}} = l/h$. The truncation ratio r is set equal to 2 because larger ratios do not significantly change the shape of the objects but make the ellipsoids larger. The other parameters are independently drawn from uniform probability distributions, i.e.,

$$\begin{aligned} \phi &\sim \mathcal{U}(-\phi_{\max}, \phi_{\max}) \,, & l &\sim \mathcal{U}(l_{\min}, l_{\max}) \,, \\ r_{\mathrm{w}} &\sim \mathcal{U}(r_{\mathrm{w,min}}, r_{\mathrm{w,max}}) \,, & r_{\mathrm{h}} &\sim \mathcal{U}(r_{\mathrm{h,min}}, r_{\mathrm{h,max}}) \,. \end{aligned} \tag{6.4}$$

Therefore, the distributions of w and h follow the ratio of two uniform distributions (see Box 6.1).

The relationship between the object parameters and the corresponding ellipsoid defined by the semi-axis (a, b, c) and coordinate center (x_e, y_e, z_e) is given by

$$\begin{aligned} a &= \frac{r}{2\sqrt{2r-1}} \cdot l \,, & x_e &= x \,, \\ b &= \frac{r}{2\sqrt{2r-1}} \cdot w \,, & y_e &= y \,, \\ c &= r \cdot h \,, & z_e &= z + h\,(r-1) \,, \end{aligned} \tag{6.5}$$

where (x, y, z) are the coordinates of the objects defined by the Strauss and Poisson processes (Figure 6.5).

Box 6.1: Ratio of two uniform distributions

Assume that the random variables X and Y are uniformly distributed as follows:

$$X \sim \mathcal{U}(a, b)$$
$$Y \sim \mathcal{U}(c, d) \text{ with } c > 0$$

The random variable Z is defined as $Z = \frac{X}{Y}$. Then the probability distribution function of Z (for the case $a, b > c, d$) is:

$$f_Z(z) = \begin{cases} \frac{(zd)^2 - a^2}{2z^2} \\ \frac{b^2 - a^2}{2z^2} \\ \frac{b(b-a)}{z^2} + \frac{1}{2}\left(\frac{2ab - b^2}{z^2} - c^2\right) \end{cases}$$

Figures 6.2.3A and B (below) show how to compute f_Z from geometrical considerations. The cumulative density function (CDF) and probability density function (PDF) of f_Z are presented on Figures 6.2.3C and D.

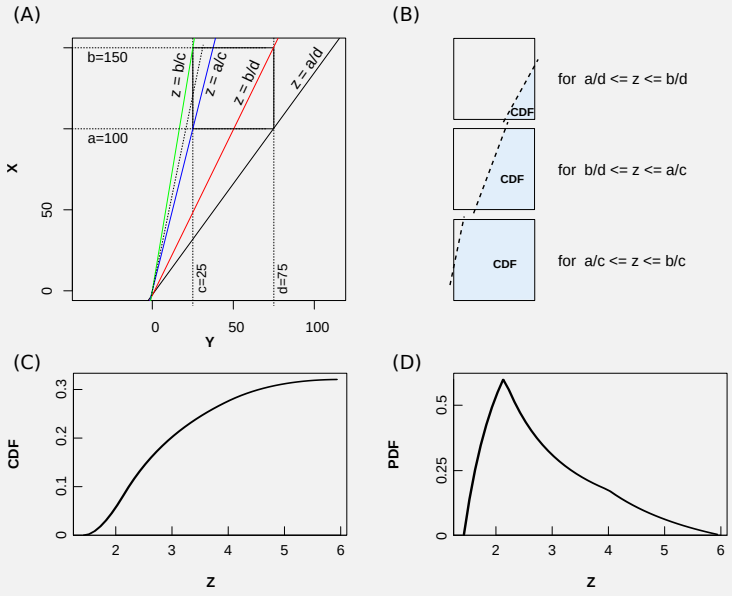

Figure 6.6 – (A) The four lines (black, red, blue and green) are four particular values taken by the variable $z = x/y$ as function of the parameters of the uniform distributions. (B) The CDF of f_Z can be geometrically computed by taking into account the four special values of z. The CDF corresponds to the shaded area. (C) CDF and (D) PDF of f_Z

Simulations

The MPP parameters are

$$\boldsymbol{\theta} = \{\lambda_z, \beta, \gamma, d, \kappa, \phi_{\max}, l_{\min}, l_{\max}, r_{\mathrm{w,min}}, r_{\mathrm{w,max}}, r_{\mathrm{h,min}}, r_{\mathrm{h,max}}\}. \quad (6.6)$$

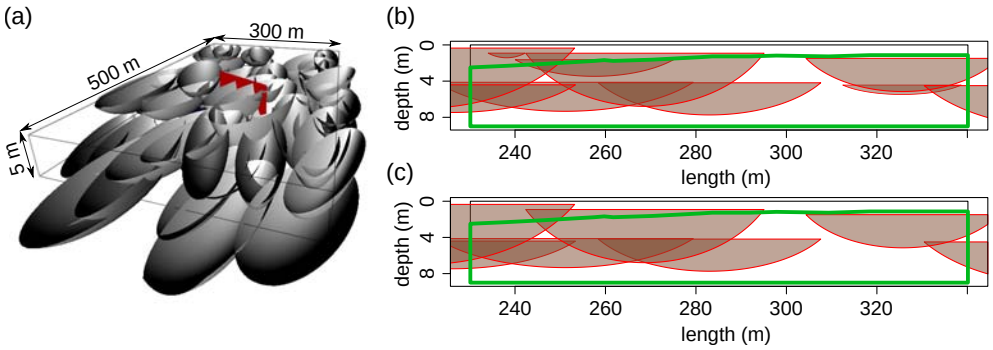

Figure 6.7 – (A) Three-dimensional visualisation of an unconditional realisation from prior 2. The model size is 500 m × 300 m × 5 m. The red plane corresponds to the section plane show in (B) and (C). (B) Section of the realisation of prior 2 shown in (A). The green boundary shows the part of the section considered for the computation of the attributes and of the likelihood. (C) Section (A) after the removal of (i) the structures outside the green boundary and (ii) the eroded structures.

A realisation $\mathbf{m}$ of the MPP (Fig. 6.7(a), Algorithm 6.1) consists in all the truncated ellipsoids $\boldsymbol{\mathcal{E}}_t$ at layer z_t with $(t = 1, \ldots, k)$, i.e.,

$$\mathbf{m} = \begin{bmatrix} \boldsymbol{\mathcal{E}}_{t=1} \\ \ldots \\ \boldsymbol{\mathcal{E}}_{t=k} \end{bmatrix} \text{ with } \boldsymbol{\mathcal{E}}_t = \begin{bmatrix} x_1, y_1, z_t, \phi_1, l_1, w_1, h_1, r_1 \\ \vdots \\ x_{n_t}, y_{n_t}, z_t, \phi_{n_t}, l_{n_t}, w_{n_t}, h_{n_t}, r_{n_t} \end{bmatrix}, \tag{6.7}$$

with n_t the number of objects on layer t.

Algorithm 6.1: Unconditional simulation of the marked point process

$k \sim Pois\left(\lambda_z \cdot (z_{\max} - z_{\min})\right)$ ▷ k layers/iterations
$\mathbf{z} = \{z_1, \ldots, z_k\} \sim \mathcal{U}_k\left(z_{\min}, z_{\max}\right)$ ▷ layer elevation
for $t = 1$ **to** k **do**
  $(\mathbf{x}, \mathbf{y}) \sim \text{Strauss}\left(\gamma, \beta, d\right)$ ▷ Strauss process for object centers
  $p \leftarrow \#\left(\mathbf{x}, \mathbf{y}\right)$ ▷ number of object at iteration t
  $\boldsymbol{\theta} \sim \mathcal{U}_p\left(\theta_{\min}, \theta_{\max}\right)$
  $\mathbf{l} \sim \mathcal{U}_p\left(l_{\min}, l_{\max}\right)$
  $\mathbf{l/w} \sim \mathcal{U}_p\left(l/w_{\min}, l/w_{\max}\right)$
  $\mathbf{l/h} \sim \mathcal{U}_p\left(l/h_{\min}, l/h_{\max}\right)$
  $\mathcal{E}_t \leftarrow [\mathbf{x}, \mathbf{y}, z_t, \boldsymbol{\theta}, \mathbf{l}, \mathbf{w}, \mathbf{h}, r]$
end

To ensure that objects intersecting the model boundary Ω_{xy} but with position $(x_i,\, y_i)$ (s) outside Ω_{xy} can be simulated, and to minimise bias due to lesser object interactions near the model boundary, the model domain Ω is enlarged to Ω' for all computations and then clipped to Ω (Allard et al., 2005).

Because only the object positions and properties (i.e., the points and their marks) must be stored, the MPP is light in computer memory and grid independent. Furthermore, vertical sections of $\mathbf{m}$ can be algebraically computed:

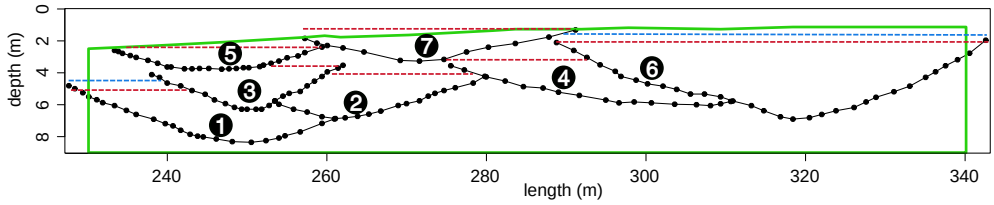

Figure 6.8 – The data consists of (i) the erosional lower-bounding surfaces of scour fills (black dots), (ii) the age hierarchy of the scour fills indicated by the numbering (whereby the scour fills pairs 3–4, and 5–6 can have the same age) and (iii) elevations below (respectively above) which a penalty is applied in the likelihood function (dashed red, respectively blue, lines)

a vertical section of a truncated ellipsoid is a truncated ellipse ϵ_i defined by its position on the section as well as its length, height and truncation ratio (Fig. 6.7(b)).

6.2.4 Data simulation

The observed data $\mathbf{y}^o$ are the erosional lower bounding surfaces interpreted from the GPR data, i.e., a set of l^o curves. Data are simulated from a MPP realisation $\mathbf{m}$

by first computing algebraically a vertical section of $\mathbf{m}$ (Fig. 6.7(b)) and then filtering the objects on the section (i.e., truncated ellipses) to account for geological erosional processes, resolution issue of the GPR imaging and identification issue for small structures (Fig. 6.7(c)). More specifically, the truncated ellipses of the vertical section are therefore clipped to the observation section and the older ellipses are eroded by the younger ellipses (that who lay above). Then, the ellipse remnants that are very small (area $<0.5\,\%$) or very thin (area/perimeter ratio <0.3) are removed from the section. The ellipse arcs that are not eroded defines the simulated data $\mathbf{y}$.

6.2.5 Prior on the parameters

The parameters of the MPP are uncertain because of a paucity of available information on braided river systems. Therefore, a prior distribution $p(\boldsymbol{\theta})$ is assigned to the MPP parameters. The Poisson and Strauss parameters $\lambda_z, \beta, \gamma, d, \kappa, \phi_{\max}$ are drawn from uniform distributions, i.e.,

$$\theta_i \sim \mathcal{U}(\theta_i^{\min}, \theta_i^{\max}) \quad \text{with} \quad \theta_i = \lambda_z, \beta, \gamma, d, \kappa\,. \tag{6.8}$$

The pairs of object parameters, $(l_{\min}, l_{\max})$, $(r_{\mathrm{w,min}}, r_{\mathrm{w,max}})$, and $(r_{\mathrm{h,min}}, r_{\mathrm{h,max}})$ are of the form $(\theta_{i,\min}, \theta_{i,\max})$ and are sampled as follows

$$\begin{aligned} \vartheta_1 &\sim \mathcal{U}(\theta_{i,\min}^{\min}, \theta_{i,\min}^{\max}) \\ \vartheta_2 &\sim \mathcal{U}(\theta_{i,\max}^{\min}, \theta_{i,\max}^{\max}) \\ \theta_{i,\min} &= \min(\vartheta_1, \vartheta_2) \\ \theta_{i,\max} &= \max(\vartheta_1, \vartheta_2)\,. \end{aligned} \tag{6.9}$$

Note that $\theta_{i,\min}$ and $\theta_{i,\max}$ are therefore not independent.

6.3 Bayesian Approach

6.3.1 Latent model and data

The three-dimensional subsurface structure $\mathbf{m}$ is simulated with a stochastic latent model $\mathcal{G}(\cdot,\cdot)$, the MPP described in Section 6.2.3,

$$\mathbf{m} = \mathcal{G}(\boldsymbol{\theta}, \cdot)\,, \tag{6.10}$$

where $\boldsymbol{\theta} = \{\theta_1, \ldots, \theta_M\}$ are the latent model parameters and '$\cdot$' symbolises calls to a random number generator (Section 6.2.3). Simulations from $\mathcal{G}(\boldsymbol{\theta}, \cdot)$, even for a given choice of $\boldsymbol{\theta}$, produce random draws. The prior on the latent model, $p(\mathbf{m} \mid \boldsymbol{\theta})$ can only be estimated from a sample $(\mathbf{m}_1, \mathbf{m}_2, \ldots)$ by means of simulation, because of the analytically intractable normalisation constant (Section 6.2.3). Therefore, the posterior has not a simple analytical expression and a Monte Carlo sampling approach is required.

The observed data are an interpreted two-dimensional image $\mathbf{y}^o$ consisting in a set of l^o curves whose spatial arrangement on the two-dimensional section defines spatial dependence, namely an age hierarchy of the curves. Data are simulated from MPP realisations with

$$\mathbf{y} = \mathcal{H}(\mathbf{m})\,, \tag{6.11}$$

where $\mathcal{H}(\cdot)$ is a mapping function that extracts a vertical section of $\mathbf{m}$ and filters it (Section 6.2.4). The simulated data consist in a set of l curves that define an age hierarchy too. Note that (i) identical data can be simulated from different MPP realisations, (ii) l can vary from simulation to simulation, and (iii) l is not necessarily equal to l^o.

The aim of the present study is to solve the stereological problem, i.e., to quantify the uncertainty on the three-dimensional subsurface structure given the observed data $\mathbf{y}^o$ (a set of l^o curves defining an age hierarchy). More specifically, the conditioned simulated subsurface structure must well approximate the observed curves and honour the observed number of curves l^o as well as the age hierarchy of the observed curves.

6.3.2 MCMC sampling of the posterior

The distribution from which we aim to draw samples (i.e., the target distribution) is the posterior $p(\mathbf{m} \mid \mathbf{y}^o)$, i.e., the uncertainty on the subsurface heterogeneity $\mathbf{m}$ conditional on the observed data $\mathbf{y}^o$ that accounts for the uncertain model parameters $\boldsymbol{\theta}$.

Although the posterior is the target distribution, the MCMC draw samples $(\mathbf{y}_i, \mathbf{m}_i, \boldsymbol{\theta}_i)$ from the augmented posterior (Sisson and Fan, 2011)

$$p(\mathbf{y}, \mathbf{m}, \boldsymbol{\theta} \mid \mathbf{y}^o) \propto p(\mathbf{y}^o \mid \mathbf{y}, \mathbf{m}, \boldsymbol{\theta}) p(\mathbf{y} \mid \mathbf{m}, \boldsymbol{\theta}) p(\mathbf{m} \mid \boldsymbol{\theta}) p(\boldsymbol{\theta}) \,, \tag{6.12}$$

where $p(\mathbf{y}^o \mid \mathbf{y}, \mathbf{m}, \boldsymbol{\theta})$ is the augmented likelihood function of the data $\mathbf{y}^o$.
The target $p(\mathbf{m} \mid \mathbf{y}^o)$ is the joint posterior (Equation 6.12) integrated over the data space $\mathcal{Y}$ and parameter space Θ,

$$\begin{aligned} p(\mathbf{m} \mid \mathbf{y}^o) &= \int_\Theta \int_\mathcal{Y} p(\mathbf{y}, \mathbf{m}, \boldsymbol{\theta} \mid \mathbf{y}^o) \, \mathrm{d}\theta \, \mathrm{d}y \\ &\propto \int_\Theta p(\mathbf{m} \mid \boldsymbol{\theta}) p(\boldsymbol{\theta}) \int_\mathcal{Y} p(\mathbf{y}^o \mid \mathbf{y}, \mathbf{m}, \boldsymbol{\theta}) p(\mathbf{y} \mid \mathbf{m}, \boldsymbol{\theta}) \, \mathrm{d}\theta \, \mathrm{d}y \,. \end{aligned} \tag{6.13}$$

In practice, the integration is obtained by simply discarding the samples $\mathbf{y}$ and $\boldsymbol{\theta}$. Note that the nested integral term (integral over $\mathcal{Y}$) in Equation 6.13 is the likelihood function.
One of the most popular MCMC schemes is the Metropolis-Hastings update (Metropolis et al., 1953; Hastings, 1970; Geyer, 2011) that consists in

1. simulating a candidate sample $(\mathbf{y}^\star, \mathbf{m}^\star, \boldsymbol{\theta}^\star)$,

$$(\mathbf{y}^\star, \mathbf{m}^\star, \boldsymbol{\theta}^\star) \sim K(\cdot \mid \mathbf{y}_i, \mathbf{m}_i, \boldsymbol{\theta}_i) \,, \tag{6.14}$$

   where $K(\cdot \mid \cdot)$ is the proposal distribution and $(\mathbf{y}_i, \mathbf{m}_i, \boldsymbol{\theta}_i)$ is the previous state of the Markov chain.

2. setting $(\mathbf{y}^\star, \mathbf{m}^\star, \boldsymbol{\theta}^\star)$ as the current state of the Markov chain with probability

$$\alpha_{\mathrm{MH}} = \min\left(1, \frac{p(\mathbf{y}^\star, \mathbf{m}^\star, \boldsymbol{\theta}^\star \mid \mathbf{y}^o)}{p(\mathbf{y}_i, \mathbf{m}_i, \boldsymbol{\theta}_i \mid \mathbf{y}^o)} \cdot \frac{K(\mathbf{y}_i, \mathbf{m}_i, \boldsymbol{\theta}_i \mid \mathbf{y}^\star, \mathbf{m}^\star, \boldsymbol{\theta}^\star)}{K(\mathbf{y}^\star, \mathbf{m}^\star, \boldsymbol{\theta}^\star \mid \mathbf{y}_i, \mathbf{m}_i, \boldsymbol{\theta}_i)}\right) \,, \tag{6.15}$$

   where α_{MH} is the Metropolis-Hastings acceptance probability.

By replacing in Equation 6.15 the posterior by its expression given in Equation 6.12, the Metropolis-Hastings acceptance probability becomes,

$$\begin{aligned} \alpha_{\mathrm{MH}} = \min\Bigg(1, &\frac{p(\mathbf{y}^o \mid \mathbf{y}^\star, \mathbf{m}^\star, \boldsymbol{\theta}^\star) p(\mathbf{y}^\star \mid \mathbf{m}^\star, \boldsymbol{\theta}^\star) p(\mathbf{m}^\star \mid \boldsymbol{\theta}^\star) p(\boldsymbol{\theta}^\star)}{p(\mathbf{y}^o \mid \mathbf{y}_i, \mathbf{m}_i, \boldsymbol{\theta}_i) p(\mathbf{y}_i \mid \mathbf{m}_i, \boldsymbol{\theta}_i) p(\mathbf{m}_i \mid \boldsymbol{\theta}_i) p(\boldsymbol{\theta}_i)} \cdot \\ &\frac{K(\mathbf{y}_i, \mathbf{m}_i, \boldsymbol{\theta}_i \mid \mathbf{y}^\star, \mathbf{m}^\star, \boldsymbol{\theta}^\star)}{K(\mathbf{y}^\star, \mathbf{m}^\star, \boldsymbol{\theta}^\star \mid \mathbf{y}_i, \mathbf{m}_i, \boldsymbol{\theta}_i)}\Bigg) \,. \end{aligned} \tag{6.16}$$

It is now evident that this expression involves the ratio $\frac{p(\mathbf{m}^\star \mid \boldsymbol{\theta}^\star)}{p(\mathbf{m}_i \mid \boldsymbol{\theta}_i)}$, i.e., the ratio of intractable normalisation constants that depends on $\boldsymbol{\theta}$, and, therefore, this ratio does not cancel out (Bognar, 2005; Berthelsen and Møller, 2006; Bognar,

2007). The challenge is to specify the proposal distribution $K(\cdot \mid \cdot)$ to cancel out the ratio $\frac{p(\mathbf{m}^\star|\boldsymbol{\theta}^\star)}{p(\mathbf{m}_i|\boldsymbol{\theta}_i)}$.
Per se, the candidate sample $(\mathbf{y}^\star, \mathbf{m}^\star, \boldsymbol{\theta}^\star)$ is independent from $\mathbf{y}_i$ (Equation 6.11). Therefore, the proposal distribution can be decomposed into

$$K(\mathbf{y}^\star, \mathbf{m}^\star, \boldsymbol{\theta}^\star \mid \mathbf{y}_i, \mathbf{m}_i, \boldsymbol{\theta}_i) = K(\mathbf{m}^\star, \boldsymbol{\theta}^\star \mid \mathbf{m}_i, \boldsymbol{\theta}_i) p(\mathbf{y}^\star \mid \mathbf{m}^\star, \boldsymbol{\theta}^\star)\,. \tag{6.17}$$

The only way to cancel out the ratio $\frac{p(\mathbf{m}^\star|\boldsymbol{\theta}^\star)}{p(\mathbf{m}_i|\boldsymbol{\theta}_i)}$ is to further decompose Equation 6.17 in

$$K(\mathbf{y}^\star, \mathbf{m}^\star, \boldsymbol{\theta}^\star \mid \mathbf{y}_i, \mathbf{m}_i, \boldsymbol{\theta}_i) = K(\boldsymbol{\theta}^\star \mid \boldsymbol{\theta}_i) p(\mathbf{m}^\star \mid \boldsymbol{\theta}^\star) p(\mathbf{y}^\star \mid \mathbf{m}^\star, \boldsymbol{\theta}^\star)\,. \tag{6.18}$$

Equation 6.18 implies that $\mathbf{m}^\star$ is drawn independently from $\mathbf{m}_i$, and the Metropolis-Hastings acceptance probability simplifies to

$$\alpha_{\text{MH}} = \min\left(1, \frac{p(\mathbf{y}^o \mid \mathbf{y}^\star, \mathbf{m}^\star, \boldsymbol{\theta}^\star) p(\boldsymbol{\theta}^\star)}{p(\mathbf{y}^o \mid \mathbf{y}_i, \mathbf{m}_i, \boldsymbol{\theta}_i) p(\boldsymbol{\theta}_i)} \cdot \frac{K(\boldsymbol{\theta}_i \mid \boldsymbol{\theta}^\star)}{K(\boldsymbol{\theta}^\star \mid \boldsymbol{\theta}_i)}\right). \tag{6.19}$$

Although the analytical intractable ratio is cancelled out, a MCMC based on the Metropolis-Hastings acceptance probability defined in Equation 6.19 is very inefficient: if $\mathbf{m}^\star$ is drawn independently from $\mathbf{m}_i$, i.e., $\mathbf{m}^\star = \mathcal{G}(\boldsymbol{\theta}, \cdot)$, the MCMC reduces to a rejection scheme that samples uncorrelated realisations $\mathbf{m}^\star$. The probability to draw $\mathbf{m}^\star$ such that $\mathbf{y}^\star$ is very close to $\mathbf{y}^o$ is infinitesimal small.
To get out of this dead-end issue, $\boldsymbol{\theta}$ is set to the maximum a posteriori (MAP) estimate of the model parameters, $\boldsymbol{\theta}_{\text{MAP}}$, that is defined by

$$\boldsymbol{\theta}_{\text{MAP}} = \arg\max_{\boldsymbol{\theta}} p(\boldsymbol{\theta} \mid \mathbf{y}^o)\,. \tag{6.20}$$

Section 6.3.4 shows how $\boldsymbol{\theta}_{\text{MAP}}$ is estimated. The posterior $p(\mathbf{m} \mid \mathbf{y}^o)$ is therefore approximated by $p(\mathbf{m} \mid \mathbf{y}^o, \boldsymbol{\theta}_{\text{MAP}})$ that can be sampled with MCMC. The MCMC algorithm draws samples $(\mathbf{y}_i, \mathbf{m}_i)$ from the joint posterior distribution $p(\mathbf{y}, \mathbf{m} \mid \boldsymbol{\theta}_{\text{MAP}})$. To simplify the notation, we now omit the dependence on $\boldsymbol{\theta}_{\text{MAP}}$. The Metropolis-Hastings acceptance probability (Equation 6.15) becomes

$$\alpha_{\text{MH}} = \min\left(1, \frac{p(\mathbf{y}^o \mid \mathbf{y}^\star, \mathbf{m}^\star) p(\mathbf{y}^\star \mid \mathbf{m}^\star) p(\mathbf{m}^\star)}{p(\mathbf{y}^o \mid \mathbf{y}_i, \mathbf{m}_i) p(\mathbf{y}_i \mid \mathbf{m}_i) p(\mathbf{m}_i)} \cdot \frac{K(\mathbf{y}_i, \mathbf{m}_i \mid \mathbf{y}^\star, \mathbf{m}^\star)}{K(\mathbf{y}^\star, \mathbf{m}^\star \mid \mathbf{y}_i, \mathbf{m}_i)}\right). \tag{6.21}$$

Because the candidate $(\mathbf{y}^\star, \mathbf{m}^\star)$ is independent from $\mathbf{y}_i$ (Equation 6.17), the proposal distribution can be written

$$K(\mathbf{y}^\star, \mathbf{m}^\star \mid \mathbf{y}_i, \mathbf{m}_i) = K(\mathbf{m}^\star \mid \mathbf{m}_i) p(\mathbf{y}^\star \mid \mathbf{m}^\star)\,, \tag{6.22}$$

and Equation 6.21 simplifies to

$$\alpha_{\mathrm{MH}} = \min\left(1, \frac{p(\mathbf{y}^o \mid \mathbf{y}^\star, \mathbf{m}^\star)p(\mathbf{m}^\star)}{p(\mathbf{y}^o \mid \mathbf{y}_i, \mathbf{m}_i)p(\mathbf{m}_i)} \cdot \frac{K(\mathbf{m}_i \mid \mathbf{m}^\star)}{K(\mathbf{m}^\star \mid \mathbf{m}_i)}\right). \tag{6.23}$$

Mosegaard and Tarantola (1995) proposed to design the proposal distribution $K(\cdot \mid \cdot)$ such that the Markov chain equilibrates to the prior $p(\mathbf{m})$. In this case the detailed balance equation must hold, i.e.,

$$\frac{K(\mathbf{m}_i \mid \mathbf{m}^\star)}{K(\mathbf{m}^\star \mid \mathbf{m}_i)} = \frac{p(\mathbf{m}_i)}{p(\mathbf{m}^\star)} \quad \text{for all } \mathbf{m}_i \neq \mathbf{m}^\star. \tag{6.24}$$

By plugging the detailed balance equation (Equation 6.24) into the Metropolis-Hastings acceptance probability (Equation 6.19), α_{MH} simplifies to the ratio of the augmented likelihood functions,

$$\begin{aligned}\alpha_{\mathrm{MH}} &= \min\left(1, \frac{p(\mathbf{y}^o \mid \mathbf{y}^\star, \mathbf{m}^\star)p(\mathbf{m}^\star)}{p(\mathbf{y}^o \mid \mathbf{y}_i, \mathbf{m}_i)p(\mathbf{m}_i)} \cdot \frac{p(\mathbf{m}_i)}{p(\mathbf{m}^\star)}\right) \\ &= \min\left(1, \frac{p(\mathbf{y}^o \mid \mathbf{y}^\star, \mathbf{m}^\star)}{p(\mathbf{y}^o \mid \mathbf{y}_i, \mathbf{m}_i)}\right).\end{aligned} \tag{6.25}$$

Mosegaard and Tarantola (1995) called this special case of the Metropolis-Hastings update the *extended Metropolis* update.

6.3.3 ABC MCMC with extended Metropolis update

Despite its simple form, the Metropolis-Hastings acceptance probability (Equation 6.25) cannot be easily computed because of the a priori unknown augmented likelihood function $p(\mathbf{y}^o \mid \mathbf{y}, \mathbf{m})$. The augmented likelihood function involves two sets of curves $\mathbf{y}$ and $\mathbf{y}^o$ that can have different dimensions (l curves in $\mathbf{y}$ and l^o curves in $\mathbf{y}^o$ with l not necessarily equal to l^o). Furthermore, the curves in the data are not independent but correlated through an age hierarchy (Section 6.3.1). Therefore, the augmented likelihood function cannot be specified as a residuals-based likelihood function, such as the Gaussian of a misfit function as it is usually done in Bayesian stochastic modelling (Tarantola, 2005).
ABC MCMC (Marjoram et al., 2003) approximates the augmented likelihood function by

$$p(\mathbf{y}^o \mid \mathbf{y}, \mathbf{m}) \approx p_\varepsilon(\mathbf{y}^o \mid \mathbf{y}, \mathbf{m}) = \frac{1}{\varepsilon}\mathcal{K}\left(\frac{\rho(\mathbf{y}, \mathbf{y}^o)}{\varepsilon}\right), \tag{6.26}$$

where $\mathcal{K}(\cdot)$ is a standard kernel density function, $\rho(\cdot, \cdot)$ a similarity measure and ε a tolerance level.

$$\alpha_{\mathrm{MH}} = \min\left(1, \frac{p_\varepsilon(\mathbf{y}^o \mid \mathbf{y}^\star, \mathbf{m}^\star)}{p_\varepsilon(\mathbf{y}^o \mid \mathbf{y}_i, \mathbf{m}_i)}\right). \tag{6.27}$$

If a uniform kernel density function is chosen, $\mathcal{K}\left(\frac{\rho(\mathbf{y},\mathbf{y}^o)}{\varepsilon}\right) \propto \mathbb{1}\left(\rho(\mathbf{y}^o,\mathbf{y}^\star) \leq \epsilon\right)$, the ABC MCMC corresponds to a rejection sampler with correlated outputs (Marjoram et al., 2003, , see Algorithm 6.2).

Algorithm 6.2: ABC MCMC: Extended Metropolis update with uniform kernel

current state of the Markov chain $\mathbf{m}_i$
sample candidate $\mathbf{m}^\star \sim K(\cdot \mid \mathbf{m}_i)$
simulate data $\mathbf{y}^\star = \mathcal{H}(\mathbf{m}^\star)$
if $\rho(\mathbf{y}^o,\mathbf{y}^\star) \leq \epsilon$ **then**
    $\mathbf{m}_{i+1} \leftarrow \mathbf{m}^\star$
else
    $\mathbf{m}_{i+1} \leftarrow \mathbf{m}_i$
end

6.3.4 Model parameter estimation

The estimation of $\boldsymbol{\theta}_{\text{MAP}}$ requires the quantification of the posterior on the model parameters, $p(\boldsymbol{\theta} \mid \mathbf{y}^o)$, that can be written as

$$p(\boldsymbol{\theta} \mid \mathbf{y}^o) \propto p(\boldsymbol{\theta}) \int_{\mathcal{M}} p(\mathbf{y}^o \mid \mathbf{m}, \boldsymbol{\theta}) p(\mathbf{m} \mid \boldsymbol{\theta}) \, \mathrm{d}\mathbf{m} \,. \tag{6.28}$$

The integral term in Equation 6.28 is the marginalised likelihood. Because the latent model is of stochastic nature and its prior $p(\mathbf{m} \mid \boldsymbol{\theta})$ has an intractable normalisation constant that depends on $\boldsymbol{\theta}$, it is not possible to take full advantages of MCMC approaches.

An alternative to MCMC sampling is rejection sampling (Robert and Casella, 2004): draw $\boldsymbol{\theta}^\star$ from $p(\boldsymbol{\theta})$, simulate $\mathbf{m}^\star$ from the stochastic latent model (Equation 6.10), compute $\mathbf{y}^\star$ (Equation 6.11) and accept $\boldsymbol{\theta}^\star$ if $\mathbf{y}^\star = \mathbf{y}^o$. This sampling approach is very inefficient because the probability that $\mathbf{y}^\star = \mathbf{y}^o$ is infinitesimal small. ABC rejection approaches (Pritchard et al., 1999; Beaumont, 2010; Marin et al., 2012; Lintusaari et al., 2017) relax the acceptance criterion '$\mathbf{y}^\star = \mathbf{y}^o$'. The classical ABC regression algorithm is first presented, followed by a novel ABC regression scheme based on canonical correlation analysis (CCA) space regression.

ABC Regression

Classical regression-based ABC methods (see Algorithm 6.3, Pritchard et al., 1999; Beaumont, 2010) consist in approximate rejection sampling followed by a post-sampling regression-adjustment scheme. The approximate rejection sampling introduces a distance metric between the simulated data and the observed data, $\rho(\mathbf{y}^\star,\mathbf{y}^o)$, as well a threshold level $\varepsilon > 0$. The acceptance criterion becomes $\rho(\mathbf{y}^\star,\mathbf{y}^o) \leq \varepsilon$. Because of the complexity of the stochastic

latent model, the probability to simulate realisations that are close to the data is still infinitesimal small. Furthermore, it is not trivial to define a distance metric between $\mathbf{y}^\star$ and $\mathbf{y}^o$. The distance metric is therefore often replaced by a similarity measure such as the distance between some summary statistics. The ABC rejection algorithm is defined as follows

Algorithm 6.3: ABC rejection

for $i = 1$ **to** P **do**
  repeat
    draw $\boldsymbol{\theta}^\star \sim p(\boldsymbol{\theta})$
    sample $\mathbf{m}^\star = \mathcal{G}(\boldsymbol{\theta}^\star, \cdot)$
    simulate $\mathbf{y}^\star = \mathcal{H}(\mathbf{m}^\star)$
  until $\rho\left(\boldsymbol{\psi}(\mathbf{y}^\star), \boldsymbol{\psi}(\mathbf{y}^o)\right) \leq \epsilon$
  Set $\boldsymbol{\theta}_i \leftarrow \boldsymbol{\theta}^\star$
end

where $\boldsymbol{\psi}(\mathbf{y}) = \{\psi_1(\mathbf{y}), \ldots, \psi_N(\mathbf{y})\}$ are summary statistics.

The samples $(\boldsymbol{\theta}_1, \boldsymbol{\theta}_2, \ldots)$ are drawn from the distribution

$$p_{\varepsilon,\rho}(\boldsymbol{\theta} \mid \mathbf{y}^o) = p(\boldsymbol{\theta} \mid \rho\left(\boldsymbol{\psi}(\mathbf{y}^\star), \boldsymbol{\psi}(\mathbf{y}^o)\right) \leq \epsilon), \tag{6.29}$$

that approximates the posterior on the model parameters, $p(\boldsymbol{\theta} \mid \mathbf{y}^o)$. Beaumont (2010) proposed regression-adjustment scheme based on local linear regression to correct for the sampling approximation introduced with the threshold ε (see also the review of Lintusaari et al., 2017).

ABC CCA-regression

The new approach called 'ABC CCA-regression' does not require a similarity measure $\rho(\cdot, \cdot)$ nor a post-sampling regression adjustment. Samples are drawn from the joint probability distribution $p(\boldsymbol{\theta}, \boldsymbol{\psi}(\mathbf{y}))$ and projected on the CCA space. The statistics of the observed data, $\boldsymbol{\psi}(\mathbf{y}^o)$, are also projected on the CCA space and the posterior is quantified in the CCA space with Bayesian linear regression. Samples drawn from the CCA posterior are then back-transformed into the parameter space providing an approximation of $p(\boldsymbol{\theta} \mid \mathbf{y}^o)$. CCA-based prediction approaches have a long history in hydrology (Rice, 1972; Barnett and Preisendorfer, 1987; Mo, 2002; Cannon and Hsieh, 2008) and was recently applied in hydrogeophysics and petroleum geology (Satija and Caers, 2015; Hermans et al., 2016; Satija et al., 2017). CCA-regression is defined as follows

Algorithm 6.4: CCA-regression ABC

draw P samples $(\boldsymbol{\theta}_i, \boldsymbol{\psi}(\mathbf{y}_i))_{1 \leq i \leq P}$ from $p(\boldsymbol{\theta}, \boldsymbol{\psi}(\mathbf{y}))$
  $\boldsymbol{\theta}_i \sim p(\boldsymbol{\theta})$
  $\mathbf{m}_i = \mathcal{G}(\boldsymbol{\theta}_i, \cdot)$
  $\mathbf{y}_i = \mathcal{H}(\mathbf{m}_i)$
  $\boldsymbol{\psi}_i = \boldsymbol{\psi}(\mathbf{y}_i)$
apply CCA to $\boldsymbol{\Psi} = [\boldsymbol{\psi}_1, \ldots, \boldsymbol{\psi}_P]^T$ and $\boldsymbol{\Theta} = [\boldsymbol{\theta}_1, \ldots, \boldsymbol{\theta}_M]^T$
  $\mathbf{U} = (\mathbf{u}_1, \ldots, \mathbf{u}_Q) = \boldsymbol{\Psi}\mathbf{A}$
  $\mathbf{V} = (\mathbf{v}_1, \ldots, \mathbf{v}_Q) = \boldsymbol{\Theta}\mathbf{B}$
project $\boldsymbol{\psi}(\mathbf{y}^o)$ on the CCA space
  $\mathbf{u}^o = (u_1^o, \ldots, u_Q^o) = \boldsymbol{\psi}(\mathbf{y}^o)^T\mathbf{A}$
for $j \leftarrow 1$ **to** Q **do**
  infer $p(v_j \mid u_j^o)$ with Bayesian linear regression
  draw samples $\mathbf{v}_j = (v_j^{(1)}, v_j^{(2)}, \ldots)$ from $p(v_j \mid u_j^o)$
end
back-transform $\mathcal{V} = (\mathbf{v}_1, \ldots, \mathbf{v}_Q)$ onto the parameter space
  $\mathcal{O} = \mathcal{V}\mathbf{B}^\dagger$

CCA (Hotelling, 1936) maximises the linear relationship between pairs of linear combinations of the variables in each space (i.e., summary statistic space and parameter space) such that each pair are orthogonal to the other pairs. The canonical variates $\mathbf{U}_{(P\times Q)}$ and $\mathbf{V}_{(P\times Q)}$ are a linear combination of the variables $\boldsymbol{\Psi}_{(P\times N)}$ and $\boldsymbol{\Theta}_{(P\times M)}$, respectively,

$$\begin{aligned} \mathbf{U} &= \boldsymbol{\Psi}\mathbf{A} \\ \mathbf{V} &= \boldsymbol{\Theta}\mathbf{B}\,, \end{aligned} \tag{6.30}$$

where the matrices $\mathbf{A}_{(N\times Q)}$ and $\mathbf{B}_{(M\times Q)}$ are the canonical weights and $Q = \min(N, M)$.

Let denote $\mathbf{u}_i$ and $\mathbf{v}_i$ the i^{th} canonical variates, i.e., the i^{th} columns of $\mathbf{U}$ and $\mathbf{V}$. The following properties hold:

- ▷ $\mathbf{u}_i$ and $\mathbf{u}_j$ are uncorrelated for $i \neq j$.
- ▷ $\mathbf{v}_i$ and $\mathbf{v}_j$ are uncorrelated for $i \neq j$.
- ▷ $\mathbf{u}_i$ and $\mathbf{v}_i$ are uncorrelated for $i \neq j$.
- ▷ The correlation between pairs $\mathbf{u}_i$ and $\mathbf{v}_i$ is the canonical correlation r_i.

The observed data statistics are then projected on the CCA space with

$$\mathbf{u}^o = (u_1^o, \ldots, u_Q^o) = \boldsymbol{\psi}(\mathbf{y}^o)^T\mathbf{A}\,. \tag{6.31}$$

For each pair of canonical variates $(\mathbf{u}_i, \mathbf{v}_i)$, a Bayesian ordinary linear regression with standard noninformative prior distribution is applied independently (Figure 6.9, see Gelman et al., 2014, Chap. 14). The posterior predictive distribution $p(v_i \mid u_i^o)$ is then multivariate t with $n - 2$ degrees of freedom. Samples $\mathbf{v}_j = (v_j^{(1)}, v_j^{(2)}, \ldots)$ are drawn from $p(v_i \mid u_i^o)$. Then, the samples from all the

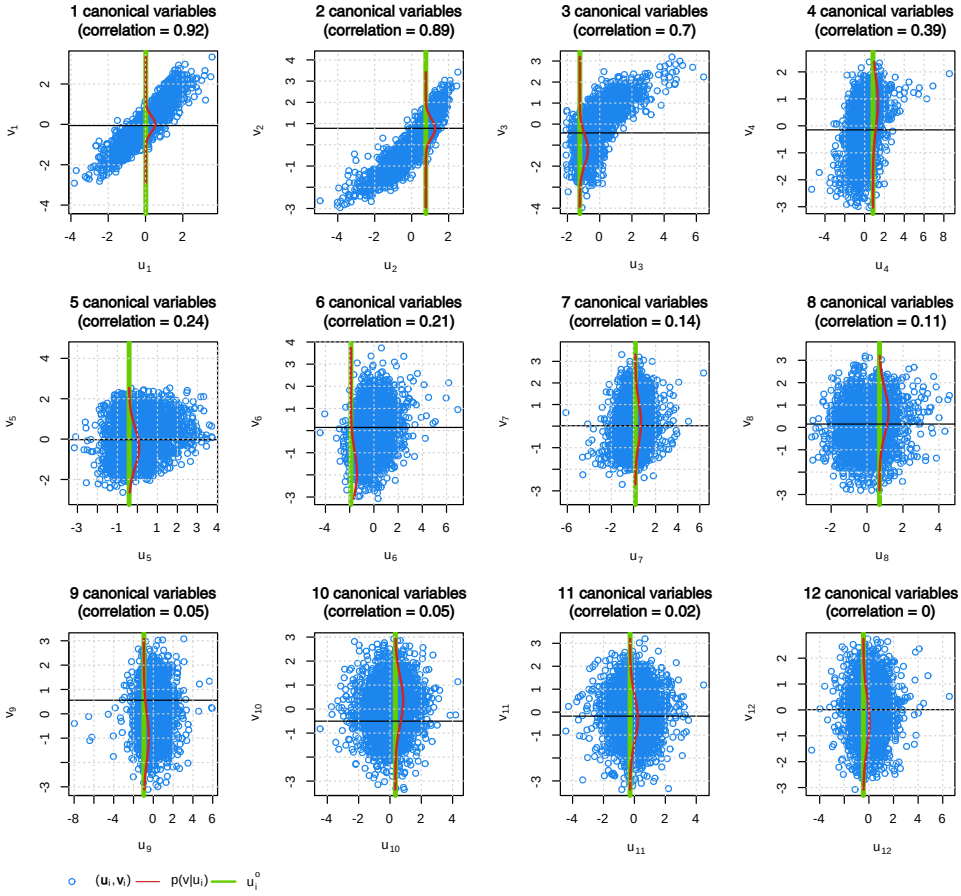

Figure 6.9 – Bayesian linear regression in the CCA space. Blue dots: pairs of canonical variates $(\mathbf{u}_i, \mathbf{v}_i)$. Green line: u_i^o, projection of the observed data statistics. Red line: predictive probability distribution $p(v_i \mid u_i^o)$.

canonical variates $\mathcal{V} = (\mathbf{v}_1, \ldots, \mathbf{v}_Q)$ are back-transformed into the parameter space with

$$\mathcal{O} = \mathcal{V}\mathbf{B}^\dagger\,, \tag{6.32}$$

where $\mathbf{B}^\dagger$ is the pseudo-inverse of canonical weights $\mathbf{B}$.

The samples $\mathcal{O} = [\boldsymbol{\theta}_1, \boldsymbol{\theta}_2, \ldots]^T$ approximate the posterior on the model parameters $p(\boldsymbol{\theta} \mid \mathbf{y}^o)$ and allow $\boldsymbol{\theta}_{\text{MAP}}$ to be estimated. Then, the approximate posterior $p(\mathbf{m} \mid \mathbf{y}^0, \boldsymbol{\theta}_{\text{MAP}})$ can be quantified.

6.4 Application to the case study

6.4.1 Designing the proposal distribution

To take advantage of the ABC MCMC with extended Metropolis update (Section 6.3.3), the proposal distribution $K(\cdot \mid \cdot)$ (Equation 6.25) must be carefully designed such that the Markov chain equilibrates to the prior $p(\mathbf{m})$. In this study, the Markov chain consists in updating the current realisation of the MPP $\mathbf{m}$ into a candidate $\mathbf{m}^\star$ by applying randomly one of the following update:

1. update the number of objects per layers, n_t (birth-and-death update of a Strauss process, Section 6.4.1).
2. update the horizontal object positions, $\mathbf{s}$ (move update of a Strauss process, Section 6.4.1).
3. update the number of layers, k (birth-and-death update of a Poisson process, Section 6.4.1).
4. update the layer elevations, $\mathbf{z}$ (move update of a Poisson process, Section 6.4.1).
5. update the object properties, ϕ, l, r_w, and r_h (update of a uniformly distributed variable, Section 6.4.1).

It may be tempting to apply only local updates close to the vertical model section to improve the convergence of the Markov chain. However, such local updates result in biased posterior and they don't preserved the symmetry of the detailed balance equation. Furthermore, the study objective is not to simulate the vertical section but the three-dimensional subsurface structure to perform further investigation in a later phase. The next sections provide more details about these updates that are not trivial.

Birth-and-Death Update of a Strauss Process

A birth-and-death update of a Strauss process cannot be simply performed by randomly adding and removing points, because the points of a Strauss process are not independent from each other as they interact when their pairwise distance is smaller than d. Therefore, the probability to add or remove a point must be first evaluated to ensure that the updated set of points honours the statistical characteristics of the Strauss process (Eq. 6.2). Concretely, the birth-and-death update of a Strauss process for a given set of points $\mathbf{s} = \{s_1, \dots, s_n\}$ consists in the following steps. (i) Chose to add (birth) or remove (death) a point, (ii) propose a candidate point, i.e., draw either a new point s_new or an existing point s_ℓ to remove, with $1 \leq \ell \leq n$, (iii) compute the probability that the proposed new set of points honours the Strauss process, (iv) accept the proposed new set of points according to this probability.

The probability of birth, p_b, is set equal to the probability of death, p_d. The birth proposal (i.e., draw a new object s_{new} within the horizontal model domain Ω_{xy}) is the uniform distribution over Ω_{xy} given by

$$q\left(\mathbf{s} \cup \{s_{\text{new}}\} \mid \mathbf{s}\right) = \frac{1}{\nu\left(\Omega_{xy}\right)}, \tag{6.33}$$

with $\mathbf{s} \cup \{s_{\text{new}}\}$ the set $\mathbf{s}$ augmented with the point s_{new} and $\nu\left(\Omega_{xy}\right)$ the area of Ω_{xy}.

The death proposal (i.e., draw a point s_ℓ (with $1 \leq \ell \leq n$)) is the uniform distribution over the n points of $\mathbf{s}$, given by

$$q\left(\mathbf{s} \setminus \{s_\ell\} \mid \mathbf{s}\right) = \frac{1}{n}, \tag{6.34}$$

with $\mathbf{s} \setminus \{s_\ell\}$ the set $\mathbf{s}$ without point s_ℓ. When $n = 0$, the death proposal is replaced by the identity proposal, i.e., 'do nothing' (Geyer, 2011).

The probability to accept the proposed set of points (either $\mathbf{s} \cup \{s_{\text{new}}\}$ or $\mathbf{s} \setminus \{s_\ell\}$) is $\min\left(1, r_{\text{G}}\right)$, with r_{G} the Green ratio (Green, 1995). In case of a birth proposal, the Green ratio is (Geyer and Møller, 1994; Illian et al., 2008; Geyer, 2011)

$$\begin{aligned} r_{\text{G}}\left(\mathbf{s} \cup \{s_{\text{new}}\} \mid \mathbf{s}\right) &= \frac{p_d}{p_b} \frac{q\left(\mathbf{s} \mid \mathbf{s} \cup \{s_{\text{new}}\}\right)}{q\left(\mathbf{s} \cup \{s_{\text{new}}\} \mid \mathbf{s}\right)} \frac{f_{\text{Strauss}}\left(\mathbf{s} \cup \{s_{\text{new}}\}\right)}{f_{\text{Strauss}}\left(\mathbf{s}\right)} \\ &= \frac{\nu\left(\Omega_{xy}\right)}{n+1} \cdot \beta\gamma^{\left(\sum_{i=1}^{n} \mathbb{1}\left(\|s_i - s_{\text{new}}\|_\kappa \leq d\right)\right)}. \end{aligned} \tag{6.35}$$

In case of a death proposal, the Green ratio is

$$\begin{aligned} r_{\text{G}}\left(\mathbf{s} \setminus \{s_\ell\} \mid \mathbf{s}\right) &= \frac{p_b}{p_d} \frac{q\left(\mathbf{s} \mid \mathbf{s} \setminus \{s_\ell\}\right)}{q\left(\mathbf{s} \setminus \{s_\ell\} \mid \mathbf{s}\right)} \frac{f_{\text{Strauss}}\left(\mathbf{s} \setminus \{s_\ell\}\right)}{f_{\text{Strauss}}\left(\mathbf{s}\right)} \\ &= \frac{n}{\nu\left(\Omega_{xy}\right)} \cdot \beta^{-1}\gamma^{-\left(\sum_{i=1, i\neq\ell}^{n} \mathbb{1}\left(\|s_i - s_\ell\|_\kappa \leq d\right)\right)}. \end{aligned} \tag{6.36}$$

Algorithm 6.5: Birth-and-death update of a Strauss process

$\mathbf{s} = \{s_1, \ldots, s_n\}$ ▷ start with n points
$u \sim \mathcal{U}(0,1)$
draw $\delta = \{+1, -1\}$ with probabilities $\{1/2, 1/2\}$
if $\delta == +1$ **then** ▷ birth proposal
  $s_{\text{new}} \sim \mathcal{U}(\Omega_{xy})$ ▷ draw a new point
  $r_{\text{G}} \leftarrow \frac{1}{n+1} \cdot \beta\gamma^{\left(\sum_{i=1}^{n} \mathbb{1}\left(\|s_i - s_{\text{new}}\|_\kappa \leq d\right)\right)}$ ▷ Green ratio
  if $u \leq \min(1, r_G)$ **then**
    $\mathbf{s} \leftarrow \mathbf{s} \cup \{s_{\text{new}}\}$ ▷ add the new point to s
  end
else if $n > 0$ **then** ▷ death proposal
  $\ell \sim \mathcal{U}(1, n)$ ▷ draw a point to delete
  $r_{\text{G}} \leftarrow n\beta^{-1}\gamma^{\left(-\sum_{i=1, i\neq\ell}^{n} \mathbb{1}\left(\|s_i - s_\ell\|_\kappa \leq d\right)\right)}$ ▷ Green ratio
  if $u \leq \min(1, r_G)$ **then**
    $\mathbf{s} \leftarrow \mathbf{s} \setminus \{s_\ell\}$ ▷ remove the point from s
  end
end

Move Update of a Strauss Process

Similarly, the move of a point from a set of points following a Strauss process cannot be done arbitrarily (spatial interaction). The update mechanism is as follows. First draw a point s_ℓ (with $1 \leq \ell \leq n$) and move it to a new position s'_ℓ. Then compute the probability that the proposed new set of points $\mathbf{s}' = \mathbf{s} \setminus \{s_\ell\} \cup \{s'_\ell\}$ honours the Strauss process (Eq. 6.2) and accept the move according to this probability (Algorithm 6.6).

Here, the new position s'_ℓ is uniformly drawn within a window centred around s_ℓ. This proposal is symmetric (the probability for a point to be selected is the same for every point and the probability to move s_ℓ to s'_ℓ is equal to the probability to move s'_ℓ to s_ℓ) except when the window centred around s_ℓ intersect the horizontal model boundary Ω_{xy}. To ensure complete symmetry and space continuity, Ω_{xy} is folded by connecting for each dimension the lower with the upper boundary (Vrugt, 2016). Because of the symmetry of the proposal, the Green ratio simplifies to the Metropolis ratio r_{M} (Metropolis et al., 1953). The probability to accept the proposed move is $\min(1, r_{\text{M}})$, with r_{M} given by

$$\begin{aligned} r_{\text{M}}\left(\mathbf{s} \setminus \{s_\ell\} \cup \{s'_\ell\} \mid \mathbf{s}\right) &= \frac{f_{\text{Strauss}}\left(\mathbf{s} \setminus \{s_\ell\} \cup \{s'_\ell\}\right)}{f_{\text{Strauss}}\left(\mathbf{s}\right)} \\ &= \frac{f_{\text{Strauss}}\left(\mathbf{s} \setminus \{s_\ell\} \cup \{s'_\ell\}\right)}{f_{\text{Strauss}}\left(\mathbf{s} \setminus \{s_\ell\} \cup \{s_\ell\}\right)} \\ &= \gamma^{\left(\sum_{i=1, i\neq\ell}^{n} \mathbb{1}\left(\|s_i - s'_\ell\|_\kappa \leq d\right) - \sum_{i=1, i\neq\ell}^{n} \mathbb{1}\left(\|s_i - s_\ell\|_\kappa \leq d\right)\right)}. \end{aligned} \tag{6.37}$$

Algorithm 6.6: Move update of a Strauss process

$\mathbf{s} = \{s_1, \ldots, s_n\}$ ▷ start with n points
$\ell \sim \mathcal{U}(1, n)$ ▷ draw a point s_ℓ to move
$s_\ell^\star \leftarrow s_\ell + \delta s$ ▷ propose a move
$r_{\mathrm{M}} \leftarrow \gamma^{\left(\sum_{i=1, i\neq\ell}^{n} \mathbb{1}\left(\|s_i - s'_\ell\|_\kappa \leq d\right) - \sum_{i=1, i\neq\ell}^{n} \mathbb{1}\left(\|s_i - s_\ell\|_\kappa \leq d\right)\right)}$ ▷ Metropolis ratio
$u \sim \mathcal{U}(0, 1)$
if $u \leq \min(1, r_M)$ **then**
    $s_\ell \leftarrow s_\ell^\star$
end

Birth-and-Death Update of a Poisson Process

The birth-and-death update of a Poisson process for a given set of points (layers) $\mathbf{z} = \{z_1, \ldots, z_k\}$ follows the same scheme as the birth-and-death update of a Strauss process (Sect. 6.4.1). Again, the birth probability p_b is set equal to the death probability p_d. The probability to accept the proposed set of points (either $\mathbf{z} \cup \{z_{\text{new}}\}$ or $\mathbf{z} \setminus \{z_\ell\}$) is $\min(1, r_{\mathrm{G}})$. The Green ratio is given by

$$\begin{aligned} r_{\mathrm{G}}\left(\mathbf{z} \cup \{z_{\text{new}}\} \mid \mathbf{z}\right) &= \frac{p_d}{p_b} \frac{q\left(\mathbf{z} \mid \mathbf{z} \cup \{z_{\text{new}}\}\right)}{q\left(\mathbf{z} \cup \{z_{\text{new}}\} \mid \mathbf{z}\right)} \frac{f_{\text{Pois}}\left(\mathbf{z} \cup \{z_{\text{new}}\}\right)}{f_{\text{Pois}}\left(\mathbf{z}\right)} \\ &= \frac{\nu\left(\Omega_z\right)}{k+1} \cdot \lambda\,, \end{aligned} \tag{6.38}$$

for a birth proposal and by

$$\begin{aligned} r_{\mathrm{G}}\left(\mathbf{z} \setminus \{z_\ell\} \mid \mathbf{z}\right) &= \frac{p_d}{p_b} \frac{q\left(\mathbf{z} \mid \mathbf{z} \setminus \{z_\ell\}\right)}{q\left(\mathbf{z} \setminus \{z_\ell\} \mid \mathbf{z}\right)} \frac{f_{\text{Pois}}\left(\mathbf{z} \setminus \{z_\ell\}\right)}{f_{\text{Pois}}\left(\mathbf{z}\right)} \\ &= \frac{k}{\nu\left(\Omega_z\right)} \frac{1}{\lambda}\,, \end{aligned} \tag{6.39}$$

for a death proposal.

Algorithm 6.7: Birth-and-death update of a Poisson process

$\mathbf{z} = \{z_1, \ldots, z_k\}$ ▷ start with k points
$u \sim \mathcal{U}(0, 1)$
$p_{+1} = \frac{1}{2} \cdot \min\left(1, \frac{\lambda}{k+1}\right)$ ▷ birth probability
$p_{-1} = \frac{1}{2} \cdot \min\left(1, \frac{k}{\lambda}\right)$ ▷ death probability
$p_0 = 1 - p_{+1} - p_{-1}$ ▷ no change probability
draw $\delta = \{+1, -1, 0\}$ with probabilities $\{p_{+1}, p_{-1}, p_0\}$
if $\delta == +1$ **then** ▷ birth proposal
    $s_{\text{new}} \sim \mathcal{U}(\Omega_z)$ ▷ draw a new point
    $\mathbf{z} \leftarrow \mathbf{z} \cup \{z_{\text{new}}\}$ ▷ add the new point to $\mathbf{z}$
else if $\delta == -1$ & $n > 0$ **then** ▷ death proposal
    $\ell \sim \mathcal{U}(1, n)$ ▷ draw a point to delete
    $\mathbf{z} \leftarrow \mathbf{z} \setminus \{z_\ell\}$ ▷ remove the point from $\mathbf{z}$
end

Move update of a Poisson process

The move update of a Poisson process is simple. For a set of points $\mathbf{z} = \{z_1, \ldots, z_k\}$, draw a point z_ℓ (with $1 \leq \ell \leq k$), then a move of this point to a new position z'_ℓ uniformly drawn within a window centred around z_ℓ. Because there is no interaction between the points in a Poisson process, any move proposal z'_ℓ within the model domain $\Omega_z = [z_{\min}, z_{\max}]$ is accepted. However, any move outside the model bounds must be correctly handled. As for the move update of the Strauss process, vertical model domain Ω_z is folded ensuring continuity of the model domain and symmetry of the detailed balance equation (Equation 6.24).

Algorithm 6.8: Move update of a Poisson process

$\mathbf{z} = \{z_1, \ldots, z_k\}$ ▷ start with k points
$j \sim \mathcal{U}(1, k)$ ▷ draw a point z_j to move
$z_j \leftarrow z_j + \delta z$ ▷ move z_j
if $z_j < z_{min}$ **then**
    $z_j \leftarrow z_{\max} - (z_{\min} - z_j)$
else if $z_j > z_{max}$ **then**
    $z_j \leftarrow z_{\min} + (z_j - z_{\max})$
end

Update of a uniformly distributed variable

For a variable l following a uniform distribution on $[l_{\min}, l_{\max}]$, a new value l' is uniformly drawn within a window centred around l. Any move proposal l' within the distribution bounds $[l_{\min}, l_{\max}]$ is always accepted. However, any move outside the distribution bounds must be correctly handled. Folding the distribution space, as for the move update of the Poisson process, creates sharp discontinuities. For example, an object with length l close the maximum length $l_{\max}$ may becomes very small after the update. Inspired by the 'reflection of a ball on the billiard table' problem (Michalewicz and Fogel, 2004) the move outside the bounds is 'reflected' on the distribution bounds, ensuring continuity and symmetry.

Algorithm 6.9: Update of a uniformly distributed variable

$l \sim \mathcal{U}(l_{\min}, l_{\max})$ ▷ initialization
δl ▷ window length such that $\frac{\delta l}{2} < (l_{\max} - l_{\min})$
$l' \sim \mathcal{U}(l - \frac{\delta l}{2}, l + \frac{\delta l}{2})$ ▷ move proposal
if $l' < l_{min}$ **then**
    $l' \leftarrow l_{\min} + (l_{\min} - l')$
else if $l' > l_{max}$ **then**
    $l' \leftarrow l_{\max} - (l' - l_{\max})$
end

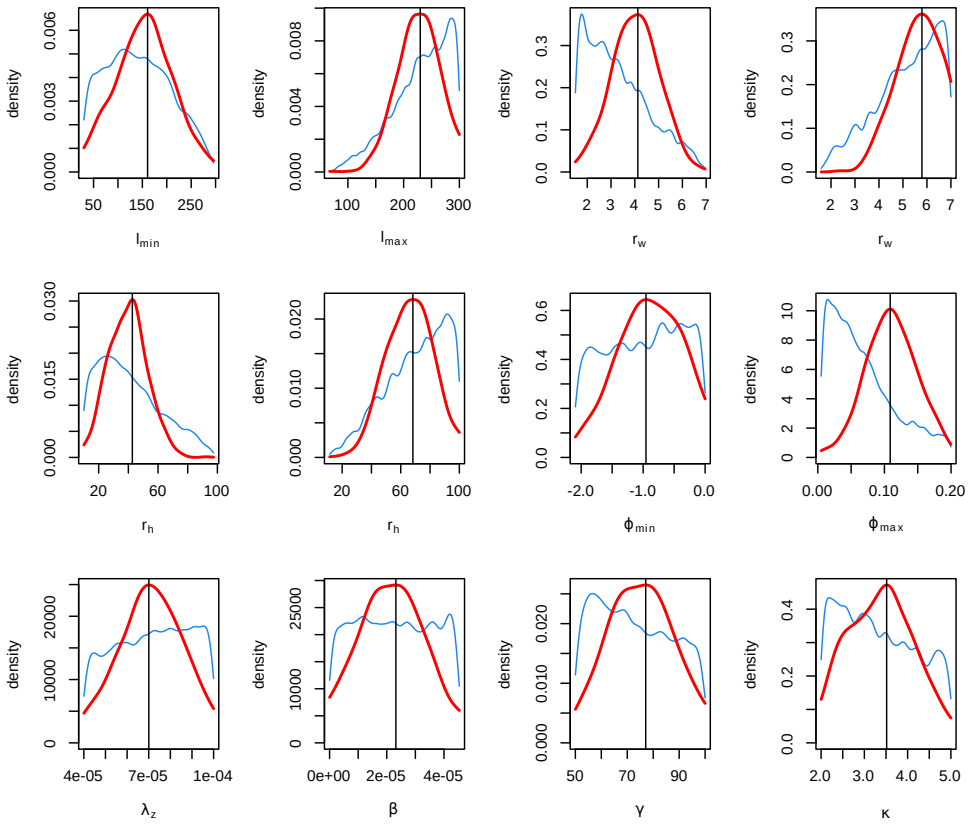

Figure 6.10 – Posterior distribution of the model parameters $\boldsymbol{\theta}$ estimated with ABC CCA-regression. Blue line: kernel density estimation of the parameter samples (prior). Red line: kernel density estimation of the posterior sample. Vertical black line: maximum a posteriori (MAP) estimate of the parameters.

6.4.2 Initialisation and convergence of the Monte Carlo Markov chain

MCMC is initialised with a MPP realisation that matches the data $\mathbf{y}_{\text{obs}}$ (Allard et al., 2005). More specifically, for each observed curve, an object is positioned close such that the age hierarchy of the objects is identical to that of the observed curves. Then, the McMC sampling is started.

The MCMC converges almost surely to $p(\mathbf{m} \mid \mathbf{y}^o, \boldsymbol{\theta}_{\text{MAP}})$ at infinite iterations. However, there is no general rule to evaluate how close the Monte Carlo sample is from the equilibrium distribution (Allard et al., 2005). Several diagnostic tools exist (some of them are based on multi-chain heuristic) but they can only inform about pseudo-convergence never about convergence (Geyer, 2011). Furthermore, the applications of such diagnostic tools are challenging when not applicable to three-dimensional MPP with different many update mechanisms. However, a few observations can be made before running the algorithm.

- ▷ The objects that match the data on the section (referred thereafter as matching objects) have less degrees of freedom than the other objects and a tiny chance to be replaced by other objects. Furthermore, the matching

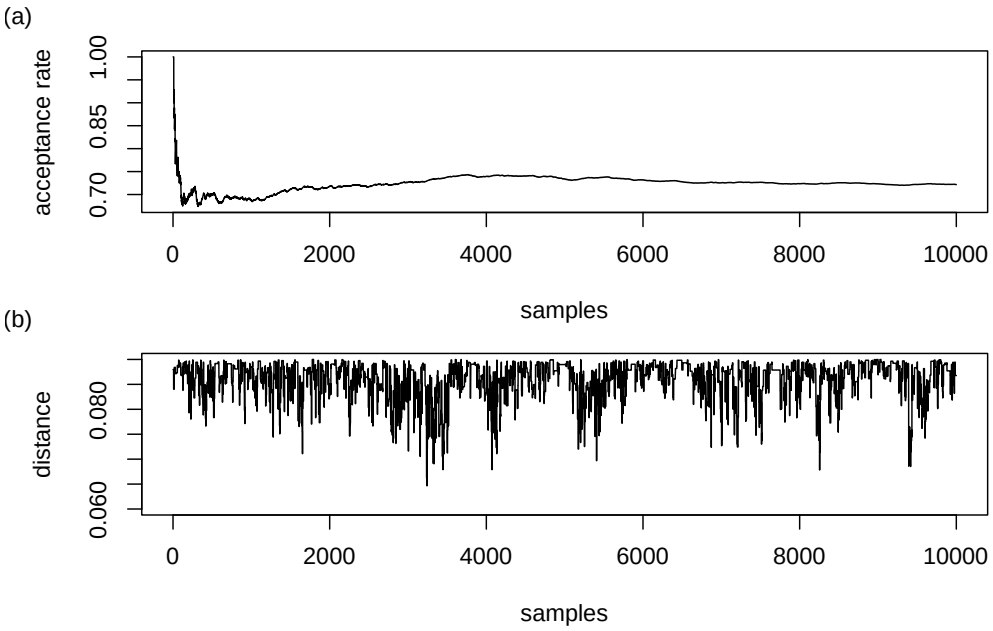

Figure 6.11 – Acceptance rate (top) and distance $\rho(\mathbf{y}_i, \mathbf{y}^o)$ (bottom) as a function of the number of samples of the MCMC chain.

objects must have the possibility to cross the section to ensure that the Markov chain can sample the whole posterior.

- ▷ The data conditioning influences the size and position of the objects close to the section. The objects cut by the section have either a small section (i.e., are enough away from the section) and are filtered out or they are almost completely eroded by the matching objects. Furthermore, these objects repulse the other objects that are on identical layers.
- ▷ The objects at a certain distance of the section are not influenced by the data conditioning. It can be expected that the posterior probability distribution of their size and orientation will be very close to the prior.

Based on these observations, the Markov chain was tuned such that (i) the objects outside the influence of the data conditioning as well as the objects on the section are perturbed many times, and (ii) the matching objects can cross the section or can be replaced by other objects. Note that the proposal $\mathbf{m}^\star$ that do not modify the section/likelihood are necessarily accepted.

The following sections outline the mathematical formulation of the latent model, based first on a conceptual description, then quantified in a marked point process model whose parameters are uncertain.

6.4.3 Scour Fill Ratio and Preservation Potential

The scour fill ratio (or scour fill proportion) and the preservation potential of the scour fills are indicators of the past dynamics of the depositional environment. These indicators can be used as proxies to describe the subsurface heterogeneity in terms of fast flow path connectivity (Siegenthaler and Huggenberger, 1993).

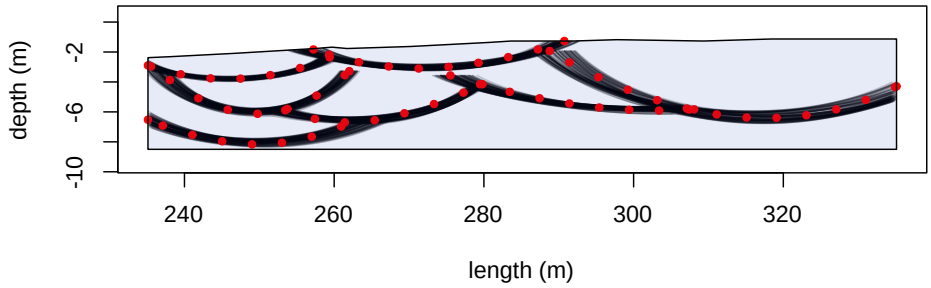

Figure 6.12 – Black lines: section of the sampled realisations (after filtering). Red dots: points defining the observed curves. Grey polygon: the model section.

The scour fill ratio is easily computed as the ratio of the scour fill volume and the model volume. The preservation potential is defined as the probability that a sedimentary unit will escape reworking over a fixed period of time (e.g., Meijer et al., 2008). The preservation potential is normally difficult to evaluate from observations solely. Here, it is estimated by the ratio of the cumulative volume of scour fill remnants to the sum of the volume of each scour fill prior any erosion (Deloffre et al., 2007),

$$p_{\text{preservation}} = \frac{\upsilon\left(\cup_{i=1,\dots,n}\boldsymbol{\mathcal{E}}_i\right)}{\sum_i^n \upsilon\left(\boldsymbol{\mathcal{E}}_i\right)}, \tag{6.40}$$

with $\upsilon\left(\cup_{i=1,\dots,n}\boldsymbol{\mathcal{E}}_i\right)$ the volume of the union of all the scour fills (i.e., the volume of scour fill remnants) and $\sum_i^n \upsilon\left(\boldsymbol{\mathcal{E}}_i\right)$ the sum of the volume of each individual scour fill prior any erosion.

6.5 Results and discussion

6.5.1 Prior Selection

The ABC CCA-regression is applied with the following summary statistics $\psi(\cdot)$:

- ▷ number of objects on the vertical model section,
- ▷ area formed by the curves,
- ▷ statistics on the curve lengths: min, max, mean, median, 1st and 3rd quantiles, cumulative length,
- ▷ median lengths of the curves projected on the horizontal and vertical axes,

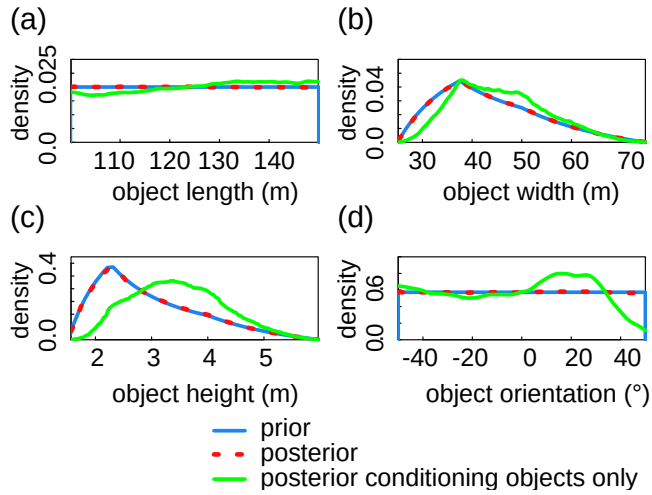

Figure 6.13 – Prior (in blue) and posterior (in red) probability densities of (a) the object length, (b) width, (c) height, and (d) orientation. The posterior probability densities of the matching objects only are displayed in green

- ▷ median ratio of the lengths of the curves projected on the horizontal and vertical axes,
- ▷ median number of layers.

Figure 6.9 shows the predictive probability distribution estimated for each pair of variates $(\mathbf{u}_i, \mathbf{v}_i)$. After back-transformation of the samples from $(\mathbf{u}_i, \mathbf{v}_i)$ into the parameter space, the MAP of the parameters is estimated with kernel density smoothing. The following MAP estimates are obtained:

- ▷ $\lambda_z = 0.11\,\mathrm{m}$
- ▷ $\beta = 7.0 \times 10^{-5}$
- ▷ $\gamma = 2.3 \times 10^{-5}$
- ▷ $d = 77\,\mathrm{m}$
- ▷ $\kappa = 3.5$
- ▷ $\phi_{\max} = 55°$
- ▷ $l_{\min} = 161\,\mathrm{m}$
- ▷ $l_{\max} = 230\,\mathrm{m}$
- ▷ $r_{\mathrm{w,min}} = 4.1$
- ▷ $r_{\mathrm{w,max}} = 5.8$
- ▷ $r_{\mathrm{h,min}} = 43$
- ▷ $r_{\mathrm{h,max}} = 68$

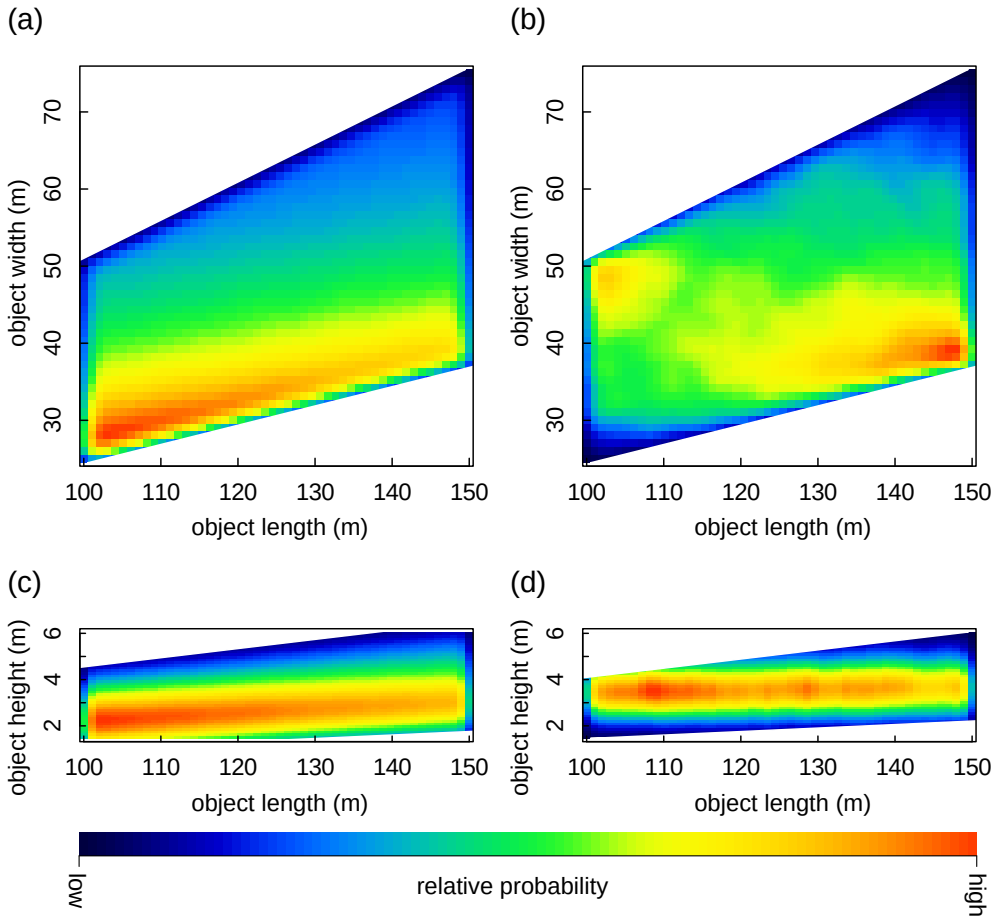

Figure 6.14 – (a) and (c): Posterior joint distribution of the object length and width, and length and height for all the objects. (b) and (d): Posterior joint distribution of the object length and width, and length and height for the matching object only

6.5.2 Posterior

One million iterations of the MCMC sampling run in about 10 hours on a personal computer (Intel Core $i7$-2,600 CPU @ 3.40 GHz). To avoid a slightly biased Monte Carlo distribution of the posterior the model sampling is started 100,000 iterations after the initialization. A model is sampled every 1,000 iteration in order to reduce the amount of data.

Figure 6.11(a) shows the acceptance rate as well the distance between simulated and observed data $\rho(\mathbf{y}_i, \mathbf{y}^o)$ as a function of the number of samples of the MCMC. As expected, the acceptance rate is very high (≈ 0.75) because not all the sampled models changed the model section and therefore many candidate realisation $\mathbf{m}^\star$ are accepted (e.g., removing an object that is not cut by the section does not change the likelihood).

As expected, the posterior probabilities of the object properties of all the objects are almost identical to the prior probability distributions, pointing out the consistency of the algorithm. On the contrary, the posterior probability distributions for the matching objects are significantly different from the prior

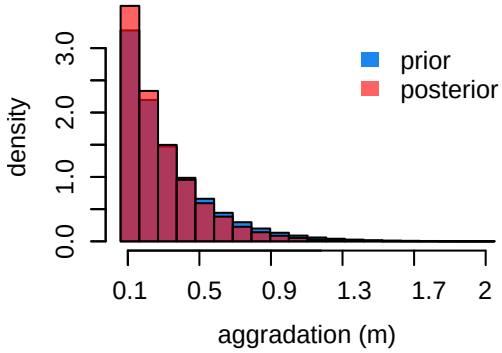

Figure 6.15 – Prior and posterior aggradation rate distribution (rate of net sediment distribution)

probability distributions (Figs 6.13 and 6.14). The matching objects are larger, wider and thicker than the prior specification, because (i) larger objects have a higher chance to be cut by the section, and (ii) only large scour fills were identified on the GPR data, indirectly specifying a minimum size for the matching objects. Contrarily to the prior that defines the object height as a function of the object length, the height of the matching objects is rather independent of the length (compare Fig. 6.14(c) and Fig. 6.14(d)). However, a bimodal joint distribution of the width and length of the matching objects is observed. Long and narrow matching objects are more probable followed by short and wide matching objects. The posterior aggradation rate is slightly smaller than the prior (Fig. 6.15).

Figure 6.16(a) shows the probability of observing objects at the vertical of a point on the x-y-plane. The influence zone of the section on the posterior is clearly visible. The area of higher probability through the section is a consequence of the data conditioning that constrains a number of matching objects on the section. The area of lower probabilities close to the section ends partly results from the repulsion property of the Strauss process and from the lower probability that objects lie near the section but without significantly crossing the section. The probability to observe objects can be used to design an additional GPR survey in order to catch the main structures. Based on Fig. 6.16(a), an additional parallel survey line should be less than 35 m apart from the section to likely probe some subsurface structures related to the first GPR data (Fig. 6.2).

The probability to observe objects at depth z (Fig. 6.16(b)) increases the first three meters and then stays almost constant with increasing depth (plateau). The first three meters below the surface have not experienced as much erosional and depositional processes as the subsurface below. This clearly illustrates that the near-subsurface is not representative of the deeper sedimentary structures. For the considered MPP, the position of the plateau observed in Fig. 6.16(b) depends on the object height (i.e., maximum erosion depth), the density of objects per layers, and the aggradation rate.

Both, the scour fill ratio and preservation potential are computed within the same volume below 3 m where the vertical probability to observe objects is almost constant (Fig. 6.16(b)). This volume includes the section as defined by

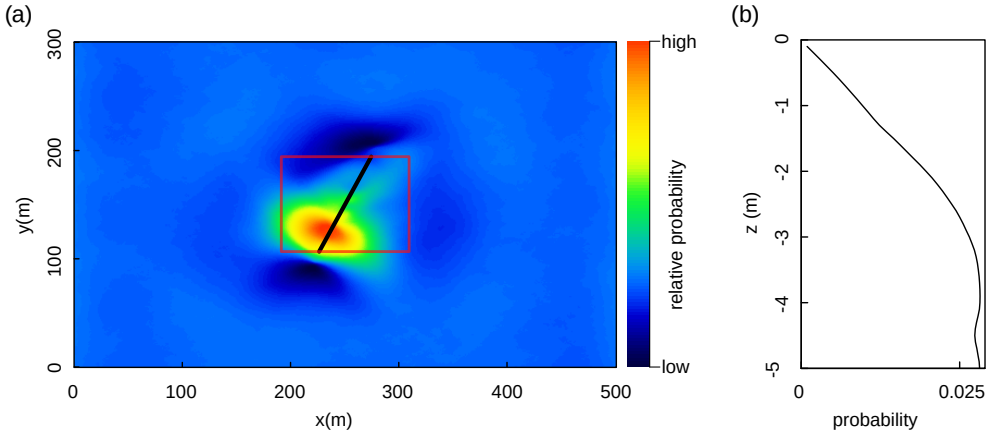

Figure 6.16 – (a) Probability to observe objects at the vertical of a point on the x-y-plane. (b) Probability to observe objects as a function of the depth

the red rectangle in Fig. 6.16(a). The posterior scour fill ratio and preservation potential are much less spread than the prior (Fig. 6.17). Contrary to the scour fill ratio, the scour fill preservation potential positively correlates with the aggradation rate (the larger the vertical distance between objects, the lower the chance that they erode each other) and negatively with the object size (larger objects have more chances to erode each other). Therefore, while the posterior scour fill ratio is larger than the prior, the posterior scour fill preservation potential is smaller than the prior. The large size of the matching objects as well as the slightly small posterior aggradation rate (Fig. 6.15) can partly explain the marked contrast between prior and posterior. Figure 6.17 indicates that the posterior exhibits significantly more remnant of scour fills than the prior and therefore, that the posterior is more heterogeneous in terms of hydraulic conductivity.

6.6 Conclusion

A Bayesian approach is applied to the stereological problem to quantify the posterior uncertainty on the three-dimensional subsurface structure based on a stochastic latent model and GPR data. In terms of mathematical formulation, the prior is a three-dimensional MPP that realistically mimics the main depositional and erosional processes of a braided system that are relevant for the understanding of subsurface heterogeneity. Such type of models is very flexible because it enables the simulation of different geological settings that result in distinct subsurface structures. Therefore, the MPP is a model from which knowledge can be learned, that is to say a basis to explore our understanding on the geological processes and a guide to geological interpretation. Although simple to simulate, the MPP is a pathological model because of its intractable prior and nontrivial likelihood. A novel ABC regression scheme is used to

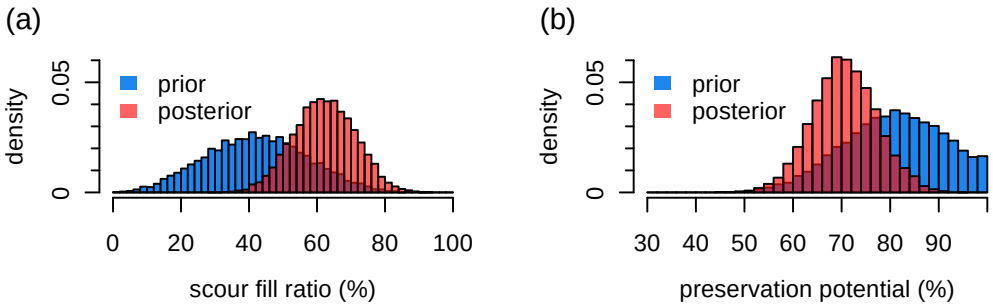

Figure 6.17 – (a) Prior and posterior the scour fill ratio. (b) Preservation potential of the scour fills. The posterior scour fill ratio and preservation potential are estimated within a volume around the section (defined by the red box on Fig. 6.16(a))

estimate the MAP parameters. The posterior for the given MAP parameter estimates is sampled with a ABC MCMC scheme based on the extended Metropolis update. The posterior allows the vertical cumulative probability of object occurrence in the x-y-plane as well as indicators of the past river dynamics such as the scour-fill ratio and preservation potential of scour fills to be computed computed. The same Bayesian approach can be applied to condition the MPP to additional GPR data and/or drill-core description (Regli et al., 2002). Furthermore, the methods presented here can serve as a template for any stochastic latent model with intractable prior and nontrivial likelihood.

References

Allard D., Froidevaux R. and **Biver P.** (2005) Accounting for Non-stationarity and Interactions in Object Simulation for Reservoir Heterogeneity Characterization, In: *Geostatistics Banff 2004* (Eds. O. Leuangthong and C. Deutsch), 14 of Quantitative Geology and Geostatistics, Springer Netherlands, 155–164.
doi: 10.1007/978-1-4020-3610-1_16

Avseth P., Mukerji T. and **Mavko G.** (2010) *Quantitative Seismic Interpretation*: Cambridge University Press, 408 pp.
ISBN:978-0-521-81601-7

Baddeley A. and **Vedel Jensen E.** (2004) *Stereology for Statisticians*: Chapman and Hall/CRC, 412 pp.
ISBN:9781584884057

Barnett T.P. and **Preisendorfer R.** (1987) Origins and Levels of Monthly and Seasonal Forecast Skill for United States Surface Air Temperatures Determined by Canonical Correlation Analysis. *Monthly Weather Review*, **115**(9): 1825–1850.
doi: 10.1175/1520-0493(1987)115<1825:oaloma>2.0.co;2

Beaumont M.A. (2010) Approximate Bayesian Computation in Evolution and Ecology. *Annual Review of Ecology, Evolution, and Systematics*, **41**(1): 379–406.
doi: 10.1146/annurev-ecolsys-102209-144621

Beres M., Green A., Huggenberger P. and **Horstmeyer H.** (1995) Mapping the architecture of glaciofluvial sediments with three-dimensional georadar. *Geology*, **23**(12): 1087–1090.
doi: 10.1130/0091-7613(1995)023<1087:MTAOGS>2.3.CO;2

Beres M. and **Haeni F.P.** (1991) Application of Ground-Penetrating-Radar Methods in Hydrogeologie Studies. *Ground Water*, **29**(3): 375–386.
doi: 10.1111/j.1745-6584.1991.tb00528.x

Beres M., Huggenberger P., Green A.G. and **Horstmeyer H.** (1999) Using two- and three-dimensional georadar methods to characterize glaciofluvial architecture. *Sedimentary Geology*, **129**(1–2): 1–24.
doi: 10.1016/S0037-0738(99)00053-6

Berthelsen K.K. and **Møller J.** (2006) Bayesian Analysis of Markov Point Processes, In: *Case Studies in Spatial Point Process Modeling* (Eds. A. Baddeley, P. Gregori, J. Mateu, R. Stoica and D. Stoyan), Springer New York, New York, NY, 85–97.
doi: 10.1007/0-387-31144-0_4

Bognar M.A. (2005) Bayesian inference for spatially inhomogeneous pairwise interacting point processes. *Computational Statistics & Data Analysis*, **49**(1): 1–18.
doi: 10.1016/j.csda.2004.04.008

Bognar M.A. (2007) Bayesian modeling of continuously marked spatial point patterns. *Computational Statistics*, **23**(3): 361–379.
doi: 10.1007/s00180-007-0073-9

Bristow C.S. and **Jol H.M.** (2003) An introduction to ground penetrating radar (GPR) in sediments. *Geological Society, London, Special Publications*, **211**(1): 1–7.
doi: 10.1144/GSL.SP.2001.211.01.01

Caers J. (2005) *Petroleum Geostatistics*: *SPE Interdisciplinary Primer Series*. Society of Petroleum Engineers, 104 pp.
ISBN:978-1-55563-106-2

Caers J. (2012) On internal consistency, conditioning and models of uncertainty, In: Ninth International Geostatistics Congress, Oslo, Norway June 11 – 15 .

Cannon A.J. and **Hsieh W.W.** (2008) Robust nonlinear canonical correlation analysis: application to seasonal climate forecasting. *Nonlinear Processes in Geophysics*, **15**(1): 221–232.
doi: 10.5194/npg-15-221-2008

Deloffre J., Verney R., Lafite R., Lesueur P., Lesourd S. and **Cundy A.** (2007) Sedimentation on intertidal mudflats in the lower part of macrotidal estuaries: Sedimentation rhythms and their preservation. *Marine Geology*, **241**(1-4): 19–32.
doi: 10.1016/j.margeo.2007.02.011

Dubrule O. (2003) *Geostatistics for Seismic Data Integration in Earth Models*: Society of Exploration Geophysicists, 283 pp.
ISBN:978-1-56080-121-4

Gelman A., Carlin J., Stern H., Dunson D., Vehtari A. and **Rubin D.** (2014) *Bayesian Data Analysis, Third Edition (Chapman & Hall/CRC Texts in Statistical Science)*: 3rd Edition. Chapman and Hall/CRC, London.
ISBN:9781439840955

Geyer C.J. (2011) Introduction to Markov Chain Monte Carlo, In: *Handbooks of Modern Statistical Methods* (Eds. S. Brooks, A. Gelman, G. Jones and X.L. Meng), Chapman and Hall/CRC, 3–48.
doi: 10.1201/b10905-2

Geyer C.J. and **Møller J.** (1994) Simulation Procedures and Likelihood Inference for Spatial Point Processes. *Scandinavian Journal of Statistics*, **21**(4): 359–373.

Glaser J.R. and **Glaser E.M.** (2000) Stereology, morphometry, and mapping: the whole is greater than the sum of its parts. *Journal of Chemical Neuroanatomy*, **20**(1): 115–126.
doi: 10.1016/s0891-0618(00)00073-9

Green P. (1995) Reversible jump Markov chain Monte Carlo computation and bayesian model determination. *Biometrika*, **82**: 711–732.

Hastings W.K. (1970) Monte Carlo sampling methods using Markov chains and their applications. *Biometrika*, **57**(1): 97–109.

Hauge R., Holden L. and **Syversveen A.R.** (2007) Well Conditioning in Object Models. *Mathematical Geology*, **39**(4): 383–398.
doi: 10.1007/s11004-007-9102-z

Hedin A. (2011) Stereological Method for Reducing Probability of Earthquake-Induced Damage in a Nuclear Waste Repository. *Mathematical Geosciences*, **43**(1): 1–21.
doi: 10.1007/s11004-010-9303-8

Heinz J., Kleineidam S., Teutsch G. and **Aigner T.** (2003) Heterogeneity patterns of Quaternary glaciofluvial gravel bodies (SW-Germany): application to hydrogeology. *Sedimentary Geology*, **158**(1–2): 1–23.
doi: 10.1016/S0037-0738(02)00239-7

Hermans T., Oware E. and **Caers J.** (2016) Direct prediction of spatially and temporally varying physical properties from time-lapse electrical resistance data. *Water Resources Research*, **52**(9): 7262–7283.
doi: 10.1002/2016wr019126

Hermans T., Vandenbohede A., Lebbe L. and **Nguyen F.** (2012) A shallow geothermal experiment in a sandy aquifer monitored using electric resistivity tomography. *Geophysics*, **77**(1): B11–B21.
doi: 10.1190/geo2011-0199.1

Hicks D.M., Duncan M., Walsh J., Westaway R. and **Lane S.** (2002) New views of the morphodynamics of large braided rivers from high-resolution topographic surveys and time-lapse video, In: *The structure, function and management of fluvial sedimentary systems* (Eds. F.J. Dyer, M.C. Thoms and J.M. Olley), 276, International Association of Hydrological Sciences, Wallingford, United Kingdom, 373–380.

Hotelling H. (1936) Relations between two sets of variates. *Biometrika*, **28**(3–4): 321–377.
doi: 10.1093/biomet/28.3-4.321

Howard C. and **Reed M.** (2010) *Unbiased Stereology*: QTP Publications.
ISBN:978-0-9565132-0-5

Huber E. and **Huggenberger P.** (2015a) Morphological perspective on the sedimentary characteristics of a coarse, braided reach: Tagliamento River (NE Italy). *Geomorphology*, **248**: 111–124.
doi: doi:10.1016/j.geomorph.2015.07.015

Huber E. and **Huggenberger P.** (2015b) Subsurface flow mixing in coarse, braided river deposits. *Hydrology and Earth System Sciences Discussions*, **12**: 9295–9316.
doi: 10.5194/hessd-12-9295-2015

Huggenberger P. and **Regli C.** (2006) A Sedimentological Model to Characterize Braided River Deposits for Hydrogeological Applications, In: *Braided Rivers* (Eds. G.H. Sambrook Smith, J.L. Best, C.S. Bristow and G.E. Petts), Blackwell Publishing Ltd., Ch. 3, 51–74.
doi: 10.1002/9781444304374.ch3

Illian J., Penttinen A., Stoyan H. and **Stoyan D.** (2008) *Statistical analysis and modelling of spatial point patterns*: John Wiley & Sons, Ltd.
ISBN:978-0-470-01491-2

Jol H.M. (2009) *Ground Penetrating Radar Theory and Applications*: Elsevier, 544 pp.

Jussel P., Stauffer F. and **Dracos T.** (1994) Transport modeling in heterogeneous aquifers: 1. Statistical description and numerical generation of gravel deposits. *Water Resources Research*, **30**(6): 1803–1817.
doi: 10.1029/94WR00162

Klingbeil R., Kleineidam S., Asprion U., Aigner T. and **Teutsch G.** (1999) Relating lithofacies to hydrofacies: outcrop-based hydrogeological characterisation of Quaternary gravel deposits. *Sedimentary Geology*, **129**(3–4): 299–310.
doi: 10.1016/S0037-0738(99)00067-6

Lantuejoul C. (2002) *Geostatistical Simulation, Models and Algorithm*: Springer, 256 pp.
ISBN:978-3-540-42202-0

Linde N., Renard P., Mukerji T. and **Caers J.** (2015) Geological realism in hydrogeological and geophysical inverse modeling: A review. *Advances in Water Resources*, **86, Part A**: 86 – 101.
doi: 10.1016/j.advwatres.2015.09.019

Lintusaari J., Gutmann M.U., Dutta R., Kaski S. and **Corander J.** (2017) Fundamentals and Recent Developments in Approximate Bayesian Computation. *Systematic Biology*, **66**(1): e66–e82.
doi: 10.1093/sysbio/syw077

Mahmoudzadeh M., Francés A., Lubczynski M. and **Lambot S.** (2012) Using ground penetrating radar to investigate the water table depth in weathered granites — Sardon case study, Spain. *Journal of Applied Geophysics*, **79**: 17 – 26.

Marin J.M., Pudlo P., Robert C.P. and **Ryder R.J.** (2012) Approximate Bayesian computational methods. *Statistics and Computing*, **22**(6): 1167–1180.
doi: 10.1007/s11222-011-9288-2

Marjoram P., Molitor J., Plagnol V. and **Tavaré S.** (2003) Markov chain Monte Carlo without likelihoods. *Proceedings of the National Academy of Sciences*, **100**(26): 15324–15328.
doi: 10.1073/pnas.0306899100

Meijer X.D., Postma G., Burrough P.A. and **de Boer P.L.** (2008) Modelling the Preservation of Sedimentary Deposits on Passive Continental Margins during Glacial-Interglacial Cycles, In: *Analogue and Numerical Modelling of Sedimentary Systems: From Understanding to Prediction* (Eds. P. de Boer, G. Postma, K. van der Zwan, P. Burgess and P. Kukla), Wiley-Blackwell, 223–238.
doi: 10.1002/9781444303131.ch10

Metropolis N., Rosenbluth A.W., Rosenbluth M.N., Teller A.H. and **Teller E.** (1953) Equation of State Calculations by Fast Computing Machines. *The Journal of Chemical Physics*, **21**(6): 1087–1092.
doi: 10.1063/1.1699114

Michalewicz Z. and **Fogel D.B.** (2004) *How to solve it - modern heuristics*: 2nd Edition. Springer, 554 pp.
ISBN:978-3-540-22494-5

Mo K.C. (2002) Ensemble canonical correlation prediction of precipitation over the Sahel. *Geophysical Research Letters*, **29**(12).
doi: 10.1029/2002gl015075

Mosegaard K. and **Tarantola A.** (1995) Monte Carlo sampling of solutions to inverse problems. *Journal of Geophysical Research: Solid Earth*, **100**(B7): 12431–12447.
doi: 10.1029/94JB03097

Neal A. (2004) Ground-penetrating radar and its use in sedimentology: principles, problems and progress. *Earth-Science Reviews*, **66**(3–4): 261–330.
doi: 10.1016/j.earscirev.2004.01.004

Pritchard J.K., Seielstad M.T., Perez-Lezaun A. and **Feldman M.W.** (1999) Population growth of human Y chromosomes: a study of Y chromosome microsatellites. *Molecular biology and evolution*, **16**(12): 1791–8.

Rauber M., Stauffer F., Huggenberger P. and **Dracos T.** (1998) A numerical three-dimensional conditioned/unconditioned stochastic facies type model applied to a remediation well system. *Water Resources Research*, **34**(9): 2225–2234.
doi: 10.1029/98WR01378

Regli C., Huggenberger P. and **Rauber M.** (2002) Interpretation of drill core and georadar data of coarse gravel deposits. *Journal of Hydrology*, **255**(1-4): 234 – 252.
doi: 10.1016/S0022-1694(01)00531-5

Rice R.M. (1972) USING CANONICAL CORRELATION FOR HYDROLOGICAL PREDICTIONS. *Hydrological Sciences Bulletin*, **17**(3): 315–321.
doi: 10.1080/02626667209493837

Robert C.P. and **Casella G.** (2004) *Monte Carlo Statistical Methods*: Springer New York.
ISBN:978-1-4419-1939-7

Russ J. and **Dehoff R.** (2000) *Practical Stereology*: Springer, New York, 381 pp.
ISBN:978-1-4613-5453-6

Satija A. and **Caers J.** (2015) Direct forecasting of subsurface flow response from non-linear dynamic data by linear least-squares in canonical functional principal component space. *Advances in Water Resources*, **77**: 69–81.
doi: 10.1016/j.advwatres.2015.01.002

Satija A., Scheidt C., Li L. and **Caers J.** (2017) Direct forecasting of reservoir performance using production data without history matching. *Computational Geosciences*, **21**(2): 315–333.
doi: 10.1007/s10596-017-9614-7

Siegenthaler C. and **Huggenberger P.** (1993) Pleistocene Rhine gravel: deposits of a braided river system with dominant pool preservation. *Geological Society, London, Special Publications*, **75**(1): 147–162.
doi: 10.1144/GSL.SP.1993.075.01.09

Sisson S.A. and **Fan Y.** (2011) Likelihood-Free MCMC, In: *Handbooks of Modern Statistical Methods* (Eds. S. Brooks, A. Gelman, G. Jones and X.L. Meng), Chapman and Hall/CRC, 313–335.
doi: 10.1201/b10905-13

Stauffer F. (2007) Impact of highly permeable sediment units with inclined bedding on solute transport in aquifers. *Advances in Water Resources*, **30**(11): 2194–2201.
doi: 10.1016/j.advwatres.2007.04.008

Storz-Peretz Y. and **Laronne J.B.** (2013) Morphotextural characterization of dryland braided channels. *Geological Society of America Bulletin*, **125**(9-10): 1599–1617.
doi: 10.1130/b30773.1

Tarantola A. (2005) *Inverse Problem Theory and Methods for Model Parameter Estimation*: Society for Industrial & Applied Mathematics (SIAM).
ISBN:978-0-89871-572-9

van Lieshout M.C. (2010) Spatial Point Process Theory, In: *Handbook of Spatial Statistics* (Eds. A.E.. Gelfand, P.J.. Diggle, M. Fuentes and P. Guttorp), CRC Press, 263–282 .
doi: 10.1201/9781420072884-c16

Vrugt J.A. (2016) Markov chain Monte Carlo simulation using the {DREAM} software package: Theory, concepts, and {MATLAB} implementation. *Environmental Modelling & Software*, **75**: 273 – 316.
doi: 10.1016/j.envsoft.2015.08.013

7

Subsurface flow mixing in coarse, braided river deposits

> *This indicates a lack of perspective on the functioning of hydrogeologic systems, as they do not realize that only some of their details are important to modeled system behavior and to the questions to be answered by the analysis. They need to understand that effective groundwater modeling involves discovery of which these factors might be.*

C.I. Voss (2011) Editor's message: Groundwater modeling fantasies — part 1, adrift in the details. Hydrogeology Journal, 19(7):1281–1284.
doi:10.1007/s10040-011-0789-z

Abstract Coarse, braided river deposits show a large hydraulic heterogeneity on the metre scale. One of the main depositional elements found in such deposits is a trough structure filled with layers of bimodal gravel (BM) and open-framework gravel (OW), the latter being highly permeable. However, the impact of such trough fills on subsurface flow and advective mixing has not drawn much attention. A geologically realistic model of trough fills is proposed and fitted to a limited number of ground-penetrating radar records surveyed on the river bed of the Tagliamento River (northeast Italy). A steady-state, saturated subsurface flow simulation is performed on the small-scale, high-resolution, synthetic model (size: 75 m × 80 m × 9 m). Advective mixing (i.e., streamline intertwining) is visualised and quantified based on particle tracking. The results indicate strong advective mixing as well as a large flow deviation induced by the asymmetry of the trough fills

E. Huber (2017) *Incorporating sedimentological observations, hydrogeophysics and conceptual knowledge to constrain 3D numerical heterogeneity models of alluvial systems.* Ph.D. thesis, Applied and Environmental Geology, University of Basel, Switzerland, 192 pp.

with regard to the main flow direction. The flow deviation induces a partial, large-scale rotational effect. These findings depict possible advective mixing found in natural environments and can guide the interpretation of ecological processes such as in the hyporheic zone.

Adapted from **Huber E.** and **Huggenberger P.** (2016) Subsurface flow mixing in coarse, braided river deposits. *Hydrol. Earth Syst. Sci.*, 20:2035–2046. doi:10.5194/hess-20-2035-2016

7.1 Introduction

The subsurface heterogeneity at the 1 m to 100 m scale can induce significant subsurface flow mixing that is relevant for aquifer remediation or drinking water extraction near a river or a contaminated area (e.g., Kitanidis, 1994; Mattle et al., 2001; Mays and Neupauer, 2012; Cirpka et al., 2015). Subsurface flow mixing is generally decomposed into an advective transport process combined with diffusion/dispersion (e.g., Mays and Neupauer, 2012). The advective transport process is best visualised with streamlines or streamtubes. Two-dimensional and three-dimensional flows exhibit a different streamline rearrangement when flowing through heterogeneities (Steward, 1998). Whereas two-dimensional, divergence-free flows locally deform the streamline geometry, three-dimensional, non-axisymetric flows permanently rearrange their streamtubes by redistributing the fluid within the subsurface (Steward, 1998; Janković et al., 2009). Janković et al. (2009) illustrated this difference by comparing two-dimensional and three-dimensional flows through an isolated, high-permeable subsurface structure, whose rotational axis was not aligned with the mean flow direction (i.e., non-axisymetric flows). For two-dimensional flows, the distance between the streamlines at a large distance upstream and downstream from the high-permeable structure remains the same. In contrast, the streamlines of three-dimensional flows are permanently deformed downstream from the high-permeable subsurface structure resulting in a complex intertwining of streamlines. Janković et al. (2009) coined the phrase *advective mixing* to describe these phenomena. Cirpka et al. (2015) identified three advective mixing phenomena that enhance solute mixing: (i) streamline focusing/defocusing, (ii) depth-dependent streamline meandering (i.e., streamline deviation), and (iii) secondary motion consisting in persistent twisting, folding, and intertwining of streamlines. Chiogna et al. (2015) demonstrated the occurrence of macroscopic helical flow in subsurface flow simulations where the hydraulic conductivity field was heterogeneous and locally isotropic. Despite the importance of advective mixing in solute mixing processes that enhance diffusion/dispersion (Hemker et al., 2004; Janković et al., 2009; Cirpka et al., 2015; Ye et al., 2015), volumetric concentration measurements on the field

cannot distinguish between advective mixing and dispersion/diffusion (Janković et al., 2009).

This study focuses on the subsurface heterogeneity of coarse, braided river deposits and its influence on advective mixing.

In this study the sedimentary heterogeneity is characterised following the hierarchy proposed by Huggenberger and Regli (2006), see also Chapter 2 for more details. In order of increasing size, this hierarchy consists of sedimentary textures, sedimentary structures, and depositional elements. As schematically represented in Fig. 2.8 (Chapter 2, page 28), coarse, braided river deposits are composed of two main depositional elements, remnants of gravel sheets (Huber and Huggenberger, 2015) and trough fills with clear-cut erosional lower-bounding surfaces (e.g., Siegenthaler and Huggenberger, 1993; Jussel et al., 1994a; Beres et al., 1995, 1999; Rauber et al., 1998; Stauffer and Rauber, 1998; Teutsch et al., 1998; Anderson et al., 1999; Klingbeil et al., 1999; Whittaker and Teutsch, 1999; Heinz and Aigner, 2003; Heinz et al., 2003; Huggenberger and Regli, 2006; Bayer et al., 2011). The sedimentary structure of the remnants of gravel sheets consists of horizontal to sub-horizontal layers with a poorly-sorted gravel (GP) texture. The sedimentary structure of the fills generally consists of alternating open-framework–bimodal gravel (OW–BM) couplet cross-beds, although fills consisting of GP cross-beds or of interfingering cross-beds of GP and sand are not uncommon (e.g., Siegenthaler and Huggenberger, 1993). Other less frequent sedimentary structures and depositional elements are described in the references above. Because the permeability contrast between the open-framework gravel (OW) texture and the other textures (bimodal gravel (BM), GP) is up to 3 orders of magnitude (e.g., Jussel et al., 1994a, Table 7.1), the spatial distribution of the OW gravel texture is expected to strongly influence the subsurface flow field and therefore to enhance advective mixing (Stauffer, 2007).

Based on observations of hydrofacies or sedimentary structures, several studies developed hydrogeological models of coarse, braided river deposits to investigate subsurface transport. Most of these studies assessed either macro-dispersion processes (e.g., Jussel et al., 1994b; Stauffer and Rauber, 1998), sorption processes (e.g., Rauber et al., 1998; Teutsch et al., 1998), or particle concentrations (e.g., Anderson et al., 1999; Heinz et al., 2003), mainly through the analysis of breakthrough curves. Stauffer (2007) modelled a trough fill of alternating OW–BM couplets by a highly permeable rectangular cuboid with an anisotropic hydraulic conductivity tensor. He quantified the subsurface flow disturbance downstream of the cuboid embedded in a homogeneous background matrix as

Table 7.1 – Hydraulic properties of the main sedimentary structures (after Jussel et al., 1994a).

	GP	BM	OW
porosity (-)	0.2	0.25	0.35
$\mathbf{K}_h$ (m/s)	$1.5 \cdot 10^{-3}$	$1.5 \cdot 10^{-3}$	$1 \cdot 10^{-1}$
$\boldsymbol{\sigma}_{lnK}$	0.5	0.1	0.1
$\mathbf{K}_h/\mathbf{K}_v$ (-)	6	1	1

a function of the angle of anisotropy of the hydraulic conductivity tensor. He noticed that 'the disturbance manifests itself by a distinct distortion of the streamtubes. Laterally, the influenced width is about 2.5 times the width of the [cuboid] for the considered case. Vertically, this influenced width makes up about 10 times the thickness of the [cuboid]' (Stauffer, 2007).

To the best of our knowledge the influence of trough fills on advective mixing has not been investigated with the exception of the work of Stauffer (2007) in which the complex trough fill structure was reduced to a simple cuboid with an homogeneous anisotropic conductivity. The present work aims to assess the influence of a *geologically realistic* representation of high-permeable trough fills on advective mixing.

The flow simulation is performed on a synthetic, conceptual model derived from ground-penetrating radar (GPR) data recorded over a small area (about 100 m × 50 m) of the river bed of the coarse, braided Tagliamento River (north-east Italy). First, the sedimentary structure of two overlapping trough fills is inferred from three GPR profiles, one 53 m long approximatively parallel to the main flow direction and two 7.5 m and 10 m long approximatively perpendicular to the main flow direction. Simple geometric objects corresponding to each sedimentary structure are manually fitted to the interpreted GPR records. Then, a high-resolution, steady-state, three-dimensional groundwater model is set up based on hydraulic properties borrowed from the literature. Finally, advective mixing is investigated with particle tracking.

7.2 Methods

7.2.1 Ground-penetrating radar data acquisition

The objective of the project was to quantify the proportion of depositional elements in the sedimentary deposits. Because the erosional lower-bounding surfaces of trough-shaped depositional elements can be followed over large distances (> 25 m), 14 widely spaced GPR lines (about 25 m line spacing on average) were acquired in a 100 m × 200 m large area on the river bed of the coarse, braided Tagliamento River downstream from the Cimano bridge (46°12′37.945″N, 13°0′50.165″E; WGS 1984). The GPR data were recorded with a PulseEkko Pro GPR system (Sensors & Software Inc., Mississauga, Canada) with 100-MHz antennae. The nominal spatial resolution length of the 100-MHz antennae is of the order of 0.3 m (Bridge, 2009). The topography of the GPR profiles was surveyed with a Total Station.

The GPR data were processed as follows:

- Time-zero adjustment.
- Direct current-offset removal based on samples before time zero.
- Dewowing of each trace by removal of the trend estimated with a Hampel filter (Pearson, 2002).

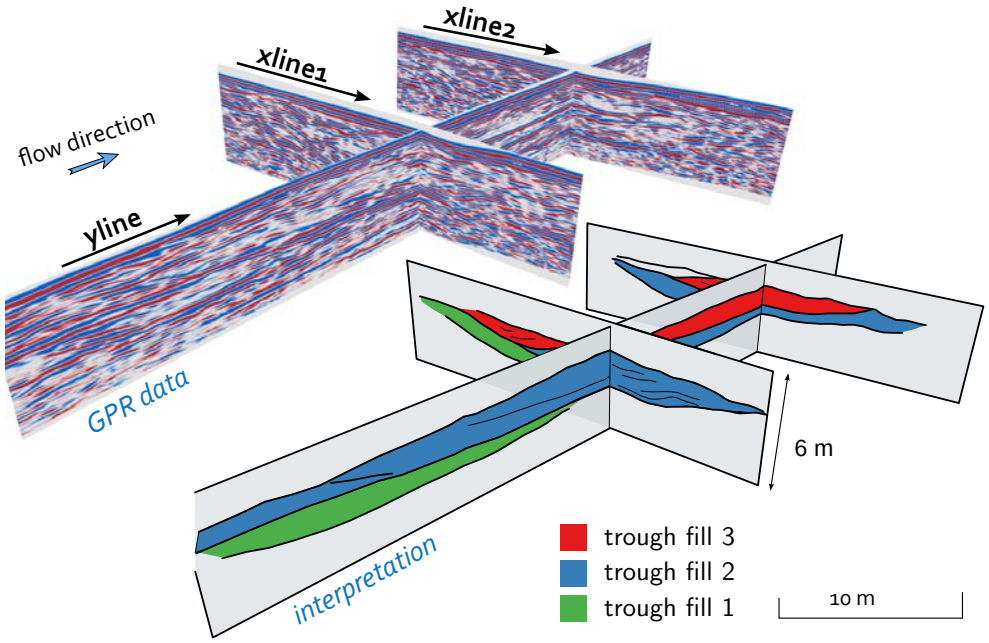

Figure 7.1 – Fence diagram of the ground-penetrating radar data and their interpretation. The black arrows indicate the GPR survey direction.

- ▷ A spherical and exponential gain was applied to compensate for geometric spreading and attenuation (Kruse and Jol, 2003; Grimm et al., 2006). This gain preserves the relative amplitudes.

- ▷ Low-pass filtering to remove the high (noisy) frequencies (corner frequencies at 150 MHz–200 MHz).

- ▷ Time-to-depth conversion with a constant velocity of 0.1 m/ns that leads to results that are sufficiently accurate for the purpose of this study. The velocity was estimated from previous common mid-point surveys recorded in the same area.

7.2.2 Ground-penetrating radar data interpretation

The interpretation of the GPR profiles is based on (i) continuity of the dominant reflectors within and between the profiles, (ii) differences of reflection patterns, and (iii) angular unconformity between the reflectors that can indicate an erosion surface or the superposition of two sedimentary structures with different sedimentary textures (Beres et al., 1995, 1999).

Three GPR profiles image three relatively well-preserved, overlapping trough fill structures that are identified by their erosional lower-bounding surfaces. Figure 7.1 shows the three GPR profiles as well as their interpretation. The GPR data indicate that the trough fills are elongated in the main flow direction (i.e., the valley orientation) with cross-tangential reflector. The GPR profile "xline1" (perpendicular to the mean flow direction; Fig. 7.3A) displays asymmetrical circular-arced reflectors that are almost symmetrical on the profile

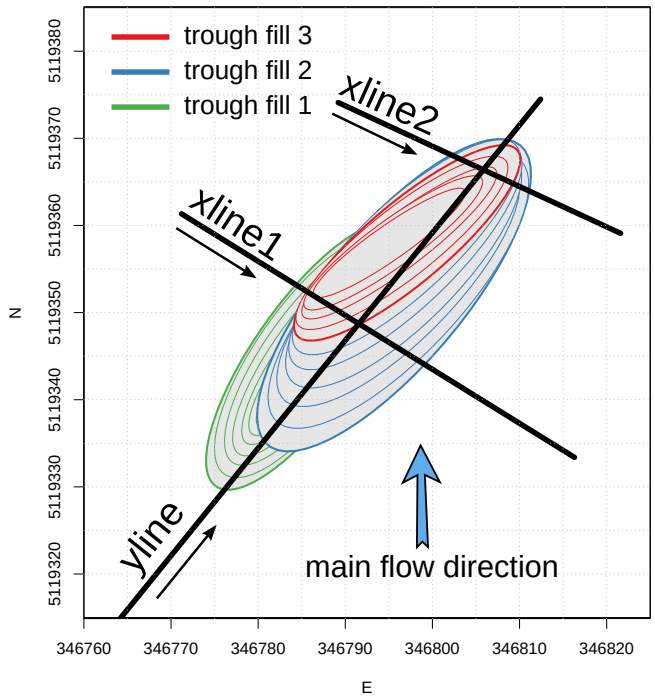

Figure 7.2 – Top view of the geometrical trough fill model (Coordinate system: WGS 1984, UTM Zone 33N). The trough fills are represented by green, blue, and red ellipses. The black lines indicate the position of the ground-penetrating radar profiles and the black arrows the ground-penetrating radar survey direction.

"xline2". Most of the older trough (represented in green in Fig. 7.1) is eroded by the younger troughs (represented in blue and red in Fig. 7.1).

7.2.3 Hydrogeological model

The three-dimensional model grid has a size of 75 m × 80 m × 9 m and a resolution of 0.5 m × 0.5 m × 0.1 m. The truncated ellipsoids are located between 0.6 m and 3.1 m below the surface. Because of the close correspondence of the GPR reflection patterns and of the sorting process with the observations made by Siegenthaler and Huggenberger (1993), Huggenberger (1993), Beres et al. (1995, 1999), and Heinz et al. (2003), we assume the hydraulic properties of the different types of gravel texture to be in the same order of magnitude as those estimated from measurements on disturbed and undisturbed samples in Quaternary coarse gravel deposits in northeast Switzerland (Jussel et al., 1994a). The hydraulic properties of the GP (see Table 7.1) are attributed to the background matrix, while the hydraulic properties of the BM and OW (Table 7.1) are alternatively assigned to the voxels located between two consecutive truncated ellipsoids, following the conceptual model shown in Fig. 2.8. For each voxel the hydraulic conductivities are drawn from log-normal distributions neglecting any spatial correlation (they are identically and independently distributed). The

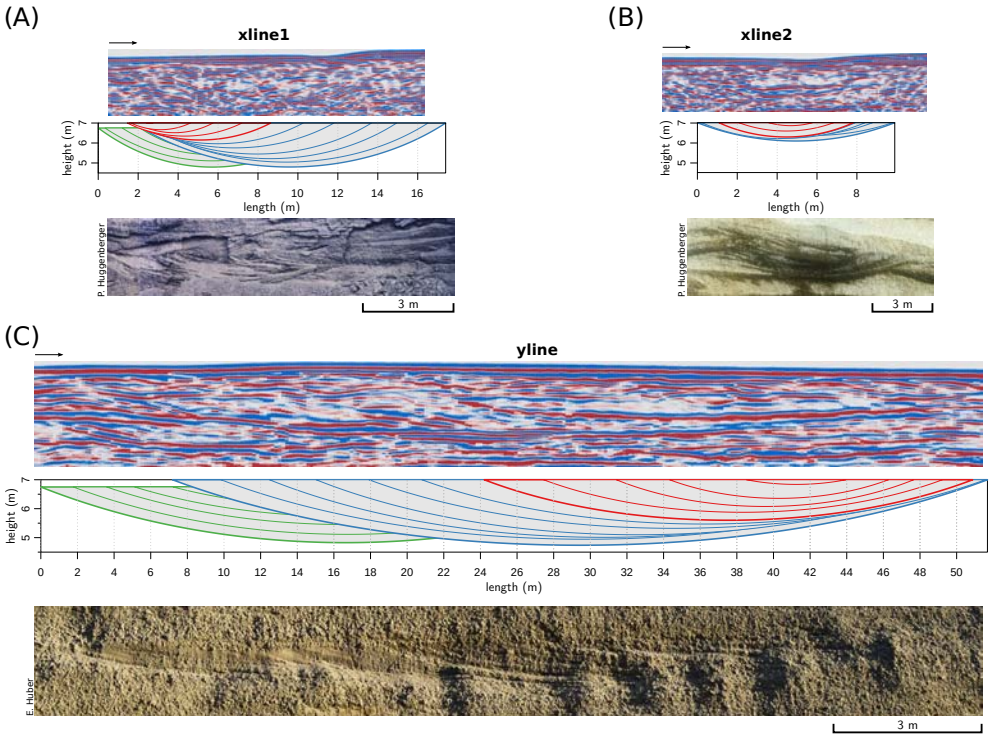

Figure 7.3 – (**A**)-(**C**) Ground-penetrating radar data, sections of the geometric model and vertical outcrop exposures (northeast Switzerland) for comparison purposes. The trough fills are represented by green, blue, and red ellipses. The black arrows indicate the GPR survey direction.

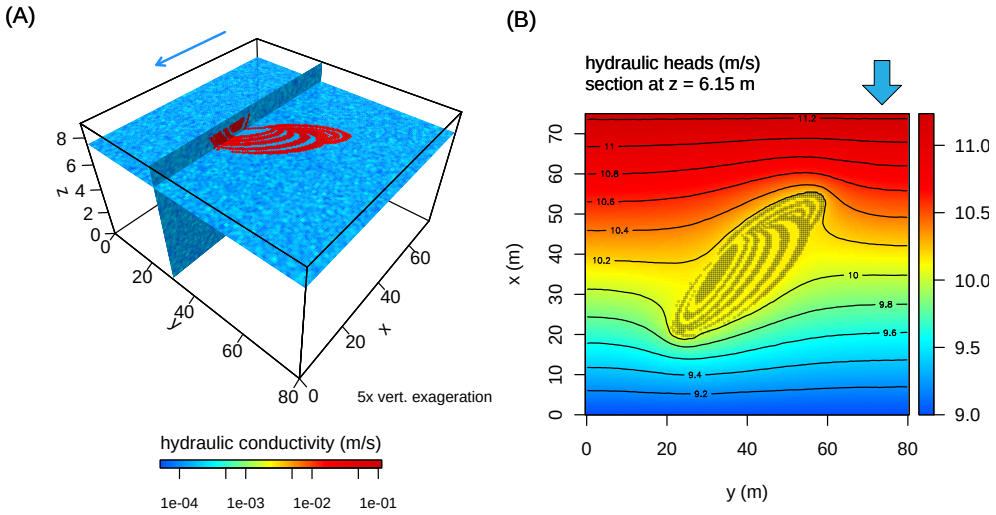

Figure 7.4 – **(A)** Hydrogeological model set-up with spatial distribution of the hydraulic conductivity values. **(B)** Hydraulic head at the upper model boundary (top view, contour every 0.2 m). The blue arrows indicate the main flow direction.

resulting conductivity field is displayed in Fig. 7.4A. The hydraulic conductivity tensors of the BM and OW are both isotropic. A vertical anisotropy of the hydraulic conductivity ($K_h / K_v = 6$) is assigned to the GP gravel texture to reflect the layered structure that hinders vertical flow.

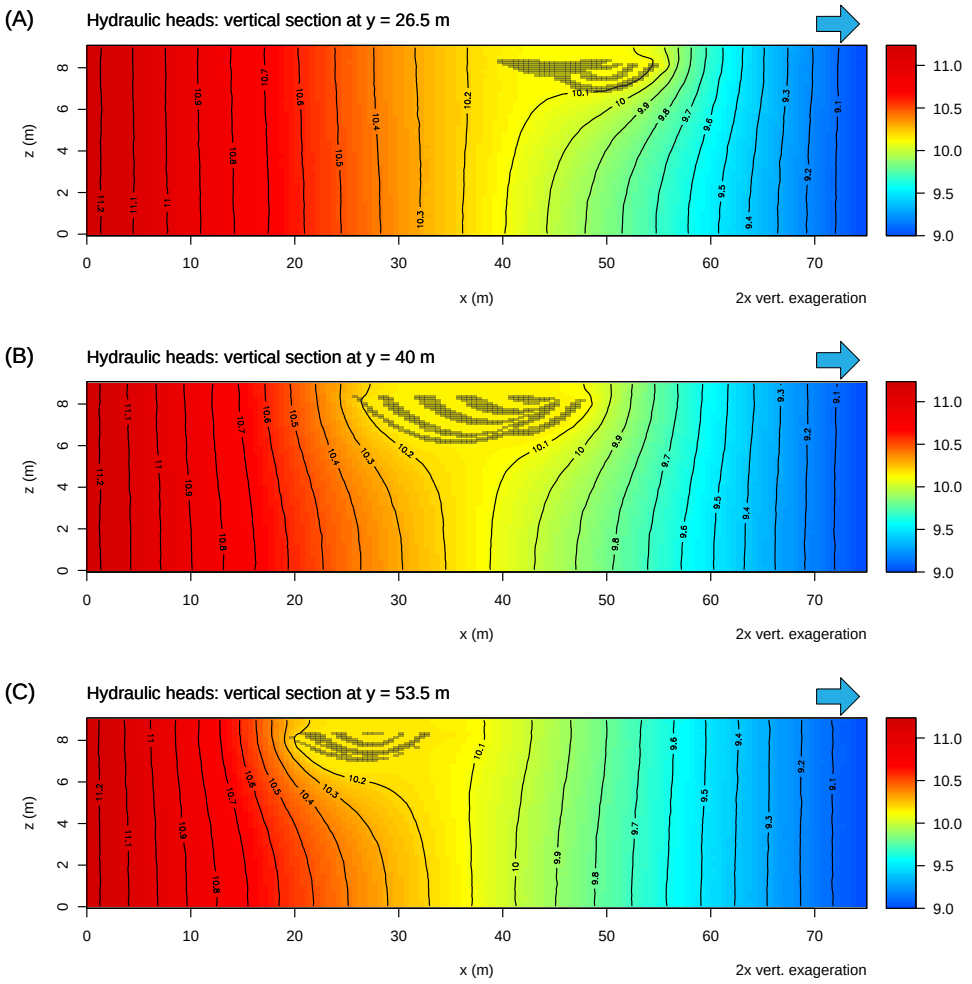

Figure 7.5 – Cross sections of the hydrogeological model along the x axis (see the coordinate system defined in Fig. 7.4A) with hydraulic head contours (every 0.2 m) superimposed on the hydraulic head values. The blue arrows indicate the main flow direction. The grey pixels correspond to the highly permeable layers of OW.

All model boundaries are set as a no-flow boundary with the exception of the inflow ($x = 0\,\text{m}$) and outflow ($x = 75\,\text{m}$) faces where constant head boundary conditions are specified (Fig. 7.4). The gradient between the inflow and the outflow model faces is 0.03 and corresponds to a locally large hydraulic gradient as found in situations where groundwater–surface water interactions occur. The saturated, steady-state subsurface flow simulation is performed with MODFLOW, the USGS three-dimensional finite-difference groundwater model (Harbaugh, 2005).

7.2.4 Advective mixing quantification

The advective flow is simulated with the particle-tracking code MODPATH (Pollock, 2012). One particle per cell is set on the model inflow face and the position of the particles travelling through the model is recorded. The resulting

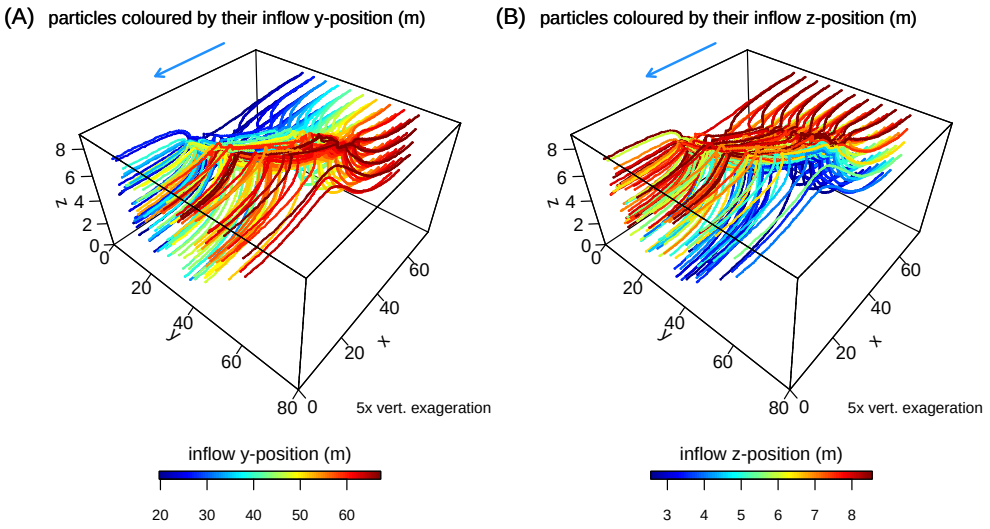

Figure 7.6 – Particles coloured by their **(A)** y coordinate position and **(B)** z coordinate position on the inflow face. The blue arrows indicate the main flow direction.

streamlines combined with a judicious colour scheme allow for visualisation of advective mixing. Furthermore, we quantify advective mixing by evaluating (i) particle deviation, (ii) particle divergence, and (iii) particle intertwining between the inflow face and the outflow face.

The particle deviation (Δ) is the transverse distance between the particle positions on the inflow face $(y_\mathrm{i}, z_\mathrm{i})$ and on the outflow face $(y_\mathrm{o}, z_\mathrm{o})$:

$$\Delta = \sqrt{(y_\mathrm{i} - y_\mathrm{o})^2 + (z_\mathrm{i} - z_\mathrm{o})^2}. \tag{7.1}$$

For each cells of the outflow face, we compute the median particle deviation from all particles within the cell.

The particle divergence indicates how far a particle flowed away from its eight particle inflow neighbours. For each particle we compute the absolute difference between (i) the median distance between the particle and its eight neighbours on the inflow face and (ii) the median distance between the particle and its eight neighbours from the inflow face on the outflow face.

The neighbours of a particle on the inflow face can be different from the neighbours of the same particle on the outflow face. Therefore, the particle intertwining is estimated for each particle by the proportion of its four inflow that are still its neighbours on the outflow face. In order to include all neighbour particles, the neighbours on the outflow face are defined as the first- and second-order neighbours of the Delaunay triangles i.e., the particles connected to the considered particle through an edge or two edges of the Delaunay triangles.

7.3 Results and discussion

7.3.1 Hydraulic heads

Similar to a high-permeable homogeneous structure, the overlapping trough fills significantly influence the hydraulic head distribution – vertically (Fig. 7.4B) and horizontally (Fig. 7.5) – inducing an asymmetric flow focusing and defocusing (compare with Fig. 7.6). Figure 7.5 shows within longitudinal cross sections how the vertical distribution of the hydraulic heads is significantly influenced by the trough fills: the hydraulic gradient is oriented upward, toward the trough fills at their upstream end and downward, away from the trough fills at their downstream end. However, even in the centre of the model this pattern is never symmetric (Fig. 7.5B) because of (i) asymmetry of the internal structure of the trough fills and (ii) non-alignment of the trough fills with the mean flow direction. The asymmetry of the vertical hydraulic head distribution becomes more asymmetric close to the lateral model boundaries. The upward gradient upstream from the trough fills slowly disappears toward the right model boundary (looking downstream; Fig. 7.5A), while the downward gradient downstream from the trough fills slowly disappears toward the left model boundary (Fig. 7.5c). The hydraulic gradient within the trough fills is very small (about 0.002).

The asymmetry of the three-dimensional hydraulic head distribution causes a permanent rearrangement of the streamlines. Therefore, in addition to a flow focusing and defocusing effect, persistent streamline deformations and rearrangements are expected.

7.3.2 Particle tracking

Figure 7.7 shows the position of the particles on the model outflow face coloured by their initial y and z coordinates on the inflow face. The convex hull of the particles on the outflow face that flowed through the trough fills as well as the shape of the trough fills projected on the outflow face are also represented. The size of the projected trough fill shape and convex hull are about 38.5 m × 2.2 m and 52.0 m × 6.7 m, respectively. On the inflow face, the shape of the convex hull of the particles that flow through the trough fills (not shown) is up to a lateral shift of 8 m nearly identical to the convex hull shown in Fig. 7.7. This could indicate a similar flow focusing and defocusing effect combined with a lateral flow deviation. However, a notable particle deviation is clearly visible inside and outside the convex hull (see also Fig. 7.8). The median particle deviation is 4.0 m whereas the maximum is 28.1 m. The particle deviation outside the convex hull is very small with the exception of some particles below the convex hull (up to 12 m). Even if small, the particle deviation outside the convex hull is smoothly varying because these particles flowed through the low heterogeneous GP. The largest particle deviations are observed within the convex hull. There, the particle deviations are irregular in amplitude and direction but still show an horizontal trend as expected from the orientation of the trough fills. Note that the asymmetry of the trough fills causes a partial, large-scale rotation of the particles.

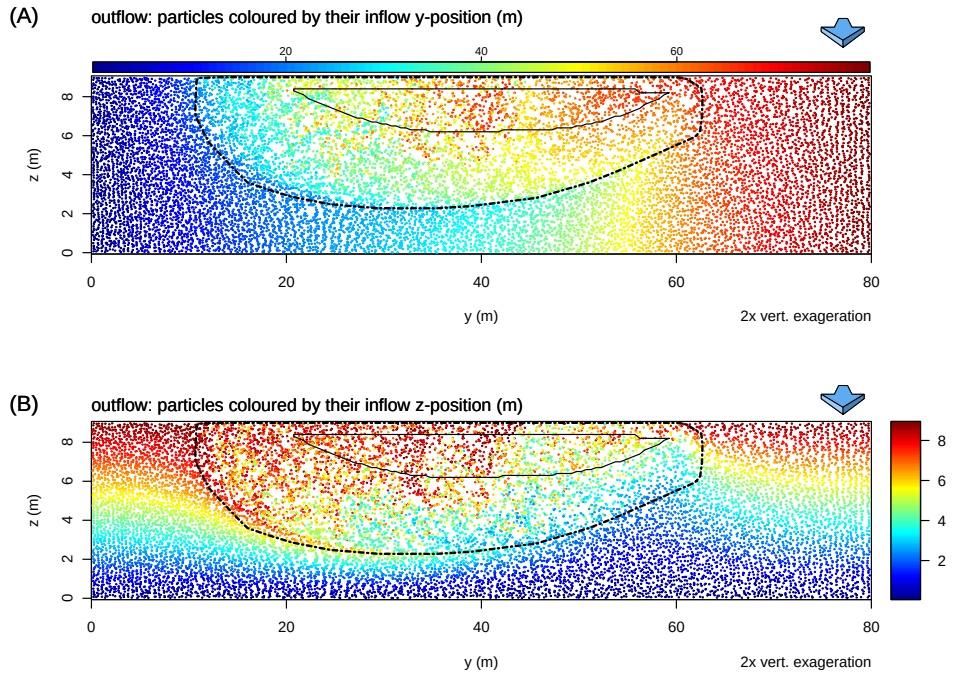

Figure 7.7 – Particles on the model outflow face coloured by their **(A)** y coordinate position and **(B)** z coordinate position on the inflow face. The black line represents the shape of the trough fills projected on the outflow face and the dashed line represents the convex hull of the particles on the outflow face that flowed through the trough fills. The blue arrows indicate the main flow direction.

The largest median distances between each particle and its eight inflow neighbours on the outflow face are found within the convex hull (Fig. 7.9A), where most of the particles lay at least 4 times farther away from their inflow neighbours as on the inflow face. The median distance between a particle and its eight neighbours is 0.1 m on the inflow face and less than 2 % of the particles are more than 10 m away from their neighbours. The largest distances are found in the central part of the convex hull that is associated to the two younger trough fills (trough fills 2 and 3 in Figs. 7.1 and 7.2). More than the half of the particles outside the convex hull lay closer to their inflow neighbours on the outflow face. The analysis of the remaining neighbours (Fig. 7.9B) attests for a strong particle intertwining as indicated by Fig. 7.9A. Indeed, about 70 % of the particles in the convex hull on the outflow face are no longer surrounded by their four initial neighbours from the inflow face.

7.3.3 Advective mixing mechanism

For clarity, Fig. 7.10 shows only a few particle paths that cross the trough fills. The particles upstream from the trough fills are attracted by the highly permeable layers of the OW. Shortly before the particles enter the trough fills, some of them show a strongly curved path toward the trough fills. The particles that enter the OW layers move horizontally within these layers until they dip upward. A closer look on Fig. 7.10 reveals series of sharp vertical zigzags of

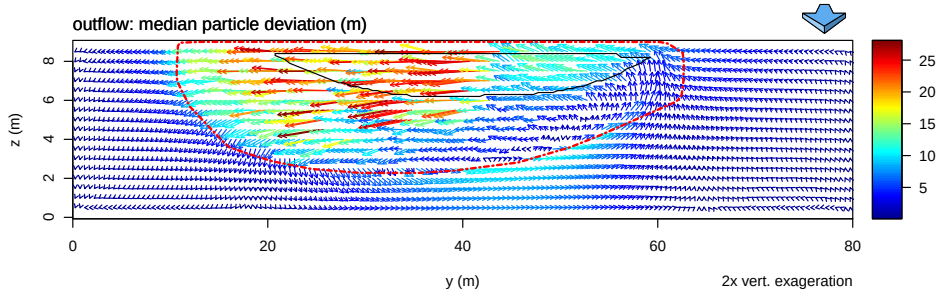

Figure 7.8 – Median particle deviation between the inflow face and the outflow face (computed vertically for every five cells) represented by arrows. The arrow length and colour correspond to the deviation magnitude. The black line represents the shape of the trough fills projected on the outflow face and the dashed, red line represents convex hull of the particles on the outflow face that flowed through the trough fills. The blue arrow indicates the main flow direction.

the particle paths, predominantly at the downstream end of the trough fills where the layers of OW dip upward. These zigzags occur where the particles tightly jump vertically between two adjacent layers of OW.

Figure 7.11 displays an enlarged view of a vertical section of the model along the main flow direction that shows the layers of OW as well as the vertical hydraulic head distribution. The arrows represent the volumetric flux (Darcy's flux) vectors projected on the vertical section for each cell of the OW layers. Note that the hydraulic conductivity tensor within the trough fills is isotropic. Therefore, the volumetric flux along each dimension of the Cartesian coordinate system is proportional to the hydraulic conductivity at the cell interface times the hydraulic gradient along the same dimension. Figure 7.11 reveals a complex spatial distribution of the volumetric flux that appears rather chaotic in the upward-dipping part. However, we observe that four of the upward-dipping layers of the OW present a similar pattern: although very small in amplitude, the volumetric flux of the lower cells of these layers tend to point downward whereas in the upper cells the flux tend to point upward. The vertical position of the particles within the OW layers is therefore critical because two closely spaced particles can flow in opposite direction. As a consequence, the volumetric flux pointing downward lets some of the ascending particles exit the trough fill earlier (see Fig. 7.10). In a similar way, two closely spaced particles do not enter the trough fills at the same position and therefore follow different paths within the trough fills. Small spatial variations of the volumetric flux (not only vertically but also horizontally) can drive the particles far away from each other (Fig. 7.10). This advective mixing illustrates the importance of the interplay between the hydraulic head field and the spatially distributed hydraulic conductivity that results in an heterogeneous volumetric flux distribution within the trough fills.

In consequence, the transport process through the trough fills can be viewed as a chaotic process where the particle positions on the outflow face depends on the initial particle positions on the inflow face (Neupauer et al., 2014). Note that the same effect is obtained with homogeneous hydraulic conductivity for each sedimentary texture. Spatial random hydraulic conductivity values increase advective mixing at a level that is negligible compared with the

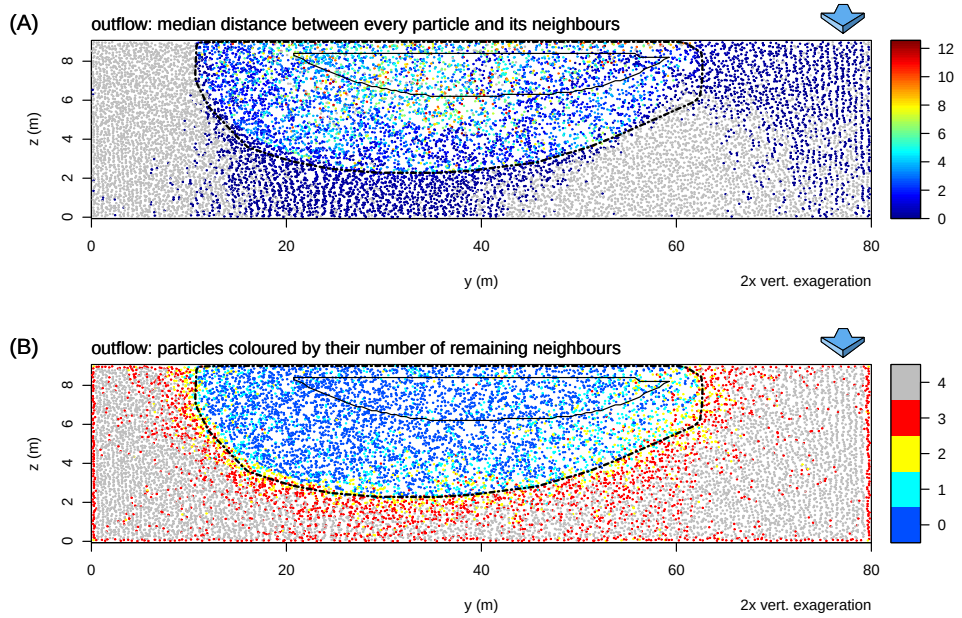

Figure 7.9 – Particles on the model outflow face. **(A)** Median distance between each particle and its eight inflow-face neighbours computed on the outflow face. **(B)** For each particle on the outflow face, number of remaining neighbours from their four inflow-face neighbours. The black line represents the shape of the trough fills projected on the outflow face and the dashed line represents convex hull of the particles on the outflow face that flowed through the trough fills. The blue arrow indicates the main flow direction.

advective mixing resulting from the three-dimensional arrangement of the different textures.

Investigation on the influence of hydraulic gradient, hydraulic conductivity of the OW, vertical anisotropy, and trough fill orientation on advective mixing showed the following: (i) the decrease of the hydraulic gradient significantly increases the lateral deviation of the particles; (ii) the extent of the convex hull of the particles that crossed the trough fills, the particle deviation, and mixing increase with increasing hydraulic conductivity of the OW; (iii) the vertical extent of the convex hull zone downstream of the trough fills as well as the vertical particle deviation are inversely proportional to the vertical anisotropy ($K_\mathrm{h} \,/\, K_\mathrm{v}$) of the GP texture (matrix) because a large vertical anisotropy of the GP texture hampers vertical flow; (iv) the angle between the trough fills and the main flow direction plays an important role for the mixing processes. The width and height of the mixing zones negatively correlate when the orientation of the trough fills changes impacting significantly advective mixing. Furthermore, when the trough fills are aligned with the main flow direction, a partial, transverse rotation of the particles is observed within the convex hull. When the trough fills are perpendicular to the main flow direction, the advective mixing is the smallest. The largest convex hull, particle deviation and mixing are found when the trough fills form an 45° angle with the main flow direction.

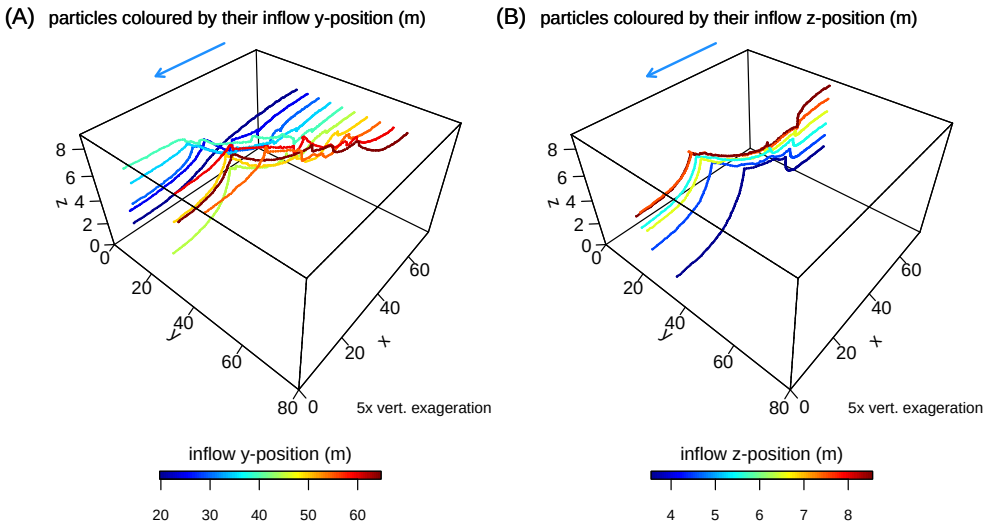

Figure 7.10 – Selected particles coloured by their **(A)** y coordinate position and **(B)** z coordinate position on the inflow face. The blue arrow indicates the main flow direction.

7.4 Discussion

Advective mixing is enhanced by the spatial distribution of trough fills in the sedimentary record and by the unsteady flow magnitude and direction. The advective mixing zones of closely spaced trough fills can interfere, resulting in a more complex pattern of subsurface flow. Under transient boundary conditions the mean flow direction and therefore the angle between the trough fills and the main flow direction change with time. In such a situation, the advective mixing zone as well as the flow patterns are expected to vary spatially and temporally, most likely leading to enhanced advective mixing. Because of this complexity, the present experiment is a starting point for further investigations into the influence of different proportions and types of trough fills on advective mixing in coarse fluvial aquifers on the 1 m–100 m scale.

In the presented synthetic model, the layers of GP are modelled by an uniform, anisotropic matrix because the interface between the layers of GP are barely identifiable on the GPR records. While the model set-up (isolated trough fills embedded in GP) was observed in gravel quarries (e.g., Siegenthaler and Huggenberger, 1993), thin, finite layers of OW can also be found within the layers of GP (e.g., Huggenberger and Regli, 2006). However, the contribution of these thin, high-permeable structures to advective mixing is expected to be negligible compared to that of the trough fills. The hydraulic conductivity tensors of the BM and OW are both isotropic. However, upon upscaling, the OW–BM couplets lead to an anisotropic hydraulic-conductivity tensor (e.g., Jussel et al., 1994a; Stauffer, 2007) with the thickness-weighted arithmetic mean of the two conductivities within the layering and the thickness-weighted harmonic mean perpendicular to it. Therefore, on larger scales, the flow direction may not be parallel to the hydraulic head gradient.

Note that the use of an interpolation scheme is superfluous if densely sampled GPR data are available (e.g., pseudo three dimensional GPR survey) and the

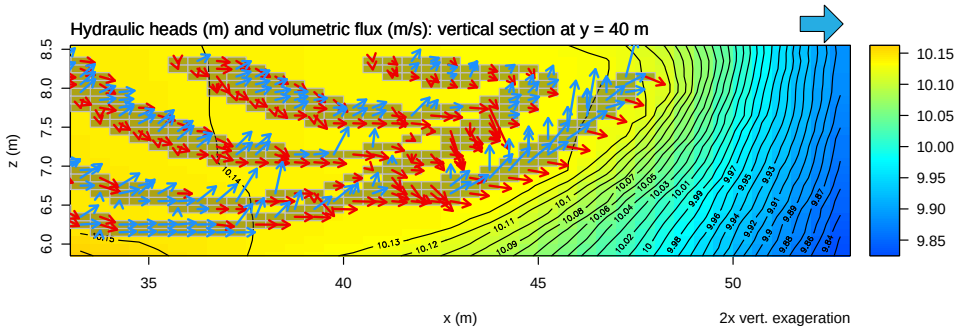

Figure 7.11 – Enlarged view of the vertical section of the hydrogeological model along the x axis with the hydraulic head contours (every 0.01 m) superimposed on the hydraulic head values. The grey rectangles represent the OW cells. The arrows correspond to the volumetric flux vectors projected on the model section; red indicates that the flux flows downward, blue upward. The large blue arrow on top indicates the main flow direction

different sedimentary textures are well-resolved by GPR.

7.5 Conclusion

In this study, the hydraulic heterogeneity of coarse, braided river deposits is modelled through a simple geometrical model based on geological observations. The modelled trough fills (i) act as an attractor for the groundwater upstream of the trough fills, (ii) induce a significant intertwining of the streamlines that flow through it, resulting in strong advective mixing, and (iii) cause a strong horizontal streamline deviation that results in a partial, large-scale flow rotation. Furthermore, the anisotropy of the hydraulic conductivity of the GP strongly influences vertical advective mixing whereas the orientation of the trough fills determine the flow patterns and therefore the degree of mixing. The advective mixing produced by the trough fills resembles a chaotic process that is very sensitive to the initial positions of the streamlines. While the emphasis is often put on the fast flow pathways and their connectivity, this study demonstrates the importance of the sedimentary structure of the *whole* geological fabrics in interaction with the hydraulic boundary conditions (see also Voss, 2011).

This study is only valid for the considered type of trough fills, i.e., trough fills consisting of layers of BM and OW, and for the proposed conceptual model. Trough fills consisting of cross-bedded GP or of interfingering cross-beds are very likely to lead to different flow structures and therefore to different mixing patterns. The subsurface structure could more accurately be modelled with high-resolution GPR data, thereby making the use of the geometrical model unnecessary.

The study findings shed light on possible advective mixing in natural environments and indicate complex advective mixing in dynamic systems such as in

systems characterised by significant groundwater–surface water interactions. A better understanding of the sedimentary structure can provide an additional support to the interpretation of the ecological processes in the hyporheic zone.

Acknowledgement

Special thanks go to T. Hermans for constructive comments. The critical review from the editor (M. Giudici) and three anonymous referees helped to improve the quality of the manuscript.

References

Anderson M., Aiken J., Webb E. and **Mickelson D.** (1999) Sedimentology and hydrogeology of two braided stream deposits. *Sedimentary Geology*, **129**(3–4): 187–199. doi: 10.1016/s0037-0738(99)00015-9

Bayer P., Huggenberger P., Renard P. and **Comunian A.** (2011) Three-dimensional high resolution fluvio-glacial aquifer analog: Part 1: Field study. *Journal of Hydrology*, **405**(1–2): 1–9. doi: 10.1016/j.jhydrol.2011.03.038

Beres M., Green A., Huggenberger P. and **Horstmeyer H.** (1995) Mapping the architecture of glaciofluvial sediments with three-dimensional georadar. *Geology*, **23**(12): 1087–1090. doi: 10.1130/0091-7613(1995)023<1087:MTAOGS>2.3.CO;2

Beres M., Huggenberger P., Green A.G. and **Horstmeyer H.** (1999) Using two- and three-dimensional georadar methods to characterize glaciofluvial architecture. *Sedimentary Geology*, **129**(1–2): 1–24. doi: 10.1016/S0037-0738(99)00053-6

Bridge J. (2009) Advances in Fluvial Sedimentology using GPR, In: *Ground Penetrating Radar Theory and Applications* (Ed. H.M. Jol), Elsevier, Amsterdam, 323–359. doi: 10.1016/B978-0-444-53348-7.00011-9

Chiogna G., Cirpka O.A., Rolle M. and **Bellin A.** (2015) Helical flow in three-dimensional nonstationary anisotropic heterogeneous porous media. *Water Resources Research*, **51**(1): 261–280. doi: 10.1002/2014WR015330

Cirpka O.A., Chiogna G., Rolle M. and **Bellin A.** (2015) Transverse mixing in three-dimensional nonstationary anisotropic heterogeneous porous media. *Water Resources Research*, **51**(1): 241–260. doi: 10.1002/2014WR015331

Grimm R.E., Heggy E., Clifford S., Dinwiddie C., McGinnis R. and **Farrell D.** (2006) Absorption and scattering in ground-penetrating radar: Analysis of the Bishop Tuff. *Journal of Geophysical Research: Planets*, **111**(E6). doi: 10.1029/2005je002619

Harbaugh A. (2005) MODFLOW-2005, The U.S. Geological Survey modular ground-water model — the ground-water flow process. Survey Techniques and Methods 6–A16, U.S. Geological Survey.

Heinz J. and **Aigner T.** (2003) Three-dimensional GPR analysis of various Quaternary gravel-bed braided river deposits (southwestern Germany). *Geological Society, London,*

Special Publications, **211**(1): 99–110.
doi: 10.1144/gsl.sp.2001.211.01.09

Heinz J., Kleineidam S., Teutsch G. and **Aigner T.** (2003) Heterogeneity patterns of Quaternary glaciofluvial gravel bodies (SW-Germany): application to hydrogeology. *Sedimentary Geology*, **158**(1–2): 1–23.
doi: 10.1016/S0037-0738(02)00239-7

Hemker K., van den Berg E. and **Bakker M.** (2004) Ground Water Whirls. *Ground Water*, **42**(2): 234–242.
doi: 10.1111/j.1745-6584.2004.tb02670.x

Huber E. and **Huggenberger P.** (2015) Morphological perspective on the sedimentary characteristics of a coarse, braided reach: Tagliamento River (NE Italy). *Geomorphology*, **248**: 111–124.
doi: doi:10.1016/j.geomorph.2015.07.015

Huggenberger P. (1993) Radar facies: recognition of facies patterns and heterogeneities within Pleistocene Rhine gravels, NE Switzerland. *Geological Society, London, Special Publications*, **75**(1): 163–176.
doi: 10.1144/GSL.SP.1993.075.01.10

Huggenberger P. and **Regli C.** (2006) A Sedimentological Model to Characterize Braided River Deposits for Hydrogeological Applications, In: *Braided Rivers* (Eds. G.H. Sambrook Smith, J.L. Best, C.S. Bristow and G.E. Petts), Blackwell Publishing Ltd., Ch. 3, 51–74.
doi: 10.1002/9781444304374.ch3

Janković I., Steward D.R., Barnes R.J. and **Dagan G.** (2009) Is transverse macrodispersivity in three-dimensional groundwater transport equal to zero? A counterexample. *Water Resources Research*, **45**(8): n/a–n/a.
doi: 10.1029/2009WR007741

Jussel P., Stauffer F. and **Dracos T.** (1994a) Transport modeling in heterogeneous aquifers: 1. Statistical description and numerical generation of gravel deposits. *Water Resources Research*, **30**(6): 1803–1817.
doi: 10.1029/94WR00162

Jussel P., Stauffer F. and **Dracos T.** (1994b) Transport modeling in heterogeneous aquifers: 2. Three-dimensional transport model and stochastic numerical tracer experiments. *Water Resources Research*, **30**(6): 1819–1831.
doi: 10.1029/94WR00163

Kitanidis P.K. (1994) The concept of the Dilution Index. *Water Resources Research*, **30**(7): 2011–2026.
doi: 10.1029/94WR00762

Klingbeil R., Kleineidam S., Asprion U., Aigner T. and **Teutsch G.** (1999) Relating lithofacies to hydrofacies: outcrop-based hydrogeological characterisation of Quaternary gravel deposits. *Sedimentary Geology*, **129**(3–4): 299–310.
doi: 10.1016/S0037-0738(99)00067-6

Kruse S.E. and **Jol H.M.** (2003) Amplitude analysis of repetitive GPR reflections on a Lake Bonneville delta, Utah, In: *Ground Penetrating Radar in Sediments* (Eds. C. Bristow and H. Jol), 211, Geological Society of London, 287–298.
doi: 10.1144/gsl.sp.2001.211.01.23

Mattle N., Kinzelbach W., Beyerle U., Huggenberger P. and **Loosli H.** (2001) Exploring an aquifer system by integrating hydraulic, hydrogeologic and environmental tracer data in a three-dimensional hydrodynamic transport model. *Journal of Hydrology*, **242**(3–4): 183–196.
doi: 10.1016/S0022-1694(00)00394-2

Mays D.C. and **Neupauer R.M.** (2012) Plume spreading in groundwater by stretching and folding. *Water Resources Research*, **48**(7): n/a–n/a.
doi: 10.1029/2011WR011567

Neupauer R.M., Meiss J.D. and **Mays D.C.** (2014) Chaotic advection and reaction during engineered injection and extraction in heterogeneous porous media. *Water Resources Research*, **50**(2): 1433–1447.
doi: 10.1002/2013WR014057

Pearson R. (2002) Outliers in process modeling and identification. *IEEE Transactions on Control Systems Technology*, **10**(1): 55–63.
doi: 10.1109/87.974338

Pollock D.W. (2012) User Guide for MODPATH Version 6 – A Particle-Tracking Model for MODFLOW. Techniques and Methods 6–A41, U.S. Geological Survey,.

Rauber M., Stauffer F., Huggenberger P. and **Dracos T.** (1998) A numerical three-dimensional conditioned/unconditioned stochastic facies type model applied to a remediation well system. *Water Resources Research*, **34**(9): 2225–2234.
doi: 10.1029/98WR01378

Siegenthaler C. and **Huggenberger P.** (1993) Pleistocene Rhine gravel: deposits of a braided river system with dominant pool preservation. *Geological Society, London, Special Publications*, **75**(1): 147–162.
doi: 10.1144/GSL.SP.1993.075.01.09

Stauffer F. (2007) Impact of highly permeable sediment units with inclined bedding on solute transport in aquifers. *Advances in Water Resources*, **30**(11): 2194–2201.
doi: 10.1016/j.advwatres.2007.04.008

Stauffer F. and **Rauber M.** (1998) Stochastic macrodispersion models for gravel aquifers. *Journal of Hydraulic Research*, **36**(6): 885–896.
doi: 10.1080/00221689809498591

Steward D.R. (1998) Stream surfaces in two-dimensional and three-dimensional divergence-free flows. *Water Resources Research*, **34**(5): 1345–1350.
doi: 10.1029/98WR00215

Teutsch G., Klingbeil R. and **Kleineidam S.** (1998) Numerical modelling of reactive transport using aquifer analogue data, In: *Groundwater Quality: Remediation and Protection* (Eds. M. Herbert and K. Kova), *IAHS Series of Proceedings and Reports*, **250**, International Association of Hydrological Sciences, IAHS Press, 381–390.

Voss C.I. (2011) Editor's message: Groundwater modeling fantasies —part 1, adrift in the details. *Hydrogeology Journal*, **19**(7): 1281–1284.
doi: 10.1007/s10040-011-0789-z

Whittaker J. and **Teutsch G.** (1999) Numerical simulation of subsurface characterization methods: application to a natural aquifer analogue. *Advances in Water Resources*, **22**(8): 819–829.
doi: 10.1016/S0309-1708(98)00056-6

Ye Y., Chiogna G., Cirpka O.A., Grathwohl P. and **Rolle M.** (2015) Enhancement of plume dilution in two-dimensional and three-dimensional porous media by flow focusing in high-permeability inclusions. *Water Resources Research*, **51**(7): 5582–5602.
doi: 10.1002/2015WR016962

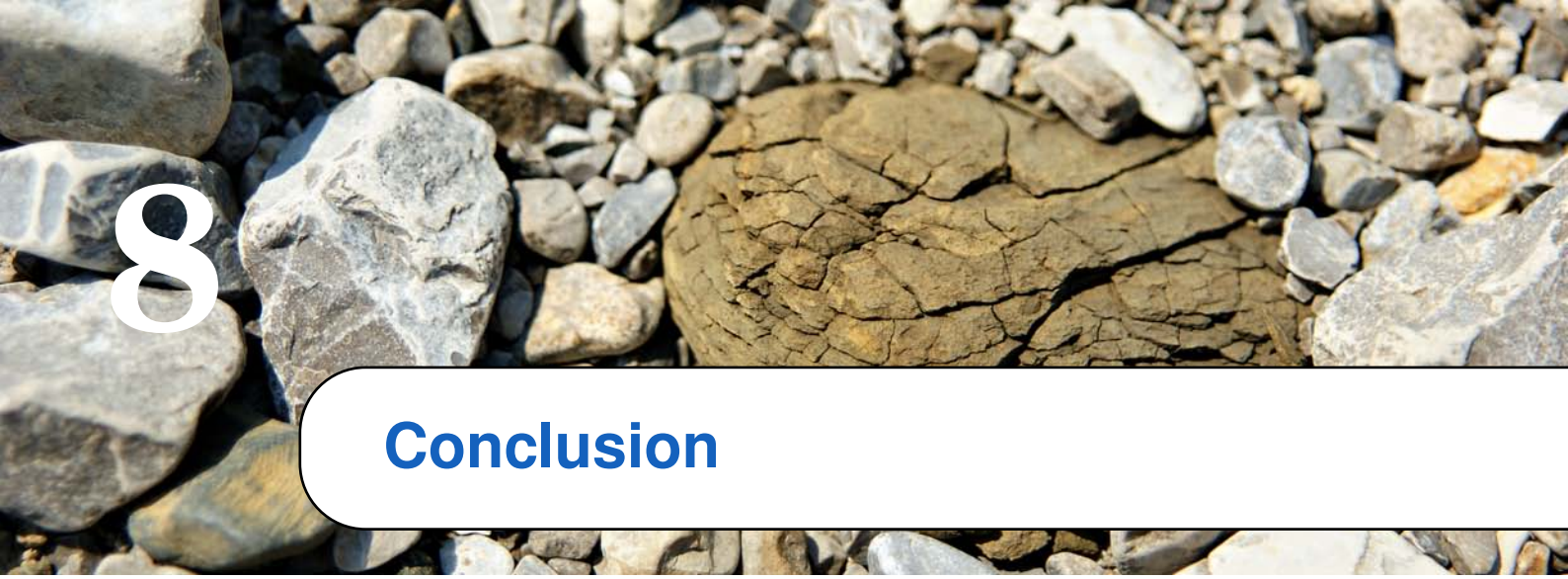

8 Conclusion

> *This is a story without end. All the world is still an America. The most promising words ever written on the maps of human knowledge are* terra incognita – *unknown territory.*
>
> **Daniel Boorstin** (1983) The Discoverers, Random House, 745 pp. ISBN: 978-0-394-72625-0

The highly heterogeneous coarse, braided river deposits form many important groundwater reservoirs in the world. Previous studies on these deposits demonstrated the importance of the trough cross stratified structures (scour fills) for subsurface flow and transport (Chapter 2). Whereas the sedimentology of coarse, braided deposits is already well described, few studies focused on the relationship between the surface processes observed in coarse, braided rivers and the resulting sedimentary structures. The main objectives of this thesis were to (i) find a relation between the morphodynamics of coarse, braided rivers and the sedimentary structures of their deposits (Chapters 4 and 5), (ii) derive a three-dimensional conceptual model to simulate braided river deposits as function of the braided river dynamics (Chapter 6), and (iii) assess the impact of braided river deposits on subsurface flow and transport (Chapter 7). A coarse, braided reach of the Tagliamento River was selected as a field laboratory to achieve the thesis objectives (Chapter 3).

E. Huber (2017) *Incorporating sedimentological observations, hydrogeophysics and conceptual knowledge to constrain 3D numerical heterogeneity models of alluvial systems.* Ph.D. thesis, Applied and Environmental Geology, University of Basel, Switzerland, 192 pp.

Main findings

This work includes the first comprehensive study on this well-studied reach of the Tagliamento River that (i) characterises the geomorphology by setting apart the trichotomy *water–vegetation–bar*, (ii) investigates the relationship between the morphology and the sedimentary characteristics probed with ground-penetrating radar (GPR), (iii) simulates the subsurface heterogeneity, and (iv) evaluates its impact on the subsurface flow field.

Relating the subsurface structure with the morphology is very challenging as the surface morphology is not representative of the subsurface heterogeneity (Chapter 4). The surface morphology must be deciphered as a low-discharge morphology (e.g., low-discharge incisions/channels, slip face lobes) superimposed on a high-discharge morphology (e.g., gravel sheets). Although the high-discharge morphology inform better on the sedimentological processes that shaped the subsurface, cut-and-fill processes at high discharge (e.g., scour formation and filling) can leave at low-discharge no clues of their occurrences. However, observations of ancient, coarse, braided river deposits indubitably highlight the important contribution of the scour fills to the subsurface heterogeneity (Chapter 2).

The morphological analysis of Chapter 4 put the importance of the low-discharge incisions/channels and higher-lying zones for the subsurface into perspective. Gravel sheets are expected to play a significant role in the formation of scours at high discharge by inducing turbulences. The migration of gravel sheets can be therefore directly related to the migration of the scours.

GPR imaging within the braidplain (Chapter 5) revealed a near-subsurface structure similar to that observed in ancient deposits (Chapter 4). A relationship between scour fills and sub-horizontal layers of gravel sheet remnants was confirmed by the GPR data. The interpretation of GPR data emphasised the role played by gravel sheets in the formation of scour fills.

A three-dimensional marked point process (MPP) simulating coarse, braided river deposits was developed (Chapter 6). An original Bayesian approach to condition this nontrivial stochastic model was presented. Such a model allows information on the three-dimensional subsurface structure to be inferred from two-dimensional GPR data. Furthermore, simple hypotheses regarding the aggradation rate and the size of the objects could be tested in light of the data. The preservation potential of the scour fill as well as their proportion can be easily quantified with the MPP.

A subsurface flow and transport simulation trough an isolated trough fill complex highlighted the marked effect of the three-dimensional distribution of open-framework–bimodal gravel (OW–BM) texture on the subsurface flow and transport (Chapter 7).

Outlook

The degree of heterogeneity in the subsurface is a function of the braided river dynamics. Future work could therefore focus the relationship between braided river dynamics, subsurface heterogeneity and its impact on subsurface flow

mixing. The braided river dynamics expressed in the deposits could be described by the preservation potential and the proportion of the scour fills. Various heterogeneity patterns could be simulated with the MPP and their impact on the subsurface flow and transport could be quantified, helping to better understand the groundwater systems. Field experiments (e.g., the combination of GPR imaging and hydraulic testing) would allow the theoretical results to be tested.

The link between morphology and subsurface heterogeneity is far from being fully explored. We suggest to monitor at a high frequency the topography of a coarse, braided reach to gain knowledge (i) on the aggradation/degradation dynamics in time and space and (ii) on the geomorphological processes. Further research should focus on the geomorphological processes at high discharge, namely the formation and migration of gravel sheets and scours. A comprehensive geomorphological analysis would serve as a basis to advance hypotheses about the subsurface heterogeneity. These hypotheses could be systematically tested with GPR imaging on the field.

Understanding the relationship between surface and subsurface is a key to integrating conceptual knowledge in subsurface process modelling and, therefore, has the potential to deepen our understanding of subsurface flow through coarse, braided river deposits.

Appendix

A Efficient deconvolution of ground-penetrating radar data

Abstract The time (vertical) resolution enhancement of ground-penetrating radar (GPR) data by deconvolution is a long-standing problem due to the mixed-phase characteristics of the source wavelet. Several approaches have been proposed, which take the mixed-phase nature of the GPR source wavelet into account. However, most of these schemes are usually laborious and/or computationally intensive and have not yet found widespread use. Here, we propose a simple and fast approach to GPR deconvolution that requires only a minimal user input. First, a trace-by-trace minimum-phase (spiking) deconvolution is applied to remove the minimum-phase part of the mixed-phase GPR wavelet. Then, a global phase rotation is applied to maximize the sparseness (kurtosis) of the minimum-phase deconvolved data to correct for phase distortions that remain after the minimum-phase deconvolution. Applications of this scheme to synthetic and field data demonstrate that a significant improvement in image quality can be achieved, leading to deconvolved data that are a closer representation of the underlying reflectivity structure than the input or minimum-phase deconvolved data. Synthetic-data tests indicate that, because of the temporal and spatial correlation inherent in the GPR data due to the frequency- and wavenumber-bandlimited nature of the GPR source wavelet and the reflectivity structure, a significant number of samples are required for a reliable sparseness (kurtosis) estimate and stable phase rotation. This observation calls into question the blithe application of kurtosis-based methods within short time windows such as that for time-variant deconvolution.

Adapted from **Schmelzbach C.** and **Huber E.** (2015) Efficient deconvolution of ground-penetrating radar data. *IEEE Transactions on Geoscience and Remote Sensing*, 53(9):5209–5217. doi:10.1109/TGRS.2015.2419235 doi: 10.1109/TGRS.2015.2419235

E. Huber (2017) *Incorporating sedimentological observations, hydrogeophysics and conceptual knowledge to constrain 3D numerical heterogeneity models of alluvial systems.* Ph.D. thesis, Applied and Environmental Geology, University of Basel, Switzerland, 192 pp.

A.1 Introduction

Surface-based ground-penetrating radar (GPR) reflection imaging is a well-established tool for high-resolution sub-surface investigation (e.g., Beres et al., 1995, 1999; Neal, 2004; Gross et al., 2004; Annan, 2005; McClymont et al., 2008; Slob et al., 2010; Schmelzbach et al., 2011b; Rodriguez et al., 2014). The detailed stratigraphic interpretation of GPR reflection images critically depends on the accuracy and optimized temporal resolution of the recordings. Unprocessed GPR data can only provide a distorted image of the subsurface because of the suboptimal shape of the wavelet embedded in the data (e.g., Dam and Schlager, 2000). This embedded wavelet is not an ideal delta function spike but is modified by the transmitter-pulse shape (e.g., Streich and van der Kruk, 2007; Warren and Giannopoulos, 2011), the antenna-to-ground-coupling (e.g., Lampe and Holliger, 2003), and the filtering effect of the Earth. All of these factors introduce amplitude distortions and time delays relative to the Earth's true reflectivity structure (impulse response).

Convolution is a linear mathematical operation that is widely used to model wave propagation in one-dimensional Earth models (e.g., Robinson and Treitel, 2000; Yilmaz, 2001). In the time domain, convolution can be illustrated with the superposition principle; given an arbitrary time series of spikes with different amplitudes and occurrence times representing, for example, the Earth's reflectivity structure and a wavelet, a convolved trace (model of the GPR trace) can be obtained by shifting a replica of the wavelet to the occurrence time of a spike, scaling it by the amplitude of the spike, and adding it to the output trace. Closely spaced spikes may lead to overlapping (interfering) waveforms. Deconvolution is the inverse operation of convolution and aims at recovering from the convolved trace the spike series given the wavelet. Under noise-free conditions, the spike series can be recovered perfectly, which means that also interference patterns due to closely spaced spikes will be perfectly resolved. Noise, however, affects deconvolution in that only a frequency-bandlimited version of the spike series can be recovered.

Deconvolution is an inverse-filtering technique used to increase the temporal (vertical) resolution of reflection data by removing the embedded wavelet (all deleterious filtering effects described previously) and recovering an estimate of the underlying reflectivity series (Robinson and Treitel, 2000). Deconvolution is widely considered to be a key step in seismic reflection processing for resolution enhancement (e.g., Yilmaz, 2001). Inverse filtering may be carried out as statistical deconvolution (spiking and predictive deconvolution; e.g., Robinson and Treitel, 2000; Yilmaz, 2001; Robinson and Treitel, 1967) , deterministic, wavelet, or signature deconvolution (e.g., Berkhout, 1977; Wood et al., 1978), or blind deconvolution (e.g., Wiggins, 1978). In contrast to seismic exploration, only a few reports of successful GPR data deconvolution have been published to date using standard deconvolution techniques (e.g., Lafleche et al., 1991; Fisher et al., 1996; Arcone et al., 1998), deterministic deconvolution employing estimates of the emitted or embedded wavelet (Gottsche et al., 1994; Neves and Miller, 1996; Xia et al., 2003, 2004; Chen and Chow, 2007; Belina et al., 2009; Economou and Vafidis, 2011, 2012), or blind-deconvolution approaches

(e.g., Porsani and Ursin, 1996; Chahine et al., 2009; Schmelzbach et al., 2011a; Li, 2014). The lack of reliable deconvolution procedures for GPR data is unsatisfactory because the image accuracy and temporal resolution of many GPR data sets could be further improved.

Standard spiking and predictive deconvolution are based on the assumption that the embedded wavelet is minimum phase (i.e., the energy distribution of the wavelet is as much front-loaded as possible for the given amplitude spectrum and the restriction of causality). However, GPR antennas usually radiate mixed-phase wavelets with maximum amplitudes roughly in the center of the wavelet (Annan, 2005). This discrepancy in energy distribution (phase characteristics) is likely responsible for the often poor performance reported for standard deconvolution applied to GPR data (Belina et al., 2009).

In contrast to standard deconvolution approaches, blind-deconvolution techniques involve less restrictive assumptions or none at all about the wavelet phase spectrum (e.g., Sacchi and Ulrych, 2000). Rather, the deconvolution process is constrained by introducing additional assumptions on the reflectivity series itself. For example, the reflectivity series may be assumed to be sparse, which means that the reflectivity series has a higher probability of extreme values compared to a Gaussian (normal) distribution. Kurtosis is a statistical measure to describe the probability distribution of a real-valued random variable; high kurtosis values are found for distributions that are more tail-loaded (sparser; more extreme values) than a Gaussian distribution. Non-Gaussian distributions of (seismic) reflection coefficients have been observed for a wide range of rock sequences (Walden and Hosken, 1986). The assumption of a sparse reflection coefficient distribution likely also holds for the electromagnetic case and hence may be used in the context of GPR deconvolution.

In reflection seismology, several deconvolution and data enhancement approaches based on maximizing the kurtosis of the deconvolution output have been presented (e.g., Wiggins, 1978; Levy and Oldenburg, 1987; White, 1988; Donoho, 1981; Longbottom et al., 1988; van der Baan, 2008; van der Baan and Fomel, 2009). For example, Economou and Vafidis (2012) applied the time-varying phase-correction technique of van der Baan (2008) to GPR data, which had been previously deconvolved deterministically with an estimated reference wavelet.

Here, we present a GPR deconvolution technique that requires only a minimal user input yet allows for an effective inverse filtering (deconvolution) of mixed-phase GPR data. We begin by demonstrating that a mixed-phase GPR wavelet can be decomposed into its uniquely determined minimum-phase equivalent and an all-pass filter. An all-pass filter is a pure phase-shift filter with unit amplitude spectrum. It passes the amplitude spectrum unaltered but changes the phase spectrum by applying frequency-dependent delays (e.g., Robinson and Treitel, 2000). We then show that, in most cases, the phase spectrum of the all-pass component can be approximated by a linear function corresponding to a time shift and a phase rotation term. This lends itself to a simple and efficient deconvolution approach for GPR data. Using a standard spiking deconvolution, the minimum-phase equivalent of the embedded GPR can readily be estimated from the reflection data and be removed. Then, in an automatic search for the

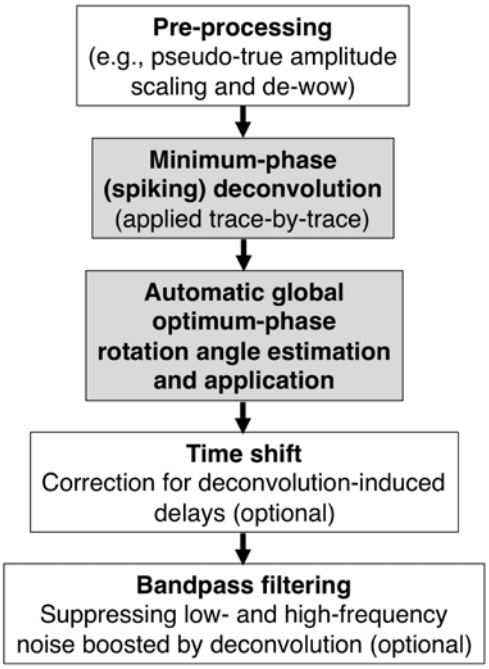

Figure A.1 – Processing scheme for ground-penetrating radar deconvolution. The elementary deconvolution steps are shown in light-gray boxes, and optional pre- and post-processing steps are shown in white boxes.

sparsest possible solution, the phase rotation angle is sought, which maximizes the kurtosis of the deconvolution output and corrects for any remaining phase distortion. Finally, we demonstrate the efficacy of our scheme for a realistic synthetic two-dimensional finite-difference data set and a field data set.

A.2 Methodology

A.2.1 Theory

We assume that a GPR trace $x(t)$ represents the convolution of a reflectivity series $r(t)$ with a stationary wavelet $w(t)$ plus some noise $n(t)$ (e.g., [14])

$$x(t) = r(t) * w(t) + n(t) \tag{A.1}$$

where $*$ denotes convolution and t represents time. For further analysis, we assume that $n(t)$ and $r(t)$ are uncorrelated and that the variance of $n(t)$ is much smaller than the variance of $r(t)$, and therefore, we ignore $n(t)$.

A mixed-phase wavelet $w(t)$ can be decomposed into a minimum-phase wavelet $m(t)$ convolved with a causal dispersive all-pass filter $p(t)$ (canonical representation of a wavelet; Robinson and Treitel, 2000; Claerbout, 1985; Robinson and Treitel, 2008)

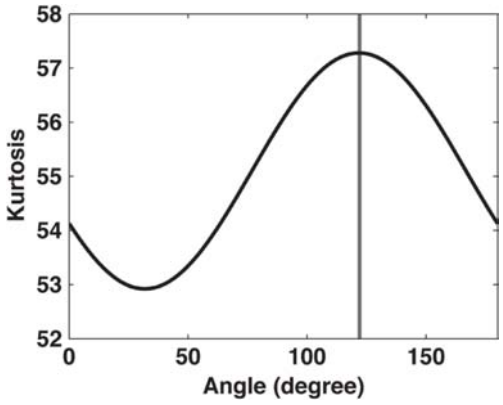

Figure A.2 – Kurtosis values plotted against the rotation angle from a sequential application of phase rotations to the minimum-phase equivalent shown in Figure A.3b. The maximum kurtosis value is found for a rotation angle of 122°.

$$w(t) = m(t) * p(t) \tag{A.2}$$

We can therefore view $m(t)$ as the minimum-phase equivalent of $w(t)$. In the frequency domain, the canonical representation is

$$|W(f)|e^{i\phi_w(f)} = |M(f)|e^{i\phi_m(f)} \cdot |P(f)|e^{i\phi_p(f)} \tag{A.3}$$

where f denotes frequency and $|W(f)|$, $|M(f)|$, and $|P(f)|$, and $\phi_w(f)$, $\phi_m(f)$, and $\phi_p(f)$ are the amplitude and phase spectra of $w(t)$, $m(t)$, and $p(t)$. $|P(f)|$ is unity, and $|W(f)|$ is equal to $|M(f)|$. The action of $p(t)$ is contained exclusively in the phase spectrum $\phi_p(f)$.

Given Equation A.1, the deconvolution objective is to compute an inverse filter $f(t)$ that converts $w(t)$ into a spike at the origin $\delta(t) = f(t) * w(t)$, where $\delta(t)$ is 1 for $t = 0$ and 0 for $t \neq 0$. Employing Equation A.2, the inverse filter for the mixed-phase deconvolution is

$$\begin{aligned} f_{\text{mixed}}(t) &= w^{-1}(t) \\ &= m^{-1}(t) * p^{-1}(t) \end{aligned} \tag{A.4}$$

Note that $m^{-1}(t)$ is minimum-phase and causal but $p^{-1}(t)$ is purely noncausal ($p^{-1}(t)$ is a time-reversed version of the causal $p(t)$ mirrored at $t = 0$).

A.2.2 Implementation

The canonical representation of a wavelet (Equations A.2 and A.3) has been used to estimate mixed-phase wavelets (Schmelzbach et al., 2011a; Porsani and Ursin, 1998; Ursin and Porsani, 2000; Misra and Sacchi, 2007; Schmelzbach and Scherbaum, 2011). These schemes differ in the way the individual components are found, but all use computationally expensive schemes to find the mixed-phase wavelet. Here, we demonstrate that the representation of $\phi_p(f)$ as a linear function is a sufficiently good approximation for wavelet estimation and

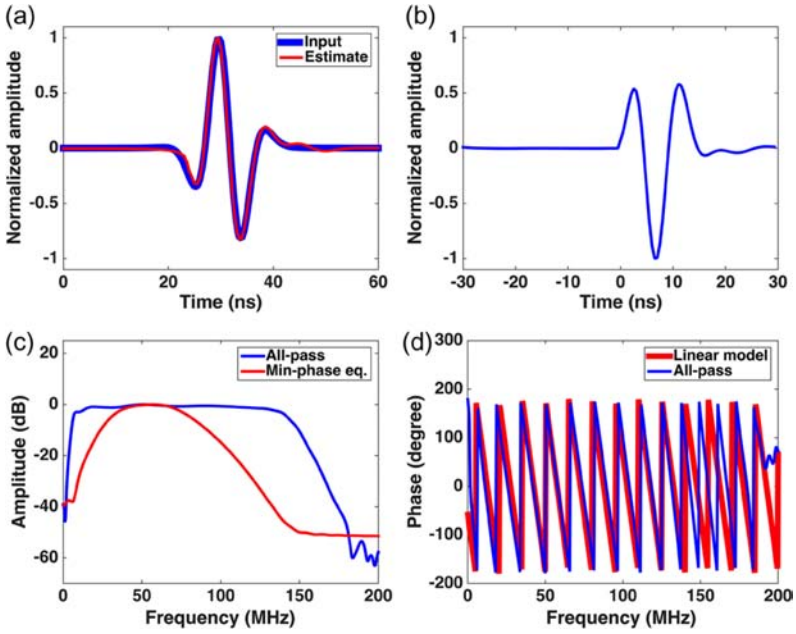

Figure A.3 – Synthetic data example. (a) Input and estimated mixed-phase ground-penetrating radar wavelet. (b) Estimated minimum-phase equivalent of the input wavelet shown in (a). (c) Amplitude spectrum of the all-pass filter and minimum-phase equivalent shown in (b). (d) Phase spectrum of the true all-pass filter plotted together with the estimated linear model for the all-pass phase spectrum.

deconvolution of GPR data. The components of $\phi_p(f)$ can then be found by an automatic search and involve minimal user input.

By taking advantage of the canonical decomposition of a mixed-phase wavelet, the estimation of $w^{-1}(t)$ (Equation A.4) can be carried out in two steps. First, $m^{-1}(t)$ is estimated from a recorded data trace $x(t)$ by, for example, solving the normal equations using the auto-correlation fucntion (ACF) of $x(t)$. In principle, this procedure corresponds to applying a standard minimum-phase spiking deconvolution (e.g., Yilmaz, 2001), requiring as user input the determination of an estimation time window and the definition of the inverse filter length. Once $m^{-1}(t)$ is computed, $m(t)$ is found by solving a second time the normal equations using the ACF of $m^{-1}(t)$.

Second, $p^{-1}(t)$ has to be estimated (Equation A.4), which involves determining the phase spectrum $\phi_p(f)$ (Equation A.3). Here, we assume that $\phi_p(f)$ can be approximated by a linear function

$$\phi_p(f) = \phi_{\text{rot}} + bf \tag{A.5}$$

The intercept ϕ_{rot} corresponds to a phase rotation, whereas the slope b relates to a time shift $\tau = \frac{b}{(2\pi f)}$. Applying a fixed (constant) phase rotation changes the shape of a wavelet. For example, $\phi_{\text{rot}} = 90°$ converts a symmetric wavelet into an antisymmetric wavelet, whereas $\phi_{\text{rot}} = 180$ corresponds to a polarity change. A phase rotation is conveniently applied to a trace $x(t)$ by employing the Hilbert transform of the trace $\mathcal{H}(x(t))$

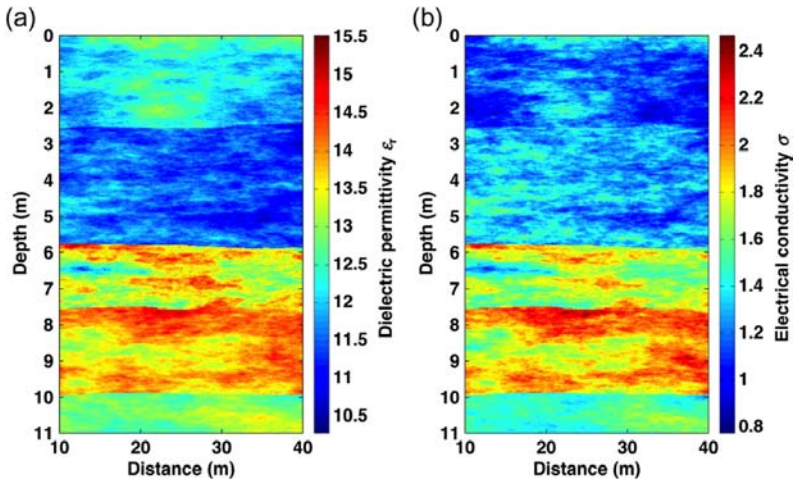

Figure A.4 – Physical parameter models for the two-dimensional finite-difference modeling. (a) Dielectric permittivity (ε_r) model. (b) Electrical conductivity (σ) model.

$$x_{\mathrm{rot}}(t) = x(t)\cos(\phi_{\mathrm{rot}}) - \mathcal{H}(x(t))\sin(\phi_{\mathrm{rot}}) \tag{A.6}$$

In order to find the optimum $\phi_{\mathrm{opt}}^{\mathrm{rot}}$, we apply a suite of phase shifts to the data after inverse minimum-phase filtering and seek the sparsest possible output. Thereby, it is sufficient to scan the rotation angle range from 0°–180°. We use the kurtosis k to measure the sparseness (e.g., White, 1988; Dodge, 2003)

$$k = \frac{\frac{1}{n}\sum_{j=1}^{n}(x_j - \bar{x})^4}{\left(\frac{1}{n}\sum_{j=1}^{n}(x_j - \bar{x})^2\right)^2} \tag{A.7}$$

where $\bar{x}$ is the mean of all samples and j denotes the sample index. The kurtosis is a statistical measure to describe the shape of a distribution. A Gaussian distribution has a kurtosis value of 3; distributions with more extreme values than the Gaussian distribution have higher kurtosis values. Once $\phi_{\mathrm{opt}}^{\mathrm{rot}}$ is found, an estimate of $w(t)$ can be obtained by applying a phase shift of $-\phi_{\mathrm{opt}}^{\mathrm{rot}}$ to $m(t)$. A remaining time shift τ will delay the deconvolved output relative to the underlying reflectivity structure. Borehole information can, for example, be used to correct for this delay. However, we deem the delay τ for most GPR applications as unimportant because the interpretation of GPR images is usually done in time relative to the first arrivals (air/ground wave). The processing flow for applying the GPR deconvolution scheme proposed here is summarized in Figure A.1.

A.3 Synthetic data example: mixed-phase wavelet estimation

In the following, we demonstrate the application of the wavelet estimation and deconvolution procedure based on the canonical model and employing a linear phase model on a simple but realistic GPR wavelet. The goal is to reconstruct the wavelet shown in Figure A.3a by applying the workflow outlined previously (Figure A.1). The minimum-phase equivalent was found by solving the normal equations twice (Figure A.3b). A sequential application of phase rotations to the minimum-phase equivalent (Figure A.3b) revealed that a phase shift of 122° yielded the highest kurtosis value (Figure A.2). The resultant estimated mixed-phase wavelet after phase rotation very closely matches the input waveform (red line in Figure A.3a).

In order to verify that a simple phase rotation is a sufficient representation of the all-pass filter, we estimated the true all-pass filter by dividing the Fourier spectrum of the input wavelet by the Fourier spectrum of the minimum-phase equivalent. The amplitude and phase spectra of the all-pass filter are displayed in Figure A.3c and d, respectively. The amplitude spectrum of the all-pass filter is flat, as expected over the signal bandwidth of $\approx 20\,\mathrm{MHz}$–$120\,\mathrm{MHz}$ (Figure A.3c). The phase spectrum closely matches a linear function of frequency: $\phi(f) = -58° + \left(-24\frac{°}{\mathrm{MHz}}\right) f$ (Figure A.3d). The intercept of −58° corresponds, after correcting for the cyclic nature of the phase spectrum, to 122° as found by the kurtosis maximization. The slope $\left(-24\frac{°}{\mathrm{MHz}}\right)$ corresponds to a time shift, which has to be defined by the user.

The observation that a short-duration mixed-phase wavelet can be decomposed into its minimum-phase equivalent and an all-pass filter with a simple linear phase spectrum is likely applicable to other GPR cases because short-duration wavelets are produced by many pulsed GPR transmitters (e.g., Streich and van der Kruk, 2007; Warren and Giannopoulos, 2011). Short pulses have a broad and smooth amplitude spectrum and consequently also a simple and smooth phase spectrum.

A.4 Realistic two-dimensional synthetic data example

Electromagnetic wave propagation depends not only on the medium dielectric permittivity (ε_r) distribution, which primarily controls the wave speed and reflectivity, but also on the medium electrical conductivity (σ) distribution. The conductivity σ and its changes in the subsurface are responsible for attenuation and complex reflection coefficients (e.g., Annan, 2005), which can affect the stationarity of the input traces. However, the convolutional model (Equation A.1) underlying the deconvolution scheme requires that the wavelet is stationary.

We tested our GPR deconvolution technique on realistic synthetic data by generating noise-free GPR recordings employing a two-dimensional finite-difference time-domain solution of Maxwell's equations (Giannopoulos, 2005).

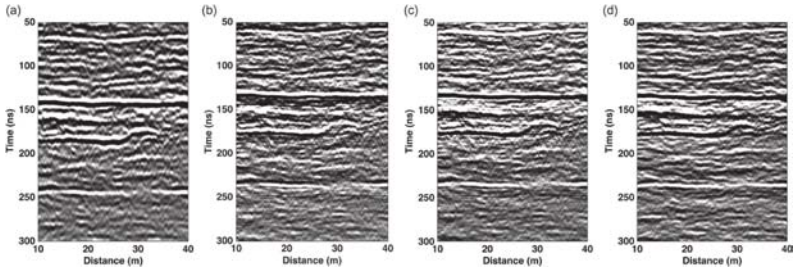

Figure A.5 – (a) Synthetic data generated using a two-dimensional finite-difference modeling scheme from the physical parameter models shown in Figure A.4 after amplitude scaling. (b) Minimum-phase (spiking) deconvolution of (a). (c) ground-penetrating radar deconvolution of (a). (d) Bandlimited reflectivity computed from the dielectric permittivity model shown in Figure A.4a.

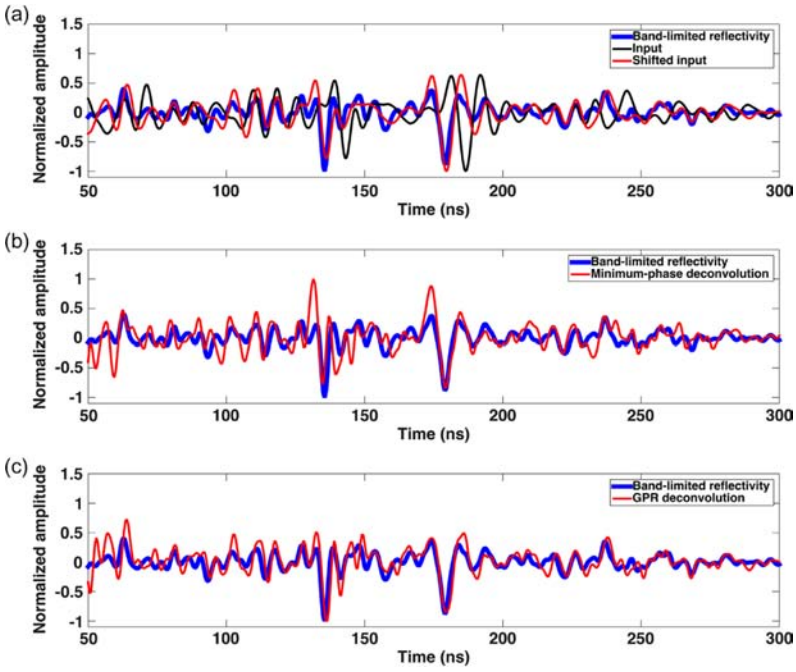

Figure A.6 – Traces extracted at 25-m distance from the synthetic data shown in Figure A.5a Bandlimited reflectivity, input data, and inputted data trace shifted to match the bandlimited reflectivity. (b) Bandlimited reflectivity and minimum-phase (spiking) deconvolution output. (c) Bandlimited reflectivity and GPR deconvolution output.

Figures A.4a and b display the sections of ε_r and σ models, respectively, that simulate a realistic water-saturated sand aquifer represented by a layered background with stochastic fine-scale structures superimposed. The stochastic variations are defined by von Kármán autocovariance functions (Holliger, 1996; Holliger K., 2003) with horizontal and vertical correlation lengths of 20 m and 1 m, respectively, leading to predominantly horizontal stratification (e.g., Western and Blöschl, 1999). The ε_r and σ values range from 10.3 mS/m to 15.5 mS/m and from 0.8 mS/m to 2.5 mS/m, with average values of 12.7 mS/m and 1.5 mS/m, respectively, which we consider realistic for saturated clay-free sediments.

We calculated a surface reflection 100-MHz GPR data set collected over the ε_r

rand σ models by moving a pair of transmitter and receiver antennas separated by 1 m in 0.1-m increments. The emitted source signal was a truncated Ricker wavelet with a central (peak) frequency of 100 MHz. Data preprocessing involved muting the highly energetic air and ground waves, and scaling the amplitudes by applying a spherical-spreading correction and an exponential-gain function. An enlarged portion of the scaled data is shown in Figure A.5a. The estimation of the spiking-deconvolution operator $m^{-1}(t)$ requires a time window that is long enough to allow for a stable estimation of the spectral properties of the operator from data. This time window should primarily contain signals (reflections). It is therefore necessary to exclude noise-dominated parts of the GPR section such as the air/ground waves and late times dominated by random noise. Because the penetration depth of GPR is limited and recording times may be short, we suggest combining the data within signal windows of several adjacent traces into one *supertrace* for a stable operator estimation but still applying the operator to the central trace only. For the synthetic example discussed here, we selected a time window ranging from 50 ns to 300 ns for the estimation of $m^{-1}(t)$ and combined 11 adjacent traces for stabilizing the filter estimation.

A comparison of the input data after minimum-phase (spiking) deconvolution (Figure A.5b) with the bandlimited reflectivity section (reflectivity derived from the ε_r model and bandpass filtered to the same frequency content as the deconvolution output) shows that minimum-phase deconvolution improves the resolution (sharpness) of the data. However, the data are contaminated by a residual phase error that is clearly visible when comparing, for example, the subhorizontal reflection at ≈ 130 ns between Figure A.5b and Figure A.5d. Also, a trace-to-trace comparison of the minimum-phase deconvolved data with the bandlimited reflectivity shown in Figure A.6b illustrates the remaining phase error in the minimum-phase deconvolved data.

A reliable estimation of the kurtosis requires a large number of samples (e.g., Schmelzbach et al., 2011a; White, 1988). We therefore estimate one global residual phase correction for all traces within the signal window (50 ns–300 ns). The GPR deconvolution output after 50 MHz–250 MHz bandpass filtering and a phase rotation of 92° of the minimum-phase deconvolution output is displayed in Figure A.5c. The deconvolved data were shifted in time to match the bandlimited reflectivity section. A comparison of the GPR deconvolution output (Figure A.5c) with the bandlimited reflectivity (Figure A.5d) and with the input data (Figure A.5a) highlights that GPR deconvolution significantly increased the vertical resolution and resulted in a section that more closely represents the underlying reflectivity structure. The averaged normalized cross-correlation between all collocated traces of the bandlimited reflectivity section and (i) the input data, (ii) the minimum-phase deconvolved section, and (iii) the GPR deconvolved section is on average −0.05, 0.61, and 0.76, respectively. These similarity values illustrate that GPR deconvolution improved to the fit of the processed data to the bandlimited reflectivity. Note that the lower correlation value of the minimum-phase deconvolved traces compared to the GPR deconvolved traces is solely due to the remaining phase error after minimum-phase deconvolution.

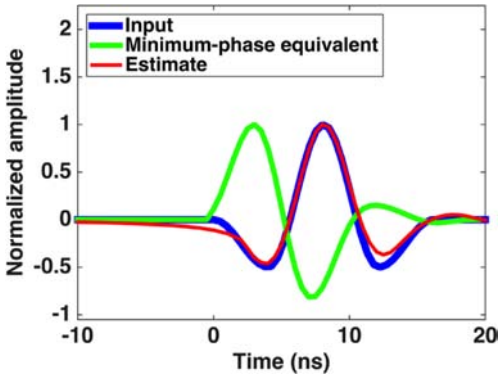

Figure A.7 – Emitted wavelet (first derivative of the injected source current in the finite-difference simulation) and average of all estimated minimum-phase equivalents and mixed-phase wavelets.

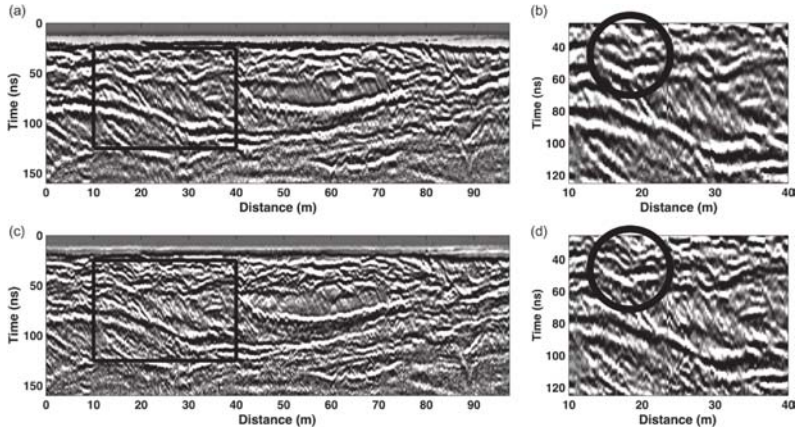

Figure A.8 – Application of the GPR deconvolution to a 100-MHz field data set. (a) Data after amplitude scaling. Black box marks zoomed-in portion shown in (b). (c) GPR deconvolution of (a). Black box marks the zoomed-in portion shown in (d). The black circle in (b) and (d) marks an example area of increased resolution.

These observations are confirmed by the trace-to-trace comparison displayed in Figure A.6; the deconvolved trace extracted from Figure A.5c matches the bandlimited reflectivity closer than the input data (e.g., at 125 ns and 175 ns). Note that the black line in Figure A.6a represents the trace extracted from the input trace data (Figure A.5a), whereas the red line corresponds to the input data shifted to match the bandlimited reflectivity (blue line) to facilitate the comparison. Furthermore, the average of all estimated mixed-phase wavelets matches the emitted source wavelet (first derivative of the injected source current) very well (Figure A.7).

A.5 Field data application

We applied our GPR deconvolution procedure to a 100-MHz GPR field data set collected over the Tagliamento braidplain in northeast Italy. The fluvial sediments at the study site consist primarily of gravel and coarse sand. The data were recorded by moving a pair of antennas separated by 1 m along

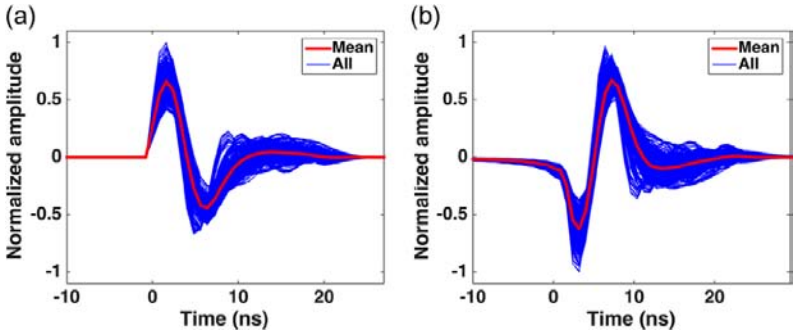

Figure A.9 – GPR wavelets estimated from the field data (Figure A.8a). (a) Minimum-phase equivalent estimated for each trace plotted in blue; the average of all estimates is superimposed in red. (b) Mixed-phase wavelet estimated for each trace plotted in blue; the average of all estimates is superimposed in red.

a 100-m-long profile at 25-cm trace spacing (391 traces, 32 stacks, and 0.8-ns sampling interval). Initial processing included interpolating the clipped airwave/ground wave amplitudes, removing the dc shift of each trace, time-zero corrections, spherical-spreading corrections, *de-wow* by high-pass frequency filtering (20 MHz–400 MHz passband), and exponential-gain scaling (e.g., Schmelzbach et al., 2012). The scaled data show a substantial penetrating depth of around 200 ns ($\approx$ 10 m depth for a velocity of 0.1 m/s) and an overall high signal-to-noise ratio indicating a favorable environment for GPR imaging (Figure A.8a).

For the estimation of the deconvolution operators, we focused on a signal time window ranging from 32 ns to 112 ns. The window starts just below the air/ground wave, and its length is a tradeoff between maximizing the length and excluding late times, when signals may be affected by absorption and noise. As in the synthetic-data example, $m^{-1}(t)$ was applied trace-by-trace but estimated based on the data from a time-space window including neighbouring traces. Parameter testing showed that combining 11 traces helps in stabilizing the estimation of the 35-sample (27.2 ns) spiking-deconvolution operator $m^{-1}(t)$ (see Figure A.9a) for the minimum-phase equivalent). A rotation angle of 134° provided the highest possible kurtosis value for all traces within the entire signal window. After deconvolution, filtering with a 15 MHz–175 MHz passband and scaling each trace by its root mean square (RMS) value completed the processing (Figure A.8c).

Deconvolution removed the mixed-phase wavelets displayed in Figure A.9b from the input data and thereby balanced the amplitude spectrum (Figure A.10). Compared to the input data (Figure A.88a and b), the deconvolved section (Figure A.8c and d) shows a significantly improved vertical resolution, and the visibility of interfering events has increased. Note, for example, the improved interpretability and increased amount of discernible details of the fluvial sediments.

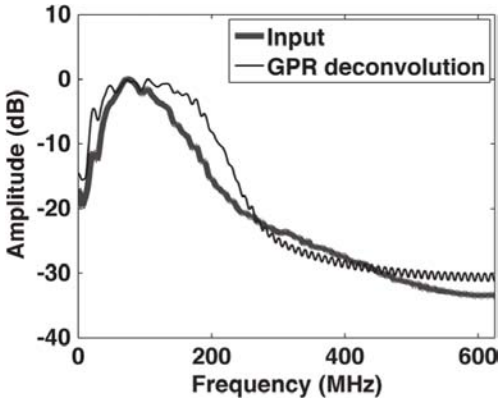

Figure A.10 – root mean square amplitude spectra of the input section (Figure A.8a) and deconvolved section (Figure A.8b).

A.6 Discussion

GPR signals may undergo changes in wavelet shape when propagating through the underground due to, for example, frequency-dependent attenuation and velocity dispersion. Significant changes in the wavelet shape may violate the stationarity assumption underlying the convolutional model (Equation A.1) and hence lead to suboptimal deconvolution results. Time-variant deconvolution techniques have been proposed to compensate for time-dependent wavelet changes (e.g., Economou and Vafidis, 2012). If kurtosis maximization is used for the deconvolution operator design, such as when applying the time-varying phase-correction technique of van der Baan (2008) or Economou and Vafidis (2012), kurtosis values may have to be estimated for short time windows or small numbers of samples.

To test the robustness of the kurtosis estimation and resultant phase correction as a function of the number of data samples, we performed the kurtosis maximization and phase-correction procedure outlined previously on data sets with increasing numbers of samples. We started by estimating the optimum phase rotation angle and corresponding kurtosis value for the first trace of the deconvolved field data set and selected the trace portion within the same signal time window as used before, which is 100 samples (80 ns) long. We then analysed progressively more neighbouring traces (combining the traces into one *super-trace*) and re-estimated the phase and kurtosis values.

For comparison, we repeated the same analysis with the synthetic reflectivity model from the tests described earlier (see FiguresA.4 and A.5). The reflectivity model was bandpass filtered to the same frequency content as the field data, and a 100-sample-long (80 ns; around 8 dominant periods for a dominant frequency of 100 MHz; Figure A.10) signal window was chosen for the analysis. Because the embedded wavelet in both the deconvolved field data and the frequency-bandlimited reflectivity is zero phase, the optimum phase rotation angle for both data sets should be 0°. The kurtosis values of the full 391-trace (39 100 samples) field data and bandlimited reflectivity are 4.6 and 9.6, respectively.

The computed phase rotation and kurtosis values are plotted against the number of samples in Figure A.11a and b, respectively. For both the field data and the bandlimited reflectivity, the kurtosis value of the entire data set (normalized value of 1) is gradually reached with an increasing number of

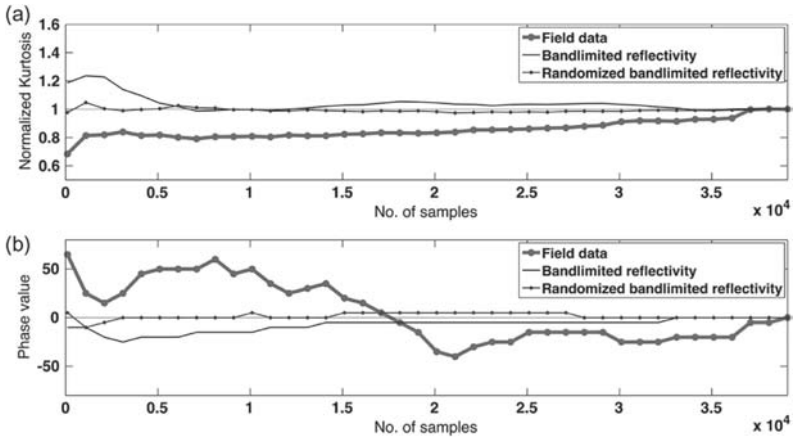

Figure A.11 – (a) Normalized kurtosis estimates as a function of increasing sample number for the deconvolved field data (see Figure A.8c), model of bandlimited reflectivity (see Figure A.5), and randomized version of the bandlimited reflectivity. Kurtosis values normalized by the corresponding value for 39 100 samples. (b) Phase estimate corresponding to the maximum kurtosis estimate shown in (a).

samples. Kurtosis value estimation of a field data set requires a consid-erable number of samples, 90 % of the final value is reached for around 30 000 samples, whereas only around 5000 samples are needed for the bandlimited reflectivity to reach close to its final value. The evolution of the kurtosis value with the number of samples, as well as the final value, may be strongly influenced by the distribution of the amplitude values within the analysis window. Prominent single reflections will dominate the kurtosis estimation, such as the reflection at around 145 ns in the bandlimited reflectivity (Figure A.5). The resultant field data phase rotation values fluctuate considerably for small sample numbers. The phase value estimates converge to a value of around $-15°$ for $>25\,000$ samples. Note that phase rotations with angles of $<15°$ are hardly visible.

GPR sections exhibit vertical as well as lateral correlation (e.g., Irving and Holliger, 2010), which are due to the frequency-bandlimited nature of GPR data and the spatial correlation (spatial bandlimited nature) of the underlying reflectivity. We assessed the influence of temporal and spatial correlation by computing the optimum phase angle and kurtosis for the bandlimited reflectivity model used before but selected the traces randomly. The resultant phase and kurtosis curves show that the full-data kurtosis value and phase angle of 0° are reached with a significantly lower number of samples (around 2000 samples). The comparison with the bandlimited reflectivity highlights the fact that a significant number of samples (number of traces and/or record length) are necessary for a stable kurtosis estimation due to the bandlimited nature of the data. Furthermore, the dependence on wavenumber and frequency band-limitation implies that the success of kurtosis estimation and, hence, the mixed-phase GPR deconvolution described here depends on the frequency bandwidth of the data and the spatial-correlation properties of the subsurface.

A.7 Conclusion

Casting the deconvolution problem of GPR data into a form that incorporates the application of a trace-by-trace minimum-phase (spiking) deconvolution followed by a global phase rotation correction to maximize the kurtosis of the GPR data enables a fast and robust resolution enhancement scheme requiring only minimal user input. The key assumptions underlying this scheme are as follows: (i) the signal stationarity within the estimation time window; (ii) the sparseness of the reflectivity; and (iii) a mixed-phase GPR wavelet can be expressed as the convolution of a minimum-phase wavelet with an all-pass filter that has a linear phase spectrum as a function of frequency. A robust estimation of the kurtosis requires a significant number of samples, with the data frequency bandwidth and the spatial-correlation properties of the underground dictating the amount.

Our GPR deconvolution approach may not only provide enhanced subsurface images with increased accuracy but should also precede any quantitative interpretation of GPR reflection amplitudes (e.g., impedance inversion and amplitude-versus-offset analysis). Our synthetic-data and field data tests showed that the approximation of the all-pass filter phase spectrum with a linear function is sufficient. However, the phase spectrum could also be approximated with other functions. The GPR deconvolution scheme discussed here requires long time series with stationary signals and hence may fail when applied to data from locations with significant frequency-dependent absorption and dispersion. Further developments could, therefore, aim at including time-dependent deconvolution approaches such as Gabor deconvolution. Whereas the examples presented here deal with GPR data, the algorithm may as well be employed to deconvolve (mixed-phase) seismic data.

Acknowledgement

The authors would like to thank S. Greenhalgh for commenting on an earlier draft of this paper and the Associate Editor and three anonymous reviewers for their comments that helped in improving the quality of this paper.

References

Annan A.P. (2005) Ground penetrating radar in near-surface geophysics, In: *Near-Surface Geophysics, Investigations in Geophysics* (Ed. D.K. Butler), Society of Exploration Geophysics, Tulsa, OK, 357–438.
ISBN:1-56080-130-1

Arcone S.A., Lawson D.E., Delaney A.J., Strasser J.C. and **Strasser J.D.** (1998) Ground-penetratinng radar reflection profiling of groundwater and bedrock in an area of

discontinuous permafrost. *Geophysics*, **63**(5): 1573–1584.
doi: 10.1190/1.1444454

Belina F., Dafflon B., Tronicke J. and **Holliger K.** (2009) Enhancing the vertical resolution of surface georadar data. *Journal of Applied Geophysics*, **68**(1): 26–35.
doi: 10.1016/j.jappgeo.2008.08.011

Beres M., Green A., Huggenberger P. and **Horstmeyer H.** (1995) Mapping the architecture of glaciofluvial sediments with three-dimensional georadar. *Geology*, **23**(12): 1087–1090.
doi: 10.1130/0091-7613(1995)023<1087:MTAOGS>2.3.CO;2

Beres M., Huggenberger P., Green A.G. and **Horstmeyer H.** (1999) Using two- and three-dimensional georadar methods to characterize glaciofluvial architecture. *Sedimentary Geology*, **129**(1–2): 1–24.
doi: 10.1016/S0037-0738(99)00053-6

Berkhout A.J. (1977) Least-square inverse filtering and wavelet deconvolution. *Geophysics*, **42**(7): 1369–1383.
doi: 10.1190/1.1440798

Chahine K., Baltazart V., Derobert X. and **Wang Y.** (2009) Blind deconvolution via independent component analysis for thin-pavement thickness estimation using GPR, In: Radar Conference - Surveillance for a Safer World, 2009. RADAR. International 1–5.

Chen Y.L. and **Chow J.J.** (2007) Ground penetrating radar signal processing improves mapping accuracy of underground voids and seawater table: an application in deteriorating coastal structure, Nanfangao Port, Taiwan. *Environmental Geology*, **53**(2): 445–455.
doi: 10.1007/s00254-007-0660-7

Claerbout J. (1985) *Fundamentals of Geophysical Data Processing*: Blackwell, Oxford, UK.

Dam R.L.V. and **Schlager W.** (2000) Identifying causes of ground-penetrating radar reflections using time-domain reflectometry and sedimentological analyses. *Sedimentology*, **47**(2): 435–449.
doi: 10.1046/j.1365-3091.2000.00304.x

Dodge Y. (2003) *The Oxford Dictionary of Statistical Terms*: Oxford Univ. Press, London, U.K.

Donoho D. (1981) On minimum entropy deconvolution, In: *Applied Time Series Analysis II* (Ed. D.F. Findley), New York, London, 565–608.

Economou N. and **Vafidis A.** (2011) Deterministic deconvolution for GPR data in the t-f domain. *Near Surface Geophysics*, **9**(5): 427–433.
doi: 10.3997/1873-0604.2011020

Economou N. and **Vafidis A.** (2012) GPR data time varying deconvolution by kurtosis maximization. *Journal of Applied Geophysics*, **81**: 117–121.
doi: 10.1109/ICGPR.2010.5550132

Fisher S.C., Stewart R.R. and **Jol H.M.** (1996) Ground Penetrating Radar (GPR) Data Enhancement Using Seismic Techniques. *Journal of Environmental and Engineering Geophysics*, **1**(2): 89–96.
doi: 10.4133/jeeg1.2.89

Giannopoulos A. (2005) Modelling ground penetrating radar by GprMax. *Construction and Building Materials*, **19**(10): 755–762.
doi: 10.1016/j.conbuildmat.2005.06.007

Gottsche F.M., Stolte C. and **Nick K.P.** (1994) Two-sided deconvolution - A Method to improve the temporal resolution in radar data, In: 56th EAEG Meeting EAGE Publications BV.

Gross R., Green A.G., Horstmeyer H. and **Begg J.H.** (2004) Location and geometry of the Wellington Fault (New Zealand) defined by detailed three-dimensional georadar data. *Journal of Geophysical Research*, **109**(B5): 1–14.
doi: 10.1029/2003jb002615

Holliger K. (1996) Upper-crustal seismic velocity heterogeneity as derived from a variety of P-wave sonic logs. *Geophysical Journal International*, **125**(3): 813–829.
doi: 10.1111/j.1365-246x.1996.tb06025.x

Holliger K. G.J. (2003) A generalised model for the 1/f-scaling nature of seismic velocity fluctuations, In: *Heterogeneity in the Crust and Upper Mantle? Nature, Scaling, and*

Seismic Properties (Eds. J.A. Goff and K. Holliger), Klu Edition, 131–154.
ISBN:0306474476

Irving J. and **Holliger K.** (2010) Geostatistical inversion of seismic and ground-penetrating radar reflection images: What can we actually resolve? *Geophysical Research Letters*, **37**(21).
doi: 10.1029/2010gl044852

Lafleche P.T., Todoeschuck J.P., Jensen O.G. and **Judge A.S.** (1991) Analysis of ground-probing radar data: predictive deconvolution. *Canadian Geotechnical Journal*, **28**(1): 134–139.
doi: 10.1139/t91-014

Lampe B. and **Holliger K.** (2003) Effects of fractal fluctuations in topographic relief, permittivity and conductivity on ground-penetrating radar antenna radiation. *Geophysics*, **68**(6): 1934–1944.
doi: 10.1190/1.1635047

Levy S. and **Oldenburg D.W.** (1987) Automatic phase correction of common-midpoint stacked data. *Geophysics*, **52**(1): 51–59.
doi: 10.1190/1.1442240

Li L. (2014) Sparsity-Promoted Blind Deconvolution of Ground-Penetrating Radar (GPR) Data. *IEEE Geosci. Remote Sensing Lett.*, **11**(8): 1330–1334.
doi: 10.1109/lgrs.2013.2292955

Longbottom J., Walden A.T. and **White R.E.** (1988) Principles and application of maximum kurtosis phase estimation. *Geophysical Prospecting*, **36**(2): 115–138.
doi: 10.1111/j.1365-2478.1988.tb02155.x

McClymont A.F., Green A.G., Streich R., Horstmeyer H., Tronicke J., Nobes D.C., Pettinga J., Campbell J. and **Langridge R.** (2008) Visualization of active faults using geometric attributes of 3D GPR data: An example from the Alpine Fault Zone, New Zealand. *Geophysics*, **73**(2): B11–B23.
doi: 10.1190/1.2825408

Misra S. and **Sacchi M.D.** (2007) Non-minimum phase wavelet estimation by non-linear optimization of all-pass operators. *Geophysical Prospecting*, **55**(2): 223–234.
doi: 10.1111/j.1365-2478.2007.00597.x

Neal A. (2004) Ground-penetrating radar and its use in sedimentology: principles, problems and progress. *Earth-Science Reviews*, **66**(3–4): 261–330.
doi: 10.1016/j.earscirev.2004.01.004

Neves F. and **Miller J.** (1996) Source signature deconvolution of ground penetrating radar data, In: 6th Int. Conf. Ground Penetrating Radar 573–578.

Porsani M.J. and **Ursin B.** (1996) Mixed-phase deconvolution of seismic and ground penetrating radar data, In: SEG Technical Program Expanded Abstracts 1996 Society of Exploration Geophysicists.

Porsani M.J. and **Ursin B.** (1998) Mixed-phase deconvolution. *Geophysics*, **63**(2): 637–647.
doi: 10.1190/1.1444363

Robinson E.A. and **Treitel S.** (1967) Principles of digital Wiener filtering ∗l. *Geophysical Prospecting*, **15**(3): 311–332.
doi: 10.1111/j.1365-2478.1967.tb01793.x

Robinson E.A. and **Treitel S.** (2000) *Geophysical Signal Analysis*: Society of Exploration Geophysicists.
ISBN:9781560801047

Robinson E.A. and **Treitel S.** (2008) *Digital Imaging and Deconvolution: The ABCs of Seismic Exploration and Processing*: 15 of Geophysical References. Soc. Exploration Geophys., Tulsa, OK, USA.

Rodriguez V., Gutierrez F., Green A.G., Carbonel D., Horstmeyer H. and **Schmelzbach C.** (2014) Characterizing Sagging and Collapse Sinkholes in a Mantled Karst by Means of Ground Penetrating Radar (GPR). *Environmental & Engineering Geoscience*, **20**(2): 109–132.
doi: 10.2113/gseegeosci.20.2.109

Sacchi M.D. and **Ulrych T.J.** (2000) Nonminimum-phase wavelet estimation using higher order statistics. *The Leading Edge*, **19**(1): 80–83.
doi: 10.1190/1.1438466

Schmelzbach C. and **Scherbaum F.** (2011) Bayesian Frequency-domain Mixed-phase Wavelet Estimation and Deconvolution, In: 73rd EAGE Conference and Exhibition incorporating SPE EUROPEC 2011 .

Schmelzbach C., Scherbaum F., Tronicke J. and **Dietrich P.** (2011a) Bayesian frequency-domain blind deconvolution of ground-penetrating radar data. *Journal of Applied Geophysics*, **75**(4): 615–630.
doi: 10.1016/j.jappgeo.2011.08.010

Schmelzbach C., Tronicke J. and **Dietrich P.** (2011b) Three-dimensional hydrostratigraphic models from ground-penetrating radar and direct-push data. *Journal of Hydrology*, **398**(3-4): 235–245.
doi: 10.1016/j.jhydrol.2010.12.023

Schmelzbach C., Tronicke J. and **Dietrich P.** (2012) High-resolution water content estimation from surface-based ground-penetrating radar reflection data by impedance inversion. *Water Resources Research*, **48**(8).
doi: 10.1029/2012WR011955

Slob E., Sato M. and **Olhoeft G.** (2010) Surface and borehole ground-penetrating-radar developments. *Geophysics*, **75**(5): A103–A120.
doi: 10.1190/1.3480619

Streich R. and **van der Kruk J.** (2007) Characterizing a GPR antenna system by near-field electric field measurements. *Geophysics*, **72**(5): A51–A55.
doi: 10.1190/1.2753832

Ursin B. and **Porsani M.J.** (2000) Estimation of an optimal mixed-phase inverse filter. *Geophysical Prospecting*, **48**(4): 663–676.
doi: 10.1046/j.1365-2478.2000.00206.x

van der Baan M. (2008) Time-varying wavelet estimation and deconvolution by kurtosis maximization. *Geophysics*, **73**(2): V11–V18.
doi: 10.1190/1.2831936

van der Baan M. and **Fomel S.** (2009) Nonstationary phase estimation using regularized local kurtosis maximization. *Geophysics*, **74**(6): A75–A80.
doi: 10.1190/1.3213533

Walden A.T. and **Hosken J.W.J.** (1986) The nature of the non-Gaussianity of primary reflection coefficients and its significance for deconvolution∗. *Geophysical Prospecting*, **34**(7): 1038–1066.
doi: 10.1111/j.1365-2478.1986.tb00512.x

Warren C. and **Giannopoulos A.** (2011) Creating finite-difference time-domain models of commercial ground-penetrating radar antennas using Taguchi's optimization method. *Geophysiscs*, **76**(2): G37–G47.
doi: 10.1190/1.3548506

Western A.W. and **Blöschl G.** (1999) On the spatial scaling of soil moisture. *Journal of Hydrology*, **217**(3–4): 203–224.
doi: 10.1016/s0022-1694(98)00232-7

White R.E. (1988) Maximum Kurtosis Phase Correction. *Geophysical Journal International*, **95**(2): 371–389.
doi: 10.1111/j.1365-246x.1988.tb00475.x

Wiggins R.A. (1978) Minimum entropy deconvolution. *Geoexploration*, **16**(1-2): 21–35.
doi: 10.1016/0016-7142(78)90005-4

Wood L.C., Heiser R.C., Treitel S. and **Riley P.L.** (1978) The deblubbling of marine source signatures. *Geophysics*, **43**(4): 715–729.
doi: 10.1190/1.1440848

Xia J., Franseen E.K., Miller R.D. and **Weis T.V.** (2004) Application of deterministic deconvolution of ground-penetrating radar data in a study of carbonate strata. *Journal of Applied Geophysics*, **56**(3): 213–229.
doi: 10.1016/j.jappgeo.2004.07.003

Xia J., Franseen E.K., Miller R.D., Weis T.V. and **Byrnes A.P.** (2003) Improving ground-penetrating radar data in sedimentary rocks using deterministic deconvolution.

Journal of Applied Geophysics, **54**(1–2): 15–33.
doi: 10.1016/s0926-9851(03)00045-4

Yilmaz O. (2001) *Seismic Data Analysis*: 2nd Edition. 10 of Investigations in Geophysics. Society Of Exploration Geophysicists, Tulsa, USA.
ISBN:1560800941

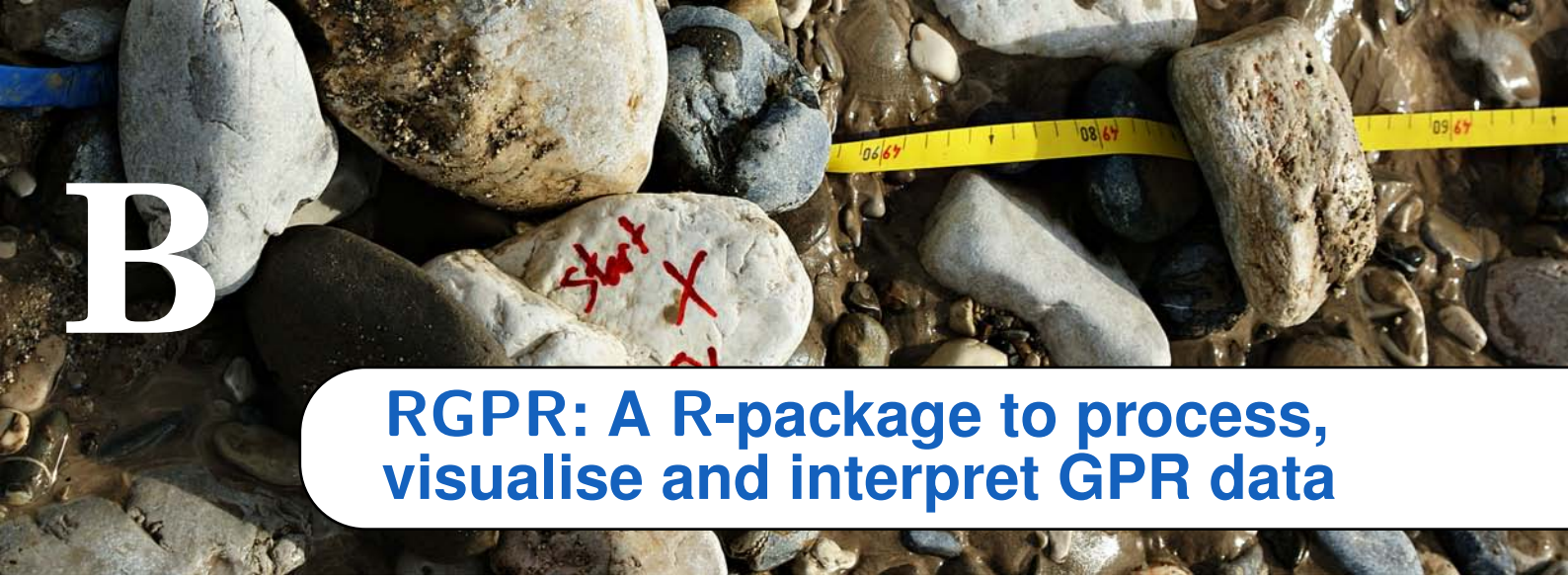

B

RGPR: A R-package to process, visualise and interpret GPR data

> *Processing of GPR data tends to improve the appearance of data, but rarely does processing substantially change the interpretation.*
>
> **Daniels *et al.*** (1997) Coincident antenna three-dimensional GPR. Journal of Environmental and Engineering Geophysics, 2(1):1–9.
> doi:10.4133/JEEG2.1.1

Abstract RGPR is an object-oriented R-package to manipulate, visualise and interpret ground-penetrating radar (GPR) data. Two classes were implemented in this package, namely GPR and GPRsurvey. While the former constitute the core of the package, the latter allows several GPR data to be manipulated at once. The package is still under construction.

Processing, visualising and interpreting GPR data with available software applications was unsatisfactory:

- I had to switch between different software applications to fully exploit some of their complementary functions;
- it was difficult to adjust the scale aspect of the plot;
- the exported plots were horrible (plot exports were based on the 'print screen' function);
- it was not easy to maintain a transparent workflow (even if some software applications allowed the processing steps to be tracked);
- adding coordinates to the GPR data was challenging.

Therefore, I started to write some R code snippets to bridge over missing functions. As the amount of code increased, I organised the code to write

E. Huber (2017) *Incorporating sedimentological observations, hydrogeophysics and conceptual knowledge to constrain 3D numerical heterogeneity models of alluvial systems.* Ph.D. thesis, Applied and Environmental Geology, University of Basel, Switzerland, 192 pp.

a R-package. The GPR data were represented by matrices (each column corresponding to a GPR trace). But some other information such as the wave velocity, the temporal and spatial sampling, the survey elevation had to be updated along with the processing of the GPR data. To avoid that the complexity of the code obscures the functionality of the package, I implemented an object-based representation of GPR data in R. Two S4 classes were created, namely the GPR class and the GPRSurvey class.

The code is freely available at

github.com/emanuelhuber/RGPR.

Some tutorials are available on the companion website

emanuelhuber.github.io/RGPR.

References

Pearson R. (2002) Outliers in process modeling and identification. *IEEE Transactions on Control Systems Technology*, **10**(1): 55–63. doi: 10.1109/87.974338

Polzehl J. and **Spokoiny V.** (2006) Local Likelihood Modeling by Adaptive Weights Smoothing. *Probability Theory and Related Fields*, **135**: 335–362.

Sabbione J.I. and **Velis D.** (2010) Automatic first-breaks picking: New strategies and algorithms. *Geophysics*, **75**(4): 67–76.

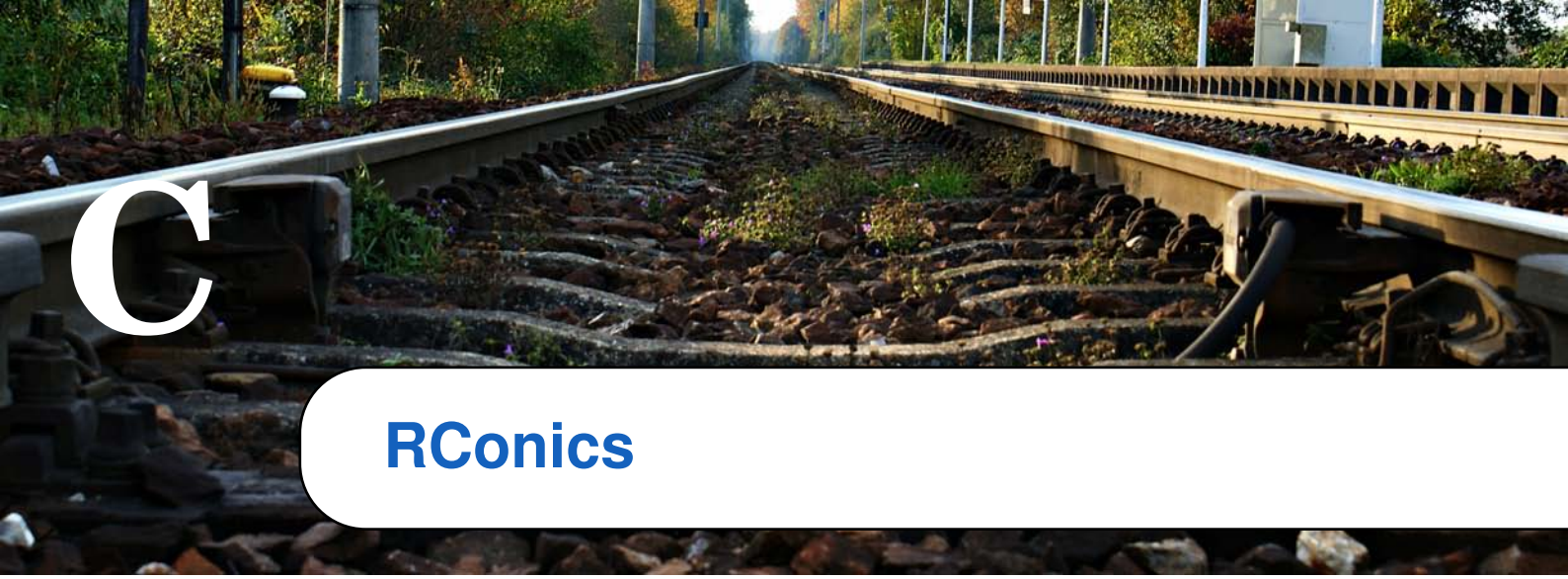

C

RConics

Abstract The R-package RConics solves some conic related problems using projective geometry: intersection of conics with lines and conics, arc length of an ellipse, polar lines, etc. This package was developed to compute algebraically the intersection of a horizontal ellipsoid with a vertical plan, as required for the stereological problem of Chapter 6.

Many of the functions of the R-packsge RConics are based on *projective* geometry. In projective geometry parallel lines meet at an infinite point and all infinite points are incident to a line at infinity. Points and lines of a projective plane are represented by *homogeneous* coordinates, that means by 3D vectors: (x, y, z) for the points and (a, b, c) such that $ax + by + c = 0$ for the lines. The Euclidean points correspond to $(x, y, 1)$, the infinite points to $(x, y, 0)$, the Euclidean lines to (a, b, c) with $a \neq 0$ or $b \neq 0$, the line at infinity to $(0, 0, 1)$. The interested reader is referred to the excellent book of Jürgen Richter-Gebert on projective geometry (Richter-Gebert, 2011). We recommend to use the R-package conics from Bernard Desgraupes to plot conics.

The R-package RConics (including the source code and the documentation) is distributed under the GNU General Public Licence version 3 at cran.r-project.org/package=RConics. Examples are provided in the package documentation.

References

Richter-Gebert J. (2011) *Perspectives on Projective Geometry - A Guided Tour Through Real and Complex Geometry*: Springer, Berlin.
ISBN:978-3-642-17285-4

Glossary

ABC Approximate Bayesian computation (ABC) constitutes a class of computational methods rooted in Bayesian statistics. [...] ABC methods bypass the evaluation of the likelihood function [...] and therefore approximate the posterior.. 103–105, 118–120, 123, 128, 130, 134, 135

accretion 'The accumulation of sediments from any cause, representing an excess of deposition over erosion' (Allaby, 2013). 21

ACF auto-correlation fucntion. 169

aggradation 'The general accumulation of unconsolidated sediments on a surface, which thereby raise its level. A large range of mechanisms may be involved, including fluvial, aeolian, marine, and slope processes.' (Allaby, 2013). 1, 8, 21, 48, 49

angular unconformity 'A discordant surface of contact between the deposits of two episodes of sedimentation in which the older, underlying strata have undergone folding, uplift, and erosion before the deposition of the younger sediments, so that the younger strata truncate the older.' (Allaby, 2013). 84, 146

asl above sea level. 33

BM bimodal gravel: A gravel consisting 'of a matrix of well-sorted medium sand that fills interstices of a framework of well-sorted pebbles and occasional cobbles' (Huggenberger and Regli, 2006). 14, 16, 19, 22, 27, 91, 141, 143, 147, 154, 155, 189

cataclasite 'Rock that has been deformed by the process of shearing and granulation (cataclasis). Cataclasites are the products of dislocation metamorphism and tectonism' (Allaby, 2013). 34

CCA canonical correlation analysis. 103, 119–122, 128, 130

CDF cumulative density function. 112

clast 'clast Particle of broken-down rock. These fragments may vary in size from boulders to silt-sized grains, and are invariably the products of erosion followed by deposition in a new setting.' (Allaby, 2013). 13, 17, 26

CMP common mid-point. 84, 89

DEM digital elevation model. 49, 50, 59

depositional element The formation of depositional elements is the result of either depositional (accretionary) processes or erosional and depositional (cut-and-fill) processes (Huggenberger and Regli, 2006) that create a morphology at a certain time. 14, 16, 17

facies 'Sum total of features that reflect the specific environmental conditions under which a given rock was formed or deposited. The features may be lithologic, sedimentological, or faunal. In a sedimentary facies, mineral composition, sedimentary structures, and bedding characteristics are all diagnostic of a specific rock or lithofacies' (Allaby, 2013).

hydrofacies 'A homogeneous, anisotropic hydrogeologic unit' (Anderson, 1989). 14, 16, 17

lithofacies 'Rock noted for a distinctive group of characteristics, e.g. composition and grain size.' (Allaby, 2013). 14, 16, 17

foreset 'The inclined surface within a cross set produced by the forward movement of the slip-face of a ripple, dune, sandwave or bar' (Allaby, 2013). 21

GM poorly-sorted, sandy gravel: A 'poorly-sorted gravel with sand and silt.' (Huggenberger and Regli, 2006). 15–18

GP poorly-sorted gravel: A 'poorly-sorted gravel, containing coarse sand, granules, pebbles and, rarely, cobbles. Clay and silt particles never make up more than 5 %' (Huggenberger and Regli, 2006). 15–19, 21, 22, 28, 64, 65, 91, 107, 108, 142, 143, 147, 151, 152, 154, 155

GPR ground-penetrating radar. 2, 4, 7, 8, 19, 79–91, 98, 104–108, 114, 133–135, 143–146, 154, 155, 160, 161, 165–169, 171–179, 183, 184

gravel sheet Relatively unaltered depositional units of gravel that form sheet-like layers that are elongated in the direction of their formative discharge, rather lobate in planform and deposited on a former topography. The gravel sheets have commonly an avalanche face at the front and lateral edges, they are a few centimetre to 2 m thick and up to 200 m wide (Hicks et al., 2002)). 18

LiDAR light detection and ranging. 57

LiDAR-derived DEM light detection and ranging derived digital elevation model. 1, 38, 42, 49–51, 54–57, 59, 68, 72, 84, 94

MAP maximum a posteriori. 103, 117, 128, 131, 135

MC Monte Carlo. 105

MCMC Markov chain Monte Carlo. 104, 105, 116–119, 123, 128, 129, 132, 135

molasse 'A term originally used to describe the mainly shallow-marine and non-marine sediments produced from the erosion of nappes (mountain belt) while uplift and deformation are still progressing' (Allaby, 2013). 38

MPP marked point process. 103–105, 109, 112–115, 123, 128, 134, 135, 160, 161

NERC U.K. Natural Environment Research Council. 49

OW open-framework gravel: 'A well-sorted gravel, in which pore space is free of sand and silt, although clay and silt particles occasionally drape the pebbles' (Huggenberger and Regli, 2006). 14, 16, 17, 27, 28, 60, 66, 67, 91, 107, 141, 143, 147, 148, 151, 152, 154, 155, 189

OW–BM open-framework–bimodal gravel: A gravel couplet of ' fining-upwards sequences consisting of bimodal gravel (BM) at the base and open-framework gravel (OW) at the top. A transition from BM to OW is generally marked by a sharp boundary between the sand in the BM and the open pores of the OW. The pebbles, however, show a continuous fining-upwards sequence from BM to OW' (Huggenberger and Regli, 2006). 16, 17, 19, 22, 28, 62, 64, 66, 107, 143, 154, 160

PDF probability density function. 112

planform The contour of an object or mass as viewed from above. 48

Pleistocene First epoch of the Quaternary period, between the Pliocene and Holocene epochs. The Pleistocene epoch lasted from 2 558 000 to about 11 800 years ago. The Pleistocene was marked by great fluctuations in temperature that caused the ice ages, with glacial periods followed by warmer interglacial periods (Allaby, 2013, Subcommission on Quaternary Stratigraphy). 1, 2, 7, 8, 13, 47, 49, 60, 98

Quaternary 'Traditionally, either a sub-era of the Cenozoic Era of geologic time that began 1.806 Ma ago and continues to the present day; it is sometimes known as the Pleistogene Period and includes the Pleistocene and Holocene epochs, during which there have been numerous ice-sheet advances in the northern hemisphere' (Allaby, 2013). 13, 19

RMS root mean square. 176

SA sand: Lenses consisting of poorly-sorted to well-sorted sand without significant silt or clay fractions (Huggenberger and Regli, 2006). 15–17, 19, 21

sedimentary structure The spatial arrangement of one or tow alternating sedimentary textures. 1, 14, 16, 17, 28

sedimentary texture A characteristic particular grain-size distribution and sediment sorting. 14, 16

SG silty gravel: A 'poorly-sorted gravel, often containing up to 30 % sand and nearly 20 % silt and clay' (Huggenberger and Regli, 2006). 15, 16

SI silt: Lenses consisting of poorly graded silt (Huggenberger and Regli, 2006). 15–17

stream Connected inundated areas of flowing water at the observation time (i.e. a planform definition that is water-stage dependent). 5

total station An electronic theodolite integrated with an electronic distance meter (EDM) that can measure slope distances.. 81, 106

References

Allaby M. (Ed.) (2013) *A Dictionary of Geology and Earth Sciences*: 4th Edition. Oxford University Press.
ISBN:978-0-199-65306-5

Anderson M.P. (1989) Hydrogeologic facies models to delineate large–scale spatial trends in glacial and glaciofluvial sediments. *Geological Society of America Bulletin*, **101**(4): 501–511.
doi: 10.1130/0016-7606(1989)101<0501:HFMTDL>2.3.CO;2

Hicks D.M., Duncan M., Walsh J., Westaway R. and **Lane S.** (2002) New views of the morphodynamics of large braided rivers from high-resolution topographic surveys and time-lapse video, In: *The structure, function and management of fluvial sedimentary systems* (Eds. F.J. Dyer, M.C. Thoms and J.M. Olley), 276, International Association of Hydrological Sciences, Wallingford, United Kingdom, 373–380.

Huggenberger P. and **Regli C.** (2006) A Sedimentological Model to Characterize Braided River Deposits for Hydrogeological Applications, In: *Braided Rivers* (Eds. G.H. Sambrook Smith, J.L. Best, C.S. Bristow and G.E. Petts), Blackwell Publishing Ltd., Ch. 3, 51–74.
doi: 10.1002/9781444304374.ch3